UNIVERSITY OF OKLAHOMA

GRADUATE COLLEGE

OPTIMIZED MICROPHYSICS RETRIEVALS FROM POLARIMETRIC RADAR DATA USING PHYSICAL CONSTRAINTS AND MACHINE LEARNING

A DISSERTATION

SUBMITTED TO THE GRADUATE FACULTY

in partial fulfillment of the requirements for the

Degree of

DOCTOR OF PHILOSOPHY

By

JUNHO HO
Norman, Oklahoma
2026

Downloaded from SHAREOK. Persistent Handle URL: https://hdl.handle.net/11244/342660

OPTIMIZED MICROPHYSICS RETRIEVALS FROM POLARIMETRIC RADAR DATA USING PHYSICAL CONSTRAINTS AND MACHINE LEARNING

A DISSERTATION APPROVED FOR THE

SCHOOL OF METEOROLOGY

BY THE COMMITTEE CONSISTING OF

Dr. Guifu Zhang, Chair

Dr. Jidong Gao, Co-Chair

Dr. David B. Parsons

Dr. Feng Xu

Dr. Vivek Mahale

Dr. Chao Lan

©Copyright by JUNHO HO 2026
All Rights Reserved.

Acknowledgements

I would like to foremost thank my family, especially my parents, for their patience, guidance, and unwavering support throughout my studies, even while I was abroad. I am also deeply grateful to my grandparents on both sides, who, despite the distance and our limited contact, have always kept me in their thoughts and supported me. I would also like to thank my brother for helping manage responsibilities that I found difficult to handle from afar. Finally, I am grateful to my uncles for their support both personally and academically, particularly for their guidance in operational meteorology and for introducing me to machine learning techniques, which became a fundamental part of my dissertation research.

I would like to express my sincere gratitude to my advisor, Professor Guifu Zhang, for his tremendous guidance and support throughout my academic journey. When I entered the meteorology program in 2017 as an undergraduate student, I was lost with limited background and direction in the field. Through his mentorship, I developed not only a foundation in radar meteorology but also the ability to think critically and approach research with a scientific philosophy that will guide my future career. I am also grateful to Professor Dave Parsons, who has known me since my freshman year. I deeply appreciate his continued interest in and support of my development as a student. I would like to extend my thanks to my committee members. Dr. Jidong Gao, my co-advisor, has provided invaluable feedback and guidance throughout my research, and I look forward to continuing to learn from him. I also thank committee members Dr. Vivek Mahale, Professor Feng Xu, and Dr. Chao Lan for their support and contributions to my work.

I am also grateful to my friends, who have been a constant and practical source of support throughout my nine years at the University of Oklahoma. Although many have graduated and moved on over time, their impact has remained significant. I would especially like to thank Xuemeng Wang for her support during both my undergraduate and graduate studies, as well as Benting Chen and Naicheng Xu for their continued encouragement, particularly during the more challenging periods of graduate school. I am also thankful to Stuart Edris, whose support as an officemate was invaluable, both in my research and on a personal level.

Lastly, I would like to appreciate the financial support by the NOAA Weather Program Office (https://ror.org/01q70bz83) under award NA25OAR459C0232 and the National Science Foundation with the grant of AGS-2527406.

This dissertation incorporates material from two studies that are either published or currently under peer review, while the final chapter is still in progress.

Ho, J., Z. Li, and G. Zhang, 2025: Quantitative error analysis of Polarimetric phased-array radar weather measurements to reveal radar performance and configuration potential. *Atmospheric Measurement Techniques*, **18**, 619–638, doi:10.5194/amt-18-619-2025.

Ho, J., G. Zhang, J. Gao, and P. Liu, 2026: Machine Learning Derived Forward Operators for Efficient Simulation and Analysis of Polarimetric Radar Data at S-, C- and X bands. Submitted to *Journal of Applied Meteorology and Climatology*

Table of Contents

Acknowledgements v

Table of Contents vii

List of Tables x

List of Figures xiii

Abstract xx

Chapter 1 Introduction 1

Chapter 2 Background 8

2.1 Polarimetric radar variables for microphysics retrievals 8

2.2 T-matrix scattering method 11

Chapter 3 Polarimetric forward operators 14

3.1 Overview of forward operators 14

3.2 Hydrometeor representation and mixing formulas 17

3.3 Scattering calculations for polarimetric radar variables 21

3.3.1 Scattering amplitudes and phases 21

3.3.2 Polarimetric variables 26

3.4 Machine learning parameterization of forward operators 35

3.4.1 ML-based parametrization 35

3.4.2 ML derived parametrized forward operator 39

3.4.3 ML-fits for C- and X-bands 45

3.5 Hydrometeor aggregation and additional physical constraints 48
3.6 Numerical experiments using WRF simulations 55
3.7 Summary 58
Chapter 4 Error analysis of polarimetric radar data 62
4.1 Overview of error analysis in polarimetric radar data 62
4.2 Polarimetric phased array radars 65
4.3 Horus and CPPAR experiment configuration 69
4.3.1 Reference measurements 72
4.3.2 Spatial and temporal calculations of errors 74
4.4 Comparison and validation of Horus and CPPAR data 75
4.4.1 Bias calculation of Horus and CPPAR data 77
4.4.2 Standard deviation estimates of Horus and CPPAR data 83
4.5 Analysis on the off-broadside dilemma of planar configuration 90
4.6 Assessing advantages and disadvantages of planar and cylindrical configurations 95
4.7 Summary 101
Chapter 5 Microphysics retrieval using physics-informed neural networks 103
5.1 Overview of microphysics retrievals 103
5.2 Design of the physics-informed neural network 106
5.3 Retrieval results from WRF simulation data 110
5.3.1 Initial experiments 110

5.3.2 Classification included retrieval 115

5.3.3 Retrieval of rain and hail 116

5.4 Retrieval results from NEXRAD data 120

5.4.1 Case overview 121

5.4.2 Data driven rain retrieval results 123

5.4.3 Rain retrieval results with physical constraint 128

5.4.4 Rain retrieval results with PINN 133

5.4.5 Additional variables and constraints for hail retrievals 137

5.4.6 Hail retrieval results with hail operator as physical constraint 139

5.4.7 Hail retrieval results with δ inclusion 142

5.5 Additional experiments 143

5.6 Summary 145

Chapter 6 Summary, conclusion and future work 148

6.1 Summary and conclusion 148

6.2 Broader impact and future work 151

Appendix 155

References 181

List of Tables

Table 3.1 The mean and standard deviation values used to standardize the neural network (NN) input variables for each hydrometeor. 37

Table 3.2. An example coefficient of ML-fitted polarimetric radar variables for hail PS mixing formulas. 41

Table 3.3. Same as Table 3.2, except for graupel. 42

Table 3.4. Same as Table 3.2, except for snow. 43

Table 4.1. Specifications relevant to the sensitivity of each PAR configuration. 69

Table 4.2. (a) Mean bias and (b) standard deviation of the differences between Horus and KTLX for each SNR range. The values in parentheses denote the median values. 79

Table 4.3. Same as Table 4.2, except for difference between CPPAR and KTLX. 82

Table 4.4. The median value for the standard deviation of six radar variables based on both (a) the spatial and (b) the temporal domain of the Horus data for five different signal-to-noise ratio (SNR) ranges. The theoretical values are selected based on middle timestep for spatial, and all 146 timesteps for temporal. The NOAA/NWS RFR represents the radar functional requirements of the NOAA and National Weather Service. 86

Table 4.5. Same as Table 4.4a, except the STDs are based on electronic scan of CPPAR. 88

Table 4.6. The table lists the advantages (+), disadvantages (-), and neutral (○) of each 2D PPAR configuration. 97

Table 4.7. The advantageous and disadvantageous properties of dish radar, 1D PPPAR, 2D PPPAR, and CPPAR for cost, data quality, update speed, calibration/maintenance methods, and potential criteria. 100

Table A1. The coefficients of ML-fitted polarimetric radar variables (Z_H, Z_{DR}, K_{DP}, ρ_{hv}, A_H, and A_{DP}) for rain at S-band. 155

Table A2. The coefficients of ML-fitted polarimetric radar variables (Z_H, Z_{DR}, K_{DP}, ρ_{hv}, δ, A_H, and A_{DP}) for hail using Maxwell Garnett water as background mixing formula (MGW) at S-band. 156

Table A3. Same as Table A2, except for graupel. 156

Table A4. Same as Table A2, except for snow. 157

Table A5. Same as Table A2, except for hail using Maxwell Garnett mixing formula with ice as the background (MGI). 158

Table A6. Same as Table A2, except for graupel using MGI. 159

Table A7. Same as Table A2, except for snow using MGI. 160

Table A8. The coefficients of ML-fitted polarimetric radar variables (Z_H, Z_{DR}, K_{DP}, ρ_{hv}, A_H, and A_{DP}) for rain at C-band. 161

Table A9. The coefficients of ML-fitted polarimetric radar variables (Z_H, Z_{DR}, K_{DP}, ρ_{hv}, δ, A_H, and A_{DP}) for hail using MGW at C-band. 162

Table A10. Same as Table A9, except for graupel using MGW. 163

Table A11. Same as Table A9, except for snow using MGW. 164

Table A12. Same as Table A9, except for hail using Polder-van Santen (PS) mixing formula. 165

Table A13. Same as Table A9, except for graupel using PS. 166

Table A14. Same as Table A9, except for snow using PS. 167

Table A15. Same as Table A9, except for hail using MGI. 168

Table A.16. Same as Table A.9, except for graupel using MGI. 168

Table A17. Same as Table A9, except for snow using MGI. 169

Table A18. The coefficients of ML-fitted polarimetric radar variables (Z_H, Z_{DR}, K_{DP}, ρ_{hv}, A_H, and A_{DP}) for rain at X-band. 170

Table A19. The coefficients of ML-fitted polarimetric radar variables (Z_H, Z_{DR}, K_{DP}, ρ_{hv}, δ, A_H, and A_{DP}) for hail using MGW at X-band. 171

Table A20. Same as Table A19, except for graupel using MGW. 172

Table A21. Same as Table A19, except for snow MGW. 173

Table A22. Same as Table A19, except for hail using PS. 174

Table A23. Same as Table A19, except for graupel using PS. 175

Table A24. Same as Table A19, except for snow using PS. 176

Table A25. Same as Table A19, except for hail using MGI. 177

Table A26. Same as Table A19, except for graupel using MGI. 178

Table A27. Same as Table A19, except for snow using MGI. 179

List of Figures

Figure 1.1. Adopted from Fig. 5 from Zhang et al. (2019). Schematic of the integrated use of polarimetric radar data (PRD), showing the linkage between observation-based retrieval and data assimilation (DA)-based methods in numerical weather prediction (NWP) model, along with the role of forward operators and statistical retrieval algorithms. The green boxes denote the main interests of this dissertation. 3

Figure 2.1. Comparison of backscattering amplitude and phase for raindrops as a function of diameter (*D*) at S-, C-, and X-band frequencies. Results from T-matrix calculations for major (light solid line) and minor axis (light dashed line) are compared with the Rayleigh scattering approximation for major (dark solid line) and minor axis (dark dashed line). Adapted from Fig. 3.20 of Zhang (2016)..... 13

Figure 3.1. Real ($\varepsilon e'$; a, c, e) and imaginary ($\varepsilon e''$; b, d, f) components of the effective dielectric constant εeat S-band as a function of bulk melting percentage γ for hail, graupel, and snow. Curves compare the Maxwell Garnett mixing formula with water background medium (MGW; blue), Maxwell Garnett with ice background medium (MGI; red), and the Polder–van Santen formula (PS; black). 20

Figure 3.2. Scattering calculations using the T-matrix numerical integration for hail at S-band with a γ of 30% under three mixing formulas: the MGW (blue), the PS (black), and MGI (red). The subplots depict (a) magnitude of the backscattering amplitudes for major ($|\ sa\pi\ |$; solid) and minor ($|\ sb\pi\ |$; dashed) axes; (b) squared ratio of major to minor backscattering magnitudes $|\ sa(\pi)\ |/|\ sb(\pi)\ |)2$; (c) backscattering phase; (d) differential backscattering phase δ; (e) real part of the

forward-scattering amplitudes; and (f) difference in the real parts of the forward-scattering amplitudes, $\mathrm{Re}sa0 - \mathrm{Re}sb0$; (g) imaginary part of the forward-scattering amplitudes; and (h) difference in the imaginary parts of the forward-scattering amplitudes, $\mathrm{Im}sa0 - \mathrm{Im}sb0$. 25

Figure 3.3. The radar variables for hail calculated using MGW, PS and MGI mixing formulas. The γ values of 0, 25, 50, 75% are shown using dotted, dash–dot, dashed, and solid line styles, respectively. Blue lines represent MGW, black lines represent PS, and red lines represent MGI. All radar variables are plotted as a function of the D_m. Reflectivity (Z_H) is shown in dBZ, differential reflectivity (Z_{DR}) in dB, specific differential phase (K_{DP}) in ° km^{-1}, and backscattering differential phase (δ) in degrees (°), horizontal specific attenuation (A_H) in dB km^{-1}, and specific differential attenuation (A_{DP}) in dB km^{-1}. 29

Figure 3.4. Same as Figure 3.3 except for graupel. 32

Figure 3.5. Same as Fig. 3.3 except for snow. 34

Figure 3.6. An example comparison plot of the fitted results of the T-matrix calculations (asterisk), polynomial fitted (red dotted line), and ML fitted (blue dotted line) hail polarimetric variables. The calculations are only depicted at 5 mm intervals of D_m, and all results are based on S-band for MGW mixing formula. The line style denotes different γ of 0 (dotted), 25 (dash-dot), 50 (dash), 75 (solid)%. 44

Figure 3.7. Same as Fig. 3.6, except for C-band without polynomial fitting. 47

Figure 3.8. Same as Fig. 3.7, except for X-band. 48

Figure 3.9. Maximum D_m as a function of γ. Results from numerical integration (solid line with circles) and the analytical formulation (dashed line with squares) are shown. The calculations are for D_0 = 5 mm..... 53

Figure 3.10. The constant altitude of polarimetric variables at 3.5 km from the WRF simulation for the three mixing formulas. The first column denotes the MGW, second PS, and the third MGI. Each row represents the radar variables, Z_H, Z_{DR}, K_{DP}, ρ_{hv}, and δ. 59

Figure 3.11. Same as Fig. 3.9, except a cross section along the 92.7 °W..... 60

Figure 4.1. Depictions of (a) Horus, (b) CPPAR, and (c) WSR–88D (KOUN) scanning strategies based on the current configuration for weather measurements. The Horus image is taken from Palmer et al. (2023). 67

Figure 4.2. Depiction of the active elements used for 5- and 13-panel measurements. The dark yellow denotes the active elements, and the lighter yellow inactive. 67

Figure 4.3. Plot of the minimum detectable reflectivity of Horus (red lines), CPPAR (blue lines), and KTLX (black lines). The solid lines are estimated from the weather measurements, and the dashed lines radar parameters..... 70

Figure 4.4. Plot of the observed Z_H from KTLX for regions of the Horus (left) at 2239 UTC on 4 October 2023, and CPPAR (right) at 1505 UTC 30 August 2019. The blue dot denotes Horus and CPPAR, and the black dot KTLX. The dashed line represents the azimuth of the Horus RHI scan, and the black solid lines the edges of the CPPAR PPI scan. 71

Figure 4.5. Spatial distribution of SNR, Z_H, Z_{DR}, and ρ_{hv} from Horus (a, c, e, and g) and KTLX (b, d, f, and h) measurements on 4 October 2023. All variables for both radars are plotted for SNR greater than 10 dB. 77

Figure 4.6. Same as Fig. 4.4, except for CPPAR and KTLX. 80

Figure 4.7. Spatial distribution of SNR, and standard deviations of Z_H, radial velocity (v_r), spectrum width (σ_v), Z_{DR}, correlation coefficient (ρ_{hv}), and differential phase shift (Φ_{DP}) for SNR greater than 10 dB from Horus weather observations based on 146 timesteps on 4 October 2023. The first column uses 17 spatial gates, and the second column only temporal samples. The black lines denote the broadside direction. 83

Figure 4.8. Same as Fig. 4.6, except for CPPAR using spatial samples on 30 August 2019..... 87

Figure 4.9. Plot of the averaged bias of Z_H, Z_{DR}, and ρ_{hv} for each steering angle away from the broadside. Only SNR greater than 20 dB, and KTLX ρ_{hv} greater than 0.95 were considered. Note that the angles range from −31.5° to 31.5°. 91

Figure 4.10. Same as Fig. 4.8 except for averaged standard deviation of Z_H, Z_{DR}, v_r, ρ_{hv}, σ_v, and Φ_{DP}. 93

Figure 4.11. Reconstructed MPAR research and development timeline based on Fig. 1 of NSSL (2014). 95

Figure 5.1. A schematic diagram of the physics-informed neural network (PINN) architecture. The architecture comprises three main components: (a) forward modelling; (b) the PINN training process; and (c) the retrieval stage, where the

trained model parameters are used to infer physical parameters from polarimetric radar inputs..... 105

Figure 5.2. The vertical cross-section of hydrometeor $D_{m,x}$ for multiple species derived from WRF simulations (left column) and corresponding PINN retrievals (right column). Each row represents a different hydrometeor class (rain, dry hail, wet hail, dry graupel, wet graupel, dry snow, and wet snow). 110

Figure 5.3. Same as Fig. 5.2, but for W_x for each hydrometeor..... 112

Figure 5.4. A cross-section of polarimetric radar variables (Z_H, Z_{DR}, K_{DP} ρ_{hv}), along with the fuzzy logic hydrometeor classification (HCA) results, compared with the two most dominant species identified from q_x..... 113

Figure 5.5. One-one scatter plots comparing the retrieved and true values of D_m and W for rain (Dmr and Wr) and hail (Dmh and Wh). The red line denotes the 1:1 relationship. Relative root-mean square error (RMSE) and bias are shown in each panel..... 115

Figure 5.6. A vertical cross-section displaying polarimetric radar variables (first row), simulated microphysics parameters for rain and hail (second row), and retrieved microphysics parameters (third row). 116

Figure 5.7. Polarimetric radar variables at 0155 UTC on 28 April 2024 during a severe weather event. Shown are (top row, left to right) Z_H, Z_{DR}, and ρ_{hv}, and (bottom row, left to right) Φ_{DP}, linear-programming estimated K_{DP}, and HCA output..... 119

Figure 5.8. The retrieval performance of the multilayer perceptron (MLP) model trained using Z_H and Z_{DR} from KTLX measurements with corresponding 2DVD data. The comparisons between 2DVD-derived and MLP-retrieved $D_{m,r}$ and W_r are shown,

along with associated error metrics (bias, RMSE, standard deviation, and correlation coefficient). 120

Figure 5.9. The rain retrieval results using a model trained using Z_H and Z_{DR} from KTLX measurements with corresponding 2DVD data. Observed radar variables (left column), retrieved (analysis) fields (middle column), and their differences (right column) are shown. 122

Figure 5.10. The retrieved rain microphysical parameters $D_{m,r}$ (left) and W_r (right) from MLP trained using Z_H and Z_{DR} from KTLX measurements with corresponding 2DVD data. 123

Figure 5.11. The rain retrieval results based on the 2DVD data training results. 124

Figure 5.12. Same as Fig. 5.8, except retrievals from MLP trained with forward operator. 125

Figure 5.13. Same as Fig. 5.9, except results from MLP trained with forward operator. 126

Figure 5.14. Same as Fig. 5.10, except results from MLP trained with forward operator. 128

Figure 5.15. Same as Fig. 5.11, except results from MLP trained with forward operator. 129

Figure 5.16. Same as Fig. 5.8, except testing results from PINN. 130

Figure 5.17. Same as Fig. 5.9, except results from PINN. 131

Figure 5.18. Same as Fig. 5.10, except results from PINN. 132

Figure 5.19. Same as Fig. 5.11, except for PINN. 133

Figure 5.20. Same as Fig. 5.9, except for hail retrievals. 136

Figure 5.21. Same as Fig. 5.10, except for hail retrievals..... 137

Figure 5.22. Same as Fig. 5.11, except for hail retrievals..... 138

Figure 5.23. The distributions of retrieved hail bulk microphysical parameter $D_{m,h}$, W_h, and γ, without δ. 139

Figure 5.24. Same as Fig. 5.23, except δ incorporated as both an input variable and a physical constraint. 139

Figure 5.25. The comparison of polarimetric radar fields (Z_H, Z_{DR}, and Φ_{DP} or K_{DP}). Observations are shown in the first row, followed by analysis fields retrieved using the Gauss–Newton iterative method (second row; Mahale et al., 2019) and the newly implemented Levenberg–Marquardt method (third row). 141

Abstract

Polarimetric weather radar observations have been widely used over the past two decades to infer precipitation structure and hydrometeor microphysics. However, their full potential remains limited by insufficient treatment of measurement and model errors, the lack of independent information in radar measurements, and the difficulty of linking polarimetric radar variables to model microphysical parameters. This dissertation aims to improve the retrieval of precipitation microphysics from polarimetric radar data (PRD), by addressing three key components: (1) development of efficient forward operators that connect model microphysical parameters to polarimetric radar variables, (2) estimation of measurement errors in polarimetric radar variables particularly polarimetric phased array radar (PPAR) measurements, and (3) development of physics-constrained retrieval algorithms that more effectively integrate or deal better with observations, forward operators, and their associated errors.

Each of these components is addressed in the following projects. First, multi-frequency polarimetric forward operators are developed to connect polarimetric variables with model state parameters, based on various mixing formulas and T-matrix scattering calculations. Machine learning (ML) parameterizations are introduced to improve computational efficiency and representativeness. Second, measurement errors in PPAR systems are analyzed using a modified error calculations that leverages their high temporal resolution to access PRD quality. The performance of planar and cylindrical PPAR configurations is evaluated, with emphasis on off-broadside observartions. Third, a physics-constrained ML approach (i.e., physically-informed neural networks, PINN) retrieval algorithm is developed to retrieve the microphysical properties of mixed hydrometeors by combining forward operators, radar observations, and improved treatment of uncertanties in both physical constraints and observations.

The developed forward operators and retrieval algorithms are evaluated through retrieval experiments using Weather Research and Forecasting (WRF) simulations, which demonstrate their capability for multispecies hydrometeor retrieval. These methods are further applied to operational NEXRAD observations for rain and hail cases. Overall, this work aims to better utilize estimated measurement errors, forward operators, and advanced retrieval algorithms to advance quantitative precipitation retrieval.

Chapter 1 Introduction

The dual-polarization upgrade of the WSR-88D systems has been a pivotal advancement for observing and interpreting both the dynamical and microphysical states of atmospheric phenomena. Early applications of polarimetric radar data (PRD) were largely qualitative, focusing on the detection and classification of severe storms, such as the identification of stratiform and convective precipitation (Yang et al., 2013; Deng et al., 2014; Yang et al., 2019; Dixon and Romatschke, 2022), hydrometeor types (Viveknanadan et al., 1999; Grazioli et al., 2014; Kouketsu et al., 2015; Besic et al., 2016; Mahale et al., 2016), and signatures associated with hail and tornado debris (Ryzhkov et al., 2005; Kaltenboeck and Ryzhkov, 2013; Snyder and Ryzhkov, 2015; Bodine et al., 2014). Over time, the use of PRD has expanded into more quantitative domains, including quantitative precipitation estimation (QPE; Ryzhkov and Zrnic, 1995; Neuper and Ehret, 2019; Ryzhkov et al., 2022; Dinh et al., 2023; Seo et al., 2026), quantitative precipitation forecasting (QPF; Bytheway et al., 2021; Liou et al., 2024), microphysical retrievals (Zhang et al., 2001; May and Keenan, 2005; Cao et al., 2010; Mahale et al., 2019; Bukovcic et al., 2018; Blanke et al., 2023; Ho et al., 2023) and convective-scale severe weather forcasts (Jung et al. 2008, 2010; Li et al. 2017; Putnam et al. 2017; Liu et al. 2026).

This dissertation focuses on improving and extending precipitation microphysics retrievals using PRD. These retrievals provide essential information for a range of downstream applications, including the estimation of precipitation-related physical parameters (e.g., rain rate), as well as model state parameters for data assimilation (DA) and forecasts (Wu et al., 2000; Yokota et al., 2016; Reimann et al., 2023). At convective scales, assimilated microphysical information strongly influence storm evolution through its impact on latent heating, cold pool generation, and

hydrometeor distributions, making accurate initialization of microphysical states critical for short-term forecasts (Hu et al., 2019; Borque et al., 2020; Chen et al., 2025).

Figure 1.1 (adapted from Zhang et al., 2019) illustrates a schematic diagram linking polarimetric radar observations, in-situ measurements, physical information from numerical weather prediction (NWP) models, and DA systems. This integrated framework demonstrates how PRD can be fully utilized to better represent the current atmospheric state and ultimately improve forecast skill. This dissertation concentrates on the components highlighted in the green boxes in Fig. 1.1. To enhance observation-based retrievals—specifically for precipitation microphysics—several key developments are required. First, efficient and physically representative polarimetric forward observation operators are needed to compensate for the limited independent information contained in PRD alone. Second, improved characterization of polarimetric measurement and model error structures is necessary to ensure accurate interpretation of radar measurements. Third, advanced retrieval algorithms should be developed to better incorporate the aforementioned uncertanties and supplementary physics-based constraints, using optimization algorithms inspired by DA methodologies, such as variational techniques. These developments enable the effective integration of observational and model-based information, leading to improved retrieval accuracy and facilitating the extension of retrievals to mixed hydrometeor species.

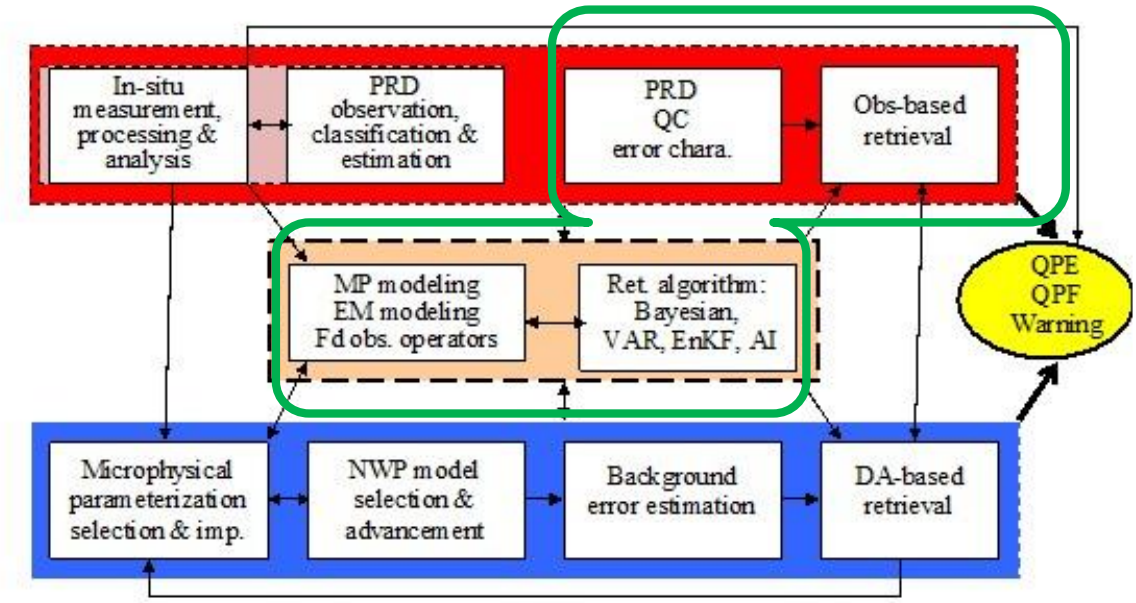

Figure 1.1 Adopted from Fig. 5 from Zhang et al. (2019). Schematic of the integrated use of polarimetric radar data (PRD), showing the linkage between observation-based retrieval and data assimilation (DA)-based methods in numerical weather prediction (NWP) model, along with the role of forward operators and statistical retrieval algorithms. The green boxes denote the main interests of this dissertation.

A major limitation in currrent PRD applications lies in the limited independent information content available from PRD alone. Many polarimetric variables are not fully independent and are influenced by overlapping microphysical properties. Especially as the retrieval problem expands to include multiple hydrometeor species, the number of independent observations is often smaller than the number of unknown microphysical state variables, leading to an underdetermined retrieval problem. This limitation necessitates the incorporation of additional constraints, such as prior information from NWP models and/or physically consistent relationships, to enable accurate and robust retrievals.

The integration of polarimetric radar measurements with model physics can further provide complementary information where the polarimetric variables alone are insufficient. This

integration balances the physical constraints from models with observational measurements, thereby enhancing forecast accuracy (Augros et al., 2015, 2018; Posselt et al., 2015; Li et al., 2017; Liu et al., 2024a, b; Chen et al., 2025). Improvements have been demonstrated in forecasting convective events—particularly heavy rainfall and hail—as well as in microphysical retrievals (Augros et al., 2015, 2018; Mahale et al., 2019; Chen et al., 2024, 2025). Furthermore, these forward operators have proven instrumental in producing more realistic representations of characteristic signatures and artifacts, such as differential reflectivity (Z_{DR}) columns, Z_{DR} arcs, and correlation coefficient (ρ_{hv}) rings (Milbrandt and Yau, 2005a, b; Kumjian and Ryzhkov, 2008; Ryzhkov et al., 2011; Kumjian et al., 2014; Snyder et al., 2017; Ilotoviz et al., 2018) from the model outputs.

A key challenge lies in the weak and often inconsistent connection between model state parameters (e.g., mixing ratios and number concentrations) and radar observables. In order to take full advantage of the dual-polarization variables, stronger linkages and constraints from the numerical model physics are necessary. However, this remains difficult because the connection between the state parameters from the numerical microphysics parameters and the polarimetric variables has not been efficiently and rigorously estabilished (Zhang et al., 2019). Despite their potential, most operational radar DA systems continue to rely primarily on reflectivity (Z_H) and radial velocity (v_r) observations (Chen et al., 2021; Park et al., 2023; Liu et al., 2024a). The commonly applied Rayleigh scattering assumption further limits accuracy because it is valid only for small and spherical particles (Ryzhkov et al., 2011; Gao and Stensrud, 2012; Pan et al., 2016). Moreover, the use of PRD within the NWP and DA communities remains limited, with only modest and often short-lived forecast improvements demonstrated to date (Posselt et al., 2015; Aksoy et al., 2010; Supinie et al., 2017; Fabry and Meunier, 2020). While some of these limitations

stem from the inherent characteristics of radar observations, such as data density, beam projection, and sampling geometry (Fabry and Meunier, 2020), model-related errors also play a significant role. In particular, inaccuracies and simplified assumptions in radar forward operators introduce correlated model and observation-operator errors, which hinder effective PRD assimilation and retrieval. These deficiencies reduce the accuracy of simulated polarimetric variables and limit the model's ability to represent the complex signatures associated with mixed-phase and non-spherical hydrometeors, including hail, graupel, and snow (Jung et al., 2010; Posselt et al., 2015; Fabry and Meunier, 2020).

Another major limitation in current PRD applications is the inadequate treatment of uncertainties in both model physics and observations. Observation errors (e.g., measurement noise and calibration bias) and background/model errors (e.g., microphysics parameterization uncertainty) are often poorly characterized or inconsistently handled (Zhang et al., 2019). This dissertation particularly focuses on the observational errors, which can be divided into observation operator errors and measurement errors. Forward operator errors—arising from simplifying assumptions in electromagnetic scattering and microphysical representations—introduce additional uncertainty and lead to correlated observation–model errors. In addition, either improved characterization of measurement errors and careful selectiion of appropriate polarimetric variables may be necessary for robust microphysical retrievals. For example, Z_{DR} and K_{DP} may be unreliable in light precipitation, where uncertainties can overwhelm the measured signals (Ryzhkov et al., 2005; Zhang et al., 2019; Aldana et al., 2025). The emergence of polarimetric phased array radars (PPAR) also introduces additional challenges, such as those associated with electronic beam steering at large off-broadside angles, particularly in planar configurations.

Current precipitation microphysics retrieval approaches are largely based on empirical and/or deterministic formulations, which often rely on simplified assumptions and do not adequately account for observation and model errors, and prior physical constraints (Zrnic et al. 2006; Zhang 2016; Zhang et al. 2019). As a result, these methods lack the ability to fully utilize the available information and to extend retrievals to mixed hydrometeor species, particularly given the insufficient independent constraints provided by PRD alone. Recent advances in ML offer an alternative by directly linking bulk microphysical parameters—such as the mass- or volume-weighted mean diameter (D_m) and water content (W)—to polarimetric radar observables, including Z_H, Z_{DR}, and specific differential phase (K_{DP}). These approaches can implicitly learn complex, nonlinear relationships and some aspects of error characteristics without explicitly specifying uncertainties. However, the fundamental limitations remains, and further advancements require addressing these underlying challenages (Ho et al., 2023). In addition, the lack of interpretability—the so-called "black box" issue—poses a significant challenge for scientific understanding and operational implementation in gaining forecaster's trust. Therefore, there is a clear need for more advanced retrieval methodologies that systematically integrate observational data, prior knowledge, and error covariance information within a unified statistical approach.

To address these challenges, this dissertation advances precipitation microphysics retrievals through three key developments. The remainder of this dissertation is organized as follows.

Chapter 2 provides background on polarimetric radar variables used in microphysics retrievals and briefly describes their connection to microphysical properties through electromagnetic scattering theory.

Chapter 3 focuses on the development and parameterization of polarimetric forward operators to bridge the gap between microphysical parameters and polarimetric radar variables. In particular,

this chapter presents T-matrix–based numerical integration calculations for computing polarimetric radar variables under different mixing formulations. These multiple operators enable the estimation of operator errors for future applications. ML–based parameter fitting is then employed to optimize the forward operators as functions of microphysical parameters. The performance of the proposed operators is evaluated using a case study of the 29 May 2019 convective event simulated with the Weather Research and Forecasting (WRF) model.

Chapter 4 addresses the characterization of measurement errors, with a focus on PPAR systems. These error characterizations are intended to inform the uncertainty estimates or error covariance matrices used to balance the various components of microphysical retrievals. Observations from planar (Horus) and cylindrical (CPPAR) PPAR configurations are evaluated against a reference operational radar, KTLX (WSR–88D). Measurement uncertainties are quantified through statistical analyses, including standard deviations, mean biases, and spatiotemporal comparisons. In particular, the impact of off-broadside sampling in planar designs is examined, and the relative advantages and limitations of CPPAR and planar configurations are discussed, along with potential directions for future system improvements.

Chapter 5 develops advanced retrieval methodologies, based on a physically constrained ML algorithm, particularly for rain–hail mixture retrievals. To the best of the author's knowledge, this represents one of the first attempts to retrieve size distributions for multiple hydrometeor species simultaneously. The variational method is used as a physically consistent benchmark to evaluate the ML approach, particularly in the absence of direct ground-truth observations. This chapter includes results from simulated experiments, and applications to real radar observations.

Chapter 6 provides a summary of the main findings and discusses implications for future research.

Chapter 2 Background

This chapter provides an overview of the polarimetric radar variables, emphasizing their physical interpretation, and relevance to microphysical retrievals. The discussion is divided into two parts. The first part presents the definitions of each variable and their relationships to microphysical quantities, including rain rate (R), D_m, and W. The second part describes the computation of scattering properties using T-matrix methods, which links the microphysical properties to the polarimetric radar variables.

2.1 Polarimetric radar variables for microphysics retrievals

The polarimetric radar variables most commonly used for rain microphysics retrievals are Z_H, Z_{DR}, and K_{DP}. The horizontal reflectivity factor Z_H (hereafter reflectivity) is the most widely used variable in both research and operational applications. Reflectivity is defined as:

$$Z_{h,v} = \frac{4\lambda^4}{\pi^4 |K_w|^2} \int |s_{hh}(\pi, D)|^2 N(D) dD \tag{2.1}$$

and is typically expressed in logarithmic units as:

$$Z_H = 10 log_{10}(Z_h). \tag{2.2}$$

Within the Rayleigh scattering regime, Z_H is proportional to the sixth moment of the drop size distribution (DSD). While such assumptions are often applied, and may be valid for rain events, they become an issue when melting hydrometeors of hail, snow, and graupel are present (Smith et al., 1975; Ferrier, 1994; Zhang et al., 2021). This high order moment dependence implies that Z_H is highly weighted toward larger drops, such that a relatively small number of large hydrometeors can dominate the signal. Because R and W are approximately proportional to the third moment of the DSD, their relationship with Z_H is inherently nonlinear. Simple Z-R relationships have been

developed (Doviak and Zrnic 1993; Rosenfeld and Ulbrich 2003), but these relationships exhibit significant variability across different precipitation regimes due to DSD dependence. To this day, DA systems often assimilate only Z_H and v_r radar variable operationally, with Z_H often being the focus of microphysics-related applications (Gastaldo et al., 2021; Kleist et al., 2024).

The Z_{DR} is the ratio between the horizontal and vertical reflectivity:

$$Z_{\mathrm{dr}} = \frac{Z_{\mathrm{h}}}{Z_{\mathrm{v}}}. \tag{2.3}$$

This variable provides information on drop shape and mean size, as oblateness increases with drop size, especially for rain. Along with Z_H, it provides additional information for microphysical applications, as it is less sensitive to the concentration than Z_H. The K_{DP} is defined as the difference between the real part of the horizontal and vertical polarizations:

$$K_{DP} = \frac{180\lambda}{\pi} \times 10^{-3} \int Re[s_{hh}(0,D) - s_{vv}(0,D)]N(D)dD. \tag{2.4}$$

This equation exhibits a lower-order moment dependence, being approximately proportional to the fourth DSD moment (~4.61; Zhang et al., 2001). This makes K_{DP} more closely related to the third DSD moment, leading to a more linear relationship with R and W. In addition, K_{DP} is immune to absolute calibration errors and is not directly affected by attenuation, which further enhances its utility for QPE, particularly in heavy rain events (Reimel and Kumjian, 2021; Aldana et al., 2025). Because K_{DP} is derived from forward propagation rather than backscattering (as in Z_H and Z_{DR}), it represents the cumulative phase shift along the radar beam. Consequently, it reflects the coherent contribution of a large number of hydrometeors and is less dominated by a small number of large drops compared to Z_H. Despite these advantages, several practical limitations remain. In light rain cases, the magnitude of K_{DP} can be small and easily overtaken by measurement errors. In addition, K_{DP} is typically estimated over multiple range gates (commonly >10) since it is the range derivative

of total differential phase (Φ_{DP}). This leads to reduced spatial resolution and potential mismatches with Z_H and Z_{DR}. These characteristics make K_{DP} highly attractive for multi-species retrievals; however, careful consideration of measurement uncertainty and robust estimation techniques are essential for its effective use.

The correlation coefficient (ρ_{hv}) is defined as the following,

$$\rho_{hv} = \frac{\int s_{hh}^{*}(\pi, D) s_{vv}(\pi, D) N(D) dD}{[\int |s_{hh}(\pi, D)|^2 N(D) dD \int |s_{vv}(\pi, D)|^2 N(D) dD]\text{^}0.5} \tag{2.5}$$

and it may not be as relevant for rain microphysics, as most of the values are very close to 1. However, for multi-species and multi-phase retrievals, ρ_{hv} may also be relevant to infer the melting stage of multiple hydrometeors. From the intrinsic value of ρ_{hv}, the backscattering differential phase (δ) can be expressed as the following:

$$\delta = -\arg(< S_{hh}^{*} S_{vv} >) \tag{2.6}$$

$$\rho_{hv} = \frac{< S_{hh}^{*} S_{vv} >}{\sqrt{Z_h Z_v}}. \tag{2.7}$$

More recently, the δ has been recognized as an important variable to be considered, especially in presence of large hail, and play a role in improving K_{DP} estimation (Trömel et al., 2013; Mishler et al., 2024).

Note that the equations provided above are based on intrinsic scattering properties. In practice, additional factors have to be accounted for including the propagation terms. If we include the propagation terms, the ρ_{hv} can be extended to

$$\tilde{\rho}'_{hv} = \frac{< n s'^{*}_{hh} s'_{vv} >}{\sqrt{< n|s'_{hh}|^2 >< n|s'_{vv}|^2 >}} = \frac{< n s^{*}_{hh} s_{vv} >}{\sqrt{< n|s_{hh}|^2 >< n|s_{vv}|^2 >}} e^{-2\int_0^r Re(K_h - K_v) dl}.$$

Then, it can be expressed as

$$\tilde{\rho}'_{hv} = \rho_{hv} e^{-j\delta_{hv}} e^{-j\phi_{dp}}.$$

where the Φ_{DP} therefore becomes the sum of δ and ϕ_{DP} (i.e., two-way sum of K_{DP}). Thus, when the δ is non-negligible, it has to be accounted for in the K_{DP} estimation process to accurately utilize K_{DP} for microphysics retrievals.

In addition, although not directly utilized in this dissertation, attenuation effects must be considered when interpreting polarimetric radar observations. In particular, two-way path-integrated attenuation (PIA) becomes significant at shorter wavelengths (e.g., C- and X-band), where signal loss due to absorption and scattering by raindrops can substantially bias measured Z_H and Z_{DR}. These attenuation effects can also be exploited for retrieval purposes. The specific attenuation (A_H) and specific differential attenuation (A_{DP}) have been used to estimate and infer microphysical properties, particularly in heavy rainfall (Huang et al., 2020; Ryzhkov et al., 2022). The specific attenuation variables are defined as:

$$A_H = \int \mathrm{Im}[s_{hh}(0,D)]N(D)dD \tag{2.8}$$

$$A_{DP} = 8.686\lambda \int \mathrm{Im}[s_{hh}(0,D) - s_{vv}(0,D)]N(D)dD. \tag{2.9}$$

2.2 T-matrix scattering method

The most important step in this work is the accurate simulation of polarimetric variables based on the hydrometeor properties. An issue in the current representations of PRD is the reliance on the Rayleigh scattering assumption. To expand our theoretical calculations to non-Rayleigh regime, the T-matrix method (Waterman 1965; Zhang, 2016) is employed. This method provides an analytical solution by linking the incident electromagnetic wave properties with the internal, and then finally onto the scattered field. The core equations are described in Eqs. (2.10–2.12).

$$\vec{E}_s(r) = \sum_{m,n}\left[a_{mn}\vec{M}_{mn}^{(4)}(kr,\theta,\phi) + b_{mn}\vec{N}_{mn}^{(4)}(kr,\theta,\phi)\right], \tag{2.10}$$

$$\vec{E}_{int}(r) = \sum_{m,n}\left[c_{mn}\vec{M}_{mn}^{(1)}(kr,\theta,\phi) + d_{mn}\vec{N}_{mn}^{(1)}(kr,\theta,\phi)\right], \tag{2.11}$$

$$\vec{E}_{i}(r) = \sum_{m,n}\left[e_{mn}\vec{M}_{mn}^{(1)}(k'r,\theta,\phi) + f_{mn}\vec{N}_{mn}^{(1)}(k'r,\theta,\phi)\right]. \tag{2.12}$$

Figure 2.1 (adapted from Fig. 20 in Zhang, 2016) compares T-matrix calculations with the Rayleigh scattering assumption for raindrops across S-, C-, and X-band frequencies, illustrating the dependence of backscattering magnitude and phase on particle diameter. As expected, the Rayleigh approximation agrees well with T-matrix results only within the small-particle (Rayleigh) regime, where the drop diameter is much smaller than the radar wavelength. However, as the diameter increases, systematic deviations emerge: the Rayleigh assumption increasingly overestimates backscattering magnitude and fails to capture the phase behavior. These discrepancies occurred at smaller diameters for shorter wavelengths (i.e., higher frequencies). These results highlight a key limitation of the Rayleigh assumption—its inability to represent non-Rayleigh scattering effects that become significant for moderate to large raindrops. In contrast, the T-matrix method provides more physically consistent results by explicitly solving the electromagnetic scattering problem for non-spherical particles. This enables more accurate simulation of polarimetric radar variables across a broader range of particle sizes and radar frequencies.

The T-matrix method also offers substantial flexibility in representing complex hydrometeor properties, including variations in particle shape, aspect ratio, surface roughness, density, and internal structure (e.g., layered, or mixed-phase particles). This capability is particularly important for modeling realistic atmospheric scatterers such as melting hydrometeors, as well as non-meteorological targets like fire ash (Zrnić et al., 2020) and tornado debris (Bodine et al., 2014), where deviations from idealized spherical assumptions are significant.

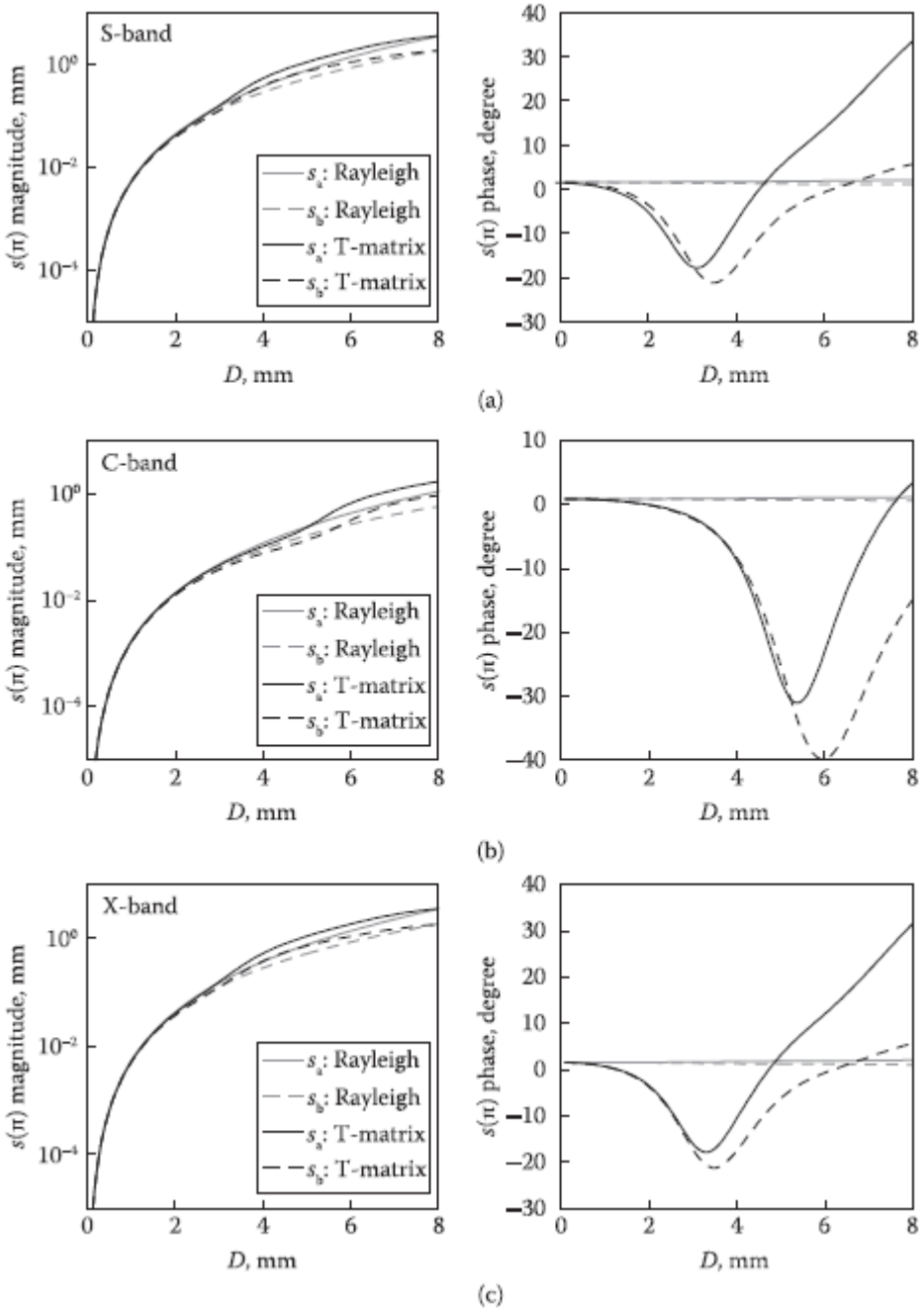

Figure 2.1. Comparison of backscattering amplitude and phase for raindrops as a function of diameter (D) at S-, C-, and X-band frequencies. Results from T-matrix calculations for major (light solid line) and minor axis (light dashed line) are compared with the Rayleigh scattering approximation for major (dark solid line) and minor axis (dark dashed line). Adapted from Fig. 3.20 of Zhang (2016).

Chapter 3 Polarimetric forward operators

This chapter addresses the first concern in the accuracy of the representation of polarimetric variables in NWP models and better connecting polarimetric information with model physics to further improve application studies. As discussed in Chapter 2.2, the initial step is to utilize the T-matrix method to calculate the polarimetric variables based on their definitions. Thus, much of the previous work on development of polarimetric forward operators relies on T-matrix numerical integrations. The objective of this study is to provide efficient, representative, and explicit polarimetric forward operators for single and double-moment microphysics schemes. Chapter 3.1 provides an overview of the previously developed T-matrix–based polarimetric forward operators. Chapter 3.2 introduces the three mixing formulas used to construct these operators. Chapter 3.3 describes the calculation of scattering amplitudes and polarimetric variables for each mixing formula. Chapter 3.4 presents the ML–based parameter fitting used to optimize the forward operators. Chapter 3.5 examines the ML-fitted and calculated polarimetric variables for the C- and X-bands, while Chapter 3.6 evaluates the performance of the proposed operators using a case study of the 29 May 2019 convective event simulated with the Weather Research and Forecasting (WRF) model.

3.1 Overview of forward operators

Polarimetric forward operators have predominantly relied on T-matrix calculations, with several studies developing and publicly releasing operators based on the numerical integration of T-matrix wave-scattering solutions (Waterman, 1965; Vivekanandan et al. 1991; Zhang et al., 2001; Jung et al., 2008, 2010). Other open-source simulators have also been released to facilitate such computations (e.g., Matsui et al., 2019). More complex multi-frequency algorithms have also

been proposed, such as the formulation of Wolfensberger and Berne (2018), which extends the operator of Ryzhkov et al. (2011) to airborne, spaceborne, and ground-based radar systems. Despite these advances, most of the current formulations are often computationally intensive, complicated, and difficult to differentiate for DA purposes.

To reduce computational cost, power-law relationships have been derived for forward and backscattering amplitudes along the major and minor axes as a function of particle size (Zhang et al., 2001; Lee et al., 2025). However, although simpler than full T-matrix calculations, these relationships can still be computationally demanding when applied across all grid points and hydrometeor categories during data assimilation. In addition, they may not fully capture the curvature and variability of scattering across realistic particle size distributions (PSD) and mixed-phase hydrometeors. Still, balancing physical rigor with computational tractability and differentiability remains challenging.

The previous PRD operators that satisfy the aforementioned criterion of efficiency, differentiability, and flexibility have been proposed and demonstrated by Zhang et al. (2021). In that work, a parameterization was introduced based on bulk microphysical properties—specifically the mass/volume-weighted mean diameter ($D_{m,x}$) and bulk melting fraction (γ)—to normalized polarimetric variables with respect to water content (W_x). In their approach, T-matrix calculations were fitted to low-order polynomial functions of bulk microphysics parameters for ice and mixed phase hydrometeors, including hail, graupel, and snow. For melting species, the fitting coefficients are further expressed as polynomial functions of the melting fraction, yielding a two-stage parameterization. The operators were shown to reproduce realistic polarimetric signatures in both idealized and real-case simulations while reducing computational cost by more than two orders of magnitude compared to direct numerical integration. Further evaluation was conducted

in Liu et al. (2024b), where an updated melting model was incorporated into the polynomial-based forward operators, leading to improved representation of melting-layer polarimetric signatures in a supercell case. Despite these advantages, the polynomial structure limits the flexibility to fully represent the complex scattering behavior. Fixed low-order polynomials in D_{m} may have difficulty capturing localized curvature, non-monotonic responses associated with resonance effects and coupled nonlinear interactions between particle size and melting state. These parameterized operators have been demonstrated for direct assimilation, while substantially improving computational efficiency and ensuring differentiability (Liu et al., 2024b, 2026).

Nevertheless, previous studies remain limited in their ability to simultaneously achieve computational efficiency and differentiability while accurately capturing the full curvature and regime-dependent variability of polarimetric signatures. This study builds on the parameterized operators introduced by Zhang et al. (2021) and presents three main developments. First, we revisit the treatment of mixing formulas for mixed-phase hydrometeors to evaluate the effect of dielectric constants on polarimetric signatures. Most previous polarimetric operators rely on the classical Maxwell Garnett (MG) mixing formula (Maxwell Garnett, 1904; Bohren and Battan 1980, 1982), which emphasizes the assumed background (host) medium. The Polder–van Santen (PS) mixing formula (Polder and van Santen, 1946) is incorporated as an alternative mixing formula to provide greater flexibility in selecting the most appropriate formulation for a given microphysical scenario. Second, a ML algorithm is employed to improve the fit of PRD as a function of $D_{\mathrm{m,x}}$, thereby reducing operator errors and increasing the robustness of the fitting and parameterization. Finally, the operators are extended to additional frequencies (C- and X-band systems) and to additional phase- and attenuation-based polarimetric variables (δ and attenuation terms). Because the WSR-

88D operational radar network operates at S-band, the results discussed here focus on S-band performance.

3.2 Hydrometeor representation and mixing formulas

The numerical calculations establish the physical basis and assumptions of the forward radar operator used in this study. First, the complex dielectric constants of the mixed-phase hydrometeors are computed under assumed microphysical compositions. These dielectric properties are then used in the T-matrix calculation to determine the scattering amplitudes for individual particles with assumed shape and orientation. Finally, by integrating the single-particle scattering quantities over an exponential size distribution, the bulk polarimetric radar variables are obtained. These numerically computed radar variables serve as the reference solutions for developing and validating the parameterized forward operators described in Chapter 3.3.

The complex dielectric constants (ε_e) of mixed-phase hydrometeors are calculated using three approaches: MG with water as background media (MGW), MG with ice as background media (MGI), and the PS. These dielectric constants are then applied in T-matrix calculations to obtain the forward- and backward-scattering amplitudes for various γ values and radar frequencies at the S-, C-, and X-bands. From these amplitudes, the polarimetric variables are computed (Zhang, 2016). The wavelengths used for the three bands (i.e., the S-, C-, and X-bands) are 10.7, 5.46, and 3.23 cm, respectively. The T-matrix calculations are conducted for particle diameters ranging from 0.08 to 80 mm, with an increment of 0.08 mm to minimize truncation errors. Other simulation parameters follow those of Jung et al. (2008) and Zhang et al. (2021): hail, snow, and graupel densities of 0.92, 0.10, and 0.50 g cm^{-3}, respectively; an axis ratio of 0.7 for all three species; and

a mean canting angle of zero, with a standard deviation defined as $\sigma = 60°(1 - 0.8\gamma)$ for hail and graupel, and 30° for snow. Although alternative equations and/or criteria for aspect/axis ratios from Ryzhkov et al. (2011) have been explored, the resulting differences were not substantial; therefore, the original values were retained.

The polarimetric radar forward operators depend on the effective dielectric permittivity ε_e, whose real (ε_e') and imaginary (ε_e'') components govern scattering intensity and dielectric losses. In radar meteorology and NWP applications, the MG mixing formula is commonly used to estimate ε_e for mixed-phase hydrometeors. However, for partially melted particles, the background-medium assumption inherent in MG becomes ambiguous. In mixtures of air, ice, and liquid water—such as melting hail, graupel, and snow—the resulting ε_e value depends on which phase is treated as the background/matrix, introducing topology-dependent variability (Meneghini and Liao, 1996; Carlin and Ryzhkov, 2019). The MG mixing formula is also less reliable when inclusion volume fractions are moderate to large or when the internal structure is highly heterogeneous (Bohren, 1986; Meneghini and Liao, 1996), as observed in melting aggregates, porous snow, and hail with liquid shells (Knight, 1979; Bringi et al., 1986a,b; Aydin and Zhao, 1990; Mitra et al., 1990; Fabry and Szyrmer, 1999). To address these limitations, weighted MG variants (Meneghini and Liao, 1996; Matrosov, 2008; Ryzhkov et al., 2011), the Bruggeman (1935), and the PS formulas have been proposed. In this study, the PS is included alongside the MG, as it treats constituent phases symmetrically and yields an intermediate effective dielectric constant when no single phase clearly dominates. Because MG and PS are based on different physical assumptions and are applicable to different mixture regimes, forward operators are calculated and developed for both mixing formulas. Note that air and ice are first combined using the PS method to form dry graupel and snow, which are then mixed with water to represent

progressive melting. For dry graupel and snow, the MG mixing formulas (whether using air or ice as the background medium) and the PS method yield only small differences in the calculated dielectric properties. Further details of the ε_e calculations for the three mixing approaches are given in Section 2.2.4 of Zhang (2016).

The real (ε_e'; left column) and imaginary (ε_e''; right column) components of ε_e at S-band as a function of γ for hail, graupel, and snow are displayed in Fig. 3.1. The MG mixing formula with water as the background medium (MGW; blue curves) produces the largest values of both ε_e' and ε_e'' over much of the melting range, reflecting the strong dielectric contrast between liquid water and ice or air inclusions. In contrast, the MG formula with ice as the background medium (MGI; red curves) yields the smallest values until near full melting, at which point all formulas converge toward water-like behavior. The PS solution (black curves) lies between the two MG limits and provides a smoother, more gradual transition across intermediate melting fractions.

The trends are consistent across the three hydrometeors. For hail, which has a relatively high bulk density (0.92 gm^{-3}), MGW tends to estimate the largest values of both ε_e' and ε_e'' (Figs. 3.1a, b). The PS produces intermediate values similar to MGI at lower γ (~20%) and to MGW at higher γ (~80%). After about 25% melting, MGI shows significantly lower ε_e' and ε_e'' compared to the other two approaches. The discrepancies among the mixing formulas become more pronounced for graupel and snow (Figs. 3.1 c–f), because these lower-density hydrometeors consist of varying proportions of air, ice, and liquid water, with lower bulk densities. MGW yields elevated ε_e' and ε_e'' even at moderate melting fractions, whereas the MGI formulation delays the increase until near-complete melting. The PS again produces intermediate values, particularly in the transition regime where neither ice nor water clearly dominates. The differences between graupel and snow primarily reflect their bulk densities, with snow exhibiting smaller real and imaginary components

than graupel throughout the melting process. The ε_e values at C- and X-band exhibit trends similar to those at S-band across the three mixing formulas, except that the real component decreases with increasing frequency as molecular polarization becomes less efficient, while the imaginary component increases due to stronger dielectric losses.

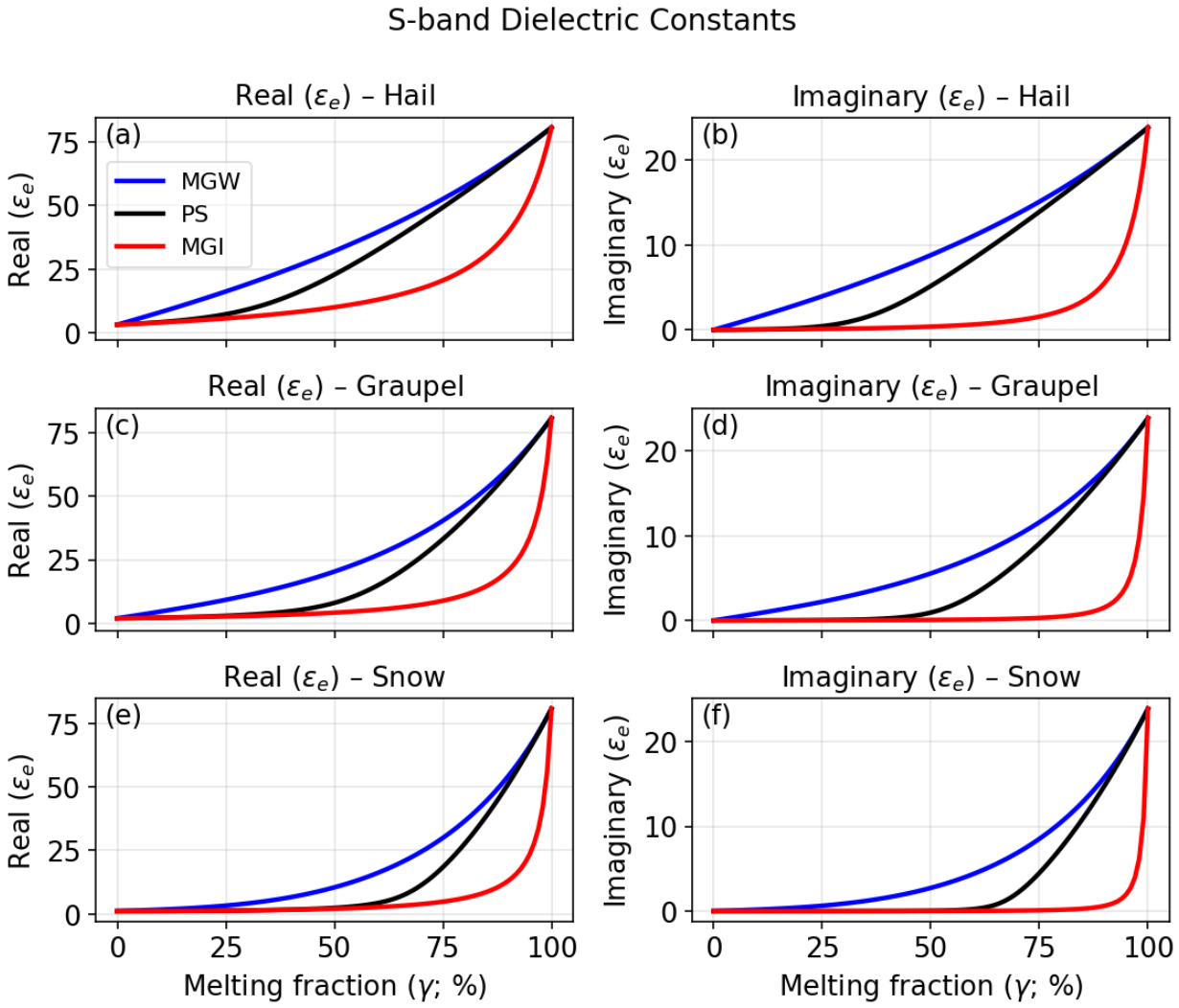

Figure 3.1. Real (ε_e'; a, c, e) and imaginary (ε_e''; b, d, f) components of the effective dielectric constant $\varepsilon_e$at S-band as a function of bulk melting percentage γ for hail, graupel, and snow. Curves compare the Maxwell Garnett mixing formula with water background medium (MGW; blue), Maxwell Garnett with ice background medium (MGI; red), and the Polder–van Santen formula (PS; black).

3.3 Scattering calculations for polarimetric radar variables

3.3.1 Scattering amplitudes and phases

To assess how differences in ε_e propagate into radar observables, T-matrix calculations are performed using the three mixing approaches discussed in Chapter 3.2. An example case of hail with $\gamma = 30\%$ melting is presented to illustrate the contrasts among the mixing formulas for realistic wet hail and their impact on scattering properties. Because wet hail can be approximated as a two-component mixture (i.e., ice–water), establishing the connection with ε_e is more straightforward than for graupel or snow, which utilize three-component mixture (i.e., air, ice, and water). Figure 3.2 presents the eight diagnostic quantities derived from the T-matrix numerical integrations. Figure 3.2a shows the magnitudes of the backscattering amplitudes for the major (horizontal; solid lines) and minor (vertical; dashed lines) axes, which are related to the horizontal and vertical reflectivity factors (Z_h and Z_v), as a function of particle diameter. Consistent with the ε_e behavior in Figure 3.1, pronounced differences are evident among the three mixing formulas. MGW (blue curves) produces larger backscattering magnitudes, reflecting its higher real and imaginary dielectric constants at this melting fraction. Resonance features appear earlier for MGW (beginning near ~25 mm), followed by the PS and MGI formulas. At larger diameters, resonance and internal absorption cause the backscattering amplitudes to respond more strongly to differences in ε_e, as demonstrated by the growing separation among the mixing formulas. The squared ratio of the backscattering magnitudes, which is proportional to Z_{DR}, remains nearly constant for diameters up to approximately 15 mm. This behavior is expected in the Rayleigh regime, where Z_{DR} is primarily controlled by particle shape under the assumption of a fixed aspect ratio. The increase beyond this range likely reflects the transition to the non-Rayleigh regime,

where resonance effects begin to influence the scattering, first appearing in the MGW case (Figure 3.2b). Beyond diameters of approximately 40–50 mm, the ratio decreases to well below 0 dB for all formulas. It is noted that the resonance effects appear at smaller diameters for higher melting percentages of wet hydrometeors.

Figure 3.2c and Figure 3.2d show the phase of the backscattering amplitudes for each polarization and the differential backscattering phase, respectively. The differential backscattering phase is defined as the phase difference between the major- and minor-axis backscattering amplitudes, $\delta = \arg(s_a) - \arg(s_b)$. Both panels exhibit strong oscillations and pronounced model-dependent phase wrapping as particle diameter increases, which governs the behavior of δ. Large excursions in δ indicate enhanced decorrelation effects and are commonly observed in melting and mixed-phase regions, where reductions in ρ_{hv} occur. Among the mixing formulas, the MGW background exhibits resonance effects at smaller diameters (around 20 mm), but with comparatively moderate fluctuations until approximately 50 mm, resulting in predominantly positive values of δ. In contrast, MGI shows strong resonance behavior beginning at 35–40 mm, leading to large positive and negative excursions in δ. The PS exhibits delayed but qualitatively similar resonance-driven fluctuations starting at about 50 mm, producing large variations in δ for very large wet hailstones. These results demonstrate that negative δ can occur in reality when large wet hail is present, regardless of the mixing formula assumptions. Because δ is a backscattering phase quantity, it is more likely to be influenced by a small number of dominant particles, such as large wet hailstones. In contrast, K_{DP} is a propagation-based variable that represents the bulk properties of the medium along the radar path (Trömel et al., 2013; Mishler et al., 2024). Therefore, when non-Rayleigh components are present, the contribution of δ to the Φ_{DP} should be carefully considered, as it may influence the estimation of K_{DP} (Mishler et al., 2024).

Figures 3.2e and 3.2f present the real parts of the forward-scattering amplitudes for the two polarizations and their difference, respectively. The polarization-dependent difference in forward scattering, which is related to K_{DP}, also shows strong model-dependent variability, with notable changes in both magnitude and sign for diameters exceeding 30 mm. In the Rayleigh and near-Rayleigh regimes, all mixing formulas produce small, monotonically increasing values of K_{DP}. For larger diameters, the MGW formula yields negative K_{DP} values beginning near 20 mm, whereas the PS and MGI delay this transition to roughly 30 mm and 35–40 mm, respectively. The MGI exhibits stronger resonance effects and larger fluctuations at greater diameters. Overall, Fig. 3.2 demonstrates that the choice of mixing formula significantly influences the simulated scattering amplitudes and derived polarimetric variables. The PS generally produces results that lie between the two MG formulations, providing a smoother transition between ice-dominated and water-dominated regimes. Differences among mixing formulas are most pronounced in phase-related variables due to resonance-induced phase wrapping. These findings highlight the importance of the physical assumptions underlying mixing formulas in achieving realistic polarimetric radar simulations in mixed-phase regions.

The attenuation-related terms are depicted in Figs. 3.2g and 3.2h, which show the imaginary parts of the forward-scattering amplitudes for each polarization and their difference, respectively. These quantities are directly associated with specific attenuation and differential attenuation. In the small-particle regime ($D < 20$ mm), all three mixing formulas produce weak and monotonically increasing imaginary components. Differences among the mixing formulas become increasingly evident as particle size enters the resonance regime. For intermediate diameters (approximately 25–40 mm), the MGW yields a gradual and nearly monotonic increase in the imaginary parts of both polarizations, resulting in relatively smooth attenuation estimates. In contrast, the PS and

MGI formulas exhibit oscillatory behavior. The MGI shows the strongest enhancement, and more pronounced internal resonance effects. Even at larger diameters ($D > 40$ mm), the MGI formulation produces the largest peak values, the PS maintains intermediate magnitudes and smoother transitions, while the MGW generally produces smaller amplitudes and fewer abrupt variations. These differences are further emphasized in Fig. 3.2h, where the polarization-dependent difference in the imaginary components exhibits sign reversals and enhanced oscillations for the MGI at large diameters. The MGW shows earlier but weaker increases, whereas the PS provides a more gradual evolution, with enhanced resonance fluctuations in MGI.

Although not shown here due to space limitations, the T-matrix scattering calculations for graupel and snow exhibit similar qualitative trends across the three mixing formulas, with differences primarily arising from their lower bulk densities and larger air fractions relative to hail. At C- and X-band, non-Rayleigh and resonance effects occur at smaller diameters, producing more pronounced scattering behavior in both backscattering magnitudes and phases.

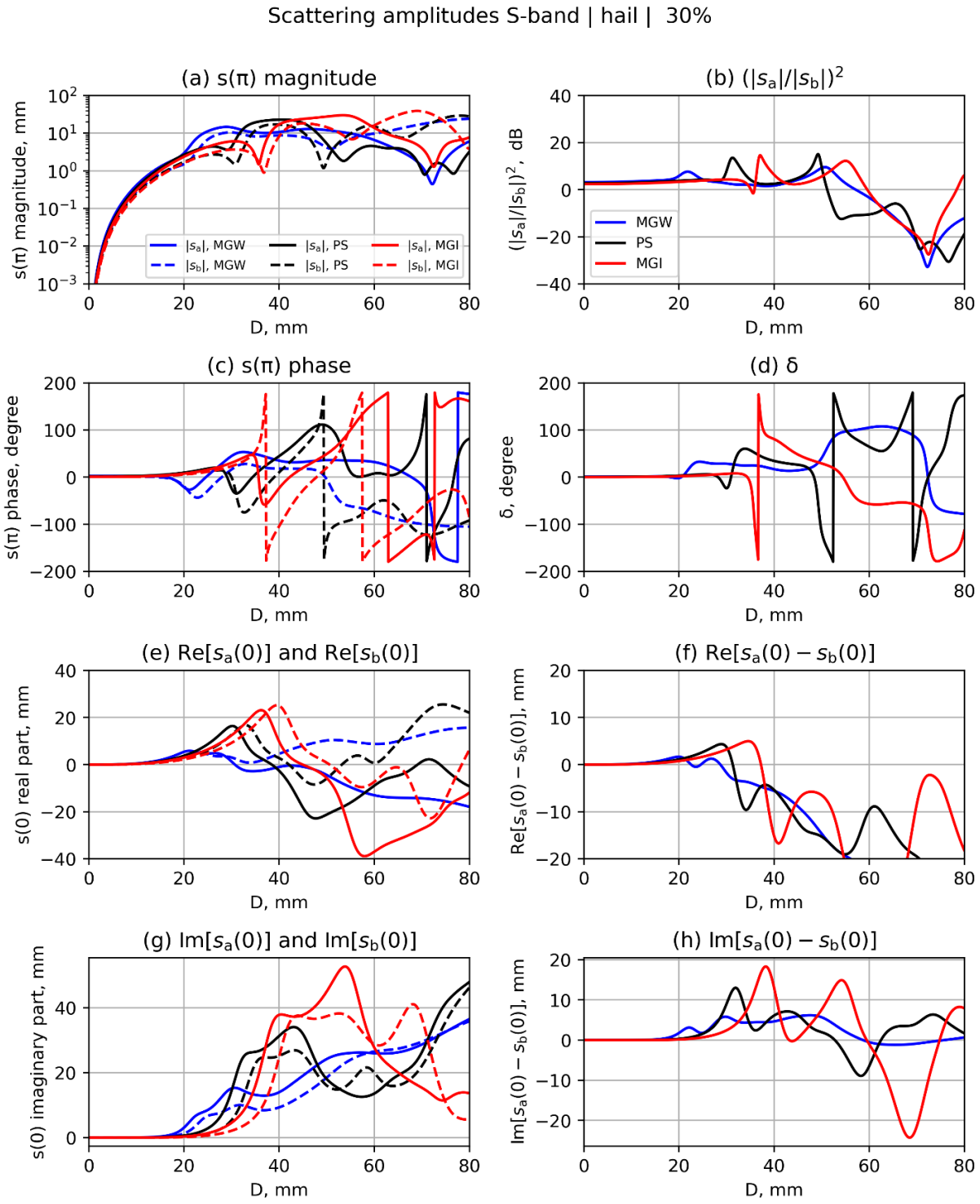

Figure 3.2. Scattering calculations using the T-matrix numerical integration for hail at S-band with a γ of 30% under three mixing formulas: the MGW (blue), the PS (black), and MGI (red). The subplots depict (a) magnitude of the backscattering amplitudes for major ($|\, s_a(\pi)\,|$; solid) and minor ($|\, s_b(\pi)\,|$; dashed) axes; (b) squared ratio of major to minor backscattering magnitudes $(|\, s_a(\pi)\,|/|\, s_b(\pi)\,|)^2$; (c) backscattering phase; (d) differential backscattering phase δ; (e) real part

of the forward-scattering amplitudes; and (f) difference in the real parts of the forward-scattering amplitudes, $\mathrm{Re}[s_a(0)] - \mathrm{Re}[s_b(0)]$; (g) imaginary part of the forward-scattering amplitudes; and (h) difference in the imaginary parts of the forward-scattering amplitudes, $\mathrm{Im}[s_\mathrm{a}(0)] - \mathrm{Im}[s_\mathrm{b}(0)]$.

3.3.2 Polarimetric variables

Figure 3.3 illustrates the impact of mixing formula assumptions on five polarimetric radar variables at S-band for hail at four γ values (0%, 25%, 50%, and 75%). The polarimetric variables are calculated for a unit water content ($W = \rho_\mathrm{a} q_\mathrm{r} = 1$ g m^{-3}) and are shown as a function of the volume-weighted mean diameters (D_m). The results from the three mixing formulas are compared, highlighting how differences in ε_e and scattering amplitudes propagate into commonly used polarimetric observables. Note that Z_h denotes the linear unit of Z_H; that is, $Z_\mathrm{H} = 10\log(Z_\mathrm{h})$. Z_h shows small differences among the mixing formulas and increases monotonically with both D_m and γ (Fig. 3.3a). As particle sizes enter the non-Rayleigh scattering regime, the growth rate of Z_h moderates, and the curves begin to converge. The MGW generally produces the largest values, followed by the PS and MGI, although MGI shows larger values at high γ and for D_m greater than approximately 10 mm. The PS solution aligns more closely with MGW at high γ and with MGI at low γ, exhibiting intermediate behavior at moderate γ. Z_DR shows varying peak magnitudes across the mixing formulas and shifts toward earlier increases (≈ 5–10 mm) as γ increases. This behavior is primarily attributed to increased particle size and higher ε_e as γ increases. As the diameter increases further and becomes comparable to the wavelength, Z_DR from all three mixing formulas decreases or stabilizes at similar values (Fig. 3.3b).

The phase variables also reveal similar features. Higher γ values correspond to earlier peaks in K_DP (Fig. 3.3c). The MGW and PS formulations generally produce larger K_DP at small D_m, whereas the MGI shows a delayed response. For lower to moderate γ cases, MGI yields smaller

values (about 0.25° km^{-1}) compared to MGW and PS. As D_m increases beyond ~33 mm, K_{DP} decreases toward near-zero or slightly negative values as particles enter deeper into the non-Rayleigh regime, where resonance and interference effects disrupt the monotonic accumulation of differential phase and lead to oscillatory behavior. These results suggest that negative K_{DP} associated with large wet hail should be rarely observed in nature, because of its small values compared with the δ values (Mishler et al., 2024). Figures 3.3d and 3.3e depict ρ_{hv} and δ, respectively. As expected, for small particle sizes within the Rayleigh regime, the ρ_{hv} remain close to one. However, dry hail exhibits significant depolarization at large D_m, with ρ_{hv} values decreasing below 0.7. For higher γ, ρ_{hv} drops earlier, although it stabilizes above 0.9 for the MGW and PS at moderate to high γ. The MGI formulation consistently yields lower ρ_{hv} values. Accordingly, the MGI produces larger δ values with a slight delay, particularly at higher γ, whereas the other two formulas yield smaller and more gradual increases in δ with D_m up to about 10°. These results indicate that δ can attain considerable values for large hailstones and should therefore be considered when estimating K_{DP} from the Φ_{DP} (Trömel et al., 2013; Mishler et al., 2024).

The attenuation related variables are shown in Figs. 3.3 f and 3.3g for A_H and A_{DP}. The A_H increases monotonically with D_m for all media and melt fractions, with the growth rate becoming more pronounced at larger sizes. The differences between mixing formulas (MGW, PS, MGI) and γ indicate that both composition and internal structure modulate absorption and scattering efficiency, with wetter or more homogeneous mixtures generally producing higher attenuation. In contrast, Fig. 3.3g shows that A_{DP} exhibits more complex behavior, including both positive and negative values depending on the medium and melt fraction. This sign variability reflects differential attenuation between horizontal and vertical polarizations, which is highly sensitive to

particle shape, orientation, and dielectric contrast. As D_m increases, resonance effects enhance these polarization-dependent interactions, leading to larger magnitudes of A_{DP}. The spread among curves highlights how mixed-phase structure and melt fraction influence, even at S-band where such effects are typically subdued. These results demonstrate that for large, partially melted hydrometeors, attenuation—particularly differential attenuation—can become non-negligible and can carry useful information about particle size and phase composition.

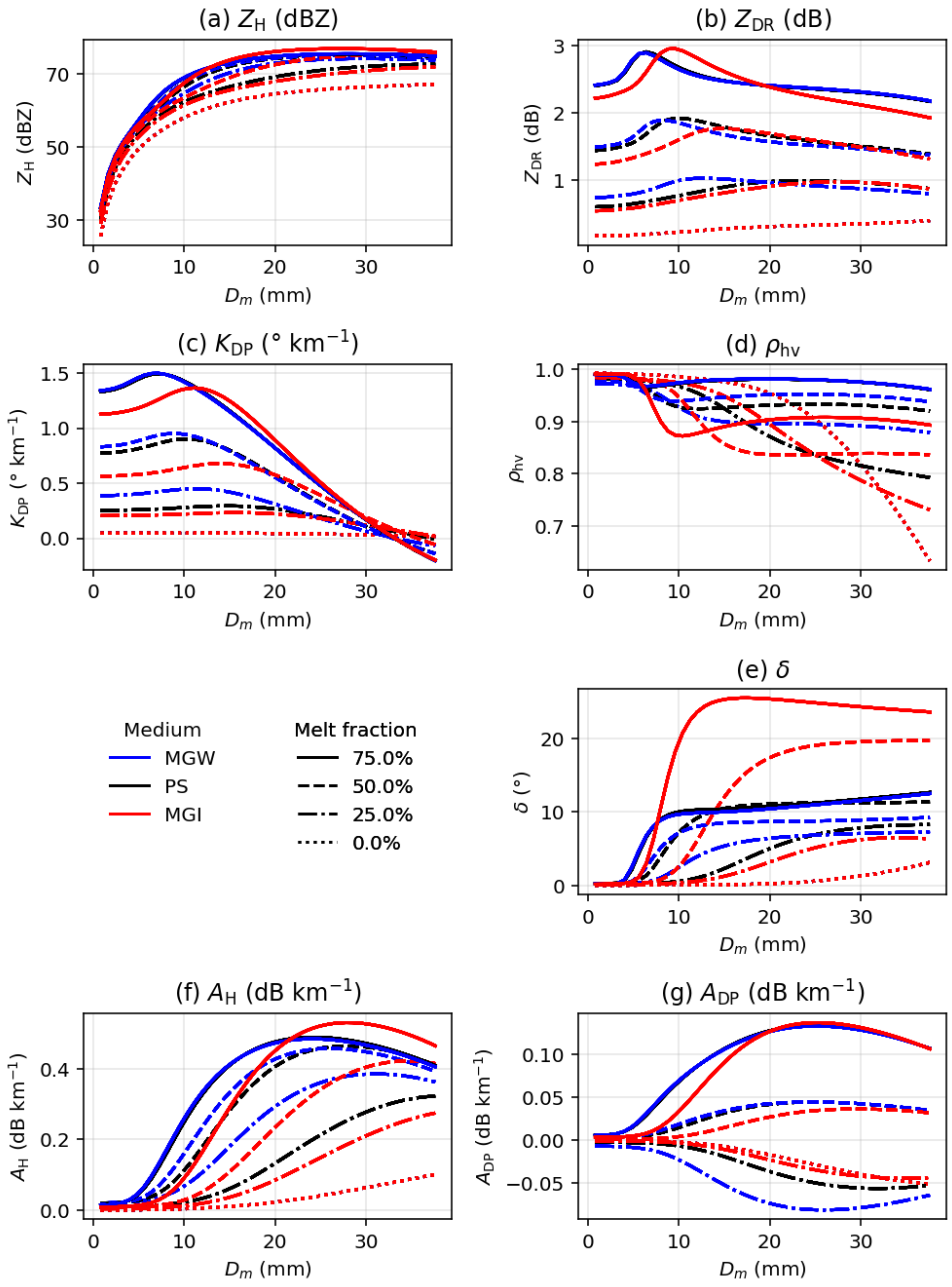

Figure 3.3. The radar variables for hail calculated using MGW, PS and MGI mixing formulas. The γ values of 0, 25, 50, 75% are shown using dotted, dash–dot, dashed, and solid line styles, respectively. Blue lines represent MGW, black lines represent PS, and red lines represent MGI. All radar variables are plotted as a function of the D_m. Reflectivity (Z_H) is shown in dBZ, differential reflectivity (Z_{DR}) in dB, specific differential phase (K_{DP}) in ° km^{-1}, and backscattering differential phase (δ) in degrees (°), horizontal specific attenuation (A_H) in dB km^{-1}, and specific differential attenuation (A_{DP}) in dB km^{-1}.

The polarimetric variables for graupel are depicted in Fig. 3.4. Note that graupel and snow are shown only up to D_m = 20 mm. Relative to hail, graupel produces smaller absolute values and exhibits greater sensitivity to the assumed mixture formulation, owing to its lower bulk density and the inclusion of air. The behavior of $Z_h$is similar to that of hail, increasing monotonically with D_m; however, the MGW consistently yields the largest values because of its higher ε_e (Fig. 3.4a). The Z_{dr} curves display more pronounced differences among the mixing formulas, with the delayed peaks of MGI not appearing within the 20 mm D_m range for moderate to high γ (Fig. 3.4b). At low γ, MGW produces substantially larger Z_{DR} than the other two formulas. For intermediate γ, Z_{DR} values for graupel can equal or exceed those of hail. This enhanced response is consistent with increased polarization sensitivity as liquid water accumulates within and on the surface of porous graupel. At γ = 50% and 75%, the peak locations diverge markedly: MGW and PS peaks near D_m ≈ 7 mm whereas MGI shift the peak to considerably larger sizes.

The K_{DP} patterns show a similar ordering, with MGW producing the largest values at small melt fractions, and MGI substantially smaller values at higher melt fractions (Fig. 3.4c). Graupel exhibits a smaller overall reduction in ρ_{hv} compared with hail; nevertheless, the dependence on the mixing formula remains evident, especially for MGI (Fig. 3.4d). The MGI formulation produces the strongest decline, while PS and MGW yield comparable magnitudes but with noticeably different curvature. The relatively higher ρ_{hv} in the PS case suggests a more coherent scattering response when the air–ice–water mixture is treated symmetrically. Finally, increases in δ begin near D_m ≈ 5 mm, with positive values emerging and growing with melting fraction, along with near zero values at larger sizes (Fig. 3.4e).

The attenuation-related variables for the graupel case are shown in Figs. 3.4f and 3.4g for A_H and A_{DP}, respectively. Similar to the hail scenario, attenuation at S-band remains relatively weak

overall; however, a systematic increase with D_m is still evident, particularly beyond ~8–10 mm as particle sizes approach the resonance regime. A_H increases smoothly and monotonically with varying magnitude among the different mixing formulas, and values remain generally lower than in the hail case. The separation between mixing formulations becomes more apparent at larger D_m, indicating that assumptions about internal structure and water distribution play an increasing role as particles grow and begin to melt. The A_{DP} remains small in magnitude across all sizes, with only modest divergence between curves as D_m increases. Unlike the hail case, the graupel results are more subdued and generally closer to zero, reflecting weaker polarization-dependent attenuation.

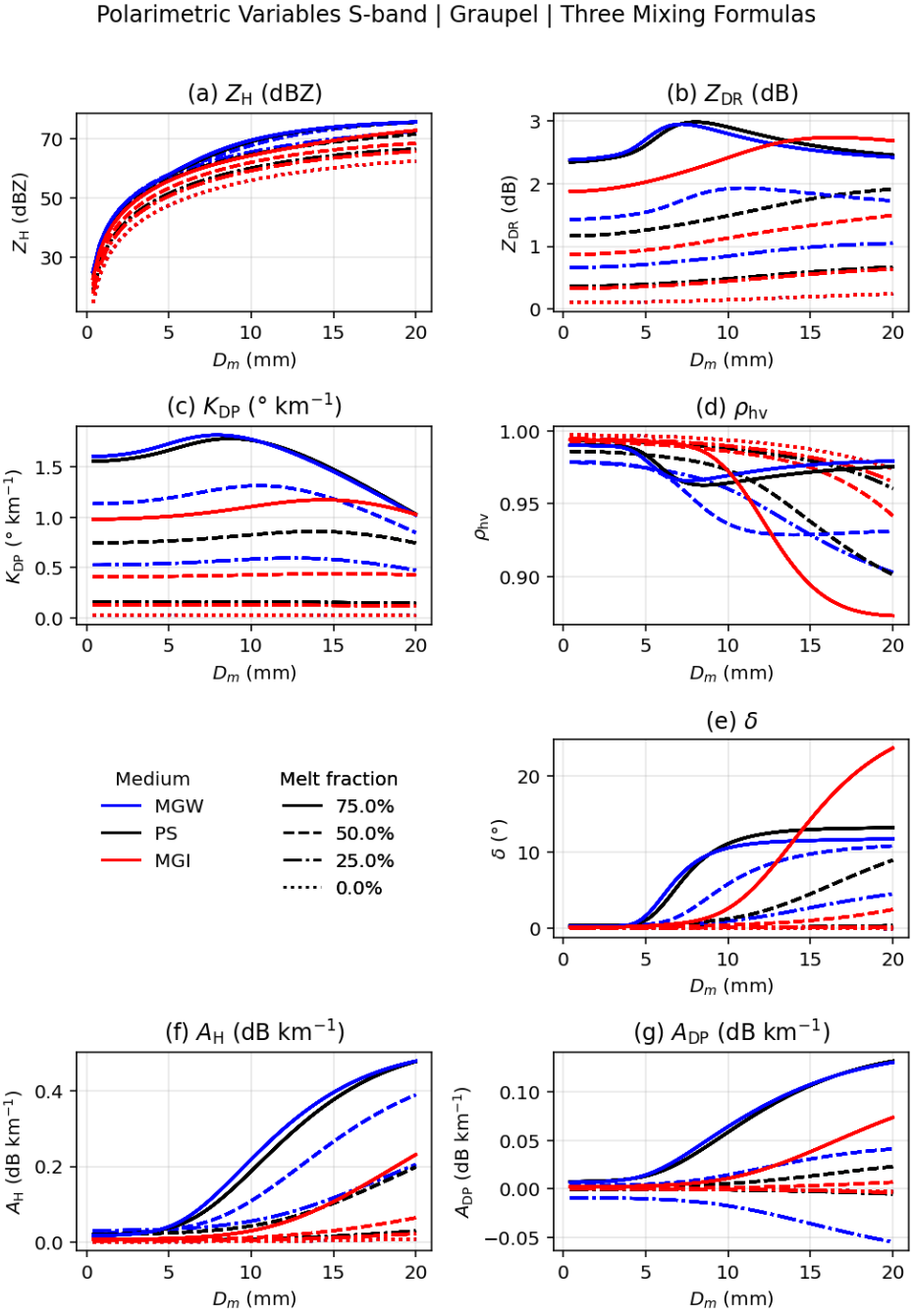

Figure 3.4. Same as Figure 3.3 except for graupel.

The polarimetric variables for snow (Fig. 3.5) follow the same general structure as those for graupel, with the primary difference being further reduction in the bulk density. However, owing to snow's low density and high air fraction, the sensitivity of all polarimetric variables to both the

melt fraction and the choice of mixing formula is amplified. Even at relatively small D_{m}, both Z_{h} and Z_{DR} values separate noticeably among the formulas, and the differences persist across the entire size range, with MGI producing significantly smaller values compared to MGW and PS. The K_{DP} responses are likewise enhanced, particularly for the MGW case, while ρ_{hv} exhibits a pronounced decline with increasing γ for both MGW and PS. The δ values also increase earlier and more rapidly, underscoring the strong depolarization potential once liquid water begins to occupy the highly porous snow matrix.

Similar to hail and graupel, A_{H} increases with D_{m}, although magnitudes are generally lower than graupel for comparable sizes. This growth reflects increasing liquid water content as melting progresses. Differences between mixing formulations become more pronounced at larger D_{m}, with MGW and PS exhibiting higher attenuation, while MGI tends to produce reduced values, consistent with a weaker effective dielectric contrast (Fig. 3.5f). In Fig. 3.5g, A_{DP} remains small and predominantly positive, with a smooth increase at larger D_{m}. MGW and PS show relatively larger values, whereas MGI remains near zero across most sizes, indicating weaker polarization-dependent attenuation. Overall, the choice of ε_{e} plays a notable role in determining simulated melting-layer signatures, underscoring the importance of physically consistent mixing formulas. Note that the differences in polarimetric variables at C-, and X-band are even more pronounced due to earlier and stronger resonance effects.

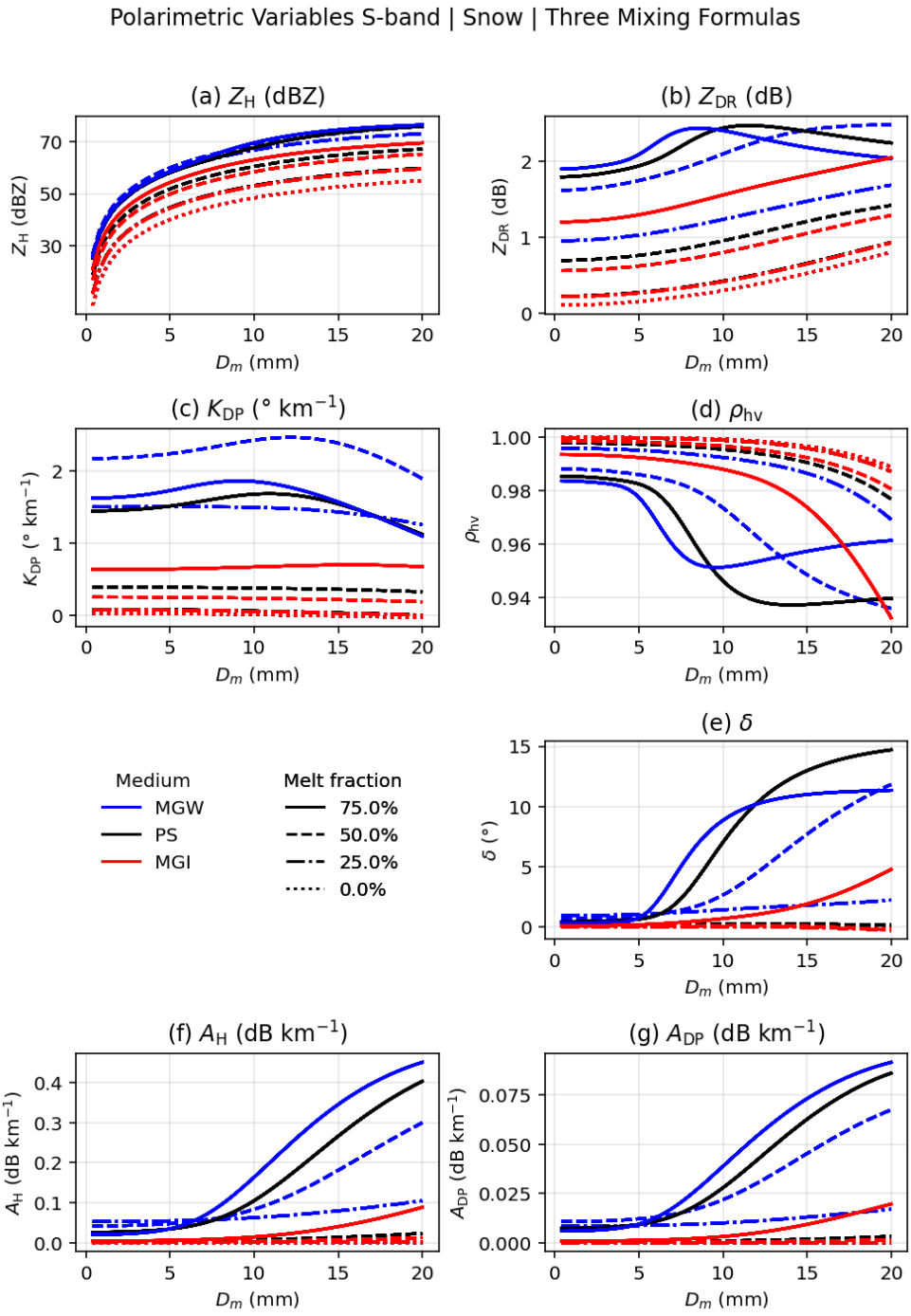

Figure 3.5. Same as Fig. 3.3 except for snow.

3.4 Machine learning parameterization of forward operators

The parameterization of polarimetric variables as a function of D_m provides a straightforward approach for the broader meteorological community, eliminating the need for users to make extensive assumptions and calculations involving dielectric constants, T-matrix calculations, numerical integrations, and subsequent PRD computations. An optimal parameterization of bulk polarimetric radar forward operators must satisfy three primary requirements: (i) computational efficiency with a limited number of parameters, (ii) differentiability and ease of implementation for DA applications, and (iii) flexibility to extend consistently across melting fractions and radar frequencies. To fulfill those requirements, an ML method is introduced in this study for parameterization.

3.4.1 ML-based parametrization

ML methods have been widely applied to parameterization problems in the meteorological community because of their improved accuracy and computational efficiency (O'Gorman and Dwyer 2018; de Burgh-Day and Leeuwenburg 2023; Cheng et al. 2024; Takeishi and Wang 2024). A key limitation of ML approaches, however, is their perceived lack of interpretability. This concern is particularly relevant in meteorology, where limited interpretability introduces uncertainty in physical parameterizations, complicates the explicit calculation of derivatives required for DA applications, and reduces user trust, as forecasters often hesitate to rely on tools they do not understand. To address this issue, a deliberately simple neural network (NN) architecture is adopted here to improve upon traditional polynomial fitting while retaining physical interpretability and DA compatibility. The network employs a small number of neurons (three or

four, depending on the polarimetric variable and hydrometeor type) and a differentiable Sigmoid activation function,

$$\sigma(t) = \frac{1}{1 + e^{-t}}, \tag{3.1}$$

where the neuron inputs t to each Sigmoid function are defined as

$$t = \sum_{j=-1}^{2} c_j \widetilde{D}_m^j + c_\gamma \tilde{\gamma}, \tag{3.2}$$

where the functional form of t consists of standardized inputs $\widetilde{D}_m^j$ and $\tilde{\gamma}$, derived from D_m^{-1}, D_m, D_m^2, and γ, respectively. Standardized variables are obtained by linearly scaling each variable using the mean (μ) and standard deviation (s) values listed in Table 3.1. The standardization is defined as

$$\tilde{x} = \frac{x - \mu}{s} \tag{3.3}$$

for each input variable $x \in \{D_m^{-1}, D_m, D_m^2, \gamma\}$. Note that a constant (bias) term is also included (i.e., $j = 0$), consistent with standard linear models (e.g., $y = wx + b$). The coefficients c_j and c_γ represent the weights (w), with $j = 0$ corresponding to the bias term (b). The inclusion of multiple orders of D_m enables the network to capture local curvature, asymptotic behavior, and peak structures associated with resonance effects and complex scattering regimes. The Sigmoid function is selected for its smoothness, bounded output, and approximately linear behavior in the central region, which promotes stable gradients and facilitates variational DA applications. Unlike polynomial approaches, the ML parameterization directly incorporates both D_m and γ within a unified fitting process, avoiding intermediate coefficient parameterizations.

Hydrometeor	Input variable	Mean (μ)	Standard deviation (s)
Hail	D_m^{-1}	0.1128	0.1952
	D_m	20.05	11.077
	D_m^2	524.5699	446.6863
	γ	50	30.2765
Snow & Graupel	D_m^{-1}	0.2250	0.3907
	D_m	10.1995	5.7716
	D_m^2	137.3422	121.4310
	γ	50	30.2765

Table 3.1 The mean and standard deviation values used to standardize the neural network (NN) input variables for each hydrometeor.

To meet the aforementioned objectives, the NN optimization process was conducted differently from many previous NN applications. Instead of selecting optimal NN parameters solely based on mean-square error (MSE) or related error metrics, the optimization emphasized smoothness, overall representativeness, and fitting performance of the curves across multiple γ values. For example, the number of nodes and batch size were adjusted to balance the representation of local variability against overall smoothness. DA and gradient-based analyses require smooth transitions without abrupt changes, large derivatives, or discontinuities. Consequently, fitting results exhibiting sharp curvature or large derivatives at specific locations were avoided, even when they yielded lower MSE values. To maintain simplicity and reproducibility, the number of coefficients was restricted to three or four nodes, depending on fitting performance, provided that the results remained within reasonable measurement uncertainties. Another consideration is that alternative NN architectures could yield improved fits. However, such improvements are not expected to substantially affect subsequent applications, as uncertainties associated with physical assumptions are likely much larger than those arising from fitting errors.

Additional criteria were applied when the fitting performance deteriorated at large values for highly melted mixtures or dry species. Because later sections apply a D_m–γ constraint that excludes

these physically unrealistic conditions, and because completely dry, large species are rare in natural systems—reduced fitting accuracy in these regions was considered acceptable. For ρ_{hv}, an additional constraint was imposed to ensure values remained below 1 under all conditions. Although some fits agreed well with the data, they occasionally yielded values that exceeded this physical limit. In such cases, physical realism was prioritized over fitting accuracy, as operator and model uncertainties are unavoidable. Nevertheless, it is recommended to enforce an upper bound of $\rho_{\mathrm{hv}} = 1$ to prevent physically unrealistic results.

The NN was trained using sets of D_{m} and melt fraction γ as input variables, where γ was sampled at 5% intervals from 0% to 100%. The inverse and squared D_{m} terms were included as additional input features, and were standardized separately (Table 3.1). The model outputs were the corresponding polarimetric radar variables. For Z_{h} and Z_{dr} (i.e., the linear units of Z_{H} and Z_{DR}), logarithmic transformations were applied prior to training to reduce dynamic range of the inputs and improve training stability. The learning rate was fixed at 0.001, a commonly used default value, and the batch size was set to 5. Given that 50 D_{m} values were used for training, this batch size provided a good balance between overfitting to local features and achieving smooth overall fitting performance. The dataset was not divided into separate training, validation, and testing subsets; instead, all available data were used for training. This approach was adopted because the primary objective was to achieve accurate parametrization of the numerically calculated dataset rather than to generalize to independent unseen data. A few intermediate values of γ (between the 5% sampling intervals) were evaluated and showed similar performance, with fitting errors generally at least an order of magnitude smaller than the measurement errors for each polarimetric variable. The inclusion of inverse and squared D_{m} terms helped capture small curvature at low D_{m} values and enhanced responses in the resonance regime at large D_{m} values.

However, when these terms introduced overly abrupt variations at small D_{m} or excessively large values at high D_{m}, the inverse and squared terms were removed, respectively.

3.4.2 ML derived parametrized forward operator

The trained ML coefficients are printed and further utilized to form the parametrized forward operators. The fitted equations for the polarimetric variables using the ML derived coefficients are provided in Eqs. (3.4–3.10). The formulation of these operators is similar to that of Zhang et al., (2021), with the polynomial terms replaced by the equations derived from the ML-fitted coefficients. The subscripts of t denote individual nodes, each with its own set of ML-fitted coefficients c_j and c_γ for a given polarimetric variable.

$$Z_{\mathrm{H}}(x) = 10\log_{10} Z_x + 20[a_{z0}\sigma(t_{z0}) + a_{z1}\sigma(t_{z1}) + a_{z2}\sigma(t_{z2}) + a_{z3}\sigma(t_{z3}) + a_{zc}] \quad (3.4)$$

$$Z_{\mathrm{DR}}(x) = 10[a_{d0}\sigma(t_{d0}) + a_{d1}\sigma(t_{d1}) + a_{d2}\sigma(t_{d2}) + a_{d3}\sigma(t_{d3}) + a_{dc}] \quad (3.5)$$

$$K_{\mathrm{DP}}(x) = \frac{\rho_a q_x}{\rho_x}[a_{k0}\sigma(t_{k0}) + a_{k1}\sigma(t_{k1}) + a_{k2}\sigma(t_{k2}) + a_{k3}\sigma(t_{k3}) + a_{kc}] \quad (3.6)$$

$$\rho_{\mathrm{hv}}(x) = a_{\rho0}\sigma(t_{\rho0}) + a_{\rho1}\sigma(t_{\rho1}) + a_{\rho2}\sigma(t_{\rho2}) + a_{\rho3}\sigma(t_{\rho3}) + a_{\rho c} \quad (3.7)$$

$$\delta(x) = a_{\delta0}\sigma(t_{\delta0}) + a_{\delta1}\sigma(t_{\delta1}) + a_{\delta2}\sigma(t_{\delta2}) + a_{\delta3}\sigma(t_{\delta3}) + a_{\delta c} \quad (3.8)$$

$$A_{\mathrm{H}}(x) = a_{h0}\sigma(t_{h0}) + a_{h1}\sigma(t_{h1}) + a_{h2}\sigma(t_{h2}) + a_{h3}\sigma(t_{h3}) + a_{hc} \quad (3.9)$$

$$A_{\mathrm{DP}}(x) = a_{p0}\sigma(t_{p0}) + a_{p1}\sigma(t_{p1}) + a_{p2}\sigma(t_{p2}) + a_{p3}\sigma(t_{p3}) + a_{pc} \quad (3.10)$$

Here, Z_x is the sixth moment of hydrometeor species x, ρ_a is air density, ρ_x is hydrometeor density, and q_x is the hydrometeor mixing ratio. All operators share a common nonlinear mapping defined by four Sigmoid nodes, with variable-specific scaling using standardized inputs derived from multiple powers of D_{m}, consistent with Eq. (3.2). The corresponding coefficients are used to compute the intermediate terms t_0–t_3 for each polarimetric variable. The "output" row lists the corresponding output-layer weights a_j and the bias (constant) term a_c. Tables 3.2–3.4 present an

example coefficients set for the ML parametrized PRD operators for hail, graupel, and snow, respectively, using the PS mixing formula at S-band. Each radar variable is represented by a single-hidden-layer NN with up to four sigmoid neurons. All coefficients are rounded to four significant figures for compactness; rounding errors are negligible relative to model uncertainty. For variables using fewer than four hidden neurons, the corresponding coefficients c_j and output weights a_j are set to zero, allowing a uniform functional form across all radar variables. While it is possible to even make the equation forms easier, the current forms are enforced for consistency and stability.

		c_{-1}	c_0	c_1	c_2	c_γ
Z_H	t_{z0}	–18.30	–1.860	–1.097	0.9850	5.965
	t_{z1}	0.006448	2.696	–0.2562	0.8047	1.776
	t_{z2}	–8.470	–4.856	0.3304	–0.05900	–0.06030
	t_{z3}	0	0	0	0	0
	output	a_{z0}	a_{z1}	a_{z2}	a_{z3}	a_{zc}
		0.1591	0.5943	–1.771	0	–0.5534
Z_{DR}	t_{d0}	0.1452	–4.636	–4.071	2.502	1.276
	t_{d1}	5.231	–1.450	–0.8387	0.4780	–2.682
	t_{d2}	–1.953	3.853	–6.625	3.673	–2.900
	t_{d3}	–0.4018	–0.6660	–1.048	0.3551	1.342
	output	a_{d0}	a_{d1}	a_{d2}	a_{d3}	a_{dc}
		0.1477	−0.09676	−0.04825	0.2253	0.1375
K_{DP}	t_{k0}	–0.4517	4.383	–6.046	11.34	–2.546
	t_{k1}	–1.017	1.138	–11.81	12.58	–1.802
	t_{k2}	0.2854	5.536	1.204	2.976	–1.280
	t_{k3}	0	0	0	0	0
	output	a_{k0}	a_{k1}	a_{k2}	a_{k3}	a_{kc}
		–0.5856	–0.4297	–1.327	0	2.313
ρ_{hv}	$t_{\rho0}$	0	5.584	–7.764	3.700	0.8572
	$t_{\rho1}$	0	–13.02	2.486	2.239	–4.114
	$t_{\rho2}$	0	0.9500	1.354	–0.2152	2.846
	$t_{\rho3}$	0	2.472	2.426	–0.4592	2.863
	output	$a_{\rho0}$	$a_{\rho1}$	$a_{\rho2}$	$a_{\rho3}$	$a_{\rho c}$
		0.1442	–0.09150	0.3175	–0.3138	0.8430
δ	$t_{\delta0}$	–15.61	–1.011	2.011	–0.7441	4.779
	$t_{\delta1}$	26.29	0.5353	4.089	–1.869	–9.457
	$t_{\delta2}$	–12.63	–10.27	0.9416	–0.6282	1.038
	$t_{\delta3}$	0	0	0	0	0
	output	$a_{\delta0}$	$a_{\delta1}$	$a_{\delta2}$	$a_{\delta3}$	$a_{\delta c}$
		4.156	–6.194	77.82	0	6.443
A_H	t_{h0}	−19.61	−3.011	−1.062	0	5.469
	t_{h1}	−17.85	−4.005	−7.363	0	3.895

	t_{h2}	−64.46	−20.71	−1.533	0	4.233
	t_{h3}	24.32	5.497	0.2129	0	-3.297
	output	a_{h0}	a_{h1}	a_{h2}	a_{h3}	a_{hc}
		0.1443	0.03848	0.09762	−0.1875	0.1986
A_{DP}	t_{p0}	0	-11.62	22.35	−14.59	3.864
	t_{p1}	0	−4.187	9.394	−4.432	4.262
	t_{p2}	0	−1.631	10.18	−8.071	4.277
	t_{p3}	0	0.8879	−1.193	4.445	−0.6477
	output	a_{p0}	a_{p1}	a_{p2}	a_{p3}	a_{pc}
		0.06700	0.07059	0.09171	−0.06760	0.009314

Table 3.2. An example coefficient of ML-fitted polarimetric radar variables for hail PS mixing formulas.

		c_{-1}	c_0	c_1	c_2	c_γ
Z_H	t_{z0}	–0.0298	0.8839	–0.1576	0.1382	1.492
	t_{z1}	–26.58	–12.83	1.350	–1.046	6.612
	t_{z2}	–0.04020	–0.5550	–0.2480	0.5150	0.3042
	t_{z3}	0	0	0	0	0
	output	a_{z0}	a_{z1}	a_{z2}	a_{z3}	a_{zc}
		1.021	0.1653	–0.7838	0	–0.6125
Z_{DR}	t_{d0}	–0.3318	–0.5014	–0.6610	0.004660	1.690
	t_{d1}	0.1905	–0.2949	4.712	–2.748	2.353
	t_{d2}	–0.08060	0.4615	0.9575	–2.026	–6.694
	t_{d3}	–0.7910	7.648	–3.645	8.871	–2.001
	output	a_{d0}	a_{d1}	a_{d2}	a_{d3}	a_{dc}
		0.1603	0.1121	–0.06010	–0.08224	0.1462
K_{DP}	t_{k0}	0.1048	–0.3790	0.5473	–0.04891	3.530
	t_{k1}	–0.6224	2.587	–8.062	7.350	–2.664
	t_{k2}	–0.08477	–3.099	–0.1370	–1.448	1.423
	t_{k3}	0	0	0	0	0
	output	a_{k0}	a_{k1}	a_{k2}	a_{k3}	a_{kc}
		0.8450	0.4358	1.101	0	0.4400
ρ_{hv}	$t_{\rho0}$	0	1.298	0.8631	0.5313	2.127
	$t_{\rho1}$	0	–2.462	7.262	–4.950	7.024
	$t_{\rho2}$	0	2.842	–4.913	1.943	–5.148
	$t_{\rho3}$	0	–2.408	3.137	–1.692	3.881
	output	$a_{\rho0}$	$a_{\rho1}$	$a_{\rho2}$	$a_{\rho3}$	$a_{\rho c}$
		–0.03220	–0.05657	0.1443	0.2279	0.8526
δ	$t_{\delta0}$	57.57	27.39	–8.138	5.778	–14.02
	$t_{\delta1}$	–14.10	–20.52	35.76	–20.58	3.952
	$t_{\delta2}$	42.98	15.04	5.038	–2.663	–8.963
	$t_{\delta3}$	0	0	0	0	0
	output	$a_{\delta0}$	$a_{\delta1}$	$a_{\delta2}$	$a_{\delta3}$	$a_{\delta c}$
		–4.787	1.485	–6.033	0	11.00
A_H	t_{h0}	35.01	14.65	0.5424	0	-4.026
	t_{h1}	16.60	6.301	0.3976	0	–4.682
	t_{h2}	17.47	6.604	−0.0974	0	–5.455
	t_{h3}	32.23	16.35	–1.323	0	–2.604
	output	a_{h0}	a_{h1}	a_{h2}	a_{h3}	a_{hc}
		–0.1995	–0.4593	0.3590	–0.1709	0.4789

A_{DP}	t_{p0}	0	8.582	−5.471	0.9840	−3.188
	t_{p1}	0	−4.714	10.75	−7.755	4.549
	t_{p2}	0	−1.040	−1.410	0.9089	8.171
	t_{p3}	0	−9.210	12.64	−6.062	6.007
	output	a_{p0}	a_{p1}	a_{p2}	a_{p3}	a_{pc}
		-0.05211	0.06033	0.01062	0.04274	0.05030

Table 3.3. Same as Table 3.2, except for graupel.

		c_{-1}	c_0	c_1	c_2	c_γ
Z_H	t_{z0}	–25.96	–8.872	–3.127	2.920	3.847
	t_{z1}	0.2312	2.319	1.764	–0.9622	–5.957
	t_{z2}	–0.01085	–0.8201	–0.1134	0.3363	–1.697
	t_{z3}	0	0	0	0	0
	output	a_{z0}	a_{z1}	a_{z2}	a_{z3}	a_{zc}
		0.09812	0.2255	1.401	0	0.07334
Z_{DR}	t_{d0}	10.16	8.665	–2.675	1.475	–6.037
	t_{d1}	6.356	1.426	1.008	–1.635	–1.159
	t_{d2}	–0.05010	–1.238	–0.7030	0.5120	3.024
	t_{d3}	–9.110	–8.398	1.391	–0.7242	5.318
	output	a_{d0}	a_{d1}	a_{d2}	a_{d3}	a_{dc}
		0.2137	0.07995	0.1919	0.2925	0.3085
K_{DP}	t_{k0}	–0.01910	2.535	0.2187	–0.4877	–4.510
	t_{k1}	0.04386	3.662	–0.01044	0.6244	–1.478
	t_{k2}	0.1370	3.422	2.027	–2.177	–3.314
	t_{k3}	0	0	0	0	0
	output	a_{k0}	a_{k1}	a_{k2}	a_{k3}	a_{kc}
		–1.410	–1.615	0.8812	0	2.140
ρ_{hv}	$t_{\rho0}$	0	3.322	3.055	–3.676	–7.455
	$t_{\rho1}$	0	7.954	–4.774	2.590	–7.288
	$t_{\rho2}$	0	–0.1269	–1.383	–1.213	–2.595
	$t_{\rho3}$	0	–7.530	6.292	–3.264	7.829
	output	$a_{\rho0}$	$a_{\rho1}$	$a_{\rho2}$	$a_{\rho3}$	$a_{\rho c}$
		0.01390	–0.1138	0.01030	–0.1177	1.089
δ	$t_{\delta0}$	4.744	6.566	0.3242	–0.5996	–6.134
	$t_{\delta1}$	5.202	7.559	1.267	–0.8089	–6.293
	$t_{\delta2}$	–24.41	–19.22	4.826	–3.133	12.62
	$t_{\delta3}$	0	0	0	0	0
	output	$a_{\delta0}$	$a_{\delta1}$	$a_{\delta2}$	$a_{\delta3}$	$a_{\delta c}$
		–22.09	21.24	5.905	0	0.8679
A_H	t_{h0}	−0.1213	3.820	0.6425	0	−4.033
	t_{h1}	18.52	12.14	−0.6533	0	−4.132
	t_{h2}	−0.1762	3.025	0.1232	0	−4.309
	t_{h3}	−16.75	−13.81	1.047	0	8.502
	output	a_{h0}	a_{h1}	a_{h2}	a_{h3}	a_{hc}
		0.2520	-0.2554	-0.2616	0.1260	0.2657
A_{DP}	t_{p0}	0	4.780	0.5629	−0.3186	−9.099
	t_{p1}	0	2.526	2.176	−3.660	−6.533
	t_{p2}	0	−5.563	9.419	−5.458	4.827
	t_{p3}	0	−8.440	9.579	−3.398	2.946
	output	a_{p0}	a_{p1}	a_{p2}	a_{p3}	a_{pc}

	−0.04256	0.03749	0.04765	0.03233	0.005029

Table 3.4. Same as Table 3.2, except for snow.

The coefficients for other mixing formulas, frequencies, and rain are provided in the supplementary material (Tables A1–A27). Additional attenuation variables, including horizontal specific attenuation (A_{H}) and specific differential attenuation (A_{DP}), are included to represent propagation effects, which become increasingly important at higher frequencies. In addition, the rain operators at S-band are slightly modified from the formulation in Mahale et al. (2019) to maintain consistency with Eq. (3.4) across all hydrometeors, using the sixth moment (Z_{x}) instead of W_{x}.

Figure 3.6 compares the T-matrix-derived polarimetric variables with polynomial and ML fits for S-band hail across a range of γ values. Both methods reproduce the overall trends of the simulated variables; however, clear differences emerge in their ability to capture local structure. For Z_{h}, the dependence on particle size is relatively smooth and monotonic, and both polynomial and ML parameterizations perform comparably well. In contrast, for Z_{DR}, ρ_{hv}, and δ, the ML approach outperforms polynomial fitting, especially in regions exhibiting local curvature. The ML fits more accurately to reproduce local peaks in Z_{DR} and K_{DP} at higher γ around $D_{\mathrm{m}} \approx 5$mm. The plateau behavior of ρ_{hv} at intermediate diameters and its decline at larger D_{m} for dry species are also well represented. The near zero values of δ in the Rayleigh regime, followed by its sharp increase, are difficult to capture using low order polynomials but are better represented by the ML fits. The larger fluctuations of these radar variables at shorter wavelengths are also reasonably well captured by the ML-derived coefficients.

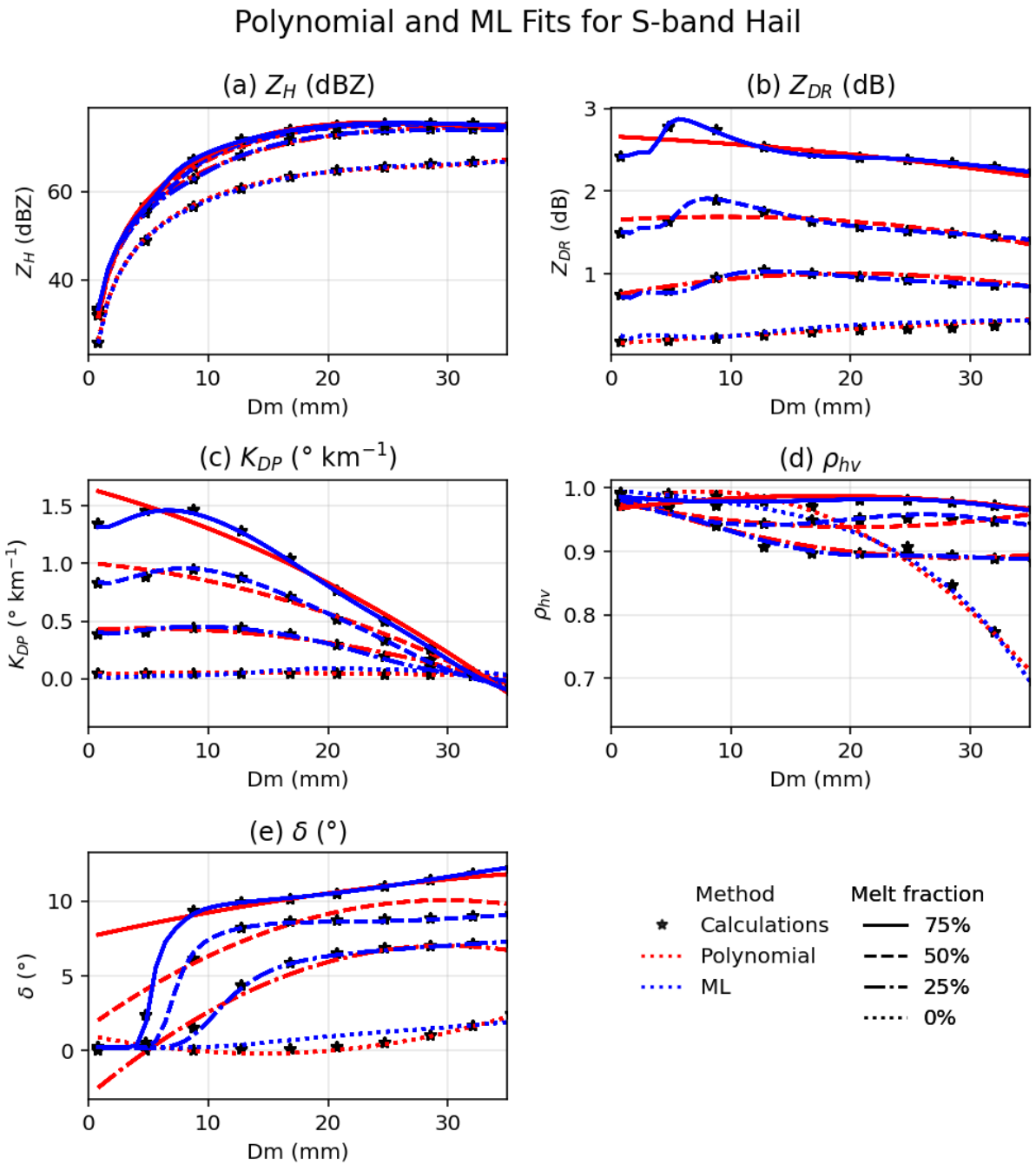

Figure 3.6. An example comparison plot of the fitted results of the T-matrix calculations (asterisk), polynomial fitted (red dotted line), and ML fitted (blue dotted line) hail polarimetric variables. The calculations are only depicted at 5 mm intervals of D_m, and all results are based on S-band for MGW mixing formula. The line style denotes different γ of 0 (dotted), 25 (dash-dot), 50 (dash), 75 (solid)%.

3.4.3 ML-fits for C- and X-bands

The ML-fitting calculations are extended to shorter wavelengths of C- and X-bands in order to extend the utility of the operators for C-band radar networks in other countries (Wang et al., 2013; Honda et al., 2022; Ueki et al., 2024), and also for field campaign usages, where mobile X-band radars are often utilized (Anagnostou et al., 2006; Pazmany et al., 2013; Honda et al., 2022; Ueki et al., 2024). The Figs. 3.7 and 3.8 each display the calculation and fitting results for the polarimetric variables for C- and X-bands, respectively.

Compared to S-band results, the functional relationships at C-band exhibit increased nonlinearity and curvature, reflecting the earlier onset of resonance scattering effects (Fig. 3.7). This added complexity makes the relationships significantly more difficult to represent using simple polynomial or low-order parametric fitting approaches. In particular, K_{DP} exhibits a sharp positive peak near $D_m \approx 4$ mm, followed by a rapid decline and a transition to negative values beyond approximately $D_m \approx 20$ mm. Such sign changes and inflection points introduce additional challenges for conventional fitting methods, which typically struggle to capture both local extrema and asymptotic behavior within a single functional form. Similarly, Z_{DR} and ρ_{hv} show varying curvature and slope changes across D_m, while δ exhibits a rapid increase followed by a gradual decline at larger diameters. These features become more pronounced at higher melt fractions, further increasing the dimensional complexity of the fitting problem.

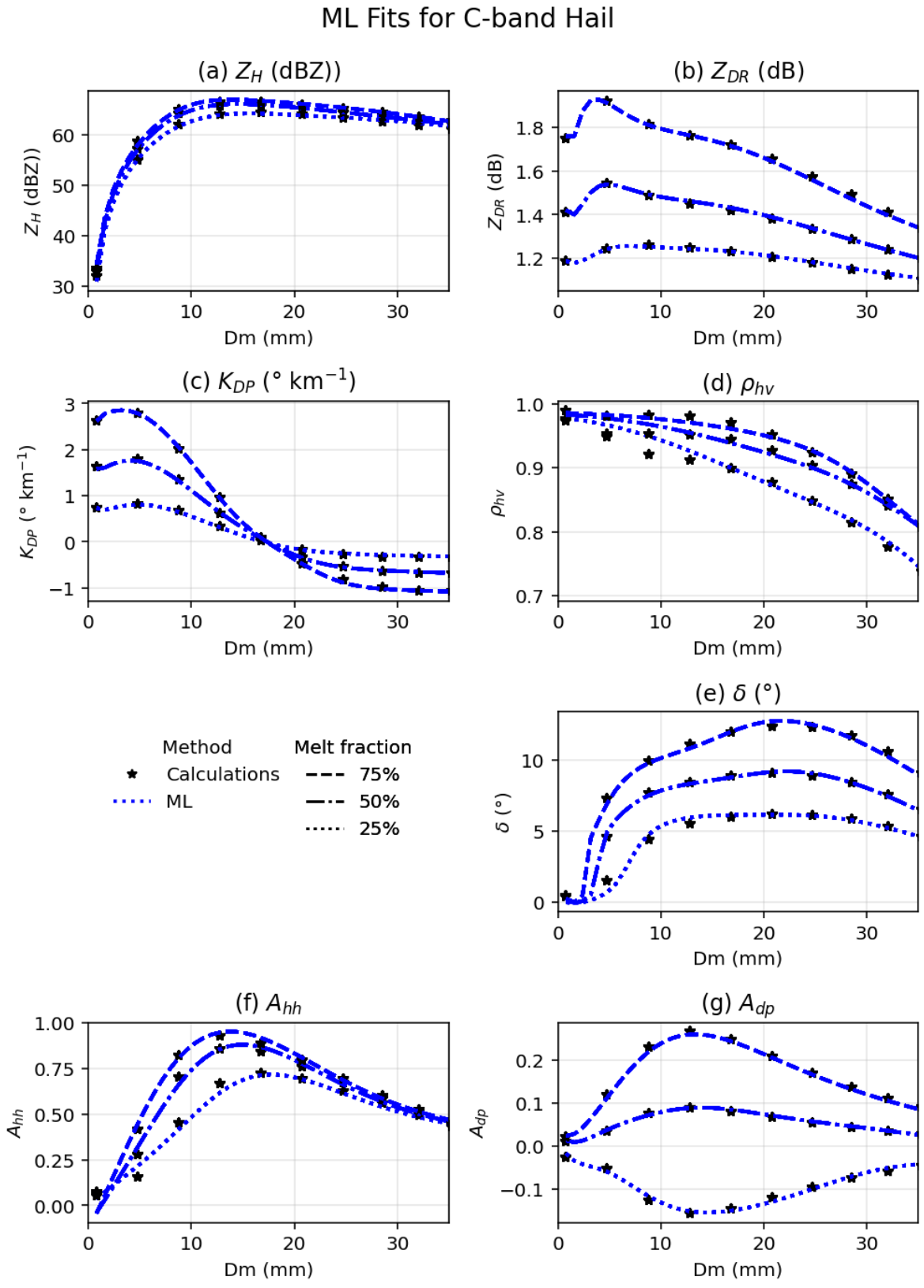

Figure 3.7. Same as Fig. 3.6, except for C-band without polynomial fitting.

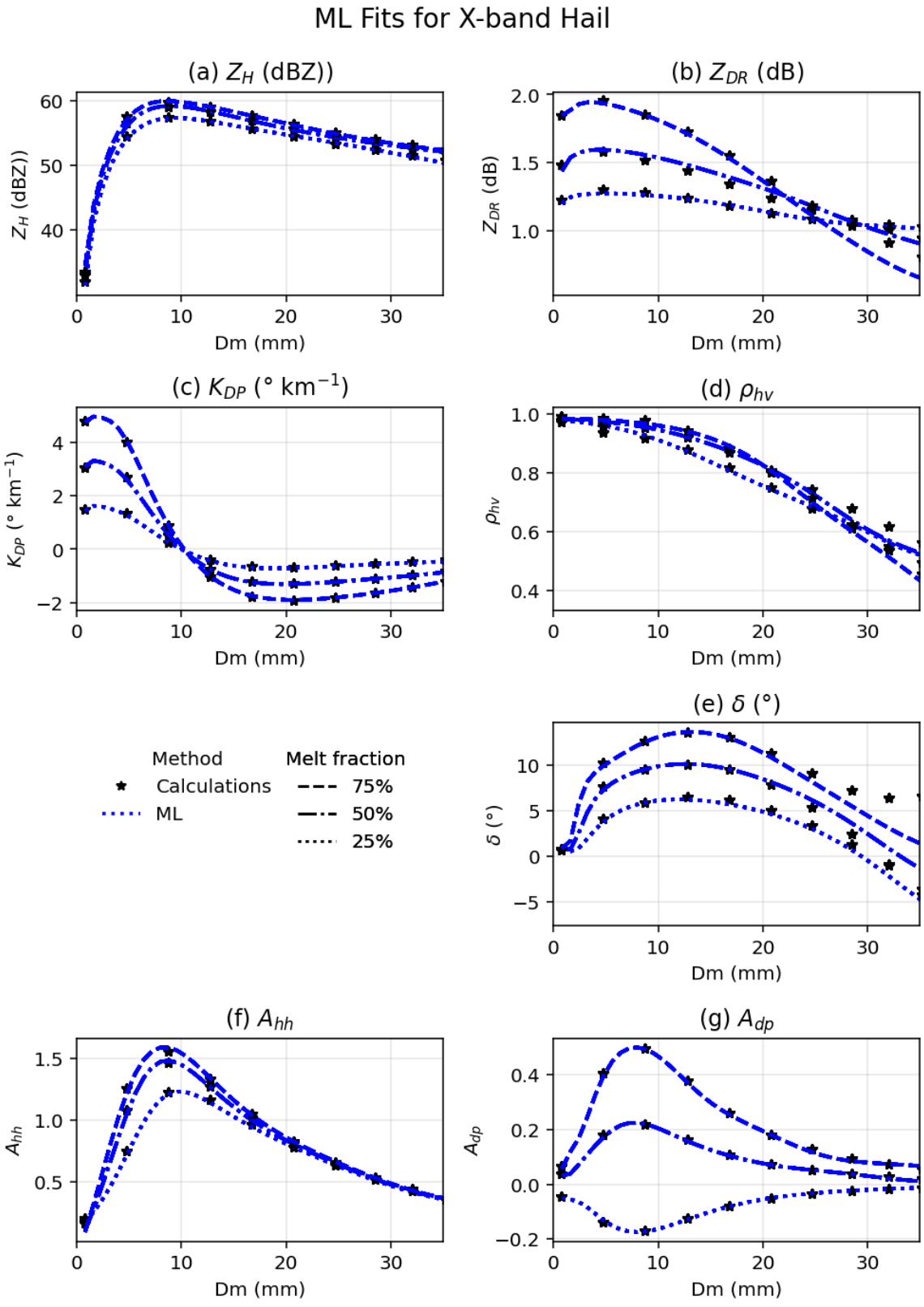

Figure 3.8. Same as Fig. 3.7, except for X-band.

The increased complexity observed at C-band becomes even more pronounced at X-band (Fig. 3.8). The K_{DP} exhibits a more abrupt transition from positive to negative values at smaller D_m, with a steeper decline following its peak. Similarly, Z_{DR} shows a more rapid decrease with increasing diameter, and ρ_{hv} degrades more quickly, reflecting enhanced variability in scattering phase and amplitude. The δ also demonstrates a more pronounced peak followed by a sharper downturn, even reaching negative values at larger diameters. This implies that fitting strategies must be sufficiently flexible to capture these nonlinearities—further motivating the use of ML-based approaches over traditional parameterizations. The flexible and physically consistent operators for S-, C-, and X-band frequencies can also provide additional information when multi-frequency polarimetric radar measurements are available.

3.5 Hydrometeor aggregation and additional physical constraints

While the polarimetric forward operators have been developed for efficiency, physical reasonableness and flexibility, there are still few limitations based on the physical assumptions. Not only are the aspect ratio and density set as constants, but the inherent bulk microphysics schemes may also result in physically unrealistic results. Additional constraints will be enforced on the relation between the bulk diameter D_m and the bulk melting percentage γ. The problem arises when the high γ is still enforced even when the D_m gets large, which is unrealistic as the high γ of very large hail, for instance, is not really realistic in nature.

A few studies have explored schemes designed to fundamentally avoid such issues, such as spectral bin microphysics (Ryzhkov et al., 2011; Carlin et al., 2019). However, in practice, retrieving microphysical properties for each bin is extremely challenging, even for relatively simple rain microphysics. Moreover, given that the assimilation of bulk microphysical parameters

is already computationally expensive, pursuing this approach is not currently feasible—especially as higher spatiotemporal resolution PPAR continues to be developed. Thus, an additional constraint on the maximum γ for each D_{m} is introduced to produce more realistic polarimetric signatures while preserving the physical assumptions of commonly used bulk double-moment microphysical schemes (e.g., Morrison, NSSL, Milbrandt & Yau) in NWP models. This also facilitates more consistent integration and combined use of information from both NWP outputs and polarimetric observations.

Earlier work by Rasmussen et al. (1984, hereafter RM84) and Rasmussen and Heymsfield (1987) demonstrated that smaller hailstones can achieve significantly higher degrees of melting than larger ones, indicating distinct melting behavior across hailstone sizes. For example, hailstones with diameters less than 9 mm can melt rapidly and may approach complete melting, whereas larger hailstones typically reach only about 20% melting. Wang et al. (2011) simplified RM84's water mass growth rate equation to express the melting fraction as a function of hailstone diameter. For an individual hailstone, the melting fraction can be written as

$$\gamma_w^{5mm} = \frac{m_w^{5mm}}{m_t^{5mm}} \tag{3.11}$$

where m_w is the melted water mass and m_t is the total mass. For short time intervals, assuming mass conservation,

$$m_t(D) = m_w(D) + m_i(D) = \frac{\pi}{6}\rho D^3. \tag{3.12}$$

The melting fraction can then be expressed in terms of the water mass growth rate R_{m} as

$$\gamma_w(D,t) = \frac{R_m(D)t}{m_t(D)}. \tag{3.13}$$

Let $\gamma_{w0} = \gamma_w(D_0, t_0)$denote the melting fraction at a reference diameter D_0, yielding

$$\gamma_w(D) = \frac{R_m(D)}{R_m(D_0)} \frac{m_t(D_0)}{m_t(D)} \,. \tag{3.14}$$

Following RM84, the water mass growth rate depends on particle size through ventilation effects,

$$R_m = \frac{dm}{dt} = -\frac{\chi A N_{Re}^{\frac{1}{2}}}{2a_i L_m}\left[N_{pr}^{\frac{1}{3}} k_a \left(T_{inf} - T_0\right) + N_{sc}^{\frac{1}{3}} L_e D_{v,a}\left(\rho_{v,inf} - \rho_{v,0}\right)\right] \tag{3.15}$$

where $N_{sc} = \frac{v}{D_{v,a}}$ where v is the kinematic viscosity of air, $D_{v,a}$ the diffusivity of water vapor in air, k_a the thermal diffusivity of air, $N_{pr} = \frac{v}{k_a}$ and $N_{Re} = \frac{2a_i U(D)}{v}$ where a_i is the semimajor axis, and A the surface area of the spherical particle. The $U(D)$ in Reynold's number can be assumed to be equivalent to the fall speed of hydrometeors. As both the denominator and numerator in Eq. (3.14) contain R_m, we can neglect all constants and environmental parameters. If we apply the assumption for the fall velocity of hail for Reynold's number calculation

$$F_D = F_G \tag{3.16}$$

$$\frac{1}{2} C_D \rho_a A v_t^2 = (\rho_h - \rho_a) V g \tag{3.17}$$

$$v_t = \sqrt{\frac{2(\rho_h - \rho_a) V g}{C_D \rho_a A}} = \sqrt{\frac{4(\rho_h - \rho_a)}{3 C_D \rho_a} g D} \tag{3.18}$$

$$v_t \propto D^{\frac{1}{2}} \tag{3.19}$$

$$\frac{A(D^2) N_{Re}\left(D D^{\beta}\right)^{\frac{1}{2}}}{a_i(D)}, \beta = 0.5. \tag{3.20}$$

Assuming that environmental parameters are constant and cancel in the ratio, and that the fall velocity scales as $v_t \propto D^{1/2}$, the Reynolds number dependence leads to

$$\frac{R_m(D)}{R_m(D_0)} \propto \left(\frac{D}{D_0}\right)^{1.75} . \tag{3.21}$$

Since $m_t \propto D^3$, the melting fraction becomes

$$\gamma_w = \gamma_{w0}\left(\frac{D_0}{D}\right)^{1.25}. \tag{3.22}$$

To extend this to a hail size distribution, a two-parameter exponential distribution is assumed

$$N(D) = N_0 \exp(-\Lambda D) \tag{3.23}$$

where N_0 (m^{-3} mm^{-1}) is the intercept parameter and Λ (mm^{-1}) is the slope parameter. The total hail water content is

$$\begin{aligned} W_t &= \int_0^\infty m_t(D)N(D)dD \\ &= \int_0^\infty \frac{\pi}{6}\rho_h D^3 N_0 \exp(-\Lambda D)\, dD \\ &= \frac{\pi}{6}\bar{\rho}_h N_0 \Lambda^{-4}\ \Gamma(4). \end{aligned} \tag{3.24}$$

The liquid water content is

$$\begin{aligned} W_w &= \int_0^\infty m_w(D)N(D)dD \\ &= \int_0^\infty m_t(D)\gamma_w(D)N(D)dD \\ &= \int_0^\infty \frac{\pi}{6}\rho_h D^3 \gamma_w(D_0)\left(\tfrac{D_0}{D}\right)^p N_0 \exp(-\Lambda D)\, dD \\ &= \frac{\pi}{6}\rho_h N_0 \gamma_w(D_0)(D_0)^p \Lambda^{-(4-p)}\ \Gamma(4-p). \end{aligned} \tag{3.25}$$

Taking the ratio between (3.25) and (3.24) yields the percentage of melting for the hail PSD as

$$\gamma_w = \frac{W_w}{W_t} = \gamma_w(D_0)\left(\frac{D_0}{D_m}\right)^p \frac{4^p}{6}\Gamma(4-p). \tag{3.26}$$

A more rigorous treatment separates the integration into two regions ($D < D_0$ and $D > D_0$):

$$W_w = \int_0^\infty m_t(D)\gamma_w(D)N(D)dD \tag{3.27}$$

$$= \int_0^{D_0} \frac{\pi}{6} \rho_h D^3 \gamma_w(D_0) N_0 \exp(-\Lambda D)\, dD + \int_{D_0}^{\infty} \frac{\pi}{6} \rho_h D^3 \gamma_w(D_0) \left(\frac{D_0}{D}\right)^p N_0 \exp(-\Lambda D)\, dD$$

$$= \frac{\pi}{6} \rho_h N_0 \gamma_w(D_0) \{\Lambda^{-4}\ \gamma(4, \Lambda D_0) + (D_0)^p \Lambda^{-(4-p)} [\ \gamma(4-p) - \gamma(4-p, \Lambda D_0)]. \quad (3.28)$$

This yields

$$\bar{\gamma}_w = \frac{\mathrm{W}_w}{\mathrm{W}_t} = \frac{\gamma_w(D_0)\{\ \gamma(4, \Lambda D_0) + (D_0)^p \Lambda^p [\ \Gamma(4-p) - \gamma(4-p, \Lambda D_0)]\}}{\Gamma(4)}. \quad (3.29)$$

Based on numerical integration and curve fitting, the bulk melting fraction as a function of D_m can be approximated by:

$$\gamma_w(D_m) = exp(4.624 + 1.698 \times 10^{-2} D_m - 1.508 \times 10^{-2} D_m^2 + 8.790 \times 10^{-4} D_m^3 - 2.104 \times 10^{-5} D_m^4 + 1.836 \times 10^{-7} D_m^5) \quad (D_0 = 5mm) \quad (3.30)$$

$$\gamma_w(D_m) = exp(4.589 + 2.508 \times 10^{-2} D_m - 6.173 \times 10^{-3} D_m^2 + 1.929 \times 10^{-4} D_m^3 - 1.955 \times 10^{-6} D_m^4) \quad (D_o = 9mm) \quad (3.31)$$

with coefficients determined for specific reference diameters (e.g., $D_0 = 5$mm and 9mm). The curve fitting results for $D_0 = 5$mm for the analytical and numerical calculations as a function of D_m are shown in Fig. 3.9.

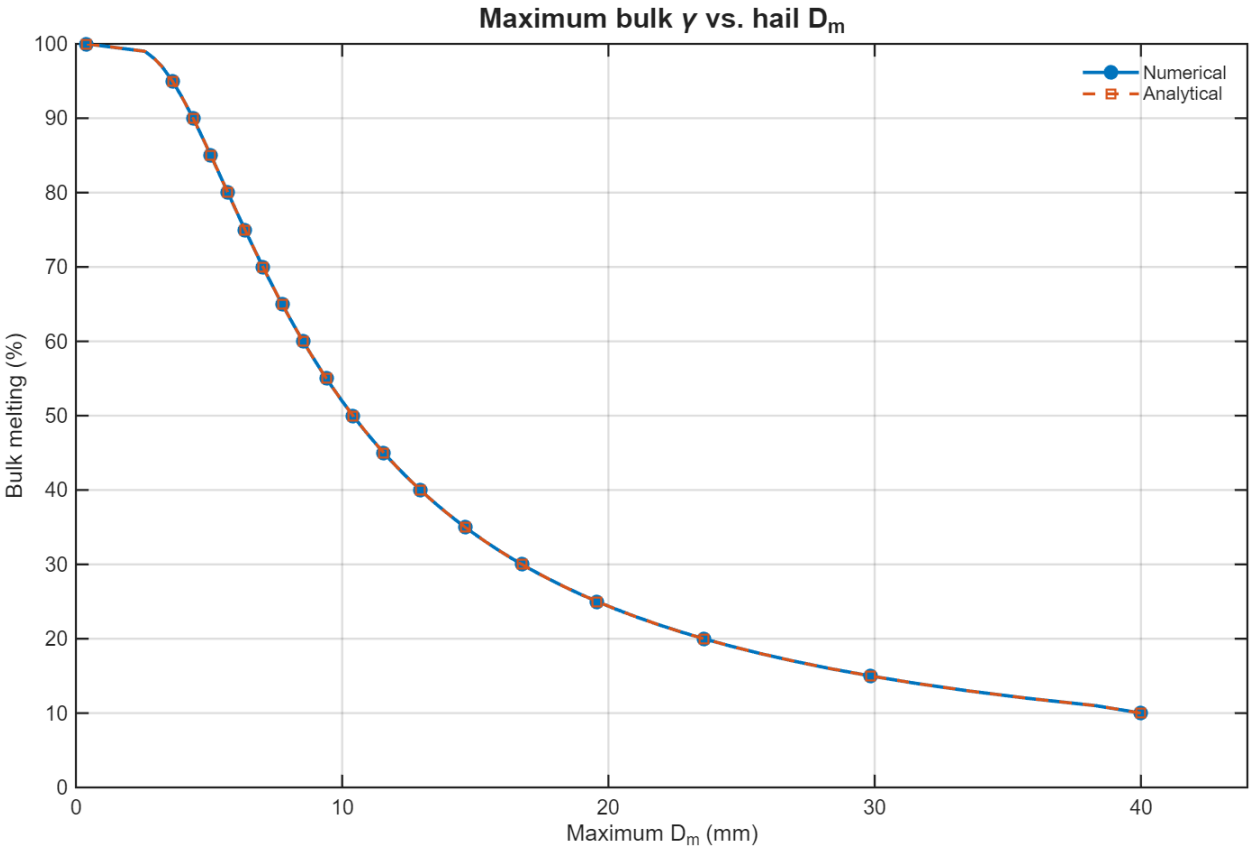

Figure 3.9. Maximum D_m as a function of γ. Results from numerical integration (solid line with circles) and the analytical formulation (dashed line with squares) are shown. The calculations are for D_0 = 5 mm.

Although the operators were extended to D_m = 35 mm for all γ values to ensure computational completeness, a hail γ constraint was applied in subsequent analyses and retrievals as a function of D_m, as discussed in aforementioned formulations. A reference diameter of 5 mm was assumed, such that full melting ($\gamma = 100\%$) was permitted for $D \leq 5\,\text{mm}$. For larger D and D_m, the maximum allowable melting fraction decreases as a function of D_m, ensuring physically consistent behavior at large hail sizes. Using the mixing formulas and the constrained hail γ, total polarimetric variables were computed by combining contributions from each hydrometeor species following Eqs. (22)–(25) of Zhang et al. (2021), which are listed below following the definitions of each polarimetric variable.

$$Z_{\mathrm{h}} = \sum Z_{\mathrm{h}}(x)$$

$$Z_{dr} = \frac{\sum Z_h(x)}{\sum \frac{Z_h(x)}{Z_{dr}(x)}}$$

$$K_{DP} = \sum K_{DP}(x).$$

The formulation for total δ is included in this study to simulate and combine δ contributions from multiple hydrometeors, as given in Eq. (3.32),

$$\delta_{tot} = -\frac{180}{\pi} \arg\left(\sum_x \rho_{\mathrm{hv}}(x) Z_{\mathrm{h}}(x) Z_{\mathrm{dr}}^{-\frac{1}{2}}(x)\, e^{-j\delta(x)} \right), \tag{3.32}$$

$$\rho_{hv} = \frac{|\sum_x Z_h(x) Z_{dr}^{-\frac{1}{2}}(x) \rho_{hv}(x) e^{i\delta(x)}|}{\sum_x Z_h(x) Z_{dr}^{-\frac{1}{2}}(x)} \tag{3.33}$$

where, $\rho_{\mathrm{hv}}(\mathrm{x})$, $Z_{\mathrm{h}}(\mathrm{x})$, $Z_{\mathrm{dr}}(\mathrm{x})$, and $\delta(x)$ represent the contributions from each hydrometeor species. The individual $\delta(x)$ values are expressed in radians, and the resulting total δ_{tot} is converted to degrees. The ρ_{hv} calculation is also updated accordingly in Eq. (3.33). The further decorrelation effects from multiple hydrometeors within a grid cell are represented using intrinsic δ values. However, as discussed in Zhang et al. (2021), these intrinsic values alone are often insufficient to reproduce the observed reduction in ρ_{hv} due to simplifying assumptions in the scattering calculations, as well as limitations within bulk microphysics schemes. To address this, additional empirical exponents are introduced. Rather than applying a single constant exponent (e.g., 1.5–2.0), a two-step factor (each set to 1.5) is implemented to separately account for (1) decorrelation due to neglected hydrometeor surface roughness, applied at the individual hydrometeor level, and (2) additional decorrelation arising from stochastic variability in particle properties and orientations, applied to the total calculated ρ_{hv}. This approach is justified because ρ_{hv} is highly sensitive to hydrometeor variability that is not fully represented in T-matrix assumptions.

Therefore, incorporating these additional exponents provides a more realistic representation of hydrometeor roughness and randomness, leading to improved simulation of ρ_{hv} reduction.

3.6 Numerical experiments using WRF simulations

The ML derived operators for the three mixing formulas are evaluated for physically realistic polarimetric signatures using WRF model output with the updated melting scheme from Liu et al. (2024b). The case examined is from a mesoscale convective system that occurred across Illinois and Missouri on 29 May 2019. The most developed stage at 0200 UTC is used for the subsequent analysis. The system contains both a stratiform region in the northern sector and convective regions extended from western to central Illinois, with a few reported hail events in these areas (https://www.spc.noaa.gov/climo/reports/190529_rpts.html). The simulation was conducted at 1.5 km horizontal resolution with 600 grid points in each horizontal direction, and 50 vertical levels. The experiment was initialized at 1800 UTC with a one-hour spin-up period. DA cycles began at 1900 UTC and were performed at 15-minute intervals through 2300 UTC. Three-hour forecasts were initialized at the top of each hour during this period. Additional details are provided in Liu et al. (2024a).

The horizontal and vertical cross sections of the WRF-simulated polarimetric variables, based on the ML-parameterized operators for the three mixing formulas, are depicted in Figs. 3.10 and 3.11. The horizontal cross-section was interpolated to a constant height of 3.5 km. The Z_H fields from the three mixing formulas (Figs. 3.10a–c) show overall similar spatial distributions, with values reaching up to 62 dBZ. All formulas depict similar features in stratiform regions north of approximately 41°N and hail-producing convective cells in the southern region. Notable differences appear in the northeastern region, where MGW produces more extensive areas

exceeding 45 dBZ. Additionally, MGW simulates slightly more convective cores in the southern domain than PS and MGI. The Z_{DR} fields (Figs. 3.10d–f) reach up to 4.2 dB, with higher values primarily in regions of stronger rain. In the southeastern portion of the convective region, MGW shows the largest spatial coverage of moderate Z_{DR} values (~1.5 dB), followed by PS and then MGI. Consistent with theoretical expectations, MGW and PS yield slightly larger values than MGI.

The K_{DP} fields (Figs. 3.10g–i) are near 0 in stratiform rain areas, and larger values mostly ranging from 0.6 to 2.0 ° km^{-1}, especially in the location of stronger rain regions, near ~ 39.5°N and 93.3°W. In the southern convective cell near 93 °W and 39 °N, the K_{DP} reaches up to 2 ° km^{-1}. MGW yields higher K_{DP} values (~0.8° km^{-1}) than the other two formulas. MGI shows limited nonzero K_{DP} outside of the most intense precipitation cores. The ρ_{hv} fields (Figs. 3.10j–l) decrease to 0.95, but significant reductions are not simulated because most regions are dominated by rain, with only small hail present in this case. A reduction in ρ_{hv} to ~0.95 is observed only in MGW, whereas the other two mixing formulas maintain values above 0.97. The δ fields (Figs. 3.10m–o) show some differences among the three mixing formulas with MGW and PS exhibiting more pronounced non-zero δ values in convective cells, whereas non-zero δ values are less evident in MGI. As indicated by the simulation results, MGI shows a delayed effect compared to MGW and PS because δ becomes nonzero only beyond certain D_m thresholds, resulting in fewer positive δ values.

The vertical cross-section was taken through the stratiform region to highlight differences near the melting layer. The cross section follows 92.7°W longitude, with latitude ranging from 39°N to 42.5°N, so that both the stratiform melting layer and the adjacent convective region are included. Similar to the horizontal cuts, the Z_H cross sections show generally similar magnitudes and spatial

patterns among the three mixing formulas, except in the melting layer (Figs. 3.11a–c). The primary differences appear in the melting layer. MGW exhibits the most distinct enhancement in Z_{H} between about 3.5 and 4 km at about 41.5°N (Figs. 3.11b–c). The Z_{DR} signatures are also similar across the three formulas, with small differences in magnitude. MGW produces slightly higher Z_{DR} values, followed by PS and then MGI (Figs. 3.11d–f). The melting layer height indicated by Z_{DR} (around 3 km) is slightly lower than that indicated by Z_{H}, consistent with previous observational studies (e.g., Andric et al., 2013). The K_{DP} fields exhibit no significant differences. Near 3.5 km altitude and around 40.3°N, MGW and PS produce higher K_{DP} values (about 1.2 ° km^{-1}) compared to MGI (about 0.8 ° km^{-1}). The ρ_{hv} cross sections show a distinct melting layer signature in MGW, where values decrease ~0.98. PS and MGI have less pronounced signatures. This difference is primarily associated with contributions from wet graupel and snow in the melting layer. Larger reduction in ρ_{hv} in melting layers may require improvements in both microphysical representation and operator assumptions. Additional exponents may also be necessary to better represent decorrelation effects from hydrometeor mixtures and randomness. Further reductions of ~0.95 ρ_{hv} are also noticed, due to hail for lower levels for MGI and snow and graupel for MGW and PS near the melting layers. Consistent with the horizontal cross sections, the δ fields show larger values in hail regions for MGW and PS compared to MGI.

The overall similarities among the three mixing formulas are expected, with differences primarily observed in regions with smaller D_{m} and higher γ. While the previous comparison plots revealed notable differences in the polarimetric variables across the different mixing formulas, the sum of multiple hydrometeors may reduce the impact of individual components. Additionally, the lack of more realistic polarimetric signatures may also be attributed to limitations in the microphysics schemes. For example, the WRF simulation results may contain biases because this

study uses the Milbrandt and Yau microphysics scheme, which—like other three–ice-species schemes—tends to overestimate convective regions and underestimate stratiform regions (Wu et al., 2013). Further work is needed to reduce uncertainties from both the forward operator and NWP simulations (Zhang et al., 2019). Overall, melting-layer polarimetric signatures are more clearly represented in the MGW and PS mixing formulas than in MGI.

3.7 Summary

This chapter focuses on the development of parameterized polarimetric forward observation operators as a key component of the overall objective for improving microphysical retrievals. Specifically, a compact ML formulation is employed, using a Sigmoid activation function with a single hidden layer of only 3–4 nodes. The resulting models require a limited number of trainable parameters (approximately 15–20) while maintaining a consistent functional form across different mixing formulations, frequencies, and radar variables.

The proposed ML-based parameterized forward operators provide high accuracy, computational efficiency, and differentiability —properties essential for operators used in DA, NWP model verifications, and retrieval applications. The formulation can also be extended to other parameterization problems to improve accuracy while reducing computational costs. Furthermore, using three different mixing formulas allows the DA and NWP model communities to choose operators consistent with their specific model assumptions and microphysical conditions. It also provides a means to quantify operator uncertainty associated with dielectric mixing assumptions.

WRF simulations were used to evaluate the physical realism of the three mixing formulas. All three approaches produced reasonable results at upper-level, near-surface, and in hail-core regions, with the primary differences occurring in the melting layer. MGW and PS produced more realistic

melting layer signatures, including enhanced Z_{H} and Z_{DR}, and reduced ρ_{hv}. In addition, the δ signature was more evident in MGW and PS within hail-core regions, consistent with physical understanding from previous studies (Mishler et al., 2024). In contrast, MGI exhibited delayed or weaker signatures. These results reinforce that assumptions within dielectric mixing formulas significantly influence the simulated polarimetric signatures. Based on physical understanding and the findings of this study, the MGW mixing formula is suggested for hail and graupel, while the PS mixing formula is recommended for snow, during their melting processes, in subsequent simulations and analyses. MGI may be used as an additional formula for operator error estimation.

Several limitations of this study on forward operators should be noted. The physical assumptions and constant parameters for aspect ratio and density adopted here may affect future algorithm development and performance, depending on assumptions regarding hail size and dielectric properties. Additional constraints, such as hail size and melting fraction, may be required to ensure physical consistency. Furthermore, the treatment of δ and its role in the decorrelation of ρ_{hv} should be further examined to better represent realistic polarimetric signatures in model simulations. When applying these operators, certain model schemes and assumptions—such as those in P3, triple-moment schemes, or those including density variability—may not be directly compatible; therefore, careful evaluation is required prior to their use in such contexts. for example, further efforts to refine both the underlying physical assumptions and the fitting methodology may be necessary for future applications. Fortunately, the ML-based parameterization developed in this study is relatively flexible and can accommodate such refinements. In summary, this work provides a new approach for parameterizing complex microphysical processes using explicit ML methods, enabling the development of efficient polarimetric radar forward operators.

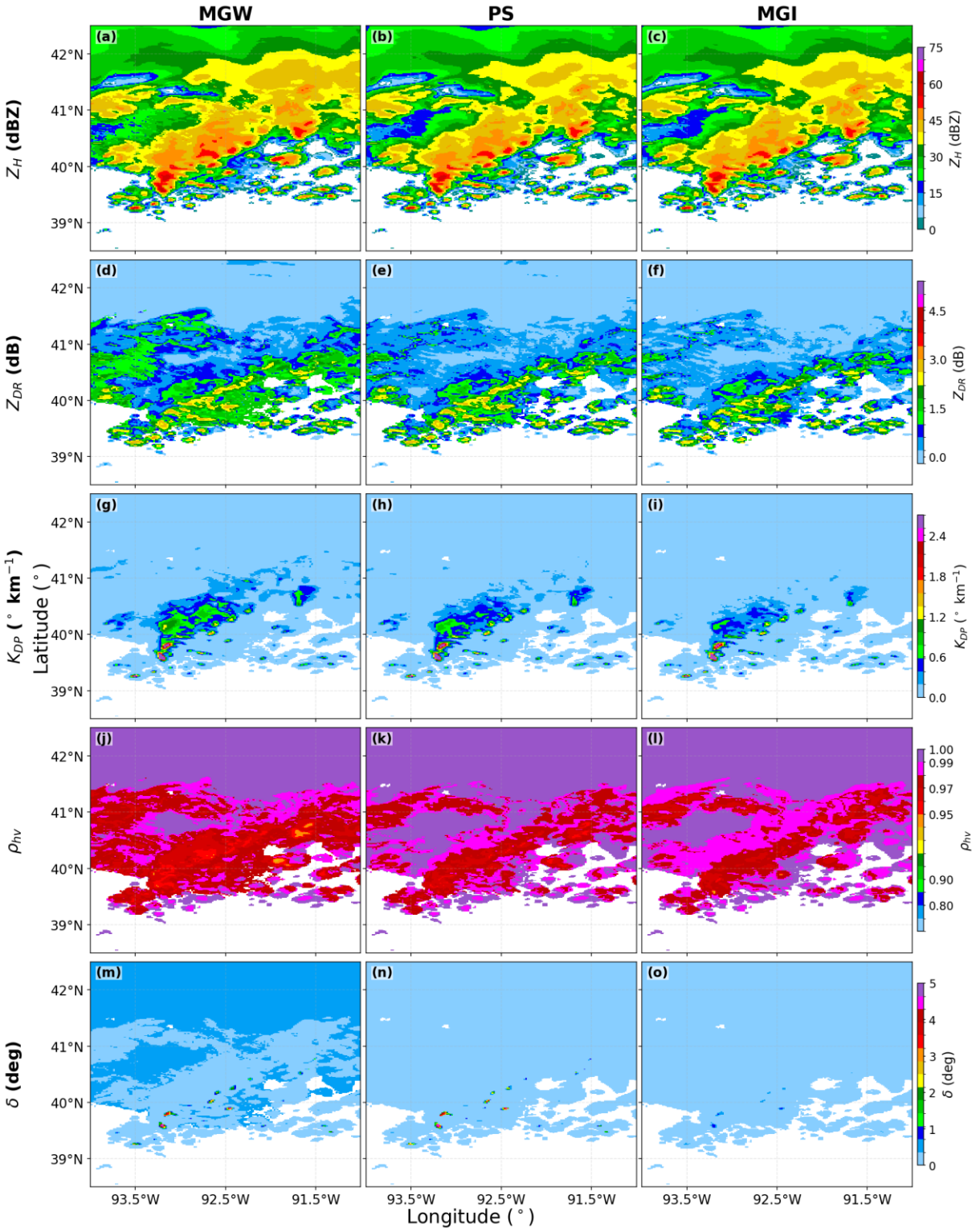

Figure 3.10. The constant altitude of polarimetric variables at 3.5 km from the WRF simulation for the three mixing formulas. The first column denotes the MGW, second PS, and the third MGI. Each row represents the radar variables, Z_H, Z_{DR}, K_{DP}, ρ_{hv}, and δ.

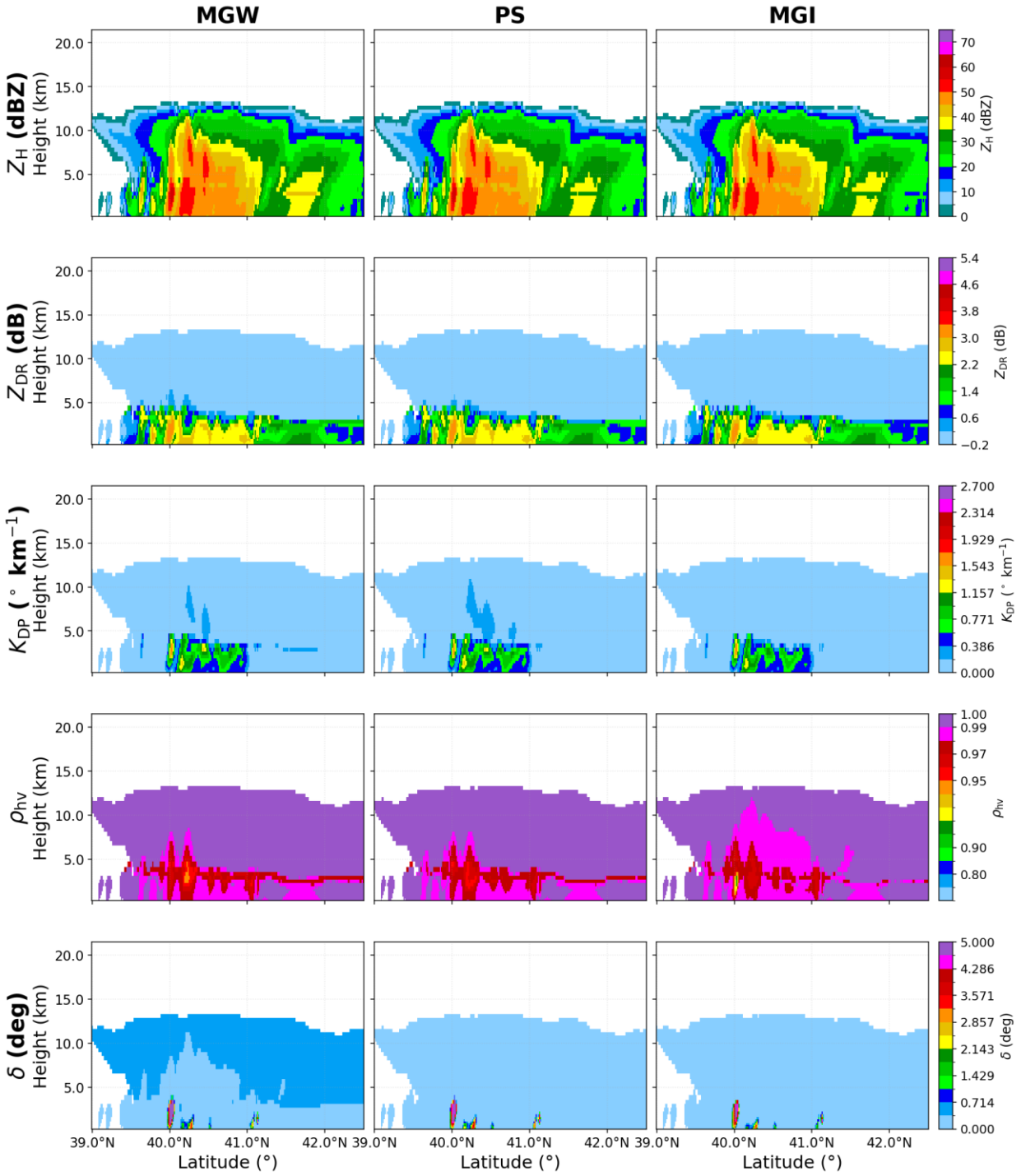

Figure 3.11. Same as Fig. 3.10, except a cross section along the 92.7 °W.

Chapter 4 Error analysis of polarimetric radar data

In the previous chapter, the development of forward operators based on multiple mixing formulas enabled the estimation of operator error. This chapter serves the role of estimating the measurement error from the polarimetric radar measurements which is the other part of the observational error needed for accurate retrievals. Particularly, this chapter utilizes the PPAR measurements to estimate the errors to evaluate the potential of each configuration of the proposed polarimetric phased array radars. The quality of PRD is critical for reliable microphysical retrievals, and quantifying these measurement uncertainties is essential for evaluating the feasibility and potential of PPAR systems.

An overview of the error analysis from PRD is presented in Chapter 4.1, and Chapter 4.2 introduces the PARs. The two PPARs, Horus and CPPAR, along with the reference KTLX measurements, are described in Chapter 4.3, including the collocation and interpolation methods used to match the measurement domains. Chapter 4.4 presents the calculation of the standard deviations for the Horus and CPPAR observations, as well as comparisons between the Horus and KTLX datasets and between the CPPAR and KTLX datasets, with the mean biases and related statistics quantified. In Chapter 4.5, the off-broadside impacts of the planar design are explored and discussed. Chapter 4.6 examines the advantages, disadvantages, and future potential of the CPPAR and 2D PPPAR configurations. Finally, Chapter 4.7 summarizes the results and discusses possible future developments and improvements of the PPARs for weather measurements.

4.1 Overview of error analysis in polarimetric radar data

The estimation of standard deviations (STD) from polarimetric radar measurements provides a fundamental means of assessing radar performance and forms the basis for specifying

observation error statistics in retrieval and data assimilation applications. Under the assumptions of statistically independent samples and sufficiently large sample sizes, the STDs of the polarimetric variables can be approximated using lag-0 estimators (Doviak and Zrnić, 2006; Zhang, 2016) as follows:

$$\mathrm{STD}(\hat{Z}_{\mathrm{H,V}}) \approx 10\log\left(1+\frac{1}{\sqrt{M_{\mathrm{I}}}}\right) \tag{4.1}$$

$$\mathrm{STD}(\hat{Z}_{\mathrm{DR}}) \approx 4.343\sqrt{\frac{2}{M_{\mathrm{I}}}\left(1-\rho_{\mathrm{hv}}^2\right)} \tag{4.2}$$

$$\mathrm{STD}(\hat{\rho}_{\mathrm{hv}}) = \frac{1-\rho_{\mathrm{hv}}^2}{\sqrt{2M_{\mathrm{I}}}} \tag{4.3}$$

$$\mathrm{STD}(\hat{\Phi}_{\mathrm{DP}}) = \frac{180}{\pi\rho_{\mathrm{hv}}}\sqrt{\frac{\left(1-\rho_{\mathrm{hv}}^2\right)}{2M_{\mathrm{I}}}} \tag{4.4}$$

$$SD(\hat{v}_r) = \frac{\lambda}{4\pi\rho(T_s)T_s\sqrt{2M_I}}[1-\rho^2(T_s)]^{\frac{1}{2}} \tag{4.5}$$

$$SD(\hat{\sigma}_v) = \frac{\lambda^2}{16\pi^2\rho(T_s)\sigma_v T_s^2\sqrt{2M_I}}\left[\left(1-\rho^2(T_s)\right)^2\right]^{\frac{1}{2}} \tag{4.6}$$

where the effective number of independent samples is given by

$$M_I = \frac{T_d}{\sqrt{\pi}\tau_c}. \tag{4.7}$$

Here, T_d denotes dwell time and τ_c is the signal correlation time. These expressions represent theoretical lower bounds on measurement uncertainty under idealized sampling conditions. In practice, however, PRD are affected by multiple sources of error, which can be broadly categorized as: (i) instrumental and calibration errors, (ii) sampling and statistical uncertainties associated with finite and correlated samples, (iii) propagation and medium effects such as attenuation and non-uniform beam filling, and (iv) beam geometry effects (Doviak and Zrnić, 2006; Zhang, 2016). The subsequent chapters focus specifically on the off-broadside behavior of 2D PPARs. Particular

attention is given to the degradation of ρ_{hv}, which is often more difficult to mitigate compared to other polarimetric variables. For example, biases in Z_{DR} can often be corrected through calibration procedures, whereas reductions in ρ_{hv} are more fundamentally tied to signal decorrelation and are not as easily corrected post-observation. As noted previously, reductions in ρ_{hv} may also arise from factors unrelated to beam geometry, including non-Rayleigh scattering effects, the presence of diverse hydrometeor populations within the resolution volume, and non-uniform beam filling (Ryzhkov 2007). Thus, while improvements in spatiotemporal resolution offer clear advantages, the quality of PRD remains the primary consideration for polarimetric applications. Further efforts to quantify and mitigate systematic errors in ρ_{hv} are therefore essential.

4.2 Polarimetric phased array radars

The debate on the next generation radars has been a debate within the radar meteorology community even before the completion of the deployment of the NEXRAD systems (e.g., Wurman, 2001). Phased array radars (PARs) are an emerging technology in the meteorological community. They offer the advantage of providing rapid and timely information that greatly enhances the understanding of severe weather phenomena as they unfold (Kuster et al., 2016; Wilson et al., 2017). PARs are also versatile and can effectively serve multiple purposes (Weber et al. 2007; Zhang and Doviak, 2007; Zrnic et al., 2007; Heinselman et al., 2008; Stailey and Hondl, 2016; Kollias et al., 2022). Many countries are actively involved in the development of PAR systems to replace or complement existing parabolic dish antenna operational radars (e.g., Wu et al. 2018, Kikuchi et al. 2020; Kollias et al., 2022; Palmer et al., 2022). Among PAR designs, the most common are 1D planar PARs, which have been investigated in the X-band polarimetric PAR (PPAR) in Japan (Kikuchi et al., 2020; Ushio et al., 2022), China (Wu et al., 2018; Yu et al., 2020), and the United States of America (USA, Wurman and Randall, 2001; Bluestein et al., 2010; Orzel and Frasier, 2018). 1D planar PPARs (PPPARs)—those with electronic scanning in elevation and mechanical steering in azimuth—can provide high-quality polarimetric data and represent a compromise between a costly-but-fully-electronic multi-face PPAR system and the less costly-but-slower-traditional rotating dish system. Preliminary error analysis and meteorological applications to improve weather forecasting using these 1D PPPARs have been performed (e.g., Orzel and Frasier, 2018; Kim et al., 2021; Baron et al., 2023).

In recent years, the most flexible and useful design of 2D PPARs for meteorological applications remains a subject of ongoing discussion since the formulation presented in Zhang et al., 2009. This is primarily due to the complexity and difficulty of providing high-quality

polarimetric measurements when the beam steers off the broadside. Two main design approaches—the cylindrical design (Fulton et al., 2017; Golbon-Haghighi et al., 2021; Zhang, 2022; Zhang et al., 2011) and planar configurations (Heberling and Frasier, 2021; Palmer et al., 2022, 2023)—have garnered the most attention for 2D electronic scanning, each with its own advantages and disadvantages.

An S-band fully digital PPPAR named Horus (Fig. 4.1a) was developed by the Advanced Radar Research Center (ARRC) at the University of Oklahoma (OU) with funding from the National Severe Storms Laboratory (NSSL) and the Office of Naval Research (ONR) (Palmer et al., 2023). The fully digital design, with element-level analog to digital converters (ADC), can provide advantageous characteristics in multi-functionality, including high flexibility in spatio-temporal resolution and sampling, beam agility, interference mitigation, and, in theory, software configurability. However, as a 2D PPPAR, Horus faces major challenges in calibrating polarimetric variables to meet weather observation requirements (Zhang et al., 2009, 2011; Lei et al., 2013, 2015; Palmer et al., 2023). Fundamental issues affecting data quality include geometrically induced copolar biases, cross-polarization coupling and sensitivity loss as well as performance degradation as the beam steers off broadside (Zhang et al., 2009, 2011; Zhang 2016; Zrnic et al., 2011). PPPARs utilize hundreds of beams with different characteristics, which necessitates beam steering-dependent calibration (Ivić et al., 2019; Weber et al., 2021). The most critical issue is the sensitivity loss and performance degradation when steering at wide angles off broadside; while the bias can be corrected, addressing the sensitivity loss is difficult and may require increased antenna size and higher transmit power to meet the sensitivity requirements at large off-broadside angles (Zhang et al., 2011). Also, the polarization purity loss is difficult to compensate/calibrate, although calibration methods (e.g., Zhang et al. 2009, Dorsey et al. 2021,

Fulton et al., 2022; Ivić, 2023) to mitigate cross-polar biases have been proposed. High quality polarimetric weather measurements have not been achieved with error quantification yet when a PPPAR steers at wide angles.

Alternatively, the cylindrical PPAR (CPPAR) design has been proposed and demonstrated, and a prototype was developed by the ARRC (Fig. 4.1b) due to its advantageous properties of scan-invariant azimuthal beams and polarization orthogonality in all directions (Zhang et al., 2011; Karimkashi and Zhang, 2013, 2015; Fulton et al., 2017; Golbon-Haghighi et al., 2021). CPPAR provides more efficient radiating power and spectrum utilization without the need for face-to-face matching. These features make CPPAR capable of delivering effective and efficient polarimetric weather observations compared to the planar design (Zhang et al., 2011; Li et al., 2021; Dorsey et al., 2022; Logan et al., 2022). Nevertheless, several challenges of CPPAR have also been mentioned such as its relatively new design and development, the all-in-one system, whereas the PPPAR would operate 4 faces independently for different directions, and the potential influence of creeping waves and interferences (NSSL, 2014). These challenges have been studied and addressed through design/development of high performance radiating elements and optimized beamforming with active element patterns, in which the creeping wave effects have been taken into account (Golbon-Haghighi et al., 2021; Li et al., 2021; Mirmozafari et al., 2019; Zhang, 2022).

As mentioned above, many of the properties and characteristics of the two 2D PPAR systems have been explored based on the physical understanding of the electromagnetic (EM) theory, simulations, and experiments. In addition, the hardware requirements and specific calibration procedures for Horus and CPPAR have been discussed in previous studies (e.g., Li et al., 2021; Palmer et al., 2023). The primary objective of this chapter is to compare the error statistics of weather observations collected by CPPAR and Horus. This comparison aims to assess the quality

of the polarimetric data in their current states, investigate the potential issues, and clarify any misunderstandings about the two configurations. This study will incorporate findings from previous research conducted over the last 10 years on 2D PPAR development. It should be noted that the two radars are at different stages of development and with different levels of investment, and the weather observations are not from the same weather event. However, the comparison results presented in this study represent the first observation-based comparison of the two radar configurations. This result will be valuable in guiding the selection of the optimal configuration of PPARs for meteorological applications. The current specifications of Horus (Fig. 4.1a) and CPPAR (Fig. 4.1b), along with the reference measurement—KTLX, a nearby operational WSR–88D radar (Fig. 4.1c)—are presented in Chapter 4.3.

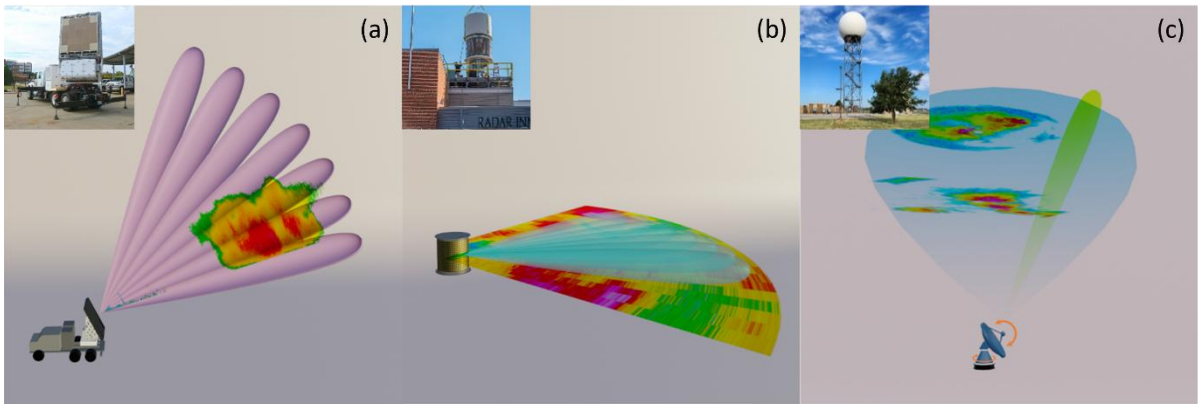

Figure 4.1. Depictions of (a) Horus, (b) CPPAR, and (c) WSR–88D (KOUN) scanning strategies based on the current configuration for weather measurements. The Horus image is taken from Palmer et al. (2023).

4.3 Horus and CPPAR experiment configuration

The Horus radar system has a planar design with 5 × 5 panels, each panel consisting of 8 × 8 dual-polarization antenna elements. Its full aperture size is 2.03 m × 2.03 m, and it operates at the S band at approximately 3.07 GHz (Table 4.1), as documented in Palmer et al. (2023). For this study, two sets of measurements are examined when the radar was configured with 13 out of 25 panels, with a transmit power of 8.32 kW and an antenna gain of approximately 31.5 dB. The distribution of active elements across the 25-panel array is illustrated in Fig. 4.2, showing the progression from the initial 5-panel setup to the 13-panel configuration.

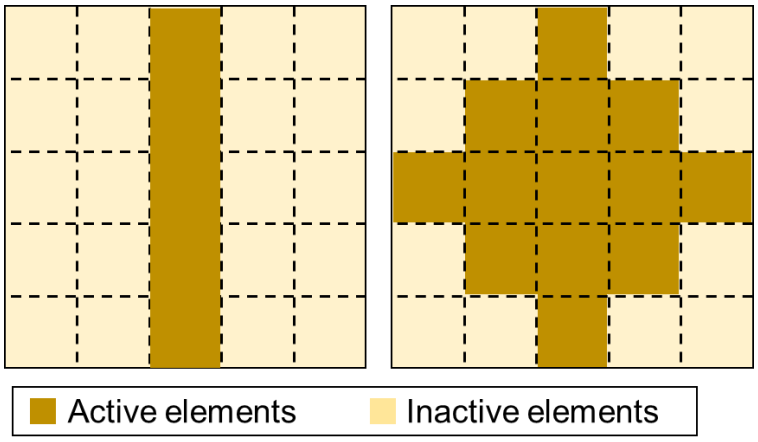

Figure 4.2. Depiction of the active elements used for 5- and 13-panel measurements. The dark yellow denotes the active elements, and the lighter yellow inactive.

The half-power beamwidth is 3.3° in both azimuth and elevation. Currently, only range-height indicator (RHI) scans have been performed with 64 elevation angles at 1° intervals. A total of eight cases have been measured by Horus, with six cases occurring prior to August 2023 using 5 panels and two subsequent cases using 13 panels. The bandwidth was approximately 7.8 MHz resulting in a range resolution of 19.2 m, with pulse compression. The progressive pulse compression

technique (Salazar Aquino et al., 2021) was utilized to remove the blind range, which used to be about 4.8 km. The temporal resolution was approximately 4 seconds, with a pulse repetition time (PRT) of 1 ms and 64 samples per dwell. The scanning strategy consists of a mechanical inclination of 31.5° with scans ranging from −31.5° to 31.5° in elevation (i.e., ~0° to 63° ground-relative elevation angles) at 1° increments. While it is true that most weather radars scan up to ~20° for weather applications, Horus in its current state only performs a 1D electronic scan along the elevation between −31.5° to 31.5°. This should reveal similar problems to those encountered when scanning in azimuth under similar weather conditions.

Radar Parameters	Horus	CPPAR	KTLX
Frequency (GHz)	3.07	2.76	2.8
Transmit power (kW/polarization)	8.32	4.32	375
Antenna gain (dB)	31.5	26	45.5
Elevation beamwidth (°)	3.3	5.35	0.925
Azimuth beamwidth (°)	3.3	6.2	0.925

Table 4.1. Specifications relevant to the sensitivity of each PAR configuration.

The 2-m prototype of the CPPAR, installed on the roof of the ARRC, also operates at the S band at a frequency of 2.76 GHz (Table 4.1). An illustration of the CPPAR is shown in Fig. 4.1b. CPPAR allows a single beam for mechanical scans and 25 commutating beams for electronic scans, with a PRT of 1 ms for 64 pulses per dwell. The range sampling interval is approximately 30 m, with the first 170 gates representing a blind range of about 5.1 km. The CPPAR consists of a total of 96 subarrays/columns (although only half of them, 48 columns, are active due to the budget constraint), each with an azimuthal spacing of 3.75° consisting of 19-element linear arrays. Of these 48 columns, 24 columns are used to form an electronic beam, yielding a total of 25 beams for the electronic scan, and among them the central beam sector (No. 13−36 columns) is used for

the mechanical scan in the study. The azimuthal beamwidth is approximately 6.2° after tapering, and the elevation beamwidth is 5.35° (Table 4.1). The transmit/receive antenna gain is 26 dB, and the peak transmit power is 4.32 kW. However, the development of CPPAR has been halted in its current state, and only single time step plan-position indicator (PPI) scans have been performed. Further specifications of CPPAR can be found in Li et al., (2021).

The radar parameters of the two PPARs listed in Table 4.1 exhibit large differences in transmit power, beamwidth, and antenna gain compared to KTLX (Fig. 4.1c vs. Figs.4.1a and 4.1b). The sensitivity difference derived from these parameters can be further discerned from the minimum detectable reflectivity plot (Fig. 4.3). The plot illustrates the calculated values from the lag-0 estimates of weather measurements (solid) from Horus (red), CPPAR (blue), and KTLX (black), compared to those from their radar parameters (dashed), as a function of range. Note that the system calibration factor of each radar was slightly adjusted to better align the two lines. As expected from the parameters of the three radars, the two 2D PPARs have much lower sensitivity of 25 dBZ for CPPAR, and 10 dBZ for Horus, compared to −10 dBZ for the operational KTLX at 45 km from the radar. Even between the two PPARs, the difference is considerable, with Horus ~ 15 dB better than CPPAR. However, these lower sensitivities of the two PPARs are not expected to introduce substantial biases in the error analysis. The errors are categorized by SNR levels, and their STD depends on the spectrum width and the copolar correlation coefficient for the same dwell time.

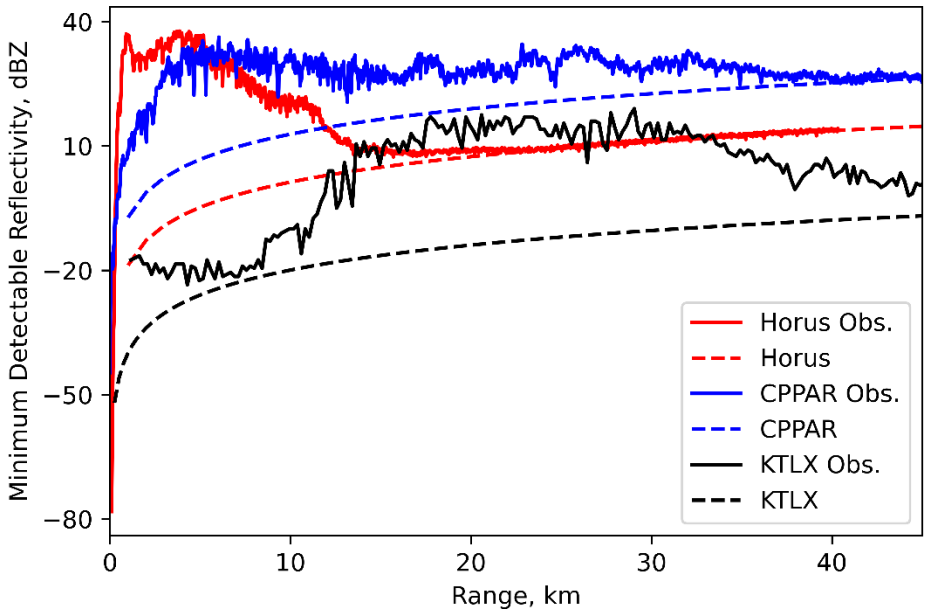

Figure 4.3. Plot of the minimum detectable reflectivity of Horus (red lines), CPPAR (blue lines), and KTLX (black lines). The solid lines are estimated from the weather measurements, and the dashed lines radar parameters.

4.3.1 Reference measurements

The three radar variables (Z_H, Z_{DR}, ρ_{hv}) from the operational KTLX radar located at Oklahoma City (34.33°N, 97.21°W) were used as a reference to calculate the mean biases and standard deviation of the differences between the radar measurements. Figure 4.4 depicts the relative positions of Horus (Fig. 4.4a) and CPPAR (Fig. 4.4b), represented by blue dots, respectively, in relation to KTLX (black dot), as well as the direction/sector of interest on the KTLX PPI for each case. The KTLX beams do not exactly coincide with the Horus RHI and the CPPAR PPI scans because the systems are not co-located and the beamwidths of the two radars are very different; therefore, other variables (v_r, σ_v, Φ_{DP}) were excluded from the comparison due to their radial dependency.

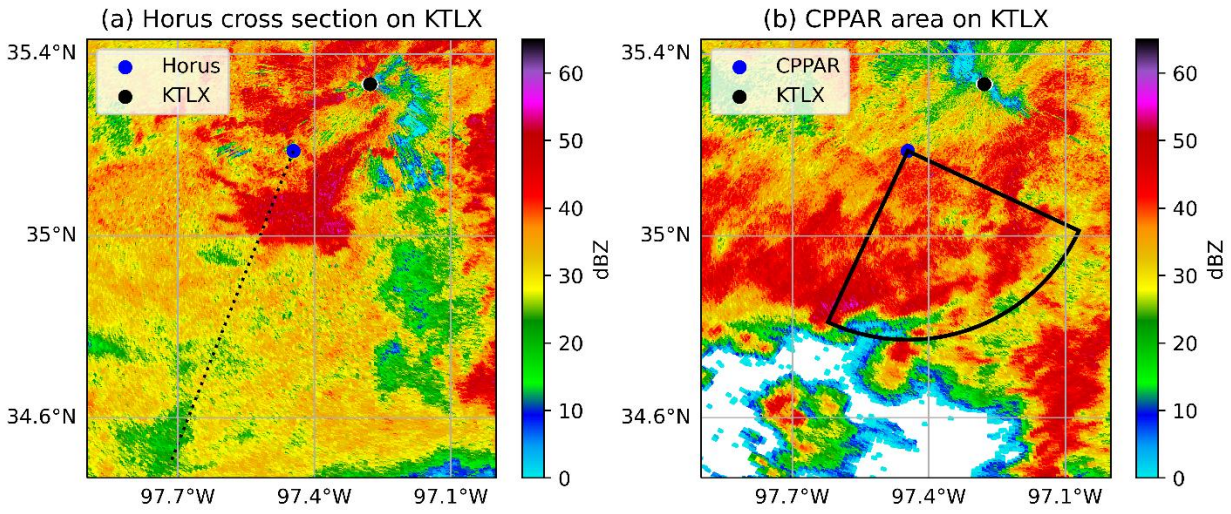

Figure 4.4. Plot of the observed Z_H from KTLX for regions of the Horus (left) at 2239 UTC on 4 October 2023, and CPPAR (right) at 1505 UTC 30 August 2019. The blue dot denotes Horus and CPPAR, and the black dot KTLX. The dashed line represents the azimuth of the Horus RHI scan, and the black solid lines the edges of the CPPAR PPI scan.

In order to minimize the influence in the difference in the positions of the radars, each elevation and time was carefully matched by selecting the Horus rays from the best-matching KTLX observation time for each elevation angle. The time can be well matched in the case of Horus and KTLX because Horus provides 4-second updates. In addition, three different types of interpolation grids were used to fit the KTLX reconstructed RHI to the Horus observations: (1) both KTLX and Horus were interpolated to the same grid with grid spacings of 10 m horizontally and 125 m vertically; (2) KTLX data were interpolated to the Horus range and elevation angles; and (3) both Horus and KTLX were objectively analyzed to a common grid of 500 m horizontally and 125 m vertically, respectively. Note that nearest-neighbor interpolation was used for both the KTLX reconstructed RHI and the gridded Horus data. Although not shown in subsequent figures, all interpolated grids showed similar results and had little effect on the error statistics. Therefore, the KTLX reconstructed RHI were converted to match the Horus RHI scans for easier error quantification in the subsequent analyses.

For CPPAR, it is not possible to match the beams perfectly in elevation and time because only one PPI data were collected for the case. The beam height of the 3.3° scan from the roof of the RIL building to approximately 45 km in range is about 2.8 km AGL, the closest elevation from the KTLX data was used for the same spatial coverage of CPPAR. Similar to the matching method with Horus, the KTLX data were extracted by interpolating the nearest points to the cross section between the CPPAR and the calculated location of 40 km in range for each azimuth angle. It should be noted that, even beyond the aforementioned matching in time and space, inherent mismatches persist between the interpolated RHIs or PPIs due to differences in radar resolution, beam width, and location.

4.3.2 Spatial and temporal calculations of errors

The standard deviation calculation for polarimetric radar measurements has traditionally been performed using spatial sampling, assuming a locally homogeneous precipitation field. This typically employs samples from a number of range gates, as demonstrated in an earlier CPPAR data analysis using N=17 range gates (Li et al., 2021) and shown in Eq. (4.8),

$$\mathrm{STD} = \sqrt{\frac{1}{2(N-m)} \sum_{l=n-\frac{N-1}{2}}^{n+\frac{N-1}{2}-m} (X_{l+m} - X_l)^2} \tag{4.8}$$

where n is the gate number at which the standard deviation is estimated, and X_l is the polarimetric data at gate l, and X_{l+m} is the value at l+m gates, with m as the spatial step after employing spatial samples. Various values of m have been tested for spatial samples, with a slight increase in standard deviations as m increases. The value m = 2 has been selected to avoid potential overlap in range samples, Considering the small sample spacing, the local homogeneity should be a valid

assumption. To maintain statistical significance, only gates with no missing data (i.e., all 15 samples from 17 range gates) were used to calculate the standard deviation.

In addition to spatial sampling, given the assumptions of ergodicity and local stationarity that apply to the Horus data due to its rapid updates every 4 seconds, it is possible to compute the standard deviation of the radar data from temporal samples. This approach involves examining the differences between successive time steps (i.e., $m = 1$) across the entire dataset. Since different range gates observe distinct parts of the precipitation field, and the movement of storms within 4 seconds generally falls within the resolution volume while signals become decorrelated, using temporal samples can provide more accurate estimates in many cases without the assumption of spatial homogeneity. The standard deviation is calculated for various polarimetric variables, including Z_H, v_r, spectrum width (σ_v), Z_{DR}, ρ_{hv}, and Φ_{DP}, for both spatial and temporal sampling. In the spatial sampling approach, 17 range gates were used based on the middle time step to calculate the standard deviation. Experimenting with different time steps or increasing the number of samples did not significantly change or improve the standard deviations. The computed values for both spatial and temporal samples are compared to theoretical values and the radar functional requirements set by the National Oceanic and Atmospheric Administration/National Weather Service (NOAA/NWS RFR). The theoretical values were derived using lag-0 estimate equations from Doviak and Zrnic (2006).

4.4 Comparison and validation of Horus and CPPAR data

To assess the data quality and system performance of the weather measurements, the error characteristics of the polarimetric data are calculated and quantified. Horus started its first weather

observations in December 2022 and continues to observe cases of shallow and deep convective precipitation. This study specifically examines a recent convective precipitation event on 4 October 2023 from 22:19 to 22:45 UTC, focusing mainly between 22:36 to 22:45 UTC. As illustrated in Fig. 4.3a, the Horus beam was directed at an azimuth of 198° from the north, penetrating the convective region of the storm. The 18:00 UTC Norman sounding of 04 October 2023 reveals favorable environmental conditions for deep convective storms, with a convective available potential energy (CAPE) of ~3078 J kg^{-1}. The combination of abundant low-level moisture and diurnal boundary layer heating with an approaching mid-level shortwave trough provided favorable conditions for thunderstorm development. The group of isolated convective cells of interest originated near the western Oklahoma/northwestern Texas border around 17:50 UTC, and a band of supercells in a loosely organized mesoscale convective system (MCS) moved across Oklahoma. According to the NWS, several reports of strong winds and hail were documented throughout central and northeastern Oklahoma (https://www.spc.noaa.gov/exper/archive/event.php?date=20231004).

Until the summer of 2020, CPPAR underwent development/testing and conducted weather measurements. This study focuses on weather observations that took place on 30 August 2019 at 15:04 UTC. Figure 4.4b depicts the measurement area of the CPPAR as observed from KTLX at 19:14 UTC. Like the convective case for Horus, the atmospheric conditions were conducive to severe storms. Around 10 UTC, the preexisting MCS from Kansas continued to move southeastward to produce thunderstorms in central Oklahoma. CAPE of up to 4000 J kg^{-1} and steep lapse rates of 2-6 °C km^{-1} have been reported, maintaining moderate instability ahead of the MCS. The NWS recorded strong gusts of up to 71 mph in northern to central Oklahoma (https://www.spc.noaa.gov/exper/archive/event.php?date=20190830).

In addition to the storm events, some radar parameters, waveforms, and calibration techniques differ between the two 2D PPARs. For example, Horus employed progressive pulse compression (Salazar Aquino et al., 2021) to eliminate the blind range and used mutual-coupling based calibration (e.g., Fulton et al. 2022; Palmer et al. 2023). On the other hand, CPPAR used a simpler calibration method by mounting a calibration horn on top of a nearby building to optimize the beams. This method aimed to match copolar patterns, maximize gain, and minimize sidelobe levels and cross-polar biases (Li et al., 2021). Also, a pulse compression waveform was used with a pulse width of 34 μs, resulting in short-range blind range of approximately 5.1 km for CPPAR. The timeseries data from the two PPARs were processed in the same way using lag-0 correlation estimators for regions with SNR greater than 20 dB and lag-1 for the rest. It should be noted that both the software and hardware of KTLX have not undergone any significant changes between 2019 and 2023 (https://training.weather.gov/wdtd/buildTraining/RPG-RDA.php).

The initial comparison is conducted between the radar measurements from the operational radar, KTLX, and the two PPARs to compute the mean bias and the standard deviation of the differences. Subsequently, a comparative analysis of the standard deviation is derived from both spatial and temporal samples for Horus, and solely spatial sampling for CPPAR.

4.4.1 Bias calculation of Horus and CPPAR data

The spatial distribution of the polarimetric variables from the two radars shown in Fig. 4.5 provides valuable information for identifying potential system deficiencies and understanding the error characteristics of Horus. KTLX, which benefits from higher antenna gain and transmit power, exhibits significantly higher SNR and sensitivity compared to Horus (Figs. 4.5a vs. 4.5b). The convective core located between 10 and 20 km demonstrates good agreement between the radars

(Figs. 4.5c vs. 4.5d). However, there are still some clear differences in the magnitude of the measurements. For example, the maximum Z_H near the ground, at about 15 km, exhibits a difference of more than 5 dB, and a lack of sensitivity in the Horus data remains apparent at further distances. Despite the bias, the ability of Horus to capture true RHIs provides much more detailed microphysical and dynamical process information due to the improved spatial and temporal resolution, demonstrating the potential of PARs to improve meteorological applications.

The polarimetric variables from Horus show more notable differences with that from KTLX. Slight Z_{DR} bias exists, with ~1.0 dB difference near the convective core (Figs. 4.5e vs. 4.5f). Additionally, the low Z_{DR} region between ~25 and 30 km for KTLX does not appear clearly for Horus, and noisy values of up to 1 dB above the melting layer. Overall, the Z_{DR} values from Horus agree well with KTLX, with positive biases of less than 0.5 dB throughout the entire domain. Note that KTLX has limited observations in the lower elevations due to its distance from the storm, and the near-ground data are interpolated from higher altitudes, leading to relatively larger differences in the lowest elevations. In addition, since the error characteristics of the polarimetric variables depend on ρ_{hv}, the lower to middle elevations of Z_{DR} may also be affected by the degraded ρ_{hv} in these regions (Fig. 4.5g). The high ρ_{hv} in Horus is notable in the lower and upper elevations, and the melting level agrees well with KTLX (Figs. 4.5g vs. 4.5h). However, Horus shows reduced ρ_{hv} values of less than 0.94 in the mid-altitude regions from 1.5 to 6 km, and these are more pronounced from about 20 km. While the reduction can be partly explained by snow melting, low SNR, and propagation effect, the reduced ρ_{hv} along the entire radials is a concerning feature. This ρ_{hv} reduction can imply error associated with electronic steering at large angles away from the broadside. Future improvements in PPAR signal processing for weather applications are planned

in light of the observed biases in the Z_{DR} and ρ_{hv}, and the need to minimize the influence of clutter and contamination by addressing sidelobes, beam width and steering loss issues.

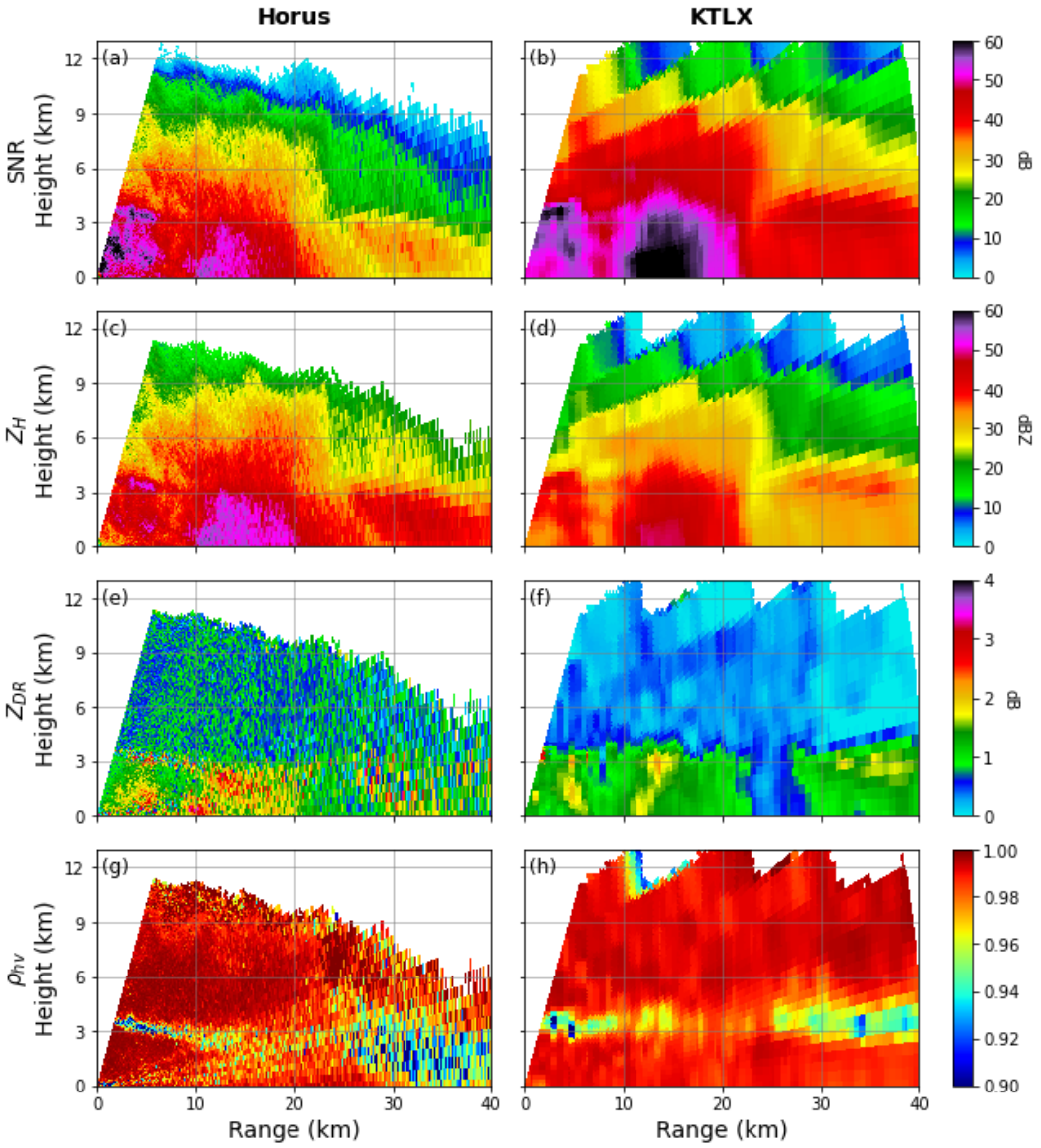

Figure 4.5. Spatial distribution of SNR, Z_H, Z_{DR}, and ρ_{hv} from Horus (a, c, e, and g) and KTLX (b, d, f, and h) measurements on 4 October 2023. All variables for both radars are plotted for SNR greater than 10 dB.

The mean bias and standard deviation of the differences from the KTLX comparison for the case shown in Fig. 4.5 are organized in Table 4.2. The values remain relatively stable and consistent across different SNR ranges. The mean bias and standard deviations for Z_H remains

around 3 to 4 dB and 5 to 6 dB, respectively (Tables 4.2a and b). Z_{DR} shows slight improvements with SNR decreasing to 0.23 dB bias and 0.72 dB standard deviation. The standard deviation values are typically similar to or greater than the corresponding mean bias values, with limited influence of beam broadening or mismatch on these statistics. There is minimal improvement in the accuracy of ρ_{hv} measurements with increasing SNR, suggesting that such a reduction is not due to lower SNR values. The consistently low ρ_{hv} bias is of concern, especially for the significant ρ_{hv} reduction between 20 and 40 km, as shown in Fig. 4.5. Further analysis of the potential causes of this degradation is discussed in Chapter 4.5.

(a) Mean bias

	SNR ≥ 0	SNR ≥ 5	SNR ≥ 10	SNR ≥ 15	SNR ≥ 20
Z_H (dB)	3.06 (3.63)	3.27 (3.76)	3.49 (3.94)	3.72 (4.15)	3.99 (4.33)
Z_{DR} (dB)	0.27 (0.32)	0.26 (0.32)	0.25 (0.31)	0.24 (0.3)	0.23 (0.29)
ρ_{hv}	−0.004 (0.002)	−0.003 (0.003)	−0.002 (0.003)	−0.002 (0.003)	−0.002 (0.003)

(b) Standard deviation

	SNR ≥ 0	SNR ≥ 5	SNR ≥ 10	SNR ≥ 15	SNR ≥ 20
Z_H (dB)	5.96	5.79	5.56	5.33	5.05
Z_{DR} (dB)	0.81	0.77	0.75	0.74	0.72
ρ_{hv}	0.036	0.032	0.032	0.032	0.033

Table 4.2. (a) Mean bias and (b) standard deviation of the differences between Horus and KTLX for each SNR range. The values in parentheses denote the median values.

The comparisons between CPPAR and KTLX are depicted in Fig. 4.6, which shows a generally similar spatial distribution as that between Horus and KTLX. The magnitude and distribution of Z_H from CPPAR agrees well with those from KTLX, except for a region of low SNR in the far ranges and a few radials influenced by a water tower close to the radar (Figure 4.6a vs. Figure

4.6b). Note that the CPPAR SNR is much lower than that of Horus and KTLX, as expected from the radar parameters. In the far ranges, CPPAR data are absent or have much smaller values, while KTLX shows values close to 20 dBZ (Figs. 4.6c vs. 4.6d). This discrepancy can be attributed to the distinct transmit power and sensitivity of the two systems. The Z_{DR} comparisons display similar trends, with a common location of Z_{DR} values up to 3.5 dB at around 40 km in range (Figs. 4.6e vs. 4.6f). Z_{DR} from CPPAR closely align with those from KTLX, showing no notable bias. In the lower SNR region, large ρ_{hv} values appear at the far edge of the CPPAR measurements, with reduced ρ_{hv} along radials with low SNR and/or the presence of the water tower in directions at azimuth of ~133° from the north (Figs. 4.6g vs. 4.6h). It is important to note that some differences in elevation and time between CPPAR and KTLX are unavoidable given that KTLX scans only every 6 min, and CPPAR did not perform additional scans at different times. There has been a misconception that cylindrical configuration may be prone to interferences or creeping waves (e.g., NSSL, 2014). However, as demonstrated from previous studies based on physical formulations (e.g., Golbon-Haghighi et al., 2021 and Li et al. 2021), such creeping wave effects are not noticeable in the CPPAR measurements. These results highlight the potential differences and biases between the two systems and provide valuable insights into the performance and error characteristics of the emerging CPPAR in comparison to the more established KTLX radar.

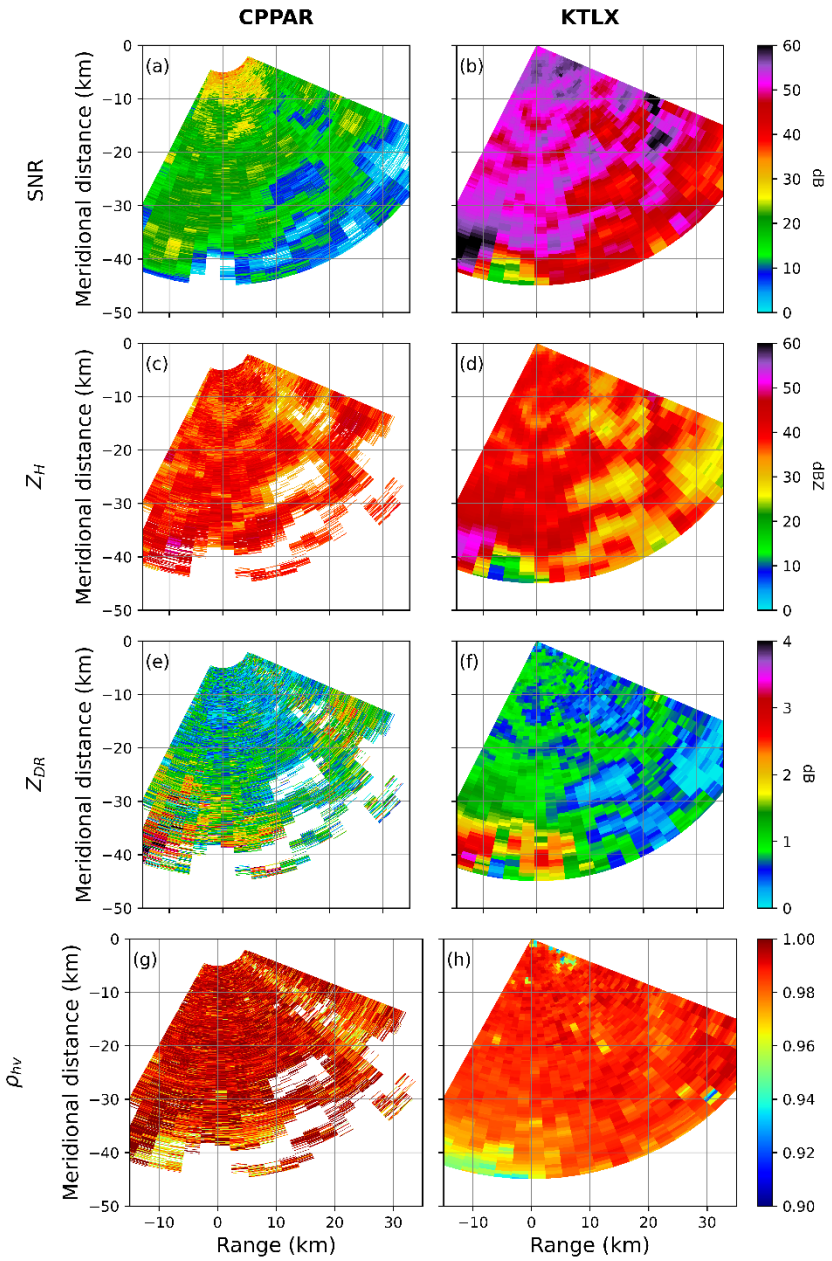

Figure 4.6. Same as Fig. 4.5, except for CPPAR and KTLX.

The calculated mean bias and the standard deviation of the differences between CPPAR and KTLX are organized in Table 4.3. The magnitude of the mean bias in all radar variables remains relatively stable with SNR ≥ 20 dB of approximately −1.29 dB, 0.04 dB, and 0.009 for Z_H, Z_{DR}, and ρ_{hv}, respectively. The small polarimetric biases compared to that of Horus is a promising

feature. Especially, the consistently low and positive bias of ρ_{hv} is an encouraging feature and implies that CPPAR is making progress towards achieving more accurate and reliable weather measurements (Table 4.3a). The standard deviation of the differences for CPPAR is generally similar to that of Horus for Z_H, Z_{DR}, and ρ_{hv} (Table 4.3b). The relatively larger overall biases in the Horus data may be attributed to errors in polarimetric calibration methods used as well as inherent design issues.

(a) Mean bias

	SNR ≥ 0	SNR ≥ 5	SNR ≥ 10	SNR ≥ 15	SNR ≥ 20
Z_H (dB)	−1.29 (−1.26)	−1.07 (−1.13)	−0.82 (−0.98)	−0.63 (−0.81)	−1.29 (−1.26)
Z_{DR} (dB)	0.04 (0.00)	0.03 (0.00)	0.03 (0.00)	0.01 (−0.02)	0.04 (0.00)
ρ_{hv}	0.009 (0.007)	0.006 (0.006)	0.006 (0.006)	0.007 (0.006)	0.009 (0.007)

(b) Standard deviation

	SNR ≥ 0	SNR ≥ 5	SNR ≥ 10	SNR ≥ 15	SNR ≥ 20
Z_H (dB)	5.22	5.05	4.83	4.59	4.17
Z_{DR} (dB)	0.96	0.85	0.77	0.73	0.69
ρ_{hv}	0.065	0.053	0.052	0.054	0.04

Table 4.3. Same as Table 4.2, except for difference between CPPAR and KTLX.

4.4.2 Standard deviation estimates of Horus and CPPAR data

Based on the Horus and CPPAR measurements (Figs. 4.5a, 4.5c, 4.5e, and 4.5g and Figs. 4.6a, 4.6c, 4.6e, and 4.6g), the standard deviation of the two measurements using spatial and temporal samples are depicted in Figs. 4.7 and 4.8 to further investigate the error characteristics. Note that the standard deviation of the differences between the PPARs and KTLX in the previous chapter are different from the standard deviation estimates of the PPARs' measurements in this chapter.

There are differences between the two PPARs; Horus has a beamwidth of 3.3°, but the elevation angles are sampled at 1° intervals. On the other hand, CPPAR used only 25 beams for the 90° sector with a beamwidth of 5.35°, which limits the influence of azimuthal oversampling. Therefore, the standard deviations were calculated along the ranges to avoid the influence of oversampling in the standard deviation estimates. In addition, the number of samples for Horus is ~3.6 times larger than CPPAR, and is even larger for higher SNR ranges.

Figure 4.7 illustrates the standard deviation estimates of six radar variables based on spatial and temporal samples for SNR larger than 10 dB. The SNR plots are shown in Figs. 4.7a and 4.7b as a reference. While the magnitudes between the spatial and temporal differ, the pattern of high standard deviation matches well (e.g., Figs. 4.7c and 4.7e). For Z_H, higher standard deviation values up to 2.5 dB are observed based on temporal samples, with ~1.5 to 2 dB throughout the majority of the RHI scan (Figs. 4.7c and 4.7e). The standard deviation values are relatively consistent with few larger values in the lowest elevations due to ground clutter effects, melting layer, and in low SNR regions for both spatial and temporal. Note that the very near ranges (i.e., < 5km) in the original blind range may have higher standard deviation values due to the influence of progressive pulse compression (Salazar Aquino et al., 2021). The v_r and σ_v also show similar features (Figs. 4.7g, 4.7i, 4.7k, and 4.7m). The most concerning features, however, are the strips of increased standard deviation of Z_{DR}, ρ_{hv}, and Φ_{DP} observed at low to mid elevations, which may be related to the performance degradation as the electronic beam is steered away from the broadside, in addition to the physics of melting that can affect multiple beams due to the relatively large beamwidth (Figs. 4.7d, 4.7f, 4.7h, 4.7j, 4.7l, and 4.7n). These strips of high standard deviation are consistent with the reduced ρ_{hv} from the Horus measurements (Fig. 4.5). The strips of increased standard deviation along the radials are also noticeable at higher elevation angles.

These features, which are only noticeable from the polarimetric variables, reinforce the possibility that these strips are contributed by the inherent limitation of 2D PPARs when electronically scanning off broadside. Overall, the standard deviation values in Fig. 4.7 exhibit reasonable distributions, consistent with the results in Table 4.4.

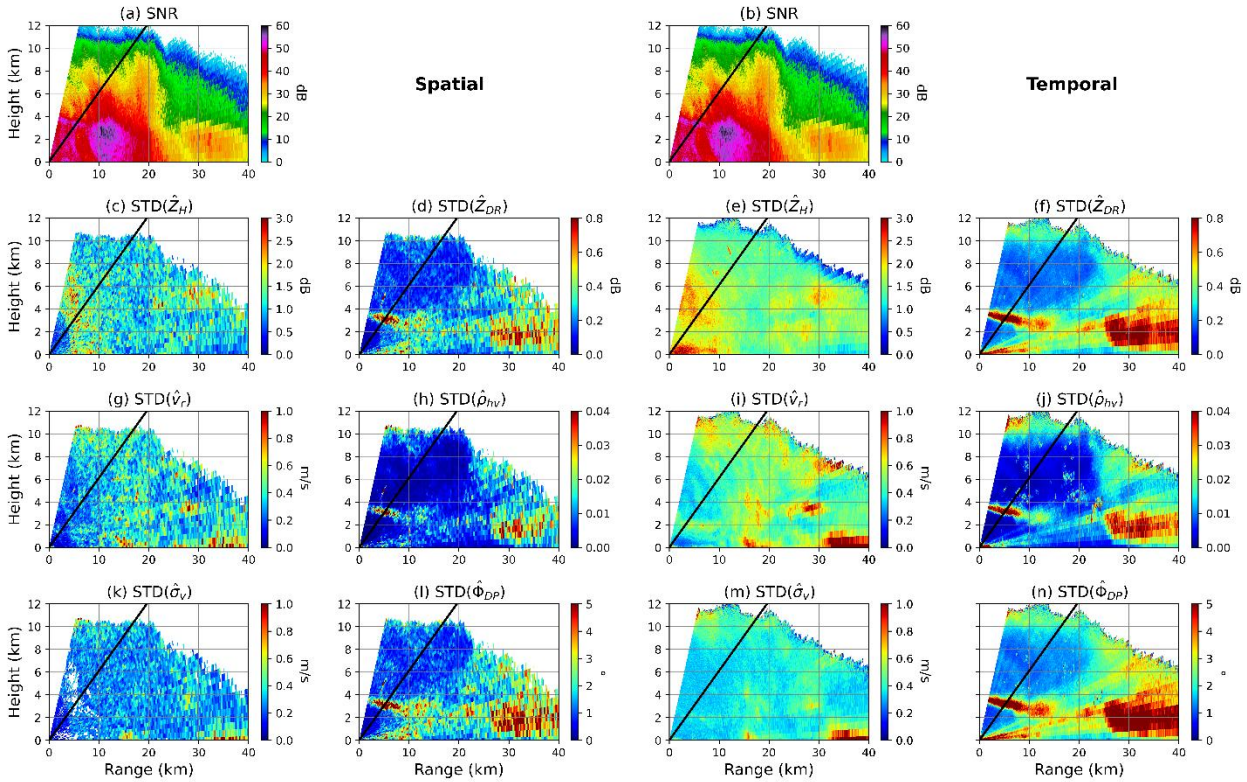

Figure 4.7. Spatial distribution of SNR, and standard deviations of Z_H, radial velocity (v_r), spectrum width (σ_v), Z_{DR}, correlation coefficient (ρ_{hv}), and differential phase shift (Φ_{DP}) for SNR greater than 10 dB from Horus weather observations based on 146 timesteps on 4 October 2023. The first column uses 17 spatial gates, and the second column only temporal samples. The black lines denote the broadside direction.

The calculated values for both the spatial and temporal samples are compared with theoretical values and the radar functional requirements set by the National Oceanic and Atmospheric Administration/National Weather Service (NOAA/NWS RFR). The theoretical values are derived using equations from Doviak and Zrnic (2006). The values of σ_v and ρ_{hv}, which influences the theoretical values of other variables, have been selected using the median value of the middle

timestep for spatial samples, and all timesteps for temporal. The median values of calculated standard deviations for each signal-to-noise ratio (SNR) range, theoretical values, and the NOAA/NWS RFR are organized in Table 4.4, based on spatial (Table 4.4a) and temporal (Table 4.4b) sampling using Horus data. As expected, the standard deviation of the polarimetric variables generally exhibits a decreasing trend with increasing SNR. However, for larger SNR ranges, slight variations are expected due to the smaller number of data points available. For SNR values exceeding 20 dB, the standard deviations are even smaller than the theoretical calculations, especially for v_r and Z_{DR}. In addition, there are considerable differences (~ 1.4 times larger for temporal) in the standard deviations between the spatial and temporal samples for all SNR regions. For instance, the standard deviations of Z_H, Z_{DR}, and Φ_{DP} of the temporal samples within the SNR range of 5 to less than 20 dB are about 1.4 times larger for the spatial samples. This could be attributed to the influence of various filters applied to the Horus data (Palmer et al. 2023), including a clutter filter (Siggia and Passarelli, 2004) and a radio frequency interference filter (Cho, 2017). It emphasizes the need to account for these filters in subsequent analyses. Nevertheless, the standard deviation for SNR values greater than 20 dB agrees well with the theoretical calculations and are less than the NOAA/NWS RFR limits for the examined case.

(a) Spatial

	0≤SNR	5≤SNR<10	10≤SNR<15	15≤SNR<20	20≤SNR	Theory	NOAA/NWS RFR
Z_H (dB)	1.10	0.85	0.91	0.86	1.09	1.39	1.8
v_r (m/s)	0.31	0.47	0.40	0.40	0.29	0.43	1.0
σ_v (m/s)	0.26	0.41	0.30	0.29	0.24	0.32	1.0
Z_{DR} (dB)	0.20	0.47	0.31	0.19	0.18	0.32	0.3
ρ_{hv}	0.005	0.032	0.015	0.010	0.003	0.005	0.006
Φ_{DP} (°)	1.40	3.24	2.17	1.42	1.20	2.07	2.0

(b) Temporal

	0≤SNR	5≤SNR<10	10≤SNR<15	15≤SNR<20	20≤SNR	Theory	NOAA/NWS RFR
Z_H (dB)	1.65	1.02	1.04	1.01	1.69	1.49	1.8
v_r (m/s)	0.47	0.67	0.53	0.51	0.44	0.45	1.0

σ_v (m/s)	0.36	0.54	0.39	0.36	0.35	0.32	1.0
Z_{DR} (dB)	0.33	0.60	0.38	0.27	0.25	0.33	0.3
ρ_{hv}	0.010	0.038	0.018	0.011	0.005	0.005	0.006
Φ_{DP} (°)	2.29	4.13	2.69	1.96	1.72	2.23	2.0

Table 4.4. The median value for the standard deviation of six radar variables based on both (a) the spatial and (b) the temporal domain of the Horus data for five different signal-to-noise ratio (SNR) ranges. The theoretical values are selected based on middle timestep for spatial, and all 146 timesteps for temporal. The NOAA/NWS RFR represents the radar functional requirements of the NOAA and National Weather Service.

The standard deviation estimates for the CPPAR measurements are shown in Fig. 4.8. As expected from the weaker power and lower sensitivity, wider beamwidth, less angular oversampling, and no spatial filtering, CPPAR exhibits larger standard deviation estimates, especially in the low SNR regions (Fig. 4.8a). Z_H shows consistent values of ~1.2 dB (Fig. 4.8b) except in the low SNR regions. For v_r and σ_v, the values are ~0.6 m/s and 0.3 m/s, respectively (Figure 4.8d and f). For Z_{DR}, ρ_{hv}, and Φ_{DP}, the values fall below 0.3 dB (Fig. 4.8c), 0.005 (Fig. 4.8e), and 2° (Fig. 4.8g) except for a few strips in the low SNR region, which may also be affected by the nearby water tower. Most of the CPPAR data points have consistent values throughout the PPI scans for all six radar variables, which is a promising feature. There are also no clear variations with scanning angle, and/or interference-like structures that could indicate interferences/creeping wave effects.

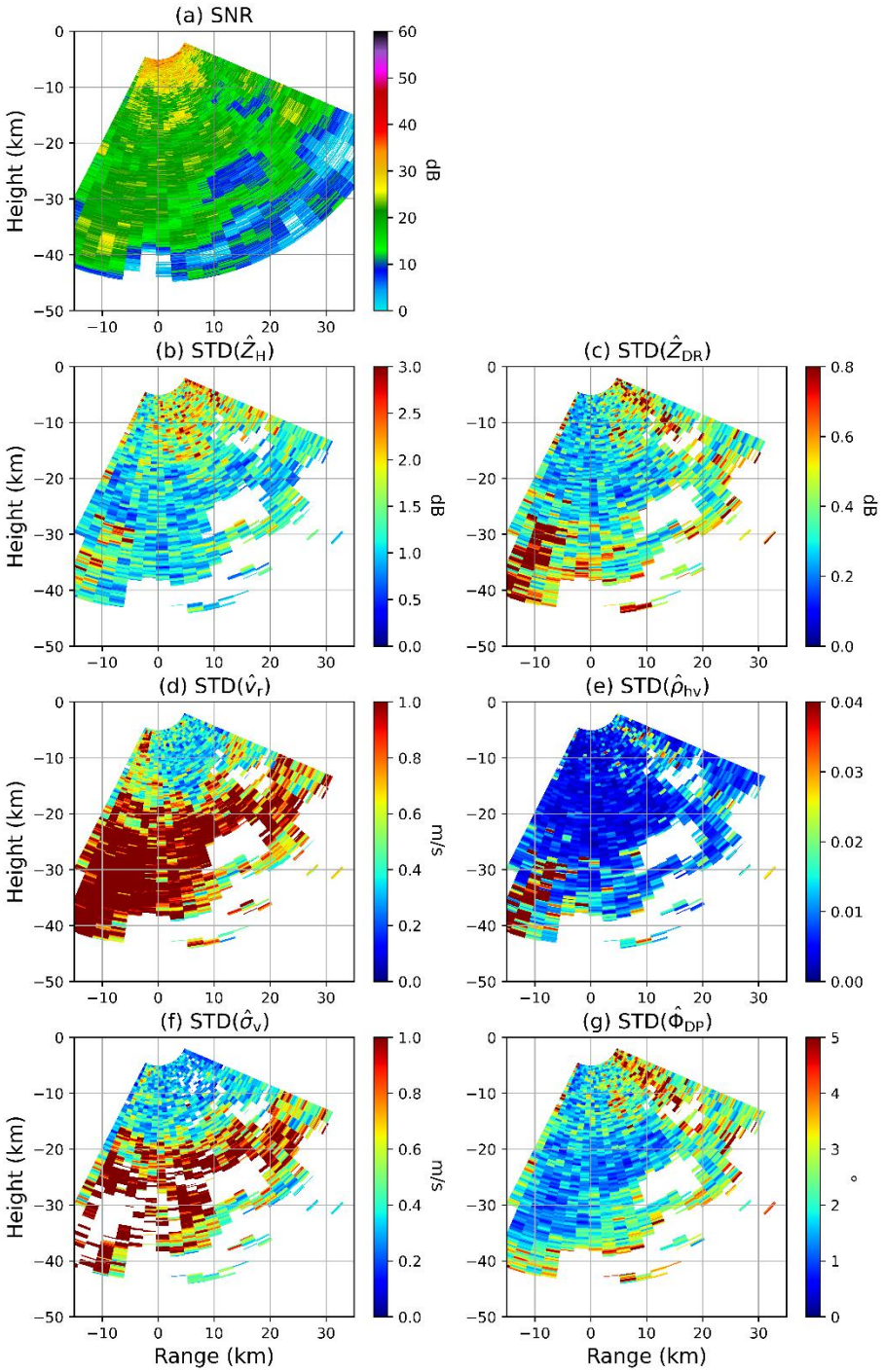

Figure 4.8. Same as Fig. 4.7, except for CPPAR using spatial samples on 30 August 2019.

Initially presented in Table 3 of Li et al., (2021), the standard deviation estimates have been extended to cover additional SNR ranges (Table 4.5). The results in Table 4.5 are very similar to

those in Table 4.5a, showing a decreasing trend in the standard deviation with increasing SNR. Furthermore, the standard deviation values for CPPAR are comparable to those of Horus within the same SNR ranges. In general, Horus displays slightly smaller standard deviations compared to CPPAR. This difference can be attributed to the use of oversampling with elevation for Horus. It should also be noted that CPPAR conducted electronic scans between full −45° and 45°, whereas Horus only −31.5° and 31.5°. For SNR values greater than 20 dB, the standard deviations observed in CPPAR are either less than or comparable to the theoretical values and are in compliance with the NOAA/NWS RFR for the examined case. Overall, the standard deviation values in Figs. 4.7 and 4.8 exhibit reasonable distributions, consistent with the results in Table 4.4 and Table 4.5. This indicates that the results are consistent across different analyses, providing a comprehensive assessment of the data quality for both radar systems.

	0≤SNR	5≤SNR<10	10≤SNR<15	15≤SNR<20	20≤SNR	Theory	NOAA/NWS RFR
Z_H (dB)	1.31	1.02	0.93	0.93	1.34	1.31	1.8
v_r (m/s)	0.73	0.87	0.94	0.96	0.52	0.5	1.0
σ_v (m/s)	0.54	0.79	0.74	0.76	0.36	0.34	1.0
Z_{DR} (dB)	0.40	0.72	0.48	0.35	0.30	0.26	0.3
ρ_{hv}	0.009	0.034	0.014	0.007	0.004	0.004	0.006
Φ_{DP} (°)	2.30	4.72	2.87	1.84	1.69	1.7	2.0

Table 4.5. Same as Table 4.4a, except the STDs are based on electronic scan of CPPAR.

4.5 Analysis on the off-broadside dilemma of planar configuration

The primary concern with the planar antenna design of 2D electronic PPARs lies in the weather data quality off broadside due to the scan-dependent beam properties of the PPPAR, unless an accurate beam-to-beam calibration is performed, which is difficult to do. While the planar configuration is relatively easy to implement and has been chosen by many fields for their applications (Brookner, 2008), including Horus, the PPPAR has inherent off-broadside problems

that cause sensitivity loss in Z_H and Z_{DR} bias. It requires a larger antenna size, higher transmit power, complicated beamforming, and polarimetric calibration when the beam is off the principal plane or far away from the broadside. Previous literatures (e.g., Zhang et al., 2011, Golbon-Haghighi et al., 2021; Zhang et al., 2022) have warned of such fundamental challenges of electronically scanning PPPARs based on theoretical analysis and simulations. These limitations have been observed by the NSSL Advanced Technology Demonstrator (ATD) where data quality degradation occurs at wide scanning angles (Ivić et al., 2019). This study reveals a glimpse of such limitations based on the 13-panel observations from Horus. Horus only performs RHI scans in the vertical principal plane in its current development state, but the effect of off-broadside scanning can be inferred by comparing the quality of the polarimetric variables. As discussed in relation to Fig. 4.7, the large area of reduced ρ_{hv} could be caused by a combination of physical causes from the low intrinsic values in the melting layer, low SNR, or wide-angle steering off the broadside. The standard deviation of Z_{DR}, ρ_{hv}, and Φ_{DP} increased at the location of the reduced ρ_{hv} as strips, strengthening the possibility of an issue in electronic scanning off broadside.

To further investigate the potential cause of the large ρ_{hv} reduction and strips of higher standard deviations, the bias calculated from the KTLX comparison, and the standard deviations estimated from the spatial samples were averaged for each elevation angle. In order to isolate the problem, regions with SNR less than 20 dB, and KTLX ρ_{hv} less than 0.95 were excluded from the analysis to minimize the effect of other causes such as ground clutter, melting level, and low SNR. The removal of SNR and ρ_{hv} threshold would increase the errors in polarimetric measurements, leading to further degradation in electronically scanning PPPARs. In this study, as the first analysis of its kind, we focus on the high SNR case for simplicity and demonstration purposes. Also, only rays with more than 300 valid values were considered for statistical significance. Note that CPPAR is

not plotted as CPPAR does not have an angular dependence issue, and the data is insufficient for statistical significance after applying those filters. Figure 4.9 depicts the averaged bias for each ray with respect to the broadside angle. For Z_H, there is a high bias in the lowest few elevations, probably from the remaining effect of ground clutter. Also, the reconstructed KTLX measurements in the lowest elevations are partially interpolated from the upper elevations increasing the potential for beam mismatch. Overall, the bias remains relatively stable around 3.5 dB. However, the polarimetric variables, Z_{DR} and ρ_{hv}, reveal different error characteristics with respect to the broadside angle. While there are slight fluctuations, Z_{DR} shows a negative trend, with much higher biases in the lower elevations (i.e., 0° to −31.5°), and lower biases in the higher elevations (i.e., 0° to 31.5°) compared to the broadside. While the Z_{DR} calibration factor can reduce biases on the broadside, the varying error characteristics (i.e., positive bias in the lower elevations and negative bias in the higher elevations) remain as the beams are steered away from the broadside. In fact, such biases start to be noticeable after ~20°, which is consistent with previous studies (e.g., Figs. 6 and 7 of Ivić, 2023; Figs. 2−5 of Zhang et al. 2009; Fig. 2 of Zrnic et al., 2011). Similar trends can be observed for ρ_{hv}, where large negative biases are evident from ~20°. The reduction in higher elevations is minor, but the decreasing trend can be seen with a reduction of ~ 0.002 compared to the broadside.

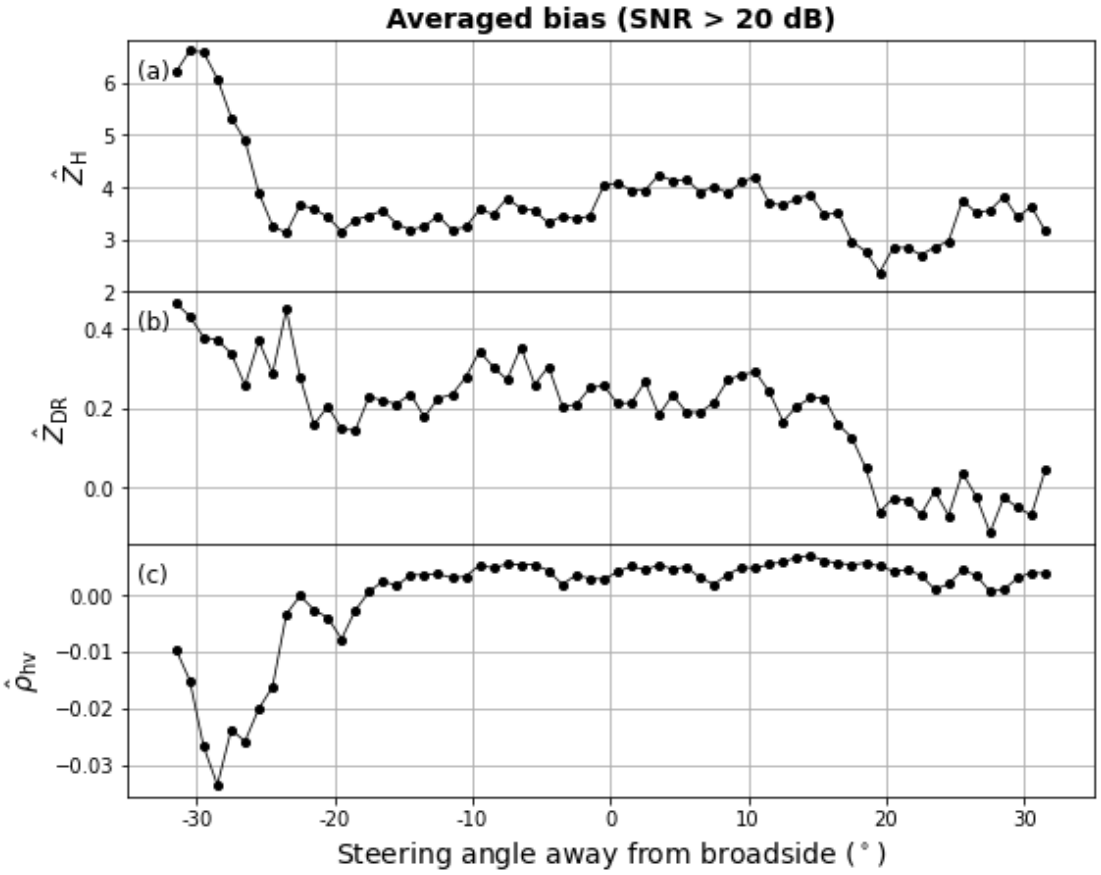

Figure 4.9. Plot of the averaged bias of Z_H, Z_{DR}, and ρ_{hv} for each steering angle away from the broadside. Only SNR greater than 20 dB, and KTLX ρ_{hv} greater than 0.95 were considered. Note that the angles range from −31.5° to 31.5°.

The averaged standard deviation plots also reveal similar features (Fig. 4.10). All polarimetric variables depict a nearly parabolic shape with a minimum near the broadside (Figs. 4.10b, 4.10d, and 4.10f). The single polarization variables (Figs. 4.10a, 4.10c, and 4.10e) show random fluctuations for Z_H, and decreasing trend with elevation for v_r and σ_v as can be expected for severe storms. As the propagation path is ~4 times different for lower and upper elevations, the magnitudes of the standard deviations between upper and lower elevations are not expected to be similar. For Z_{DR}, much larger standard deviation estimates up to 0.5 dB are noticeable even after removing low SNR and ρ_{hv} regions, with a decreasing trend closer to the broadside (Fig. 4.10b).

For the higher elevations, an increasing trend is noticeable away from the broadside. ρ_{hv} shows a clearer parabolic shape, with values up to 0.023 at lower elevations and ~0.027 at higher elevation compared to less than 0.005 near the broadside (Fig. 4.10d). Standard deviation of Φ_{DP} also show increasing trend away from the broadside, even after neglecting the high peak at the lowest elevation (Fig. 4.10f). As shown for the polarimetric biases in Figs. 4.9 and 4.10, there is an increase in the error characteristics after electronically scanning away from the broadside. Thus, such a large ρ_{hv} reduction in Horus measurements may be caused by issues associated with copolar beam mismatch and polarization purity loss at wide-angle steering off broadside, or interference from sidelobes. It can be expected that such performance degradation will be even worse when the beam steers in a wide angle range from -45° to 45°.

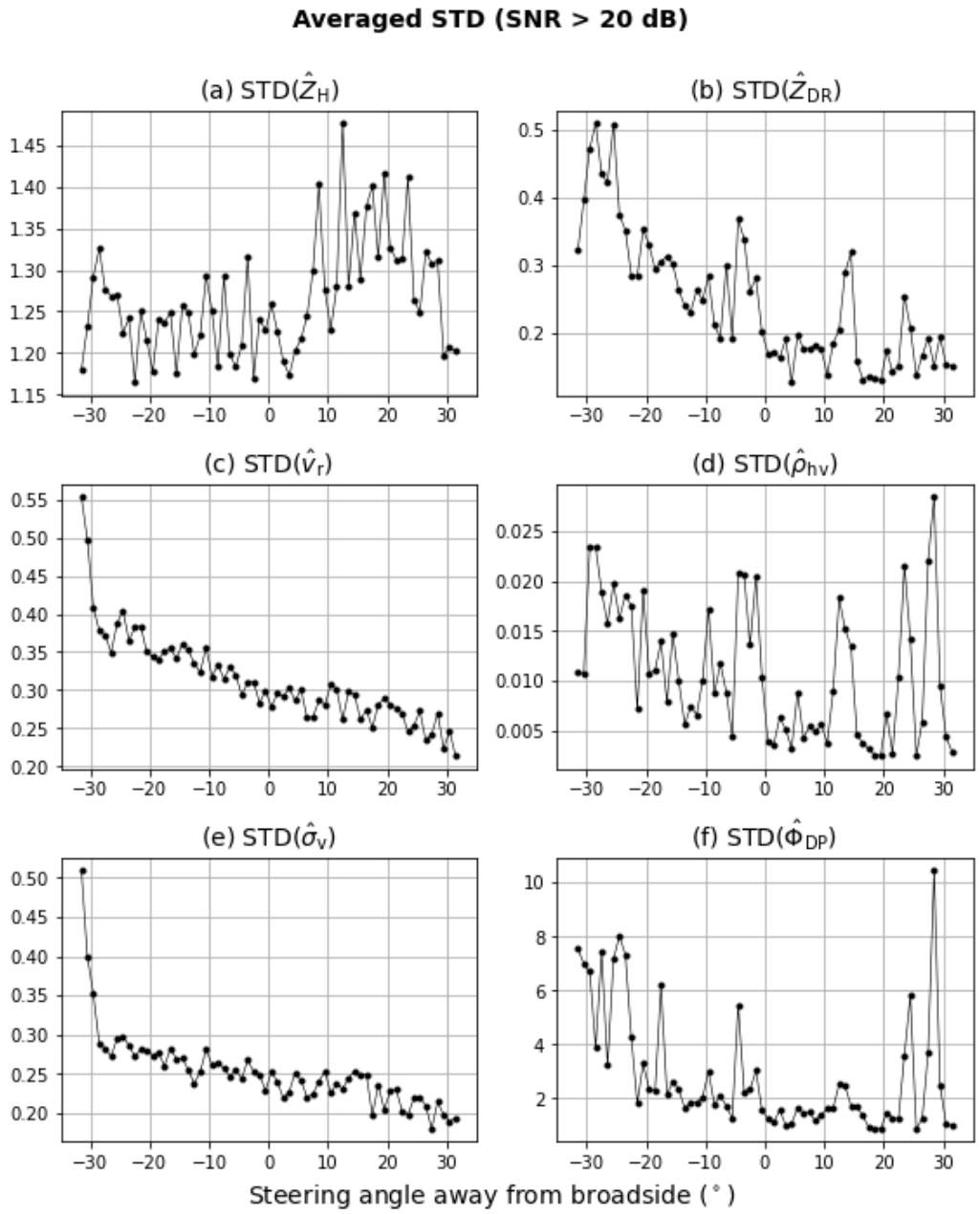

Figure 4.10. Same as Fig. 4.9 except for averaged STD of Z_H, Z_{DR}, v_r, ρ_{hv}, σ_v, and Φ_{DP}.

These results are consistent with previous studies, which have found that polarimetric calibration for each element and direction of PPPAR is more tedious and difficult compared to the cylindrical configuration. This is because the active element patterns in PPPAR are different and difficult to characterize and form high-performance beams in all directions, while the active

element/column patterns in CPPAR are all the same, yielding all formed beams the same with low sidelobes (e.g., Dorsey et al., 2022; Golbon-Haghighi et al., 2021; Logan et al., 2022; Zhang et al., 2011). Such limitations may reduce the usefulness of 2D PPPAR for accurate weather measurements, particularly as the antenna size increases and more elements are employed.

On the other hand, CPPAR provides all beam measurements in principal planes and with small angles from broadside, making it more immune to the degradation problems of electronic steering at wide angles. Nevertheless, the development of CPPAR in full-scale of the WSR-88D has been stopped, even though the main issues are solved with satisfactory results. For a better understanding of such limitations of PPPAR and other possible deficiencies of CPPAR, observations of the same case with various scanning strategies of the 2D electronic PPARs should be conducted in the future.

4.6 Assessing advantages and disadvantages of planar and cylindrical configurations

The two of the most promising configurations, planar and cylindrical, of 2D PPARs have received considerable attention over the past decade to explore future applications. The timeline and goals depicted in Fig. 4.11 are based on Fig. 1 of NSSL MPAR report (2014), with a few modifications reflected to align with the actual timeline. Initially, the NSSL, (2014) report planned to analyze both configurations (i.e., 4 faced PPPAR and CPPAR) without any moving parts to select the most optimal design for accurate meteorological measurements and potential multifunctionality. Both configurations have been developed as in the 10-panel demonstrator (TPD) and CPPAR-I, and further efforts have been planned and invested for ATD and CPPAR-II. Many of the problems and lessons learned from CPPAR-I have been addressed and resolved over

the years. Several improvements include: (i) redesigning the column antenna with matched dual-polarization patterns (Saeidi-Manesh et al. 2017b), (ii) switching from digital to analog beamforming to improve system stability, and (iii) optimized beamforming to achieve the nearly identical high-performance beams using multi-objective optimization techniques (e.g., Karimkashi and Zhang 2015; Golbon-Haghighi et al. 2018; Li et al. 2021; Zhang 2022). However, the plan changed over the years, and these 2D PPARs currently focus on weather measurements in providing efficient and high-quality PRD in all directions, especially at angles far off broadside (NSSL, 2017, 2023). Another notable deviation from the original plan concerns the two 2D PPPARs, Horus and ATD, while CPPAR development has stopped since 2020. As a rough estimation, much more investment was allocated to each of the planar designs over CPPAR, as evidenced by the much narrower beamwidth and transmit power of Horus compared to CPPAR, and the number of T/R modules. However, as shown in this study, the quality of weather measurements from these PPPARs at wide angles are questionable.

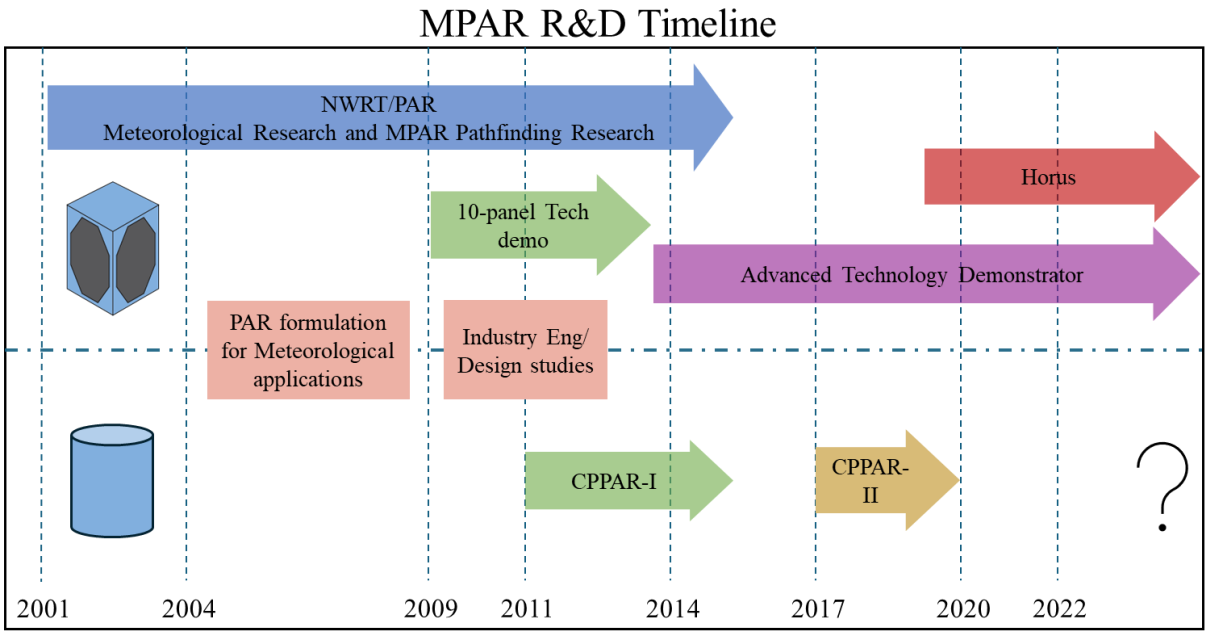

Figure 4.11. Reconstructed MPAR research and development timeline based on Fig. 1 of NSSL (2014).

The discussions on the optimal configuration (e.g., planar vs. cylindrical), and/or limitations of 2D PPPAR have been well documented and presented over the years (Doviak et al., 2011; Ivić, 2023; Karimkashi and Zhang, 2015; Lei et al., 2013, 2015; NSSL, 2014, 2020a, 2020b, 2021; Zhang et al., 2009, 2011; Zrnic et al., 2011). The advantages and disadvantages of each configuration, based on those previous studies and the quantitative error analysis of weather measurements conducted in this study, are organized in Table 4.6. As analyzed in several previous studies and confirmed in Chapter 4.4, 2D PPPARs have inherent problems with i) beam broadening, ii) sensitivity loss, iii) loss of polarization purity, and iv) higher risk of beam mismatch when steering off-broadside. These problems arise because the patterns of the elements embedded in the PPPAR vary from one to another and their patterns are not the same, making it difficult to achieve high performance PPPAR beams (e.g., polarization purity, matched dual-polar beams, low side lobes, etc.). Although all elements are designed identically in both configurations, resulting in the same isolated element patterns, the array antenna configuration causes active/embedded element patterns to be different due to the presence of surrounding elements. These active element patterns vary depending on the location of the element within the array (i.e., its electromagnetic environment). For example, the central element may have a symmetric pattern if appropriately designed, while elements at the sides or corners may have asymmetric patterns due to edge or corner effects. This variation occurs in PPPAR but not in CPPAR which maintains symmetry—ensuring that all columns have the same electromagnetic environment and therefore the same embedded column patterns. These issues can be further assessed by beam-to-beam pattern characterization and weather measurements with multi-beams. Some of these problems can be corrected by calibration, such as phase coding or appropriate antenna tilt (Ivić, 2022, 2023), but the others can only be avoided/resolved through configuration considerations, antenna design, and

optimal beamforming. For example, the performance degradation away from the broadside can only be mitigated by (i) avoiding steering at large angles away from the broadside, (ii) accurately characterizing embedded element patterns and optimally forming beams at each steering direction, (iii) performing beam-to-beam calibration for PPPAR, and (iv) using a 1D electronic scan PPPAR, where the main beam always remains in the principal plane, minimizing cross-coupling. While this study's analysis emphasized the off-broadside problem, as Horus only conducted RHI scans and CPPAR PPI, scanning off the principal plane can present an even greater challenge. Planar design is often chosen for many other applications because most do not require wide-angle scans or only require qualitative data, such as aircraft detection. However, this is not the case for meteorological applications, which require high-quality quantitative polarimetric measurements. Specifically, ρ_{hv} requires an error of less than ~0.006.

CPPAR	PPPAR (Horus, ATD)
+ Azimuthally scan invariant beam	− Scan variant beam and scan dependent biases
+ Always scanning in principle plane	− Loss of sensitivity when scanning off principal plane
+ Small angles from broadside	− Loss of polarimetric purity when scanning off-broadside or principal plane
+ Polarimetric purity and easy polarimetric calibration	− Difficulties in polarimetric calibration
○ New design and concept for the community and the industry	+ Mature design for the community and industry
	+ Flexible beam steering from isolated face

Table 4.6. The table lists the advantages (+), disadvantages (-), and neutral (○) of each 2D PPAR configuration.

CPPAR was chosen for 2D PPAR to mitigate issues such as beam broadening, sensitivity loss, and polarization purity loss. CPPAR always scans in the principal plane in azimuth with small angles in elevation, using the same physical principles as 1D PPPAR and producing polarimetric data of comparable quality (as demonstrated in Li et al., 2021). In addition, high-performance radiating elements have been designed, ideal arrangements were proposed, and beams were

optimally formed for CPPAR so that the mentioned creeping wave effect is not an issue (Golbon-Haghighi et al., 2021; Mirmozafari et al., 2017, 2019; Saeidi-Manesh et al., 2017a). There is still confusion and misunderstanding about interferences caused by surface/creeping waves in CPPAR within the meteorological community (e.g., NSSL 2014, 2023). However, surface waves can exist in any configuration and should be considered and minimized. Additionally, it is easier to control the surface wave effects in CPPAR due to its symmetry than in PPPAR (e.g., Mirmozafari et al. 2017 & 2019; Saeidi-Manesh et al. 2017a; Golbon et al. 2021). CPPAR has produced high-quality polarimetric weather data, which has been quantitatively evaluated (Li et al., 2021 and this study). Although there were concerns regarding limitations of CPPAR, such as interference or creeping waves, the analysis and demonstration of CPPAR measurements do not show these issues due to their minimal effect. This is because CPPAR beams were optimally formed from the active (embedded) element/column patterns using the multi-objective optimization so that the dual-pol beams are well-matched and sidelobes are low. Although the creeping/surface effects appear in the active element patterns as ripples, the CPPAR beams formed from the active patterns have already taken these effects into account and therefore are almost the same for all the beams with high performance (see Figs. 4 and 5 of Zhang, 2022). The beam characteristics can be further improved using dipole antennas and/or larger sizes (Mirmozafari et al., 2019; Golbon-Haghighi et al., 2021).

Aperture efficiency is another aspect that has been computed and clarified. The same number of elements is required for both cylindrical and planar configurations to achieve the same pencil beam at 45° from the broadside (Zhang et al. 2011). In fact, power efficiency is generally better for cylindrical configurations because it forms beams in the principal plane and close to the broadside, avoiding significant scanning loss at wide angles that PPPAR has to steer. The CPPAR

does have limitations in commutating scans for maintaining the polarization purity and can have limited freedom compared to that of the planar, but this is the approach worth taking in the case of weather applications. Also, CPPAR is relatively new to the community and industry. However, its feasibility is evidenced by CPPAR data and this study, making it a promising research project aimed at advancing future weather measurements.

	Dish	1D PPPAR	2D PPPAR	CPPAR (2D)
Cost	Low	Medium	High	High
Data quality	High	High	Low	High
Update speed	Low	Medium/High	High	High
Calibration	Easy	Easy/Moderate	Difficult	Moderate
Potential	High (short-term)	High (mid-term)	Low	High (long-term)

Table 4.7. The advantageous and disadvantageous properties of dish radar, 1D PPPAR, 2D PPPAR, and CPPAR for cost, data quality, update speed, calibration/maintenance methods, and potential criteria.

The cost-performance trade-offs among the current operational dish radars, 1D, and 2D PPARs are summarized in Table 4.7, taking into account previous studies and the results of this research. The potential of each system is assessed based on a combination of criteria including cost, data quality, update speed, and calibration. Dish-based operational radars provide relatively low-cost and high-quality weather measurements; however, they have a much slower update speed, which limits their potential, as the meteorological community is seeking faster update radars for the future. 1D PPPAR and CPPAR share the same physical principles (i.e., electronic scanning in the principal plane with small steering angles), with differences in cost and update speed/flexibility. It is generally agreed that 1D PPPAR is feasible and cost-effective for weather observation, and 1D X-band PPPARs have already been deployed for operational use in the USA, Japan, and China. Considering that a 4-faced 2D PPPAR is more expensive than CPPAR and 1D PPPAR, and given the known shortcomings and beamforming&calibration difficulties in providing high-quality data

in all directions, a rigorous quantification of its performance is necessary before pursuing 2D PPPAR for weather measurement.

4.7 Summary

This chapter focuses on the estimation of measurement errors, which provide uncertainty information for observations and support the overall goal of improving microphysical retrievals. Specifically, this study focused on evaluating PPAR performance under different system configurations. This work presents the first quantitative error analysis and comparison of 2D PPPAR and CPPAR data. Results show that both PPPAR and CPPAR provide accurate polarimetric weather measurements when their beams are close to the broadside. However, the PPPAR performance degrades as the beam steers away from the broadside. It is worth noting that there are several limitations in this work, including differences in range resolution between dish-based radars and PPARs, as well as challenges with the absolute calibration of polarimetric variables for the KTLX radar. In addition, the results presented here may not fully capture all the challenges of 2D electronically scanning (E-Scan) PPPARs due to limited data. Despite these limitations, and the unavailability of co-located observations with identical scanning strategies, this study provides valuable insights by comparing weather measurements from two promising PPAR configurations: planar and cylindrical. The standard deviations and mean biases of the Horus and CPPAR measurements were calculated and compared with those of an operational WSR-88D radar. The standard deviations for both PPARs agree well with theoretical expectations and are within the NOAA/NWS RFR for the cases studied. The standard deviation from spatial samples shows smaller values compared to that from temporal samples, which may be attributed to post processing filters used in Horus. Bias calculations relative to KTLX show 3.99 dB for Z_H,

0.23 dB for Z_{DR}, and −0.002 for ρ_{hv} for Horus, and −1.29 dB for Z_H, 0.04 dB for Z_{DR}, and 0.009 for ρ_{hv} for CPPAR.

The study highlights the inherent limitations and challenges of polarimetric calibration for 2D PPPARs, particularly due to the scanning loss, the loss of polarization purity, the mismatch of dual-polarimetric beams, and the difficulty of controlling sidelobes when steering away from the broadside. It should be noted that 2D PPPARs will need to steer away from the principal planes and perform even wider-angle scans. While this study has only demonstrated the effect of limited off-broadside scans, it has already revealed potential deficiencies. Accurate weather measurements with PPPARs require a thorough understanding of scanning loss issues and system performance at each beam-steering direction to apply appropriate calibrations. Dual-scan comparisons and multi-pattern measurements have proven effective in analyzing these factors. To circumvent the inherent limitations of the 2D PPPAR, the cylindrical configuration is a viable alternative; it possesses the greatest potential to enhance current operational radars by providing high-quality polarimetric data and rapid data updates. These advances are likely to improve weather forecasting and the understanding of rapidly changing weather phenomena, particularly severe storms.

Chapter 5 Microphysics retrieval using physics-informed neural networks

This chapter focuses on integrating and evaluating the combined impact of the developments presented in the previous chapters. The parameterized polarimetric forward operators derived in Chapter 3 are incorporated as physical constraints within advanced retrieval methods. The estimated observational error characteristics and the improved spatiotemporal resolution of PPARs, discussed in Chapter 4, are used to inform the weighting of different components of the retrieval, particularly when assessing the reliability of individual polarimetric variables under varying conditions. These elements are further integrated into advanced retrieval approaches, including ML-based methods that incorporate physical constraints to address the inherently underdetermined nature of microphysical retrievals.

This chapter presents a generalized framework for leveraging physically based forward operators, prior error information, and enhanced observational capabilities to improve and extend microphysical retrievals. Chapter 5.1 provides an overview of previously developed microphysics retrieval and hail sizing algorithms. Chapter 5.2 introduces the design of the physics-informed neural network (PINN). Chapter 5.3 discusses retrieval results based on WRF simulation data. Chapter 5.4 presents NEXRAD-based retrievals of rain and hail, while Chapter 5.5 further explores adaptive weighting of the different components within the PINN.

5.1 Overview of microphysics retrievals

This study aims to extend microphysical retrievals by identifying multiple hydrometeor species within each radar range gate, with a particular focus on storms containing mixtures of rain and hail. It is noted that PRD alone provides limited independent information for inferring the size distributions of multiple hydrometeor species. For radar gates containing both rain and hail, the

radar signals are largely dominated by hail. However, in terms of microphysical parameters mixing ratio (q_x) and number concentration ($N_{t,x}$), rain may remain the predominant species. As a result, the majority of previous studies have focused on less rigorous approaches, such as hail detection, estimation of maximum hail size (i.e., MESH), vertically integrated liquid (VIL) in the presence of hail (Witt et al., 1998; Depue et al., 2007; Blair et al., 2011; Ortega et al., 2016; Brook et al., 2021; Murillo and Homeyer, 2021; Goda et al., 2025). In such cases, only K_{DP} has typically been used for rainfall estimation in the presence of hail (Aydin et al., 1995; Matrosov et al., 2013). The retrieval of hail microphysics, particularly the estimation of the hail PSD, remains a notably demanding task. Previous studies have examined polarimetric signatures to estimate hail characteristics (Ryzhkov et al., 2013a, b; Ortega et al., 2016) and shape (Shedd et al., 2021). More recently, ground-based in situ sensors, such as automatic hail sensors, have been used to model hail distributions (Kopp et al., 2023; Ferrone et al., 2024).

As a simplification, instead of retrieving the PSD directly, bulk microphysical parameters ($D_{m,x}$, W_x, and γ) are derived from PRD. These parameters are then used to determine the size distributions of hydrometeors, assuming a particular functional form (e.g., exponential or Gamma distributions). These quantities are physically related to model microphysical parameters (e.g., $q_x$and $N_{t,x}$), and the corresponding bulk parameters (i.e., $D_{m,x}$ and W_x) tend to be more Gaussian distributed. Early approaches primarily relied on empirical relationships—most commonly between Z_H and q_x—due to their simplicity and computational efficiency (Liu et al., 2020; Chen et al., 2021; Chen et al., 2024). However, such approaches are susceptible to measurement, model, and operator errors, leading to significant uncertainties (Ho et al., 2023). To address these limitations, more advanced methods—such as variational approaches and ML techniques—are

needed to improve generalizability, account for nonlinearity, and incorporate additional physical and error information, to better integrate the polarimetric radar observations with model physics.

Variational retrieval methods integrate both background information (i.e., initial state estimates) and observations, allowing for properly adjustment of weights by modifying background and observational errors. These methods are widely used in the DA community (Rodgers, 2000; Kalnay, 2003) and have been applied to rain microphysics retrievals (Mahale et al., 2019). They provide a transparent framework for enforcing valid physical laws and assumptions during optimization. However, this transparency also makes them highly dependent on model assumptions and operator accuracy, which can reduce computational efficiency and flexibility. In addition, the iterative nature of variational methods can be computationally expensive and time-consuming, especially when analyzing high-resolution and rapid-update observation data, such as those by phased-array radars (Honda et al., 2022).

ML techniques offer an alternative solution by identifying complex patterns directly from data, potentially reducing reliance on explicit physical assumptions and improving computational efficiency (Ho et al., 2023). However, conventional ML methods often lack a strong physical foundation, making them less interpretable and highly dependent on extensive training data (Li et al., 2024; Flora et al., 2025). This dependence can lead to poor generalization, particularly in extreme or underrepresented cases. To address these limitations, recent studies have explored integrating ML with physical constraints, such as the boundary conditions of partial differential equations, leading to physics-informed neural networks (PINNs; Raissi et al., 2019). Although still an emerging field, PINNs have been applied in some studies to simulate or approximate weather-related processes (Kashinath et al., 2021; Brecht et al., 2025), demonstrating their potential to improve forecast accuracy and reliability.

The aim of this study is to develop a physically constrained ML approach for rain and hail mixture retrievals. To the best of the author's knowledge, no previous study has attempted to retrieve size distributions for mixed hydrometeor species. This study explores various forms of physical constraints within the ML framework to assess the physical consistency and accuracy of the approach—particularly in the absence of ground-truth data for the target microphysical parameters (i.e., $D_{m,r}$, $D_{m,h}$, W_r, W_h and γ).

5.2 Design of the physics-informed neural network

The base design of the PINN is illustrated in Fig. 5.1. The architecture is constructed based on a controlled simulation environment, where model-simulated physical parameters of q_x and $N_{t,x}$ are first used to derive microphysical parameters $D_{m,x}$ and W_x for each hydrometeor species. A melting model following Liu et al. (2024a) is then applied to partition hydrometeors into dry and wet categories. Using these microphysical parameters, forward operators are applied to compute the corresponding polarimetric radar variables, which serve as input features for the NN. The ML model is trained to learn the inverse mapping from polarimetric observations to microphysical state parameters. Since this design is developed within a controlled simulation environment, no observational, forward-operator, or model errors are introduced.

In classical PINNs, the network is trained to solve forward problems by enforcing governing equations—often in the form of differential equations—as constraints, without requiring explicit labeled solutions. In contrast, the current method addresses an inverse problem, where the goal is to retrieve microphysical parameters from observations. Here, the forward operator is incorporated as a physical constraint by enforcing consistency between the observed polarimetric variables and those recomputed from the retrieved microphysical states. In this sense, the role of the forward

model is reversed; rather than being the target of the solution, it acts as a constraint that regularizes the inverse retrieval.

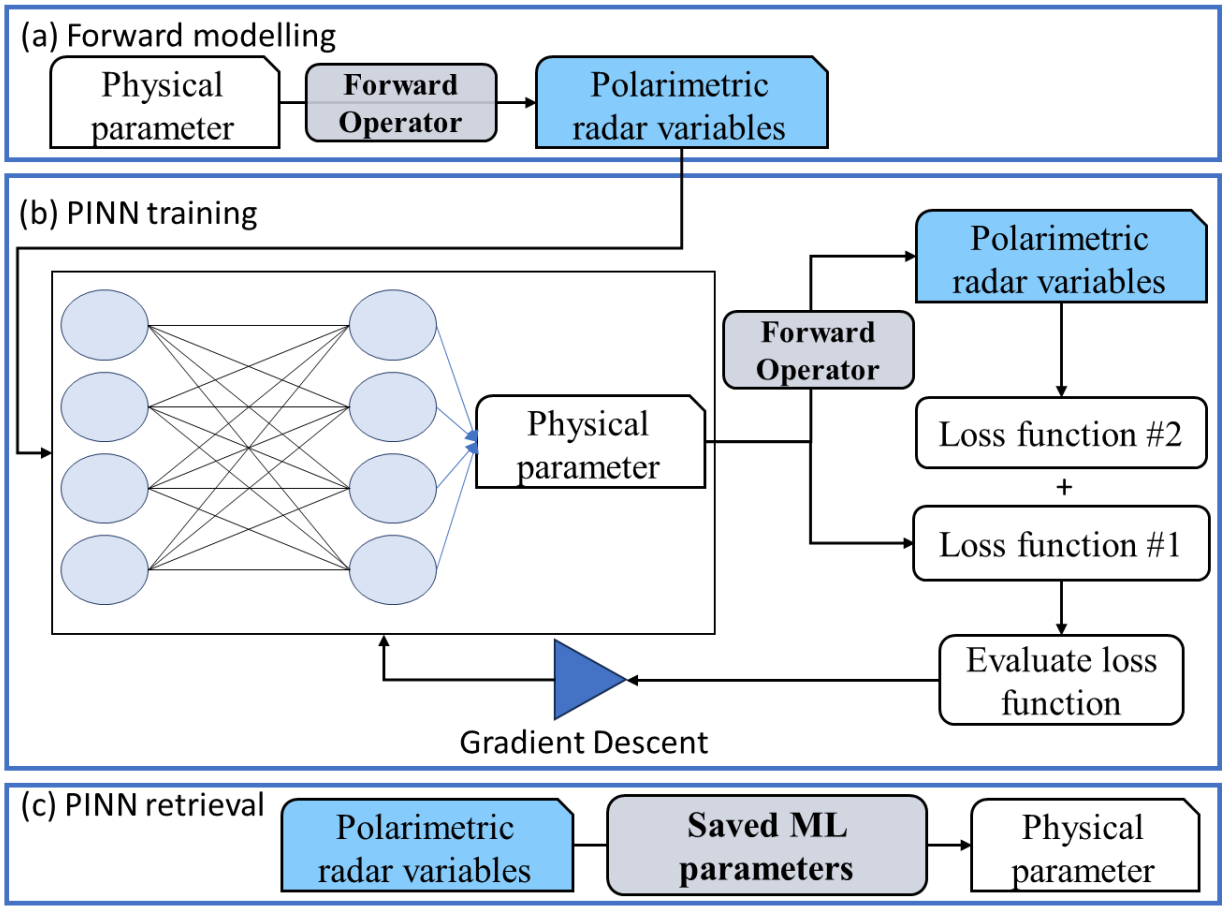

Figure 5.1. A schematic diagram of the physics-informed neural network (PINN) architecture. The architecture comprises three main components: (a) forward modelling; (b) the PINN training process; and (c) the retrieval stage, where the trained model parameters are used to infer physical parameters from polarimetric radar inputs.

The PINN can be described through the following set of simple equations. In a conventional NN, the retrieval problem is formulated as a direct mapping from observed polarimetric radar variables to microphysical state variables,

$$\hat{\mathbf{x}} = NN_{\theta}(\mathbf{y}) \tag{5.1}$$

where $\mathbf{y}$ represents the polarimetric radar variables and $\hat{\mathbf{x}}$ denotes the retrieved microphysical parameters (i.e., $D_{\mathrm{m,x}}$, W_{x}). Here, to enforce physical consistency, forward operator H is applied to the retrieved microphysical parameters:

$$\boldsymbol{y} = H(\mathbf{x}) \tag{5.2}$$

where $\mathbf{y}$ represents the polarimetric radar variables. The PINN is trained using a composite loss function consisting of two terms: retrieval loss term, where it enforces agreement between retrieved and true microphysical parameters

$$\mathcal{L}_{\mathrm{NN}} = \| \hat{\mathbf{x}} - \mathbf{x} \|^2. \tag{5.3}$$

which is analogous to the background term in variational method. The second loss term is from the forward operator term to ensure consistency between observed and forward-modeled radar variables from the retrieved parameters

$$\mathcal{L}_{\mathrm{physics}} = \| \hat{\boldsymbol{y}} - H(\hat{\mathbf{x}}) \|^2 \tag{5.4}$$

which is equivalent to the concept of innovation in DA. Thus, the total loss can be summarized as

$$\mathcal{L}_{total} = \lambda_1 \mathcal{L}_{\mathrm{NN}} + \lambda_2 \mathcal{L}_{\mathrm{physics}} \tag{5.5}$$

where $\lambda_1$and λ_2 are weighting coefficients that balance the contribution of the data-driven and physics-based constraints, respectively. Notice that this structure resembles the conventional DA systems, particularly variational method, in which the solution is obtained by minimizing a cost function that balances observational and background losses.

As such, this formulation naturally allows for multiple extensions and alternative designs. For example, the weighting coefficients λ can be prescribed as fixed constants or adaptively determined based on the total loss contributions, and/or estimates of observation and background error covariances, analogous to weighting strategies used in variational DA. This provides a mechanism to incorporate uncertainty information more explicitly into the learning process.

Additional terms can also be introduced into the loss function. For instance, additional model information or initial guesses—such as those derived from simpler yet more stable microphysical assumptions (e.g., Marshall–Palmer-type relations) —can be included as background constraints. This approach may help obtain more physically consistent results.

In the current formulation, the physics constraint is imposed in a "weak" sense, where deviations from the forward-model consistency are penalized through the loss function. Alternatively, "hard" constraints may be incorporated to explicitly enforce physical bounds or known relationships among variables. These variations highlight the flexibility of the proposed method. Further exploration of these extensions and their impact on retrieval performance is presented in subsequent chapters.

In addition, PINNs have often been reported to provide limited improvement in some applications (e.g., Jekic et al., 2025; Becerra-Zuniga et al., 2026), particularly when large amounts of high-quality training data are available. However, in this context, in situ observations—such as rain gauges or two-dimensional video disdrometers (2DVD)—are limited in both spatial coverage and domain, making them insufficient as comprehensive ground truth across all radar gates and directions. Furthermore, precipitation datasets are typically biased toward light to moderate events, which limits the ability of purely data-driven ML methods to generalize to less frequent but more impactful extreme cases. Although data augmentation techniques (e.g., Ho et al., 2023) can partially address this imbalance, they often degrade performance in light precipitation regimes and are limited in their ability to appropriately reweight different intensity ranges (e.g., Huangfu et al., 2024). PINNs are expected to mitigate these limitations by incorporating physical constraints, enabling improved performance in data-sparse regimes, including light precipitation with limited polarimetric information and underrepresented extreme events. Additionally, the inclusion of

physical constraints promotes greater physical consistency, even though the underlying ML training process remains implicit.

5.3 Retrieval results from WRF simulation data

The feasibility, as well as the strengths and limitations, of the proposed PINN are first evaluated using WRF-simulated data. As discussed in the previous chapter, extending microphysical retrievals to a broader set of parameters and hydrometeor species beyond rain using PRD is inherently challenging and represents a relatively new area of research. To address these challenges, a series of experiments is designed to evaluate the performance of the PINN under varying levels of complexity. These experiments aim to identify the conditions under which the retrieval remains stable and physically consistent, and to determine how the problem can be effectively constrained or simplified. In particular, emphasis is placed on exploring strategies that reduce the solution space to a more realistic and well-posed domain while retaining the essential microphysical characteristics of interest. Through this process, the goal is to better understand both the capabilities and limitations of the PINN, and to establish a practical pathway toward robust and physically meaningful microphysical retrievals.

5.3.1 Initial experiments

The initial experiments focused on retrieving microphysical parameters for all seven hydrometeor classes, including rain, dry and wet hail, dry and wet graupel, and dry and wet snow. This resulted in a total of 14 retrieved microphysical parameters. Because the microphysical parameters for both dry and wet hydrometeors were directly retrieved, the γ parameters associated with mixed-phase processes were not included in the retrieval. A convolutional neural network (CNN)-based U-Net architecture was employed to account for the increased complexity of the

retrieval problem. Compared to a multilayer perceptron (MLP), the U-Net is better suited to exploit spatial context by utilizing the full vertical cross-section of polarimetric radar observations (Ronneberger et al., 2015). This allows the model to capture spatial coherence and vertical structure in hydrometeor distributions, which is crucial for mixed-phase retrievals.

Physical consistency was enforced through forward operators and an updated melting model following Liu et al. (2024a), which were used to recompute polarimetric variables from the retrieved microphysical parameters. This serves as an additional constraint to ensure that the retrieved states remain physically consistent. Figures 5.2 and 5.3 compares the WRF simulation results (i.e., "Actual") with the retrieved vertical cross-sections of microphysical parameters (i.e., $D_{m,x}$, W_x) for each hydrometeor class.

The rain retrievals are generally well reproduced, with only minor spurious noise at higher elevations and occasional overestimation. This is expected, as rain is well represented in both simulations and polarimetric radar observations. In addition, the presence of isolated rain signals at the lower levels facilitates more accurate retrievals with less ambiguity. For both wet and dry hail, the retrieval captures the general location and magnitude of the core, likely because the larger sizes of hail dominate most of the polarimetric variables in these limited regions. Dry graupel retrievals also represent the main convective features but exhibit localized overestimation and increased noise. In contrast, wet graupel and both dry and wet snow are less well characterized, reflecting their greater ambiguity in polarimetric signatures. Similar behavior is noted for W_x with very noisy results for dry snow and almost no values retrieved for wet snow (Fig. 5.3).

Although the overall spatial patterns and distributions are reasonably retrieved, uncertainty due to limited information content remains significant. It should also be noted that these results are derived from simulations without any observational or model errors introduced into the retrieval

process. This suggests that accurate quantitative retrievals of microphysical parameters for all seven species, based solely on the spatial distribution of PRD, may be inherently limited. Incorporating additional constraints—such as thermodynamic and dynamical information from NWP models—may therefore be necessary to improve retrieval robustness. Alternatively, the problem could be simplified by reducing the number of retrieved parameters, for example through classification-based retrieval approaches rather than attempting to retrieve all species at every grid point.

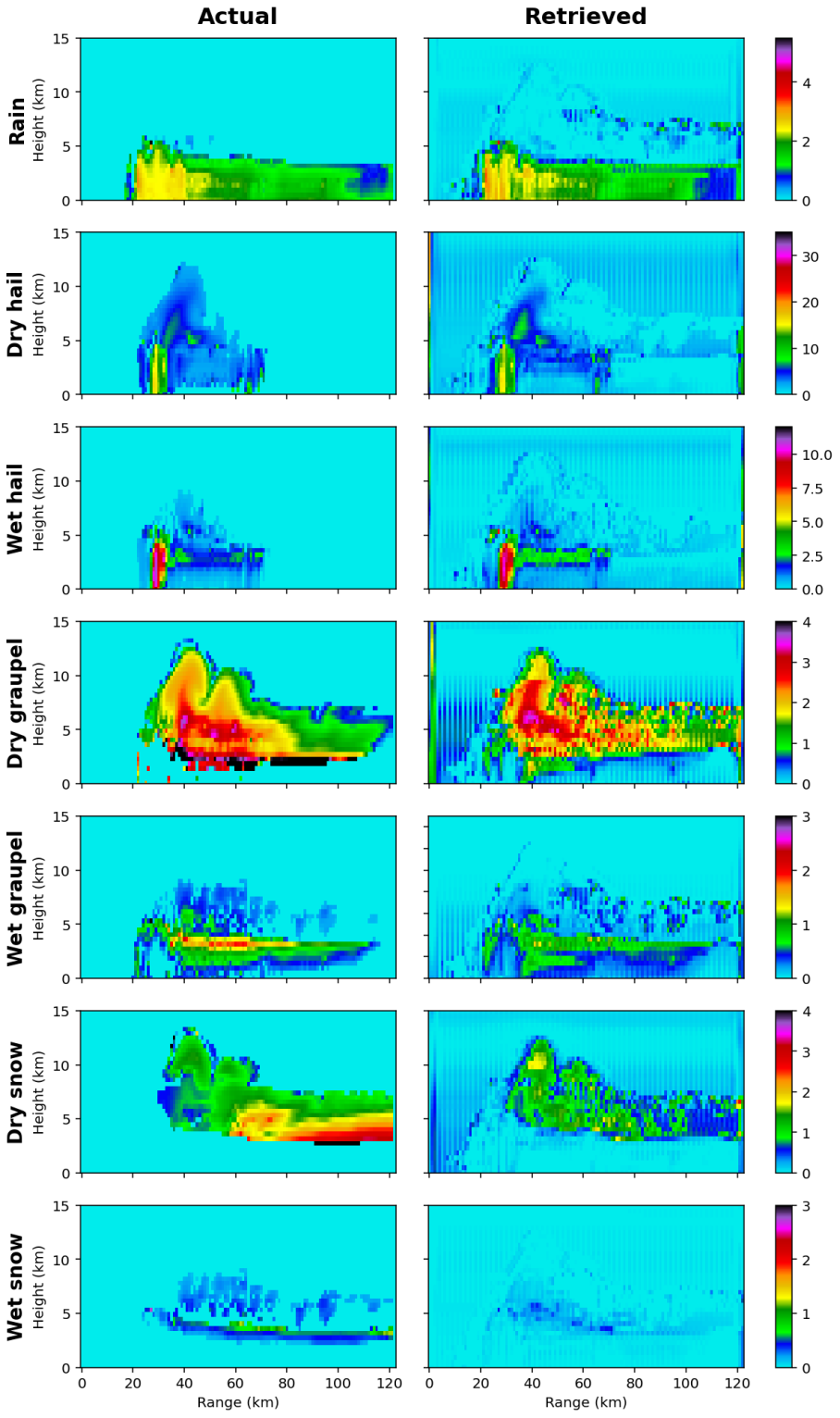

Figure 5.2. The vertical cross-section of hydrometeor $D_{m,x}$ for multiple species derived from WRF simulations (left column) and corresponding PINN retrievals (right column). Each row represents a different hydrometeor class (rain, dry hail, wet hail, dry graupel, wet graupel, dry snow, and wet snow).

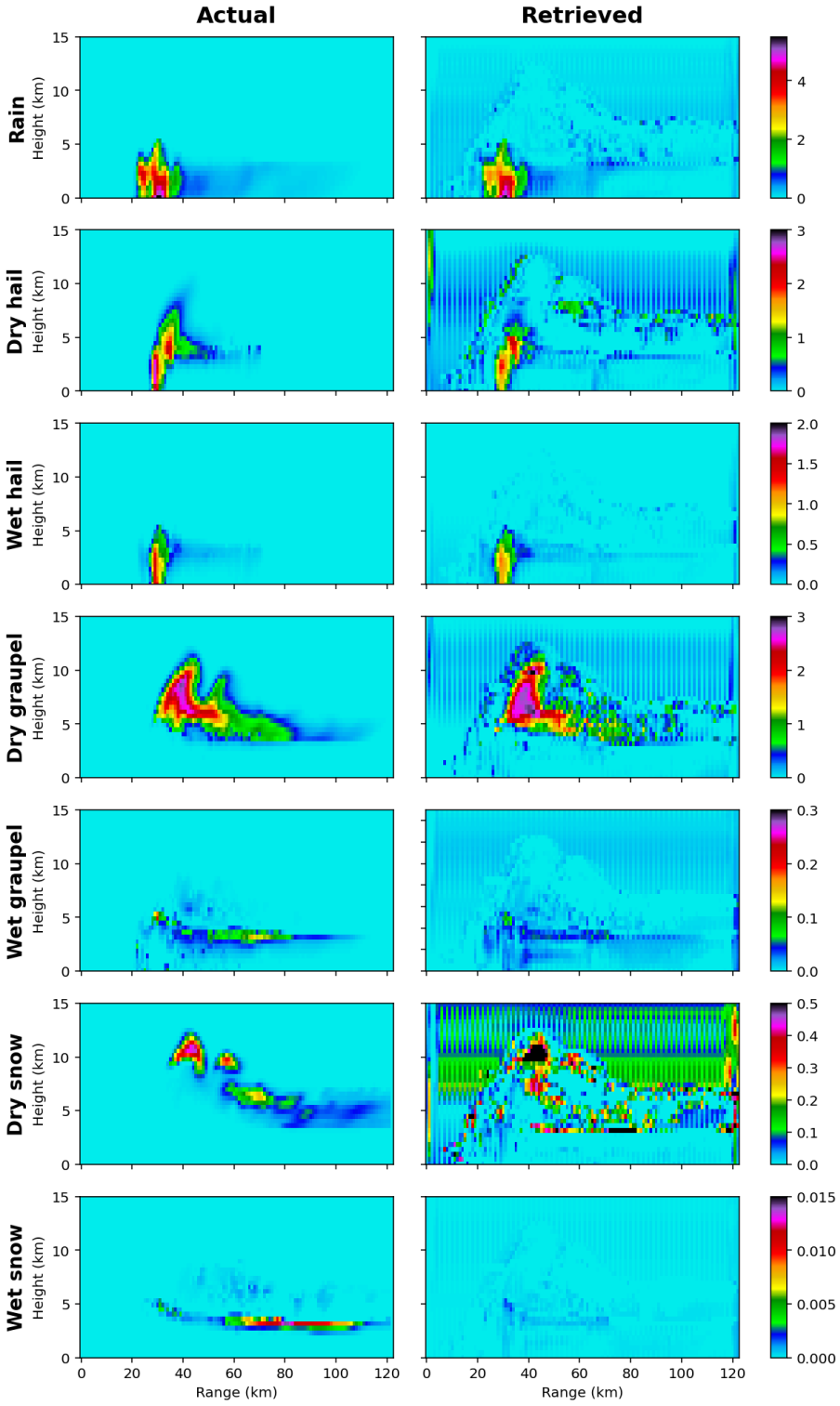

Figure 5.3. Same as Fig. 5.2, but for W_x for each hydrometeor.

5.3.2 Classification included retrieval

The fuzzy logic-based hydrometeor classification (HCA; Mahale et al., 2014) is applied to the same set of WRF-simulated polarimetric variables. The resulting HCA classifications, along with the microphysically dominant hydrometeor types derived from the q_x and $N_{t,x}$ fields, are shown in Fig. 5.4. To realistically simplify the retrieval problem—from retrieving all seven hydrometeor species at each range gate—the analysis is limited to the two most dominant species rather than all seven categories. The tertiary component typically contributes only weakly to the bulk polarimetric signatures due to its comparatively small microphysical magnitude. This approach balances the complexity introduced by including too many species, which can render the retrieval problem ill-posed, against restricting the analysis to only a single dominant species, which may neglect secondary but physically important contributors. For example, rain signals are often dominated by hail in polarimetric observations, even though rain microphysics dominate in terms of microphysical parameters. Overall, there is good agreement between the HCA results and the microphysically dominant species when the two leading contributors are considered. However, as expected, the HCA tends to indicate a stronger influence of hail, whereas the microphysical fields more often identify rain as dominant. Within and above the melting layer, all approaches show consistent behavior. Graupel is identified as the dominant species within the melting layer, while snow dominates above it. Thus, in the subsequent analysis, only the two most representative hydrometeor species are retrieved, with a primary focus on rain–hail mixtures.

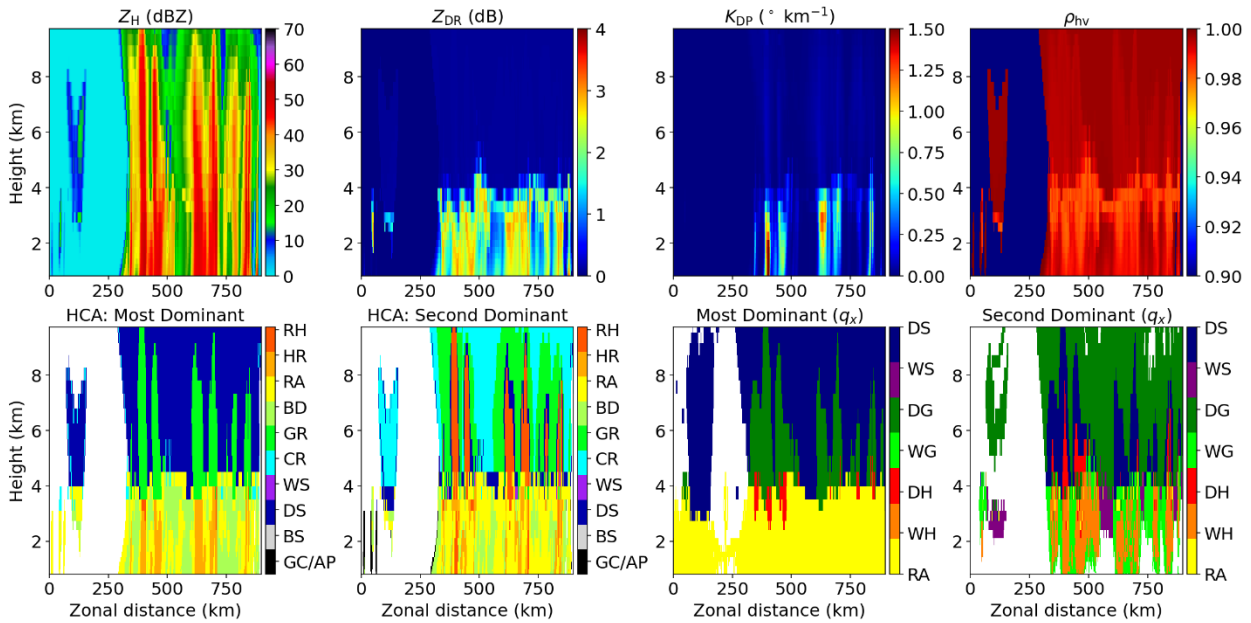

Figure 5.4. A cross-section of polarimetric radar variables (Z_H, Z_{DR}, K_{DP} ρ_{hv}), along with the fuzzy logic hydrometeor classification (HCA) results, compared with the two most dominant species identified from q_x.

5.3.3 Retrieval of rain and hail

The scope of the retrieval species is reduced to focus exclusively on rain–hail mixtures to facilitate its application to polarimetric observations after validation with simulations. After the classification, the domain is restricted to regions where rain–hail mixtures are dominant. Columns of polarimetric variables are then utilized as inputs to retrieve the rain and hail parameters. To maintain consistency with the forward operator and reduce retrieval complexity, the parameter space was constrained. Instead of retrieving separate $D_{m,x}$ and W_x for both wet and dry hail, the retrieval parameters were reduced to rain $D_{m,r}$ and W_r, along with $D_{m,h}$, W_h, and γ.

Figure 5.5 shows a comparison between retrieved and true values of D_m and W for both rain and hail. Overall, the retrieval demonstrates strong agreement with the truth, with most estimates closely aligned along the one-one line. For rain, D_m exhibits low error (RMSE ≈ 2.98%) and

negligible bias (−0.19%), indicating robust performance in estimating drop size. Similarly, W_r shows tight clustering around the one-one line,q1 with small bias (−0.46%) and moderate RMSE (≈ 4.09%), suggesting reliable water content retrieval. Although the inclusion of mixed-phase conditions introduces additional unknowns and increases retrieval complexity compared to the pure rain regime, the error metrics still indicate good agreement.

For hail, the retrieval performance is more variable. The $D_{m,h}$ estimates show reasonable agreement with the truth (RMSE ≈ 8.16%), although a slight negative bias (−1.16%) indicates a tendency to underestimate larger hail sizes. In contrast, W_h exhibits the largest spread and error (RMSE ≈ 19.24%) with a small positive bias (1.04%), indicating increased uncertainty in retrieving hail water content. This behavior suggests limitations in capturing the full range of hail properties, particularly for larger and less frequent hail sizes, and indicates that higher uncertainty in W_h remains within PINN based retrieval.

Then, the spatial distributions of the true and retrieved microphysical parameters for both rain and hail, along with the corresponding polarimetric variables are displayed in Fig. 5.6. The polarimetric fields illustrate the structure of the mixed-phase system, with enhanced Z_H and Z_{DR} indicating regions dominated by rain, while localized reductions in ρ_{hv} and increased variability in K_{DP} indicate the presence of hail and mixed-phase hydrometeors.

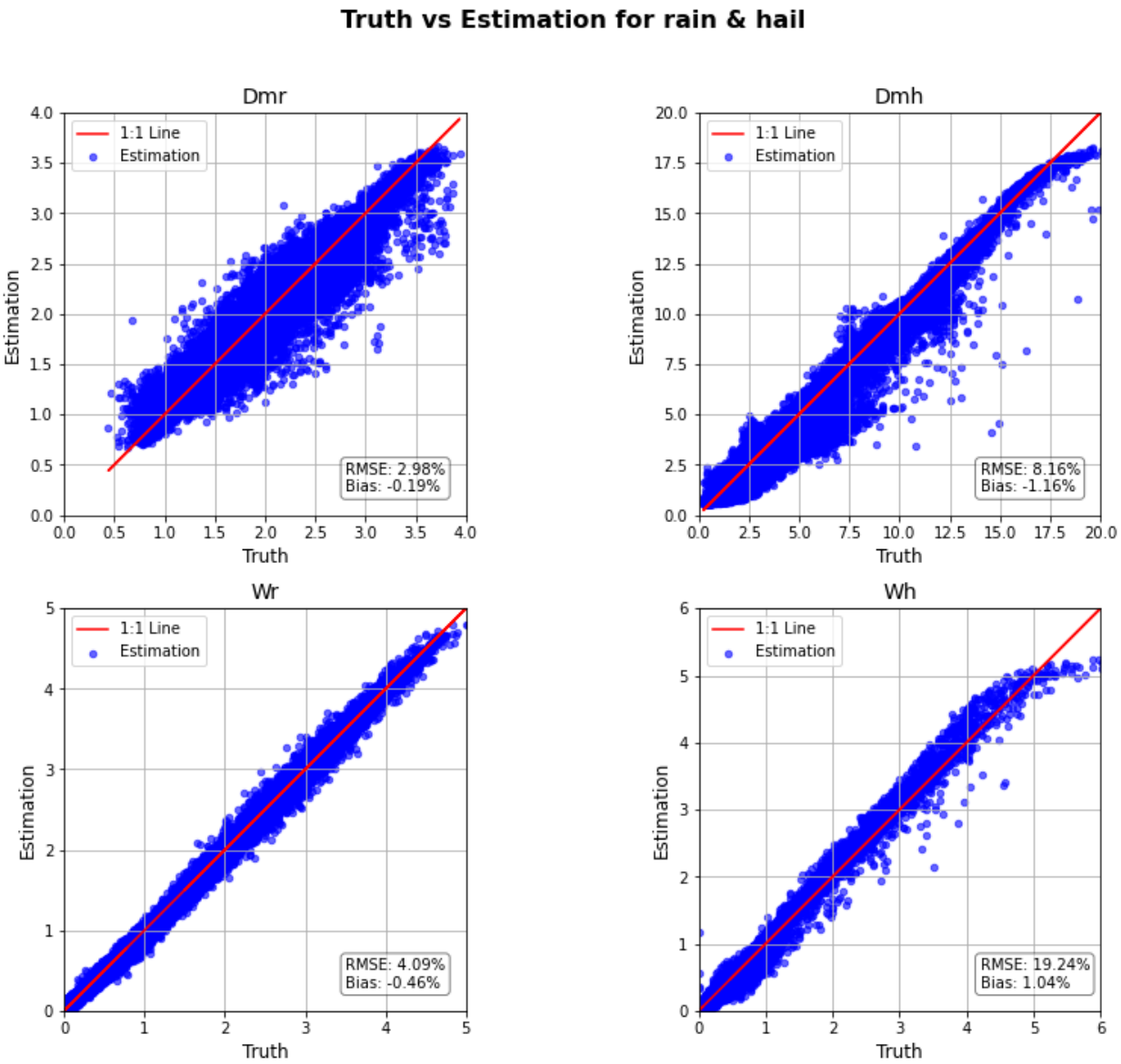

Figure 5.5. One-one scatter plots comparing the retrieved and true values of D_m and W for rain (Dmr and Wr) and hail (Dmh and Wh). The red line denotes the 1:1 relationship. Relative root-mean square error (RMSE) and bias are shown in each panel.

The retrieved fields generally reproduce the large-scale spatial patterns. For rain, the retrieved $D_{m,r}$ captures the gradual spatial variability and vertical structure seen in the truth, particularly within the main precipitation core. Similarly, W_r is well reconstructed, with the retrieval preserving

both the magnitude and spatial extent of regions with high water content. Minor smoothing is evident, especially near sharp gradients.

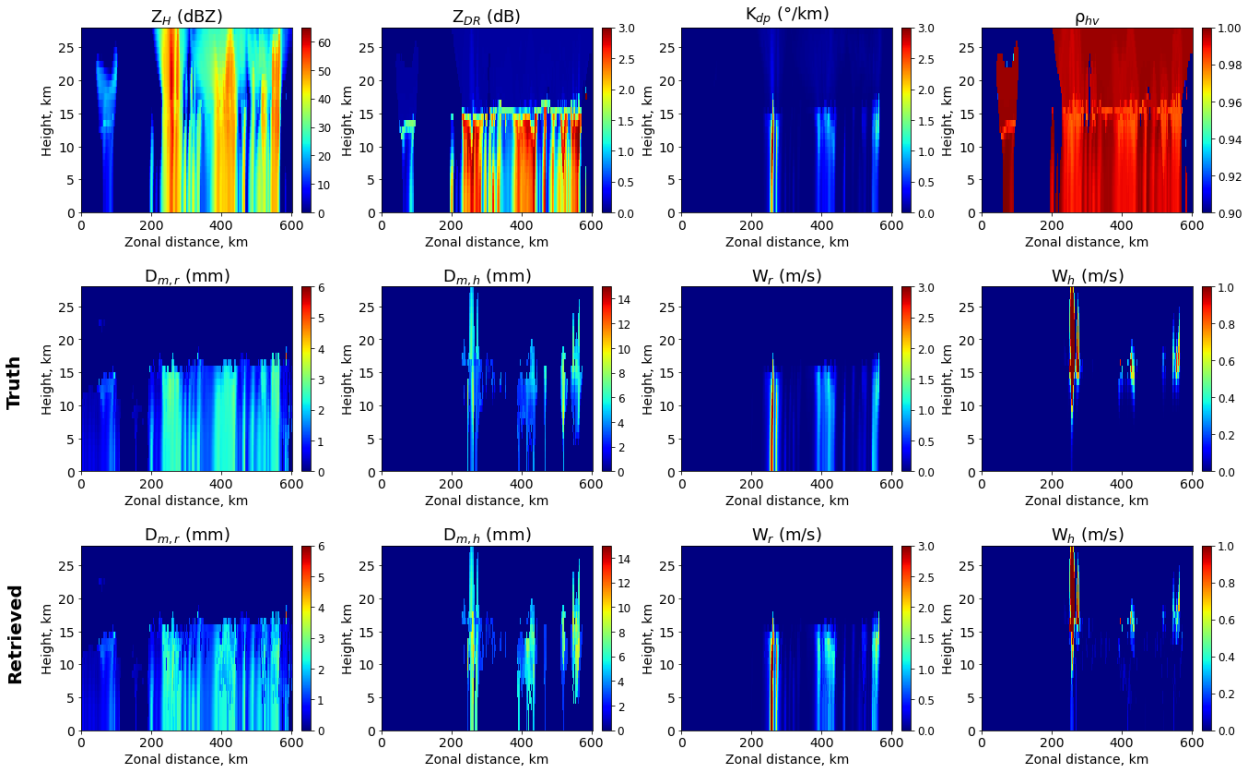

Figure 5.6. A vertical cross-section displaying polarimetric radar variables (first row), simulated microphysics parameters for rain and hail (second row), and retrieved microphysics parameters (third row).

For hail, the retrieval delineates the primary regions of occurrence, as seen in the $D_{\mathrm{m,h}}$ and W_{h} fields, with good correspondence in the locations of major hail cores. However, discrepancies are more apparent compared to rain. The retrieved $D_{\mathrm{m,h}}$ reproduces the general spatial distribution but tends to smooth localized peaks and slightly underestimate regions with large hail, consistent with the bias observed in the scatter analysis. The W_{h} field shows greater differences, with reduced intensity and spatial extent in some regions, as well as increased noise in areas of weak signal. Regions with strong polarimetric signatures correspond well to areas where both the truth and the

retrieval indicate significant hail presence, suggesting that the retrieval effectively exploits polarimetric information to identify mixed-phase regions. Overall, the spatial comparison indicates that the PINN is capable of reconstructing the dominant structures of rain and hail mixture regimes. However, it should be noted that no measurement or model errors were introduced in these simulation-based experiments.

5.4 Retrieval results from NEXRAD data

The microphysics retrievals of hail regime from PRD are inherently ill-posed, and this ill-posedness is further exacerbated when applied to real observations. For hail in particular, the problem is substantially more pronounced. Hail microphysical variability is large and ambiguous, while the amount of independent information available from PRD is limited. In addition, hail microphysical parameters are unavailable and difficult to validate in retrieved results—unlike rain microphysics—which can be constrained or trained using disdrometer or other in-situ measurements. As a result, there is insufficient information and too few constraints to robustly derive hail-specific microphysical parameters using empirical or semi-empirical retrieval relationships based solely on PRD. In principle, microphysical retrieval could be attempted through direct inversion of polarimetric forward operators. However, even for rain—where DSDs are relatively well understood—such physics-based inversion methods are highly sensitive to measurement errors, as well as to model assumptions and parameterization choices (Ho et al., 2023).

To address these limitations, more advanced retrieval methods are required. As discussed in the previous chapters, PINNs have shown promise by embedding governing physical relationships into data-driven models, potentially improving robustness and generalization, while providing

enhanced computational efficiency compared to variational approaches. The following chapters focus on evaluating the feasibility and performance of PINNs for this retrieval problem.

For the NEXRAD application, MLP/deep neural network (DNN) is employed to collocate radar gates above the 2DVD site. Although incorporating additional spatial information—such as reconstructed vertical columns or along-ray profiles—may further improve retrievals, the temporal resolution limitations of current NEXRAD dish radars (i.e., up to a 5-minute difference between the lowest and highest elevation scans) constrain such approaches. Therefore, this work focuses on demonstrating PINN using an MLP-based implementation.

5.4.1 Case overview

A prolific severe weather event occurred on April 27–28, 2024, producing over 30 tornadoes, along with widespread large hail and damaging winds (https://www.weather.gov/oun/events-20240427; https://www.spc.noaa.gov/climo/reports/240427_rpts.html). This slow-moving and intense storm system on 28 April 2024 generated numerous tornadoes across Oklahoma and western North Texas, with additional impacts including hail up to approximately 3 inches in diameter, wind gusts near 60 mph, and heavy rainfall totals ranging from roughly 4 to nearly 9 inches. These conditions led to flash flooding and river flooding in parts of the region. Post-event surveys conducted by the National Weather Service offices in Norman and Tulsa confirmed nearly 40 tornadoes across Oklahoma and adjacent areas of north Texas.

The polarimetric variables are depicted in Fig. 5.7 including Z_H, Z_{DR}, ρ_{hv}, Φ_{DP}, linear programming calculated K_{DP} (Mishler et al., 2024), and the resulting HCA output based on Mahale et al. (2014). Sounding data were utilized to estimate the melting and freezing levels for the HCA analysis to identify regions of hail (https://weather.uwyo.edu/cgi-bin/sounding?region=naconf&TYPE=TEXT%3ALIST&YEAR=2024&MONTH=04&FROM=2

800&TO=0712&STNM=72357). The Z_H field highlights a well-defined convective line, while reduced ρ_{hv} (~0.95) and enhanced Z_{DR} values (up to ~4 dB) indicate the presence of heavy rain and mixed-phase precipitation with potential hail. Elevated K_{DP} values further support regions of intense precipitation, and the HCA output identifies hydrometeor types, with rain-hail signatures concentrated within the strongest convective elements. This study focuses on retrievals in regions of both heavy rain and hail contaminated precipitation, specifically near a 1-inch hail report from MPING (Elmore et al., 2014) in McClain County (https://www.weather.gov/oun/events-20240427).

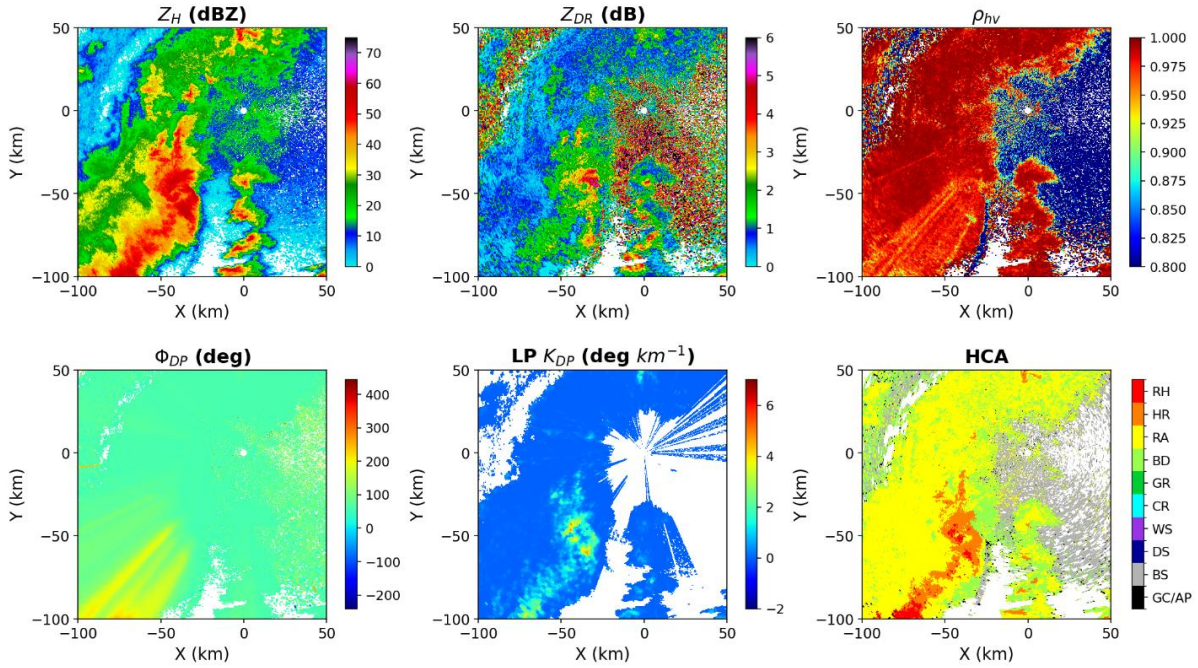

Figure 5.7. Polarimetric radar variables at 0155 UTC on 28 April 2024 during a severe weather event. Shown are (top row, left to right) Z_H, Z_{DR}, and ρ_{hv}, and (bottom row, left to right) Φ_{DP}, linear-programming estimated K_{DP}, and HCA output.

5.4.2 Data driven rain retrieval results

The initial evaluation of the PINN focused on assessing whether incorporating physical constraints can improve purely data-driven NN retrievals. To isolate this effect, the analysis was first conducted for rain microphysics using the same dataset as Ho et al. (2023). The reference dataset combines 2DVD (Kruger and Krajewski, 2002)-derived microphysical parameters with collocated polarimetric radar observations (Z_H and Z_{DR}) over a 10-year period, partitioned into training, validation, and testing subsets. As shown in Ho et al. (2023), NN-based retrievals substantially reduce bias compared to empirical relations and direct inversion of forward operators. However, notable deficiencies remain, particularly in hail-contaminated conditions and for extreme values that are underrepresented in the training data. The baseline performance of a purely data-driven DNN, evaluated at the 2DVD site, is shown in Fig. 5.8. Overall, the network produces low bias for both $D_{m,r}$ and W_r, but exhibits large standard deviations, reflecting sensitivity to measurement noise that is not explicitly accounted for in the model. This suggests that the NN can mitigate systematic model errors but struggles with random observational uncertainty. A closer examination of the retrievals reveals additional limitations. For $D_{m,r}$, predictions are concentrated within the range of approximately 1.0–2.5 mm, with performance degrading outside this interval. A similar pattern is observed for W_r: while variability is high at low values (0–0.25 g m^{-3}) due to measurement noise, retrievals at higher values (> 0.5 g m^{-3}) exhibit both increased bias and spread. These results highlight the limited generalization of the MLP beyond the dominant regimes represented in the training data.

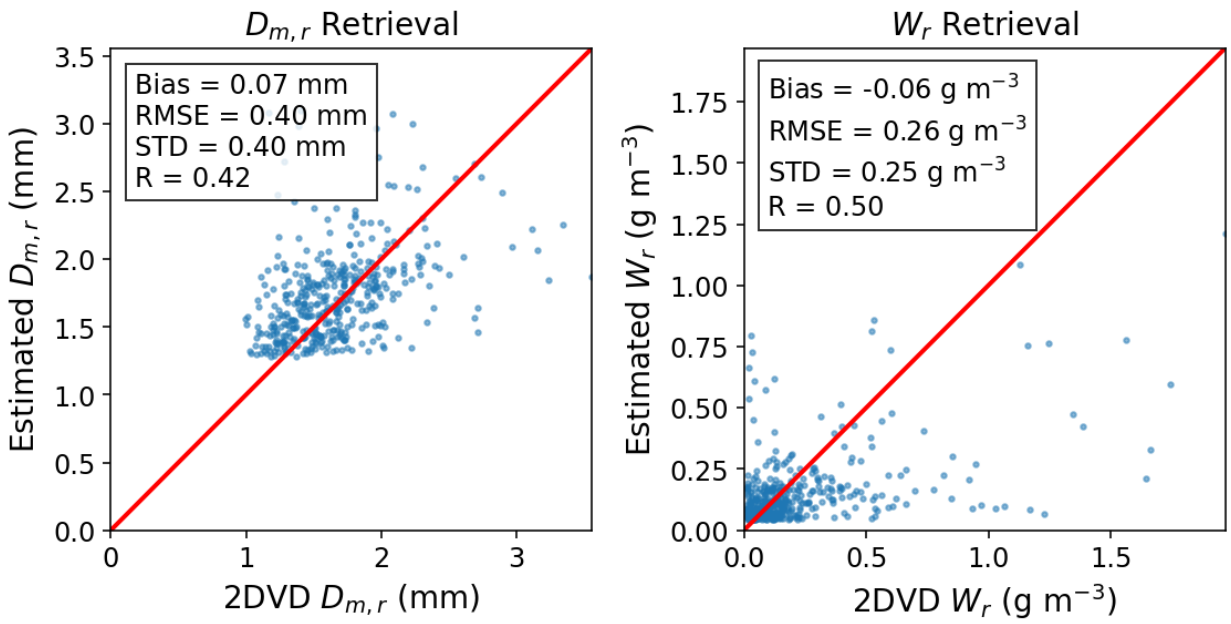

Figure 5.8. The retrieval performance of the multilayer perceptron (MLP) model trained using Z_H and Z_{DR} from KTLX measurements with corresponding 2DVD data. The comparisons between 2DVD-derived and MLP-retrieved $D_{m,r}$ and W_r are shown, along with associated error metrics (bias, RMSE, standard deviation, and correlation coefficient).

The trained model was subsequently applied across the full spatial domain using an independent case observed on 28 April 2024 at 0155 UTC. Figure 5.9 presents the observed polarimetric variables from the KTLX radar alongside the corresponding analysis fields derived from NN-retrieved microphysical parameters, as well as their differences. While the NN-based retrievals show reasonable performance at the single 2DVD site, the spatially distributed results reveal substantial discrepancies. These differences likely arise from a combination of factors, including range-dependent radar uncertainties, measurement error characteristics, and increased microphysical variability across the domain. As a result, the analysis fields fail to reproduce key structural features present in the observations, particularly in regions of strong gradients and convective cores. This behavior is evident across all polarimetric variables (Z_H, Z_{DR}, K_{DP}, and ρ_{hv}), where widespread and systematic differences are observed.

Although some discrepancies may be attributed to forward-operator limitations and could potentially be reduced through bias correction, the observed differences are not consistent with simple systematic biases. In particular, Z_H and Z_{DR} exhibit broad regions of overestimation in the stratiform regions and underestimation in the convective regions, while K_{DP} shows localized but pronounced deviations in high-intensity regions. Discrepancies in ρ_{hv} are expected, as the rain forward operator does not adequately represent hail-contaminated regimes, which are often associated with reduced observed ρ_{hv} values.

While increasing the volume of training data may offer some improvement, collocated disdrometer observations are inherently limited in spatial coverage, and underrepresented regimes and value ranges in the dataset are unavoidable. Overall, these results demonstrate that a purely data-driven model trained in point-scale observations does not generalize well to spatially complex precipitation structures, highlighting fundamental limitations in the robustness of purely data-driven retrieval approaches.

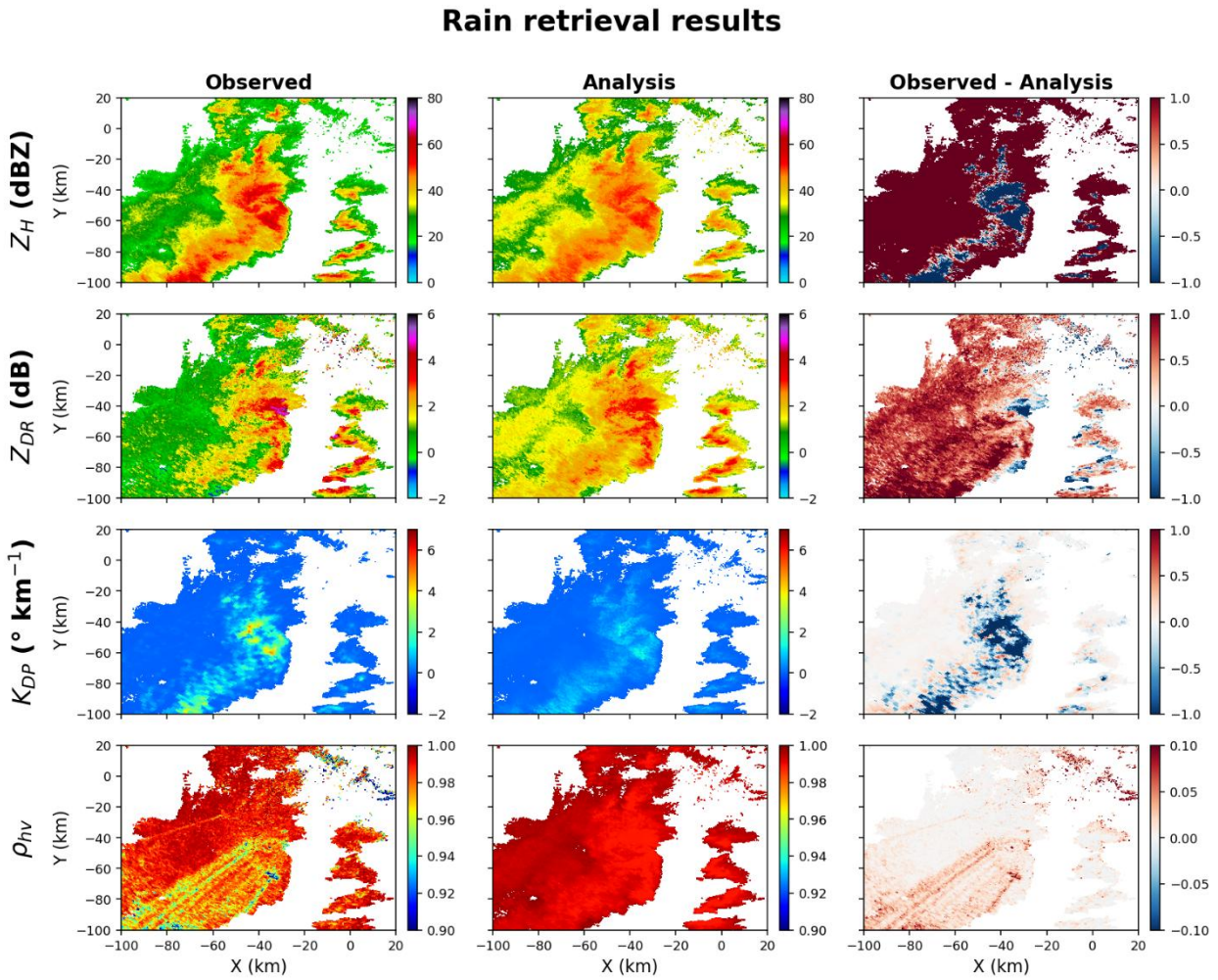

Figure 5.9. The rain retrieval results using a model trained using Z_H and Z_{DR} from KTLX measurements with corresponding 2DVD data. Observed radar variables (left column), retrieved (analysis) fields (middle column), and their differences (right column) are shown.

The spatial distributions of the retrieved microphysical parameters are shown in Fig. 5.10. Consistent with the characteristics observed in the training and testing datasets, the NN-retrieved fields exhibit a relatively limited dynamic range. Specifically, $D_{m,r}$ values are largely confined below ~3 mm, while W_r remains below ~3 g m^{-3}, even within regions of intense precipitation. This constrained range is evident when comparing different precipitation regimes. In stratiform regions, $D_{m,r}$ does not decrease below approximately 1 mm, indicating a lack of sensitivity to smaller drop sizes. This limitation likely contributes to the overestimation of Z_H and Z_{DR} in the

stratiform regions as noted in Fig. 5.9. Similarly, in convective regions, although some spatial variability is captured, the retrieved W_r field appears smaller than expected, suggesting that the model struggles to represent higher liquid water contents. This compression of dynamic range reflects the overinfluence of the training data distribution, where extreme values are underrepresented, and highlights a key limitation of the purely data-driven approach. The retrieved fields indicate that the NN tends to regress toward the mean of the training dataset, limiting its ability to capture both low-end and high-end microphysical variability across the spatial domain.

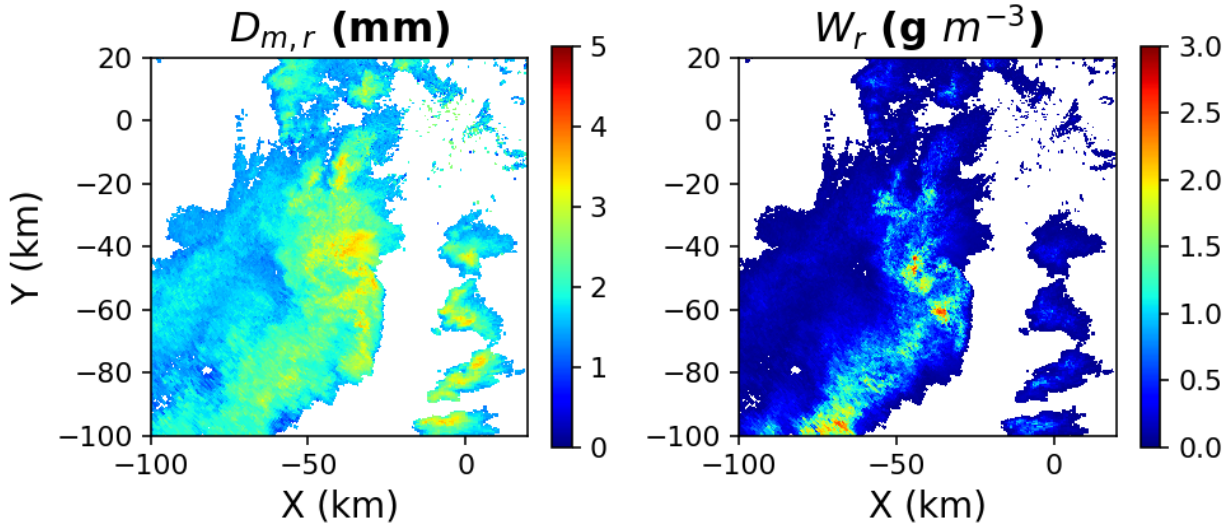

Figure 5.10. The retrieved rain microphysical parameters $D_{m,r}$ (left) and W_r (right) from MLP trained using Z_H and Z_{DR} from KTLX measurements with corresponding 2DVD data.

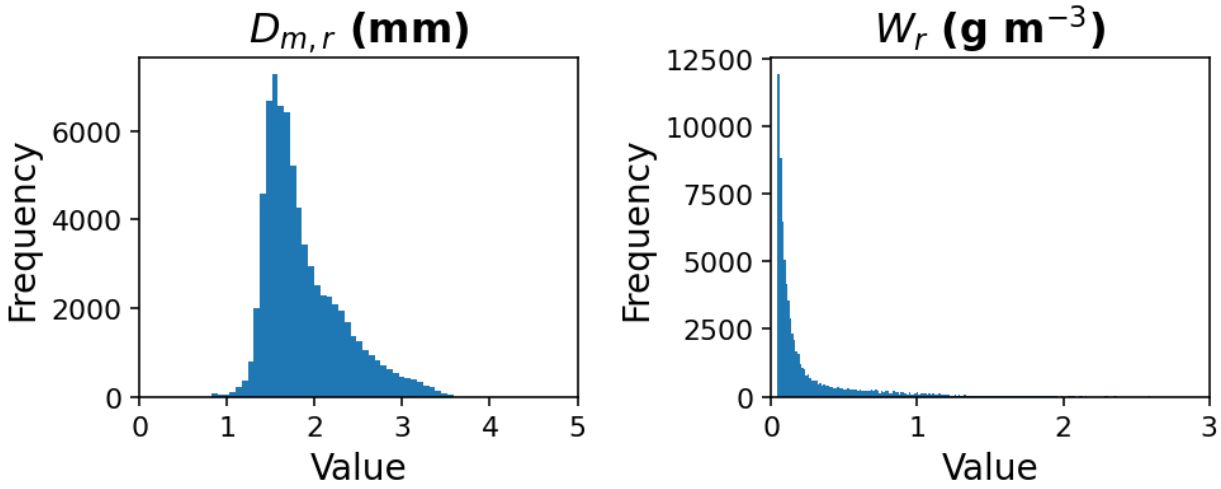

Figure 5.11. The rain retrieval results based on the 2DVD data training results.

The distributions of the retrieved microphysical parameters further emphasize these limitations (Fig. 5.11). The $D_{m,r}$ distribution is strongly peaked around ~1.5–2 mm, with relatively few occurrences outside this range, indicating that the model preferentially predicts values near the central tendency of the training data. Similarly, the W_r distribution is highly skewed, with a large concentration of values near zero and a rapid decay toward higher values. This suggests that the NN struggles to represent higher W_r values even in heavy rain conditions. As a result, both tails of the distribution—corresponding to light stratiform precipitation and intense convective cores—are underrepresented. This further underscores the need for approaches that better constrain the retrieval problem beyond the training data distribution.

5.4.3 Rain retrieval results with physical constraint

The second experiment was conducted over the 2DVD site without using the 2DVD-derived microphysical parameters, relying solely on the polarimetric forward operators. Although the formulation of the cost function differs, this approach closely resembles the variational method, in which the innovation term is minimized to solve the inverse problem, with the NN-derived

estimate serving as the background state or the initial guess. As expected, the retrieval performance over the 2DVD site degrades substantially compared to the purely data-driven NN results (Fig. 5.12). The $D_{m,r}$ retrievals exhibit increased spread and a more pronounced negative bias, while the W retrievals show significant scatter and large relative errors, particularly at low values. These results indicate that, in the absence of direct microphysical parameters, the inversion relying solely on forward operators becomes highly sensitive to measurement uncertainties and model assumptions.

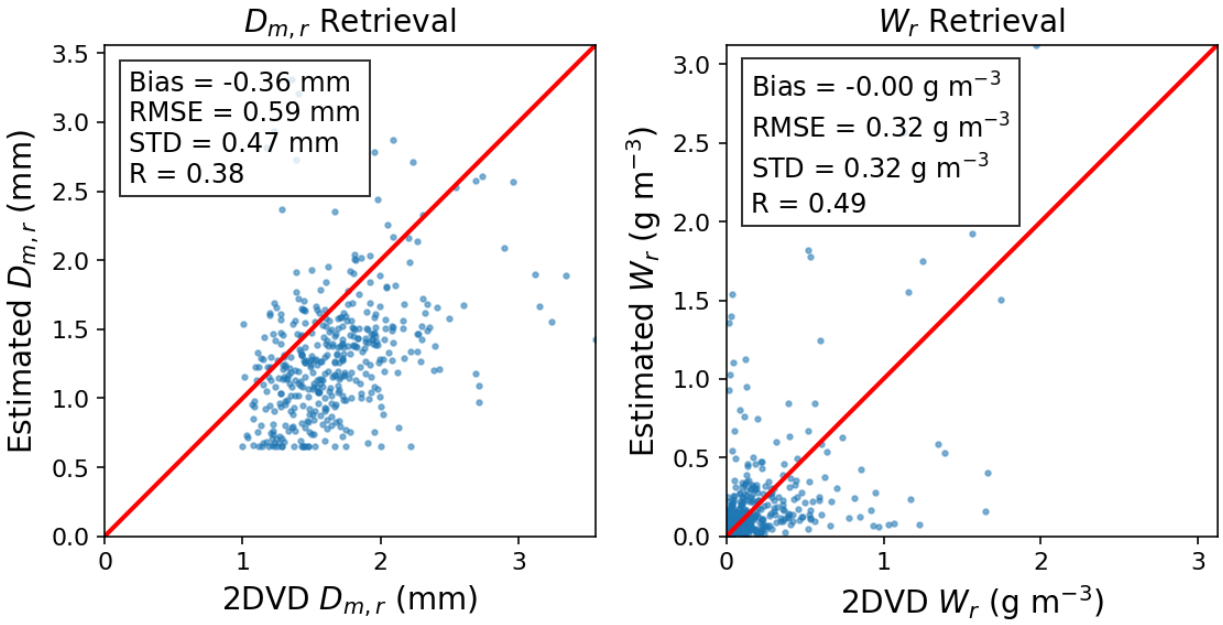

Figure 5.12. Same as Fig. 5.8, except retrievals from MLP trained with forward operator.

Similarly, the trained NN was applied to the full spatial domain of a novel case not included in the training dataset. Figure 5.13 compares the observed polarimetric fields with the corresponding analysis fields derived from the forward operator based NN-retrieved microphysical parameters, along with their differences.

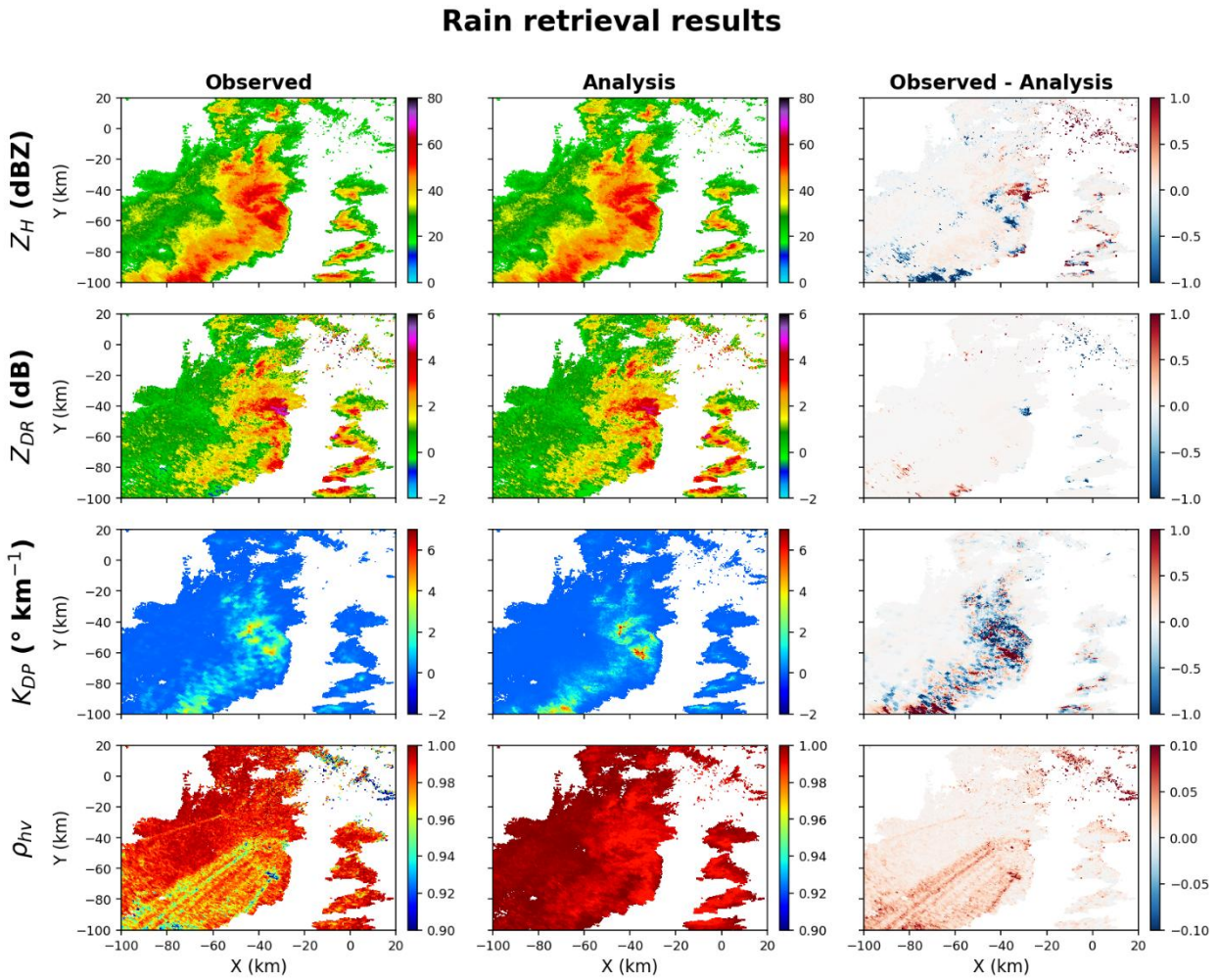

Figure 5.13. Same as Fig. 5.9, except results from MLP trained with forward operator.

In contrast to the previous experiment, agreement between the observed and analysis fields is notably improved across all variables. The model successfully captures the overall storm structure, including the spatial organization of stratiform and convective regions, as well as the gradients in Z_H and Z_{DR}. This consistency suggests that the retrieval generalizes reasonably well. For Z_H and Z_{DR}, the analysis fields closely match the observed magnitudes and spatial patterns, with only localized discrepancies. The K_{DP} field is also well represented in terms of spatial structure, although slight overestimation is evident in regions of intense precipitation, particularly where heavy rain is present. The ρ_{hv} field shows good agreement in homogeneous rain regions; however,

discrepancies remain in areas of reduced ρ_{hv}, likely associated with mixed-phase hail-contaminated conditions that are not fully captured by the rain forward operator. Despite these limitations, the magnitude of the differences is substantially smaller and less spatially coherent than in the data-driven NN.

The spatial distributions of the retrieved microphysical parameters for this case are shown in Figure 5.14. In contrast to the earlier data-driven NN results, the absence of direct 2DVD microphysical constraints allows the retrieved parameters to span a much broader range. The D_m reaches values up to ~5 mm, particularly in regions associated with intense precipitation and potential hail contamination. Similarly, the retrieved W field exceeds 3 g m^{-3} in localized areas, with pronounced maxima aligned with convective cores. These elevated values are physically plausible under extreme conditions but appear too frequently, both in extent and magnitude compared to expectations from in situ observations.

This expansion in dynamic range reflects the reduced constraints on the retrieval when relying solely on forward operators, allowing the solution to explore a wider portion of the parameter space. However, it also introduces the risk of model errors and/or increased sensitivity to measurement errors, particularly in regions where the forward model may not adequately represent mixed-phase processes or where observational uncertainties are large.

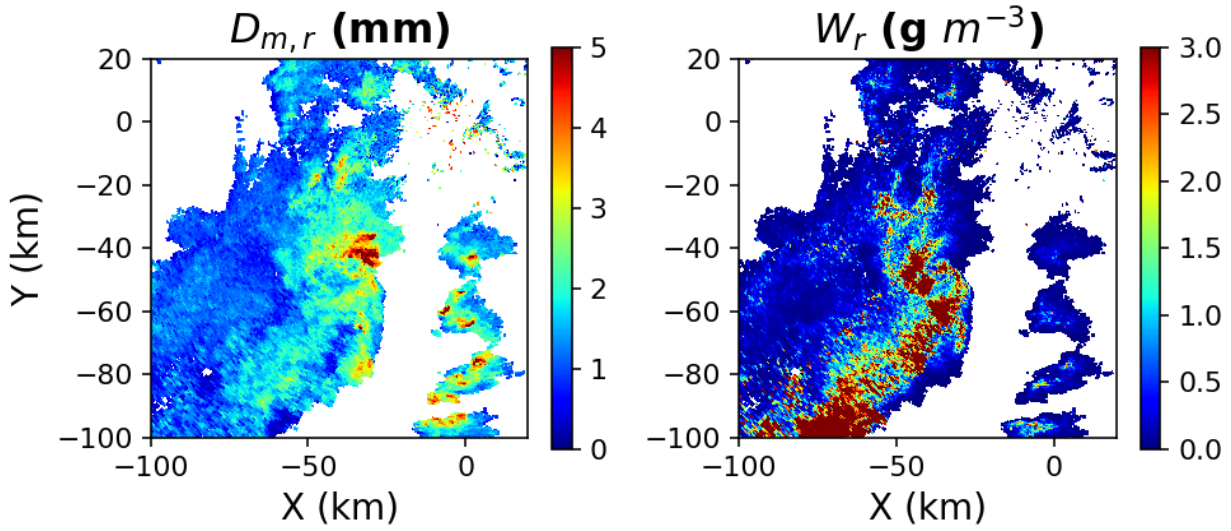

Figure 5.14. Same as Fig. 5.10, except results from MLP trained with forward operator.

The distributions of the retrieved microphysical parameters (Fig. 5.15) further illustrate this expanded variability. The $D_{m,r}$ distribution is broader, with a longer tail extending toward larger values, reflecting the increased occurrence of high-$D_{m,r}$ estimates in convective regions. Similarly, the W_r distribution remains strongly skewed toward low values but exhibits a noticeably heavier tail, indicating more frequent retrievals of higher W_r. While this broader distribution suggests improved sensitivity to extreme conditions, it also highlights the reduced constraints of the retrieval, allowing physically unrealistic or exaggerated values to occur more frequently. This behavior is consistent with the spatial patterns shown in Fig. 5.14 and underscores the trade-off between increased flexibility and reduced precision. These results suggest that both representative ground-truth data and physically based forward operators are necessary to ensure stability and physical realism, while also improving the treatment of model and measurement errors and enhancing overall retrieval accuracy.

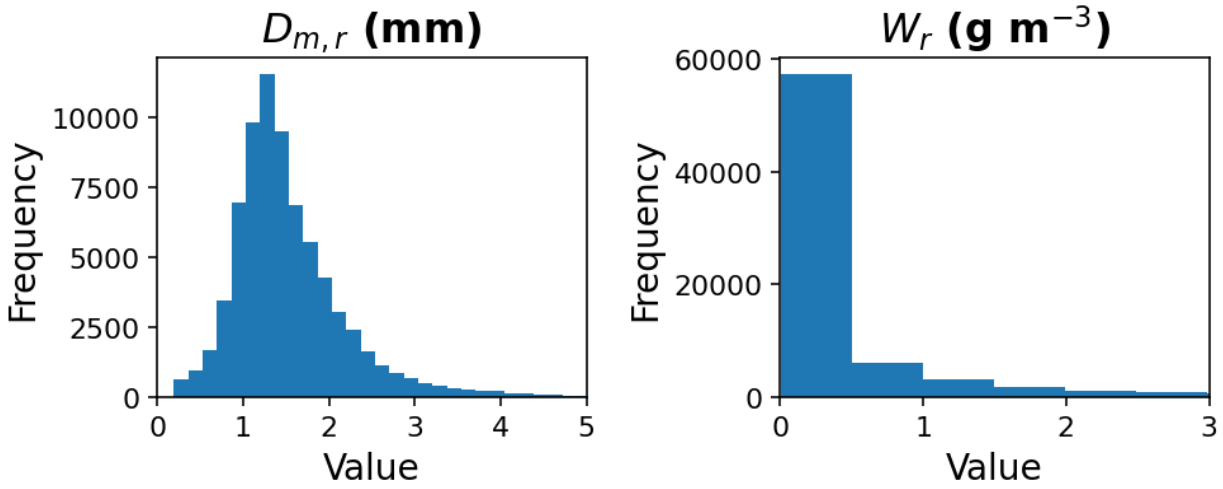

Figure 5.15. Same as Fig. 5.11, except results from MLP trained with forward operator.

5.4.4 Rain retrieval results with PINN

To balance and leverage both the reliability of limited ground-based 2DVD measurements and the flexibility of physics-based constraints, a combined loss function was formulated to incorporate contributions from 2DVD derived microphysical parameters and polarimetric forward operators. This hybrid PINN approach is designed to balance data-driven learning with physically consistent retrievals. While the optimal weighting between these components is problem-dependent and will be discussed in subsequent chapters, equal weighting is adopted here as a baseline configuration. Figure 5.16 presents the corresponding retrieval performance over the 2DVD site. Compared to previous experiments, the results demonstrate a more balanced behavior between the two sources of information. Specifically, the data-driven NN component alone tends to introduce a slight positive bias, whereas the forward-operator-based inversion exhibits a negative bias. By combining both contributions, the retrieval achieves a partial compensation of these opposing tendencies, leading to improved overall agreement with the 2DVD observations. Although the performance is not fully optimized under equal weighting, the results highlight the potential of the

PINN approach to better constrain the retrieval. The inclusion of 2DVD data helps anchor the solution toward realistic values, while the physical constraints enable improved representation of extreme conditions, thereby mitigating the individual weaknesses of each approach.

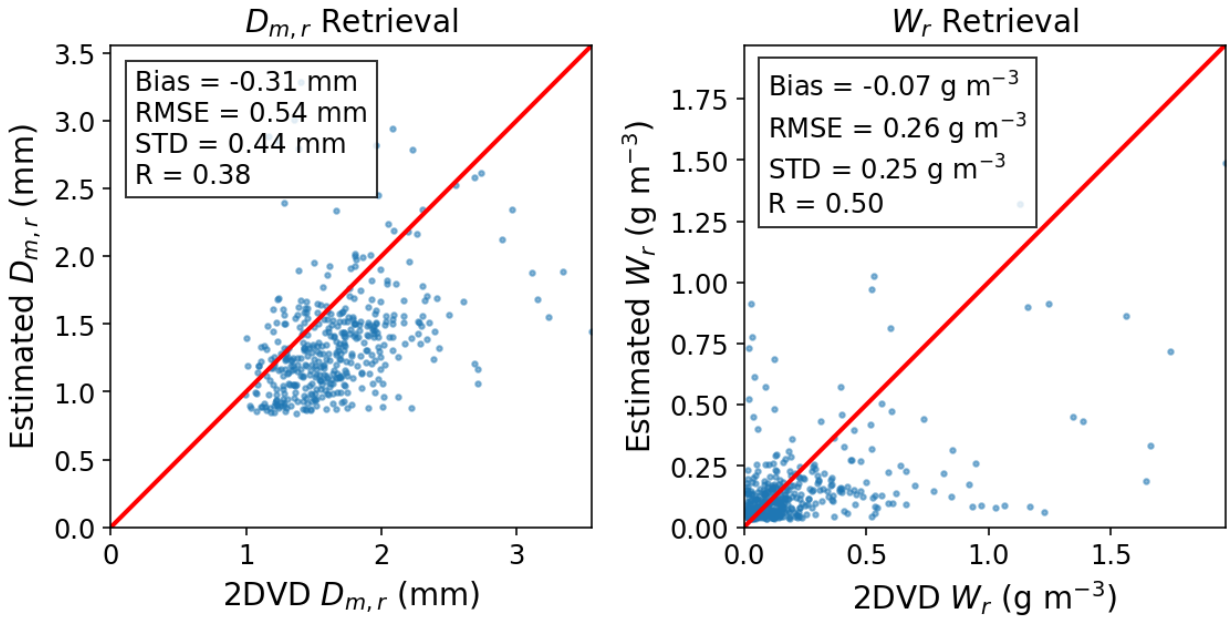

Figure 5.16. Same as Fig. 5.8, except testing results from PINN.

The trained NN is further applied to the full spatial domain, as shown in Fig. 5.17, where the observed polarimetric fields are compared with analysis fields derived from the PINN, along with their differences. Overall, the PINN approach demonstrates improved consistency with the observations compared to the data-driven NN, capturing the primary storm structure and spatial variability across both stratiform and convective regions. For Z_H, the analysis reproduces the main patterns reasonably well, although some localized under- and over-estimation remains, particularly along sharp gradients. The Z_{DR} field also shows improved agreement in both magnitude and spatial distribution, with reduced systematic biases compared to the purely data-driven approaches. The K_{DP} field captures the overall structure of high-intensity regions, though localized discrepancies persist in convective cores, likely reflecting sensitivities to both measurement noise and

microphysical assumptions. Meanwhile, ρ_{hv} remains well represented in homogeneous rain regions, with residual differences primarily confined to hail-contaminated regions. These results indicate that the spatial patterns are improved compared to the purely data-driven NN, while also maintaining better agreement with the 2DVD observations at the site. This suggests that the PINN provides a more balanced and physically consistent retrieval.

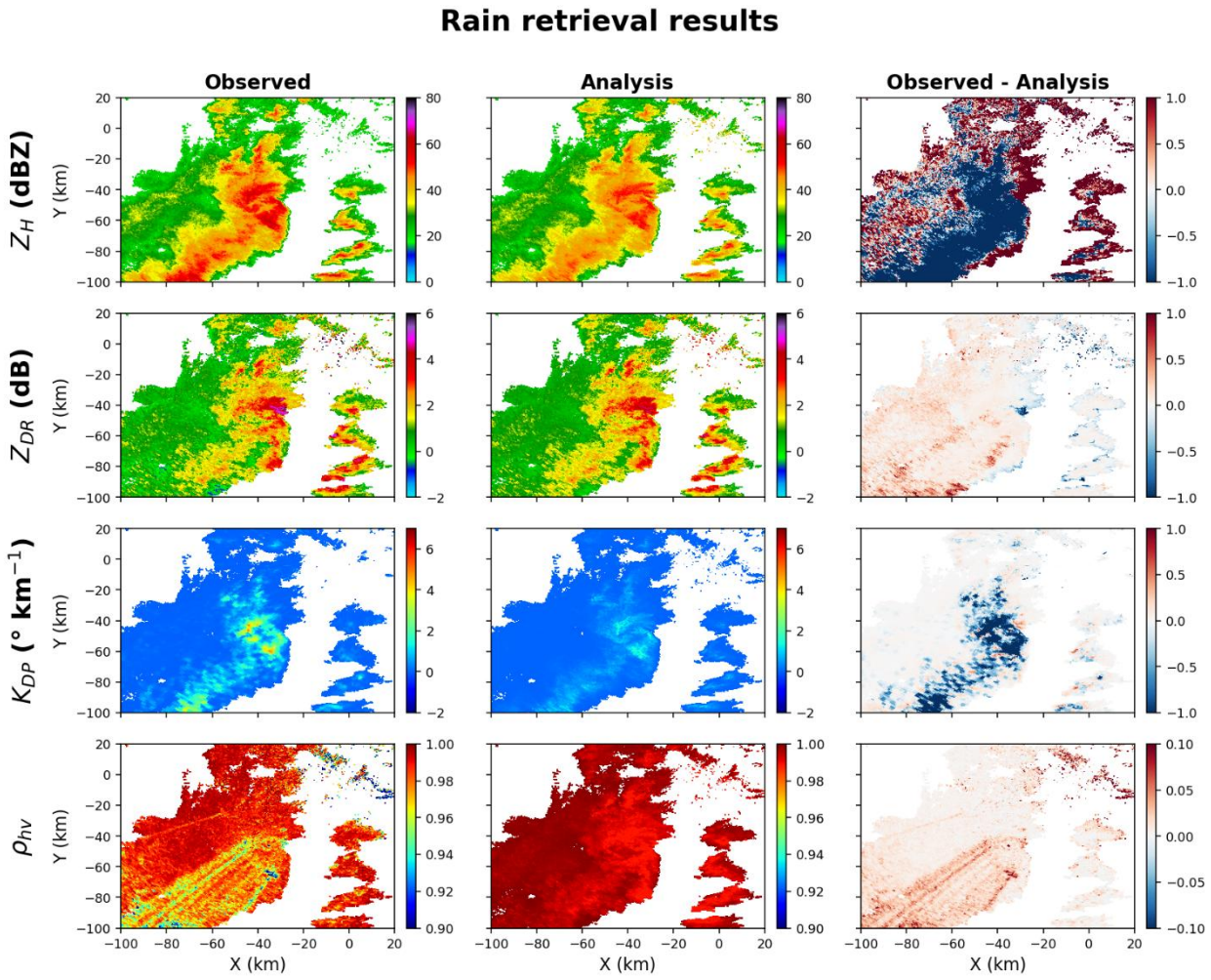

Figure 5.17. Same as Fig. 5.9, except results from PINN.

The spatial distributions of the retrieved rain microphysical parameters are shown in Figure 5.18, with their corresponding value distributions presented in Fig. 5.19. The $D_{m,r}$ field exhibits

coherent spatial variability, with larger drop sizes concentrated in convective regions and smaller values dominating stratiform areas. Compared to previous experiments, the retrieved $D_{m,r}$ range appears more physically realistic, with reduced overestimation in high-intensity regions while still preserving meaningful variability. Similarly, the W_r field captures the structure of precipitation intensity, with enhanced values aligned with convective cores and lower values in surrounding stratiform regions. The magnitude of W_r is moderated relative to the operator-only retrieval, suggesting that the inclusion of 2DVD constraints helps prevent unrealistically large estimates while still allowing sufficient dynamic range.

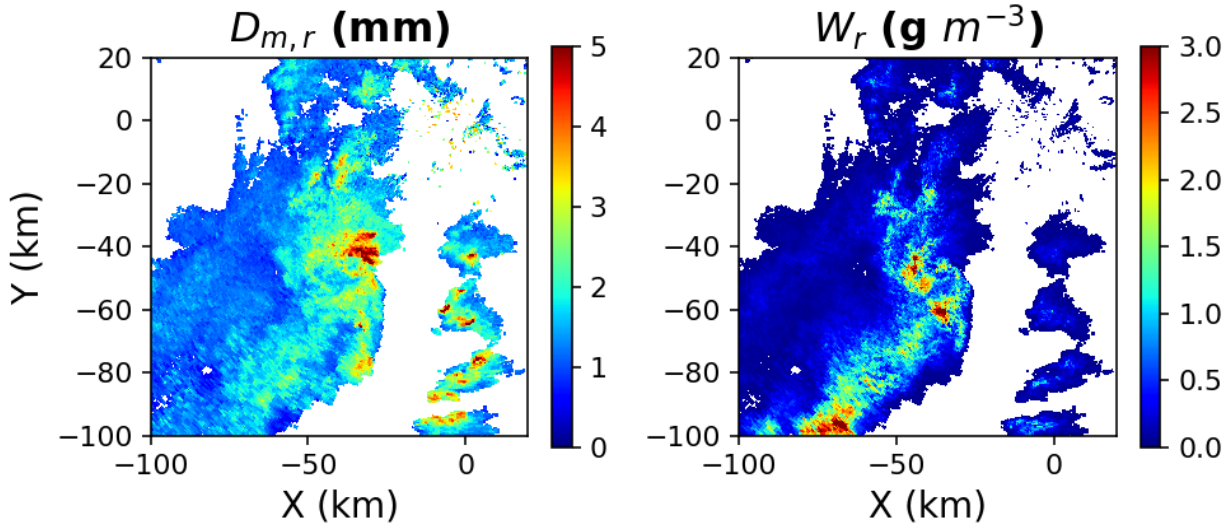

Figure 5.18. Same as Fig. 5.10, except results from PINN.

The distributions of the retrieved rain microphysical parameters are shown in Fig. 5.19. The $D_{m,r}$ distribution exhibits a well-defined peak around typical rain values (~1–2 mm), with a moderate tail extending toward larger drop sizes. It avoids both the overly narrow range seen in the purely data-driven approach and the excessively long tail associated with the operator-only retrieval, indicating a more balanced representation of variability. Similarly, the W_r distribution

remains strongly skewed toward lower values but retains an extension toward higher values. This suggests that the PINN more effectively captures higher values than the data-driven model, while avoiding the unrealistically large values produced by the operator-based approach.

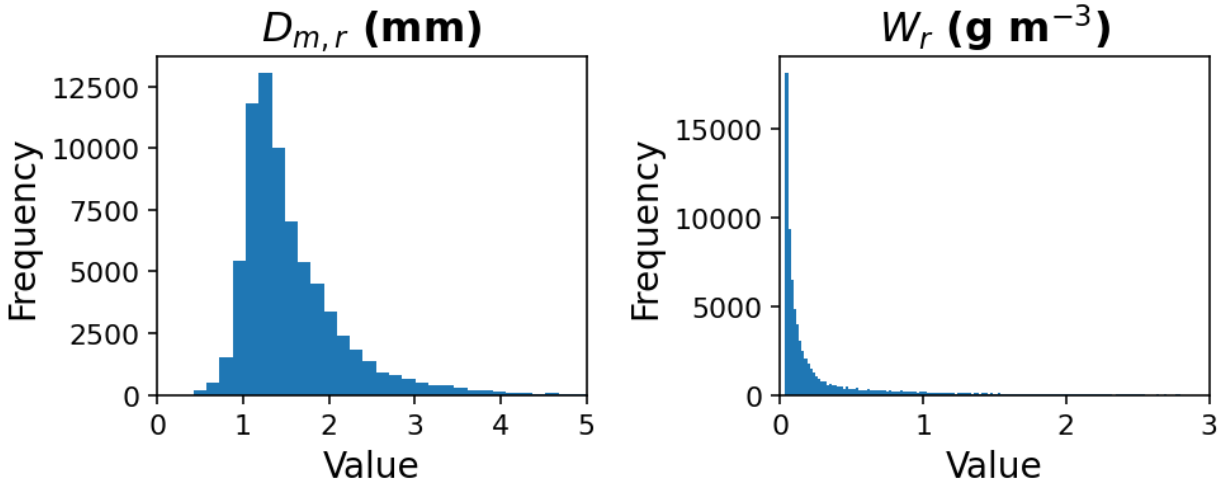

Figure 5.19. Same as Fig. 5.11, except for PINN.

5.4.5 Additional variables and constraints for hail retrievals

In the previous chapters, the usefulness of PINN has been demonstrated. However, as noted in some parts of the analysis fields, noisy artifacts are evident in hail dominated regions when rain operators are used, consistent with the results reported by Mahale et al. (2019). This indicates that appropriate forward operators are required to improve retrieval performance. To address this, a hybrid retrieval method is adopted in which the problem is separated based on the dominant sensitivities of the polarimetric radar variables, rather than retrieving all microphysical parameters simultaneously for both rain and hail. Specifically, backscatter-dominated variables (Z_H, Z_{DR}, and ρ_{hv}) are assumed to be primarily influenced by a relatively small number of large hailstones and are therefore used to constrain the hail component. In contrast, K_{DP}, which arises from the coherent

propagation effects of numerous small hydrometeors along the radar path, is assumed to be dominated by rain and is used to constrain the rain component. Due to the lack of direct microphysical measurements for hail, the retrieval relies on the forward operator for the hail component. In pure rain regions, both the forward operator and rain microphysical parameters derived from 2DVD observations (Ho et al., 2023) are incorporated within the PINN framework.

For hail retrievals, additional hard constraints are imposed to ensure physically realistic solutions. The hail size and melting state are parameterized in terms of $D_{\mathrm{m,h}}$ and γ as derived in Chapter 3. A nonlinear constraint is applied such that $D_{\mathrm{m,h}}$ is bound by a maximum allowable value that depends on γ. Specifically, $D_{\mathrm{m,h}}$ is restricted to lie within the range $\left[0, D_{\mathrm{m,max}}(\gamma)\right]$. This relationship enforces a decrease in allowable $D_{\mathrm{m,h}}$ with increasing γ, thereby preventing unphysical combinations of large, highly melted hailstones. In addition, a hard upper bound is imposed on the bulk W, which is constrained to the range $0 \leq W \leq 5\ \mathrm{g\ m^{-3}}$. This limit is enforced as a hard constraint during retrieval through a bounded transformation and serves to prevent unrealistically large mass loading that could otherwise arise from ill-conditioned inversions of the exponential distribution. Together, these constraints couple the retrieved microphysical variables ($D_{\mathrm{m,h}}$, γ, and W_{h}) and reduce the solution space to physically plausible regimes. Combined with the polarimetric forward operator, they act to regularize the retrieval and improve physical consistency across hail and mixed-phase conditions.

In addition, the impact of including δ is examined. Although δ has not been widely utilized in microphysical retrievals, it provides unique sensitivity to larger hydrometeors, particularly hail in this case. δ is negligible for small drops in the Rayleigh regime and is therefore minimally influenced by rain-dominated contributions. As a result, δ offers complementary information that is more directly related to the presence and size of large, non-Rayleigh scatterers such as hail. In

this study, the utility of δ is evaluated by comparing retrieval performance with and without its inclusion, with particular focus on its role in constraining hail size and γ in mixed-phase regimes.

5.4.6 Hail retrieval results with hail operator as physical constraint

The observed polarimetric radar variables and the corresponding analysis fields, calculated from the retrieved hail microphysical parameters within hail-classified regions, are presented in Fig. 5.20. Overall, the retrieved analysis fields closely reproduce the spatial structure and magnitude of the observed variables. For Z_H, the analysis captures the high-reflectivity hail cores and their spatial gradients with minimal bias. Agreement in Z_{DR} is lacking, especially the enhancement up to ~2dB are not well captured in the analysis. The K_{DP} field is reasonably well reproduced in terms of spatial pattern; however, the difference panel indicates localized discrepancies, particularly in regions of enhanced phase shift, where the analysis tends to underestimate observed values. This behavior is expected, as the contribution of hail parameters to K_{DP} is limited. The agreement in ρ_{hv} further emphasizes the need for appropriate physical constraints, with differences generally confined to small magnitudes, indicating that the retrieval effectively captures hydrometeor diversity and mixing characteristics within hail regions. The δ fields show larger variability in the difference field compared to other variables, with both positive and negative deviations. This is likely due to noisy estimates of δ in the current KDP estimation algorithm, as well as the limitations of the forward operators, especially in representing the negative δ values. Further work is needed to better utilize δ for microphysical retrievals and related applications.

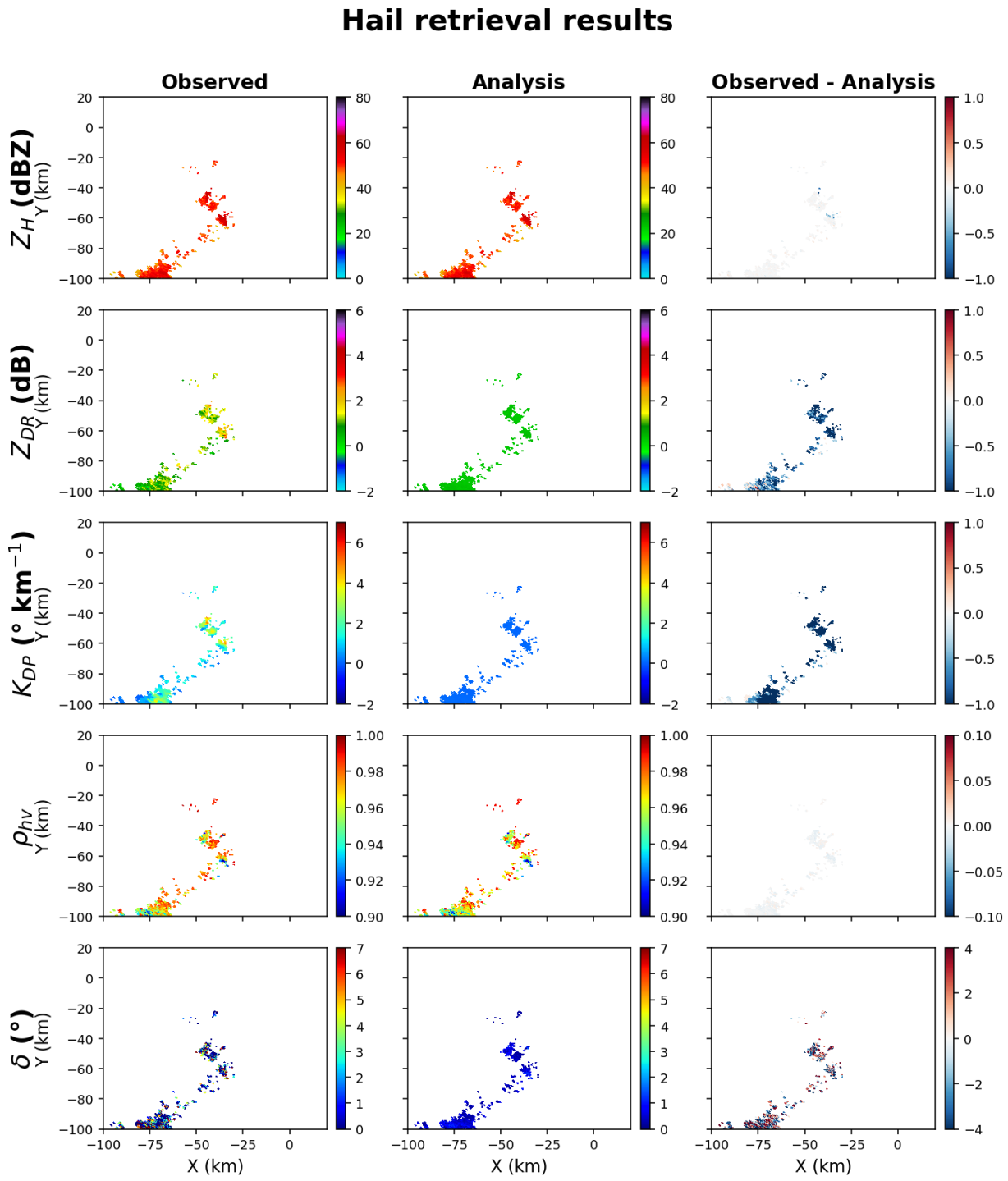

Figure 5.20. Same as Fig. 5.9, except for hail retrievals.

The spatial distributions of the three bulk hail parameters ($D_{m,h}$, W_h, and γ) are shown in Figure 5.21. Larger hail sizes, with $D_{m,h}$ values locally exceeding ~20 mm, are observed, while smaller

values in the range of 10-15 mm dominate the overall structure. This is consistent with ~1 inch hail (i.e., 25 mm) reported from ground reports. The W_h field exhibits a similar pattern, with peak values collocated with the largest hail sizes reaching up to ~ 4 g m^{-3}. The γ values are generally high (> 70–80%), indicating that these regions are dominated by relatively small, melting hailstones, with lower fractions toward the edges suggesting increased sizes.

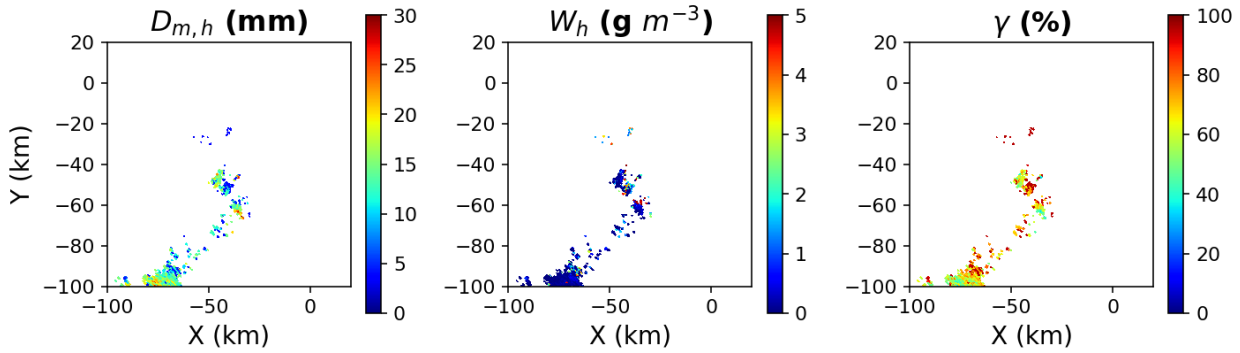

Figure 5.21. Same as Fig. 5.10, except for hail retrievals.

The distributions of hail parameters are depicted in Fig. 5.22. The distribution of $D_{m,h}$ is concentrated at smaller sizes, with a primary peak at ~4–6 mm and a broader secondary peak between ~10–20 mm, indicating a mixture of small and larger hail populations. The W_h distribution is highly skewed toward low values, with most occurrences below ~1 g m^{-3} and a long tail extending to higher values. The γ is concentrated at high values, consistent with the prevalence of smaller hail, with fewer occurrences of mixed-phase conditions at lower fractions (~30%) associated with larger hail sizes. While observational errors exist, these results indicate that PINN produces reasonable retrievals of hail microphysical parameters from PRD.

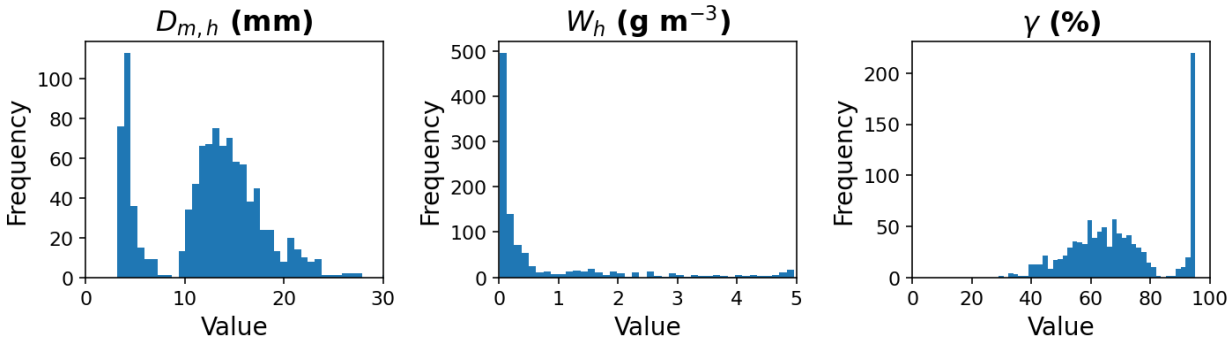

Figure 5.22. Same as Fig. 5.11, except for hail retrievals.

5.4.7 Hail retrieval results with δ inclusion

The impact of including δ in the hail microphysical retrieval was evaluated using a limited dataset of 583 samples. Only positive δ values from the LP-calculations were considered. The distributions of retrieved parameters with and without δ are broadly consistent (Figs. 5.23 and 5.24), indicating that its inclusion does not fundamentally alter the retrieval behavior. However, subtle but systematic differences are evident. The incorporation of δ leads to a slight increase in the retrieved $D_{m,h}$, accompanied by a modest reduction in γ (Fig. 5.24). This suggests a shift toward broader DSDs with relatively larger characteristic diameters. Additionally, a slight reduction in variability is observed in some parameters, particularly in the suppression of extreme values of W_h. While these differences are physically plausible and consistent with the additional microphysical constraint provided by δ, the relatively small sample size limits the statistical robustness of these findings. Further analysis with a larger dataset is required to confirm the significance and generality of these effects.

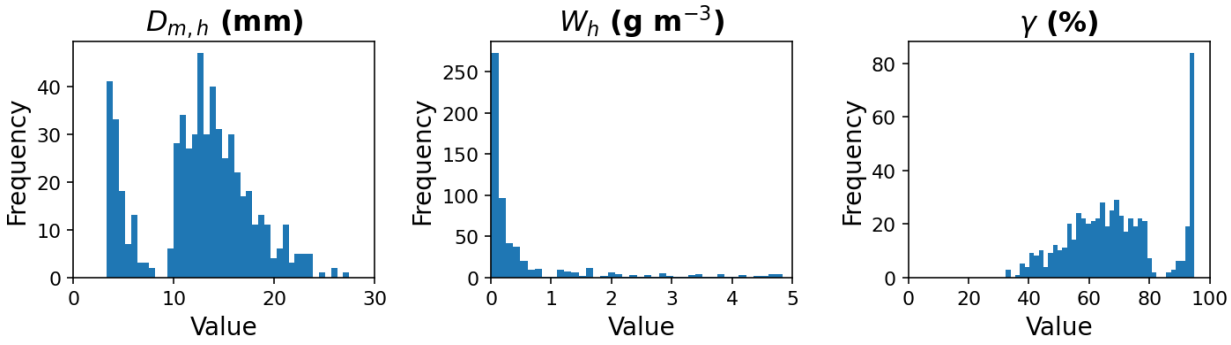

Figure 5.23. The distributions of retrieved hail bulk microphysical parameter $D_{m,h}$, W_h, and γ, without δ.

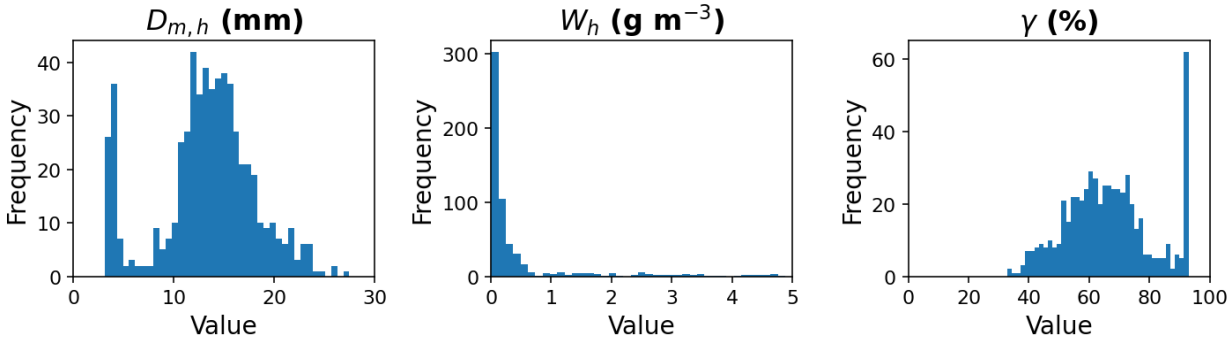

Figure 5.24. Same as Fig. 5.23, except δ incorporated as both an input variable and a physical constraint.

5.5 Additional experiments

Additional sensitivity experiments were conducted to analyze the impact of adaptive weighting between the background and observations by applying on variational retrieval with adaptively adjusted weights between the background error covariance matrix (B) and the observational error covariance matrix (R). Techniques such as the Levenberg–Marquardt method and perturbation-based inflation (Xu, 2023) were implemented to modify these covariances adaptively. These approaches are intended to stabilize the inversion and balance the model assumptions and measurement errors within the physical constraints.

The rain-only variational retrieval of Mahale et al. (2019) is adopted as a reference. This separation reduces the dimensionality of the inversion and helps alleviate ambiguities associated with mixed-phase conditions. Furthermore, the explicit use of B and R enables uncertainties to be systematically accounted for within each subproblem. As illustrated in Fig. 5.25, these adaptive strategies lead to noticeable improvements in the analyzed fields. In particular, the convective region west of the radar exhibits smoother and less noisy convergence compared to retrievals using a static B. Similarly, the analyzed Z_{DR} field shows substantial noise reduction within hail-identified regions, suggesting that tuning the error covariances enhances both consistency and spatial coherence in the retrieved polarimetric variables.

These results reinforce that adaptive covariance tuning improves the numerical behavior of the inversion. However, both variational and PINN approaches can compensate for model–observation mismatch by adjusting state variables in a mathematically optimal yet physically unrealistic manner. While adaptive specification of B and R enhances stability, reduces noise, and improves apparent agreement with observations, accurate retrieval of microphysical parameters—especially in complex regimes such as hail or mixed-phase precipitation—ultimately depends on physically consistent forward models that faithfully represent the underlying scattering processes.

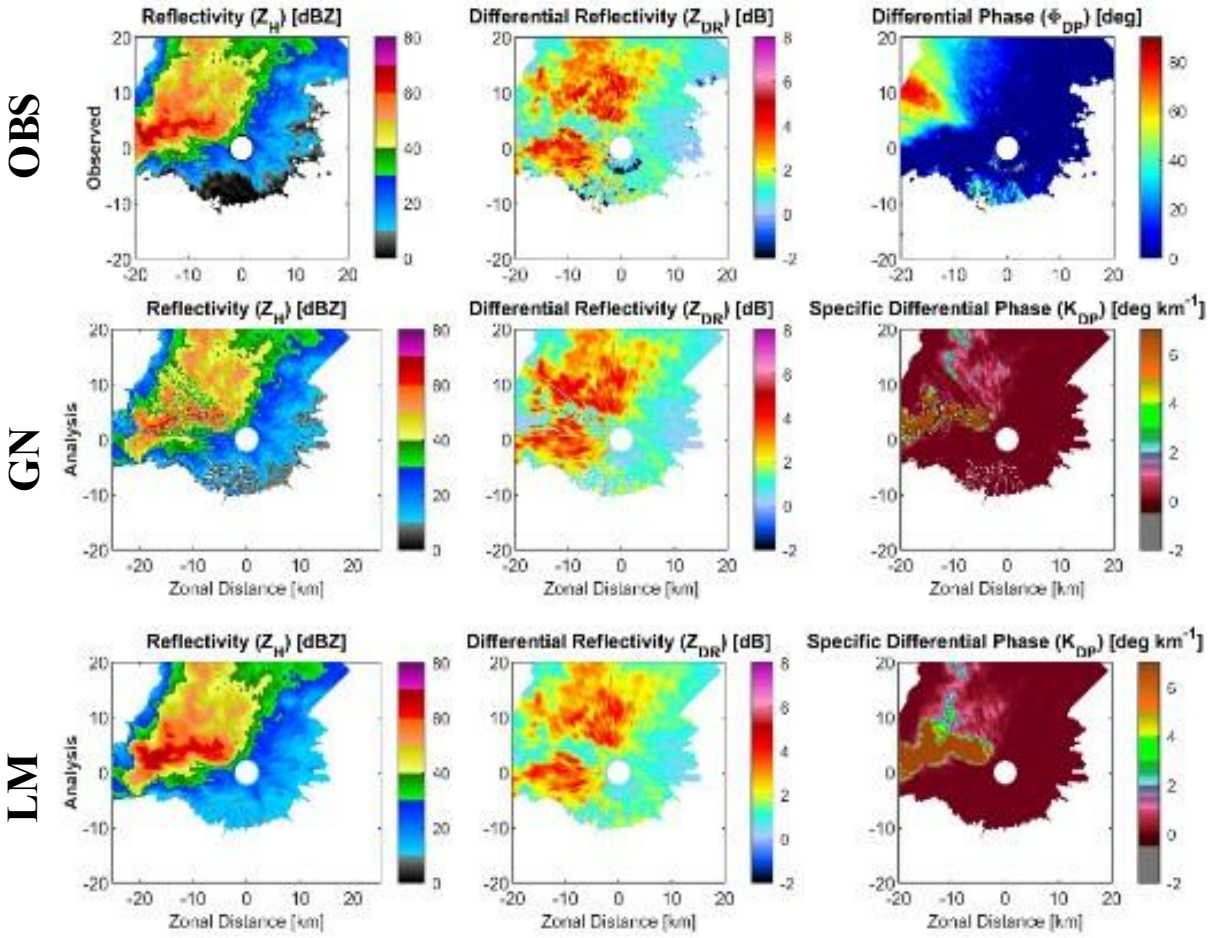

Figure 5.25. The comparison of polarimetric radar fields (Z_H, Z_{DR}, and Φ_{DP} or K_{DP}). Observations are shown in the first row, followed by analysis fields retrieved using the Gauss–Newton iterative method (second row; Mahale et al., 2019) and the newly implemented Levenberg–Marquardt method (third row).

5.6 Summary

This chapter focuses on incorporating polarimetric forward operators as physical constraints and measurement error characterizations as weighting terms (or error covariance matrices) within the PINN framework. These components are used to improve rain microphysical retrievals, with particular emphasis on extending retrieval capability to hail regimes. The WRF simulation data were initially used to evaluate the scope and feasibility of the inclusion of spatial information to

expand the retrievals into mixed-phase, multiple hydrometeor species. Due to the lack of independent information from PRD alone, the retrieval was simplified to rain and hail mixtures. In simulation data absent observational or model errors—the retrieval results were reasonable when both the polarimetric forward operators and the ground-truth microphysics parameters were available.

Subsequently, the developed PINN algorithm was evaluated on a convective case consisting of heavy rain and a few isolated hail cores. Initially, the rain PINN was tested to evaluate if the inclusion of physical constraints could improve accuracy, the generalizability, and flexibility of maintaining stable retrieval outputs in less represented or unseen data. While the inclusion of physical constraints reduced the overall accuracy of retrieval over the 2DVD site, these constraints enabled improved and more physically reasonable retrieval results across the whole domain, as shown by the analysis fields of the retrieved microphysics parameters.

Next, for the hail regions, the physical constraints were updated within the hail operators, by including additional $D_{m,h}$-γ constraints and bounds for W_h, hail retrievals were conducted. The retrieved hail D_m was about 10−15mm, which matches reasonably well with ground reports of 1 inch hail. The rain microphysics parameters over hail regions were substituted with rain retrievals derived solely from K_{DP} and other radar variables, as these radar variables are dominated by the presence of hail.

Additionally, the impact of the error covariance matrices—which serve as important weighting features for both the Variational and PINN approaches—was tested. The results demonstrated that appropriate estimates are necessary, and must be adaptively optimized, not simply based on error metrics from general data, but tailored to specific regions, and ranges of polarimetric measurements. Thus, this study demonstrates that including improved physical constraints and

accurate estimations of the observational and background errors, within an advanced retrieval algorithm, can significantly improve and expand microphysics retrievals.

Chapter 6 Summary, conclusion and future work

6.1 Summary and conclusion

The overarching goal of radar meteorology is to improve severe weather detection and warning, QPE, and ultimately QPF. Although these objectives have long guided the field, achieving substantial progress requires fundamental advances across multiple components of the radar observation and interpretation framework. A central challenge lies in the limited independent information content of polarimetric radar measurements. While four to five polarimetric variables relevant to microphysics are typically available, they often correspond to only two to three independent degrees of information. As a result, microphysical retrieval from radar observations is inherently ill-posed. Without sufficient prior knowledge of the atmospheric state or appropriate physical constraints, this limitation restricts the ability of polarimetric radar to uniquely and accurately infer microphysical properties. In addition, measurement uncertainties and forward operator errors further compound this challenge, introducing ambiguity in both the observation space and the retrieval process.

The primary focus of this dissertation is to improve observation-based microphysical retrievals by addressing these fundamental limitations. The three key components are developed and integrated. First, parameterized polarimetric forward operators are constructed to provide a computationally efficient, differentiable, and physically consistent mapping between microphysical states and radar observables. Second, measurement errors are systematically characterized—particularly for PPAR systems—to better quantify observational uncertainty and inform error covariance structures. Third, a PINN–based retrieval framework is developed,

incorporating both forward operator constraints and measurement error information to improve the stability, consistency, and generalization of microphysical retrievals.

The main objective of Chapter 3 is to develop efficient, representative, and explicitly differentiable polarimetric forward operators that maintain a consistent functional form across multiple frequencies and radar variables while using a limited number of parameters. Polarimetric forward operators serve as a critical link between observation space and model space in DA, and are also essential for model evaluation and microphysical retrieval applications. However, a major challenge lies in the complexity and computational expense of the T-matrix method. As a result, despite long-standing recognition of forward operator limitations as a bottleneck in radar DA and retrieval systems, practical improvements have remained limited (Jung et al., 2010; Posselt et al., 2015; Fabry and Meunier, 2020).

Several parameterization approaches have been proposed to address this issue, but they often involve trade-offs between accuracy and generality. Polynomial-based parameterization performs well, but may struggle to maintain stability and accuracy when extended to multiple radar variables, frequencies, or resonance-sensitive regimes, especially at C- and X-band. This ML-based approach addresses key limitations of existing parameterizations by improving both generality and computational efficiency. Furthermore, to account for uncertainty in the forward operators, three established dielectric mixing formulations—MGW, MGI, and the PS formulations—are incorporated to quantify variability arising from microphysical assumptions.

Chapter 4 focuses on the quantification and characterization of measurement errors, with particular emphasis on factors that degrade the quality of PRD in emerging PAR systems. The analysis specifically examines both cylindrical and planar PAR configurations, where system design and scanning geometry introduce distinct error characteristics. A key focus is the impact of

off-broadside sampling, which is known to degrade polarimetric variable quality due to factors such as reduced polarization purity and beam geometry effects (Zhang et al., 2009, 2011; Ivić, 2023). To quantify these uncertainties, statistical error metrics are derived using temporal variability, with standard deviations estimated from time series of PAR observations. In addition, mean biases are computed relative to observations from the operational KTLX radar, providing a reference baseline for evaluating systematic differences. The results highlight how measurement errors vary as a function of scan angle and system configuration, particularly under far off-broadside conditions. These findings provide critical insight into the structure of observational uncertainties and serve as a foundation for defining error models and covariance estimates in subsequent microphysical retrieval applications.

The microphysical retrieval of rain and hail using polarimetric radar observations, constrained by forward operators and informed by measurement and model uncertainties, is addressed in Chapter 5. This chapter develops a PINN–based retrieval framework in which polarimetric forward operators are incorporated as physical constraints, while measurement and operator errors are represented through weighting terms (or error covariance matrices) to balance observation and physics uncertainties. The proposed PINN framework is first evaluated using WRF simulation data to assess feasibility and the role of spatial information in mixed-phase retrievals. Given the limited independent information content of polarimetric radar data, the problem is simplified to hail regimes. Under idealized conditions without observational or model errors, the PINN framework produces consistent and reasonable retrievals when both forward operators and ground-truth microphysical parameters are available. The PINN is then applied to a NEXRAD measured real convective case with heavy rainfall and localized hail. Results show that incorporating physical constraints along with limited validation points improves the spatial consistency and physical

realism of retrieved fields, despite some reduction in local accuracy at validation points (e.g., 2DVD sites). In hail regions, additional constraints yield reasonable hail size estimates consistent with ground reports.

In conclusion, this dissertation advances polarimetric radar microphysical retrieval through three integrated contributions: ML-based polarimetric forward operators, characterization of measurement errors in PPAR systems, and a PINN-based retrieval framework that incorporates physical constraints and observational uncertainties. Together, these components address key limitations of traditional retrieval approaches by jointly considering forward model representation, observational uncertainty, and inverse problem regularization. This integrated framework provides a computationally tractable and physically consistent pathway toward improved microphysical retrievals, QPE, and QPF, particularly in data-sparse regimes and under complex precipitation conditions.

6.2 Broader impact and future work

The polarimetric forward operators, the quantification of measurement errors and evaluation metrics for emerging PPAR systems, and the flexible PINN framework for microphysical retrievals extend the broader impact of this work in several important ways. First, the ML-based parameterized polarimetric forward operators provide a practical and computationally efficient solution for the DA of PRD. While more sophisticated and potentially more accurate T-matrix based operators exist (e.g., Ryzhkov et al., 2011), they are often computationally prohibitive for operational DA applications. In contrast, the ML-based parameterizations developed in this study retain sufficient physical realism while remaining explicit and efficient enough for use in NWP systems. More broadly, similar ML-based parameterization approaches may be applicable across

many areas in atmospheric science where simplified, accurate, and computationally efficient representations are needed for complex physical parameterization schemes in large-scale NWP models.

Second, the quantification of measurement errors and the comparison of PPAR systems provide insight into how radar performance can be evaluated objectively and consistently. In particular, PPARs can leverage rapidly updating polarimetric observations to assess radar performance. Methods for estimating the STD of PPAR measurements, together with assumptions of local stationarity and the use of dual measurements from both broadside and off-broadside observations through combined mechanical and electronic scanning, may prove valuable for assessing the feasibility of future 2D PPPAR and CPPAR systems in providing high-quality PRD away from the broadside and principal planes. Furthermore, these estimation approaches may also be applicable to 1D PPPAR systems currently under development in other countries, including Japan and China (Kikuchi et al., 2020; Baron et al., 2023).

Lastly, the microphysical retrieval problem itself remains underexplored and continues to be an active area of research. Despite the associated challenges, improved microphysical retrievals are critical for advancing both the physical understanding of severe storms and predictive forecasting capabilities. Retrieved microphysical parameters have strong potential for nowcasting applications, where current PRD-based approaches are often limited to case-specific analyses or simple extrapolation techniques. In addition, these retrievals could be incorporated into DA systems and NWP models to improve forecasts, particularly because many existing systems still rely on simplified relationships based primarily on Z_H alone (e.g., Chen et al., 2021).

This study demonstrates both the flexibility and potential of PINNs for addressing these challenges. Depending on the complexity of the application, the design and structure of physics-

constrained machine learning methods can be adapted accordingly. For relatively simple problems, PINNs can provide computationally efficient and interpretable solutions for applications such as hydrometeor classification or maximum hail size estimation, while preserving the full spatiotemporal resolution of polarimetric radar observations—an increasingly important capability with the development of PPAR systems. Conversely, additional model information and physical constraints can be incorporated to emulate more sophisticated DA frameworks, although this generally comes at the cost of reduced spatiotemporal resolution and the introduction of model-related uncertainties. In this context, observation-based microphysical retrievals—particularly in mixed-phase or mixed-hydrometeor environments—represent an intermediate approach between purely observation-driven estimation methods and computationally expensive full DA systems.

The physical constraints incorporated within the PINN framework are also highly adaptable. The polarimetric forward operator developed in this study was designed to remain broadly compatible with the assumptions commonly used in double-moment microphysics schemes within current DA systems. However, for specific weather regimes, such as large hail events, the assumed exponential particle size distribution may not adequately represent the underlying microphysics. In such cases, alternative formulations, including monodisperse T-matrix lookup tables or gamma particle size distributions with double-moment normalization constrained by in situ observations, may provide more realistic representations of hail processes. Consequently, PINN-based microphysical retrievals offer a promising pathway toward the full utilization of polarimetric radar observations. These retrievals may support downstream applications such as indirect DA and nowcasting, ultimately contributing to improvements in QPE and QPF.

Future work should also focus on more effectively representing both observational and model uncertainties within retrieval frameworks while maintaining computational efficiency. In

particular, improved formulations of error covariance matrices that incorporate not only loss-function residuals, but also flow-dependent characteristics—such as polarimetric signatures and storm regimes (e.g., stratiform versus convective precipitation)—would provide greater insight into the sensitivities and limitations of polarimetric measurements, associated model physics, and retrieval methodologies. Such advancements would enhance the utility of PRD and ultimately contribute to improved forecasting capabilities.

Appendix

The appendix presents the ML-fitted coefficients for the two additional mixing formulas based on the MG mixing formulas at S-band, as well as for all mixing formulas at C- and X-band.

S-band coefficients

		a_{-1}	a_0	a_1	a_2	a_γ
Z_H	t_{z0}	−1.073	−0.1135	1.382	−1.622	0
	t_{z1}	−1.901	1.461	1.222	0.4841	0
	t_{z2}	2.465	−0.9719	−1.105	−0.9353	0
	t_{z3}	0	0	0	0	0
	output	a_{z0}	a_{z1}	a_{z2}	a_{z3}	a_{zc}
		0.007721	0.01019	−0.01432	0	0.01429
Z_{DR}	t_{d0}	2.512	−0.4915	−0.5638	−1.051	0
	t_{d1}	−0.0002887	−0.9053	0.5791	0.2368	0
	t_{d2}	1.165	−0.2119	−0.6556	−0.4094	0
	t_{d3}	0	0	0	0	0
	output	a_{d0}	a_{d1}	a_{d2}	a_{d3}	a_{dc}
		−0.1378	0.1929	−0.1872	0	0.3074
K_{DP}	t_{k0}	0.0734	−1.859	−0.03181	0.7985	0
	t_{k1}	0.1148	1.048	−0.3583	−0.5691	0
	t_{k2}	−2.029	−0.6412	0.6574	0.4374	0
	t_{k3}	0	0	0	0	0
	output	a_{k0}	a_{k1}	a_{k2}	a_{k3}	a_{kc}
		1.128	−0.972	0.9338	0	0.837
ρ_{hv}	$t_{\rho0}$	2.021	−1.987	−1.703	−0.5929	0
	$t_{\rho1}$	−0.02114	−1.366	−0.01945	0.9854	0
	$t_{\rho2}$	−0.2724	1.34	1.69	1.494	0
	$t_{\rho3}$	1.852	−2.129	−1.773	−1.538	0
	output	$a_{\rho0}$	$a_{\rho1}$	$a_{\rho2}$	$a_{\rho3}$	$a_{\rho c}$
		0.003814	0.007953	−0.004586	0.005323	0.9904
A_H	$t_{\delta0}$	−0.07121	0.6506	−1.748	0	0
	$t_{\delta1}$	0.0691	−2.148	1.522	0	0
	$t_{\delta2}$	0.1536	−4.285	2.032	0	0
	$t_{\delta3}$	0.07491	−2.427	1.465	0	0
	output	a_{h0}	a_{h1}	a_{h2}	a_{h3}	a_{hc}
		−0.01057	0.01441	0.02176	0.01514	0.01559
A_{DP}	t_{h0}	−0.003108	2.713	0.8411	−1.778	0
	t_{h1}	1.532	0.5775	−0.8546	−1.127	0
	t_{h2}	0.008651	−2.596	−0.007137	1.141	0
	t_{h3}	0.007218	−1.132	0.7358	0.867	0
	output	a_{p0}	a_{p1}	a_{p2}	a_{p3}	a_{pc}
		−0.007263	−0.002091	0.01387	0.009706	0.008607

Table A1. The coefficients of ML-fitted polarimetric radar variables (Z_H, Z_{DR}, K_{DP}, ρ_{hv}, A_H, and A_{DP}) for rain at S-band.

		c_{-1}	c_0	c_1	c_2	c_γ
Z_H	t_{z0}	14.72	0.7111	2.366	−1.337	−3.087
	t_{z1}	−0.0003420	0.5165	0.04928	0.7412	−0.1190
	t_{z2}	0.03838	−8.098	0.2082	−0.2313	−3.837
	t_{z3}	0	0	0	0	0
	output	a_{z0}	a_{z1}	a_{z2}	a_{z3}	a_{zc}
		−0.1907	−1.159	−1.916	0	0.6479
Z_{DR}	t_{d0}	7.329	−2.305	−0.08455	−0.01214	−2.798
	t_{d1}	0.2768	−6.784	−2.264	−1.671	1.007
	t_{d2}	1.829	−2.851	7.347	−4.376	2.301
	t_{d3}	−0.2925	−0.6474	−0.8034	0.3294	1.046
	output	a_{d0}	a_{d1}	a_{d2}	a_{d3}	a_{dc}
		−0.06915	0.1234	0.04846	0.317	0.04439
K_{DP}	t_{k0}	−0.03760	0.7836	−5.136	6.365	−1.379
	t_{k1}	−1.567	−1.556	3.378	−2.112	−0.1386
	t_{k2}	0.01017	−2.409	0.3130	−2.209	0.3892
	t_{k3}	0	0	0	0	0
	output	a_{k0}	a_{k1}	a_{k2}	a_{k3}	a_{kc}
		−0.5184	2.115	4.873	0	−0.8263
ρ_{hv}	$t_{\rho0}$	0	−6.518	9.003	−4.549	−0.8041
	$t_{\rho1}$	0	−20.18	6.977	−1.154	−7.579
	$t_{\rho2}$	0	−3.082	−1.118	−0.2282	−2.327
	$t_{\rho3}$	0	1.816	−0.1827	1.224	2.245
	output	$a_{\rho0}$	$a_{\rho1}$	$a_{\rho2}$	$a_{\rho3}$	$a_{\rho c}$
		−0.2300	−0.2186	0.2818	0.2762	0.7137
δ	$t_{\delta0}$	−0.03820	3.644	−2.661	1.108	−1.346
	$t_{\delta1}$	−16.29	−5.014	−5.329	2.465	3.436
	$t_{\delta2}$	−15.15	0.7809	−2.231	1.236	4.548
	$t_{\delta3}$	0	0	0	0	0
	output	$a_{\delta0}$	$a_{\delta1}$	$a_{\delta2}$	$a_{\delta3}$	$a_{\delta c}$
		−8.338	2.511	7.185	0	8.531
A_H	t_{h0}	−0.1043	2.533	−1.569	0	0.9678
	t_{h1}	7.68	1.825	−0.4538	0	−1.425
	t_{h2}	−79.07	4.369	−3.226	0	22.07
	t_{h3}	8.739	2.655	0.05879	0	−1.616
	output	a_{h0}	a_{h1}	a_{h2}	a_{h3}	a_{hc}
		0.4588	−1.338	0.05057	0.923	−0.01445
A_{DP}	t_{p0}	0.6301	−1.872	2.6	−5.229	4.904
	t_{p1}	−10.47	0.8872	−7.067	4.471	4.052
	t_{p2}	−3.94	−2.763	2.163	−1.686	1.972
	t_{p3}	−13.91	6.358	−1.5	0.8317	7.247
	output	a_{p0}	a_{p1}	a_{p2}	a_{p3}	a_{pc}
		0.02428	0.1477	0.1603	−0.1324	−0.01581

Table A2. The coefficients of ML-fitted polarimetric radar variables (Z_H, Z_{DR}, K_{DP}, ρ_{hv}, δ, A_H, and A_{DP}) for hail using Maxwell Garnett water as background mixing formula (MGW) at S-band.

		a_{-1}	a_0	a_1	a_2	a_γ
Z_H	t_{z0}	0.001481	−9.959	−0.02351	−0.003868	−4.219
	t_{z1}	23.56	8.553	−2.590	1.638	−4.387
	t_{z2}	0.01704	0.4978	0.1154	−0.5422	0.4856
	t_{z3}	0	0	0	0	0
	output	a_{z0}	a_{z1}	a_{z2}	a_{z3}	a_{zc}
		−9.186	−0.1658	0.6027	0	−0.2972
Z_{DR}	t_{d0}	−0.9004	1.296	−6.827	4.188	−1.900
	t_{d1}	−0.001465	−0.08129	−0.03104	−0.01283	−0.5308
	t_{d2}	0.07062	−0.7440	0.9012	−1.110	1.808
	t_{d3}	−0.7376	0.5600	−7.135	4.324	−2.444
	output	a_{d0}	a_{d1}	a_{d2}	a_{d3}	a_{dc}
		0.1653	−0.4987	0.1052	−0.1683	0.3604
K_{DP}	t_{k0}	0.1210	−2.873	−0.6252	−1.235	1.222
	t_{k1}	−0.1520	−0.2491	0.8679	−1.750	1.432
	t_{k2}	0.1578	−0.2576	3.385	−1.906	1.746
	t_{k3}	0	0	0	0	0
	output	a_{k0}	a_{k1}	a_{k2}	a_{k3}	a_{kc}
		0.9176	0.8223	0.7973	0	−0.1402
ρ_{hv}	$t_{\rho0}$	−0.05077	−0.4999	0.08968	0	−2.227
	$t_{\rho1}$	0.05731	−2.224	1.651	0	2.605
	$t_{\rho2}$	−16.80	−3.714	2.512	0	5.445
	$t_{\rho3}$	−0.07535	−1.181	−0.2383	0	−1.956
	output	$a_{\rho0}$	$a_{\rho1}$	$a_{\rho2}$	$a_{\rho3}$	$a_{\rho c}$
		−0.2189	0.04084	−0.03014	0.2430	0.9841
δ	$t_{\delta0}$	16.83	7.307	3.120	−2.869	−1.387
	$t_{\delta1}$	8.795	4.098	1.485	−1.702	−1.323
	$t_{\delta2}$	−10.84	−3.948	1.452	−0.7399	2.564
	$t_{\delta3}$	0	0	0	0	0
	output	$a_{\delta0}$	$a_{\delta1}$	$a_{\delta2}$	$a_{\delta3}$	$a_{\delta c}$
		−16.84	24.67	18.39	0	−7.473
A_{hh}	t_{h0}	0.2788	0.5863	−1.117	0	0.3692
	t_{h1}	1.04	−2.497	0.7692	0	−1.272
	t_{h2}	−7.609	−4.23	1.261	0	1.948
	t_{h3}	0.8477	−4.768	−1.01	0	−1.055
	output	a_{h0}	a_{h1}	a_{h2}	a_{h3}	a_{hc}
		−0.1998	−0.3423	0.3592	0.3713	0.2025
A_{DP}	t_{p0}	0	−8.901	9.584	−3.822	2.627
	t_{p1}	0	3.339	−14.01	10.39	−4.042
	t_{p2}	0	−0.5379	0.8692	−2.177	0.4938
	t_{p3}	0	8.098	−16.07	8.324	−5.155
	output	a_{p0}	a_{p1}	a_{p2}	a_{p3}	a_{pc}
		0.08881	−0.05554	0.06347	−0.0554	0.07033

Table A3. Same as Table A2, except for graupel.

		a_{-1}	a_0	a_1	a_2	a_γ
Z_H	t_{z0}	0.1314	2.291	3.173	−2.777	1.684
	t_{z1}	−0.04907	−1.900	−1.300	1.217	−1.225
	t_{z2}	0.03649	8.983	−0.2517	0.2307	4.672
	t_{z3}	0	0	0	0	0
	output	a_{z0}	a_{z1}	a_{z2}	a_{z3}	a_{zc}

		−1.203	−2.973	3.020	0	−1.663
Z_{DR}	t_{d0}	−2.187	−2.868	1.463	−0.2928	3.012
	t_{d1}	−0.5491	−1.934	4.617	−1.799	2.472
	t_{d2}	−1.334	−1.912	3.156	−1.243	2.662
	t_{d3}	0.001830	−2.337	−0.06491	−0.3489	−1.856
	output	a_{d0}	a_{d1}	a_{d2}	a_{d3}	a_{dc}
		−0.2533	−0.1828	0.4359	−0.2416	0.1984
K_{DP}	t_{k0}	−0.1606	3.193	−2.470	0.4696	−1.168
	t_{k1}	0.008208	−0.9311	0.01424	0.06141	−2.415
	t_{k2}	−0.07482	0.5557	−3.048	0.8061	−2.681
	t_{k3}	0	0	0	0	0
	output	a_{k0}	a_{k1}	a_{k2}	a_{k3}	a_{kc}
		0.7025	−1.047	−0.2730	0	0.5670
ρ_{hv}	$t_{\rho0}$	0	−4.186	5.030	−3.274	3.868
	$t_{\rho1}$	0	−2.714	6.232	−2.684	4.532
	$t_{\rho2}$	0	−0.1581	−1.433	2.791	−3.082
	$t_{\rho3}$	0	0.02194	7.961	−3.721	3.321
	output	$a_{\rho0}$	$a_{\rho1}$	$a_{\rho2}$	$a_{\rho3}$	$a_{\rho c}$
		0.06313	−0.05714	0.01664	−0.01567	0.9829
δ	$t_{\delta0}$	8.059	5.149	−3.065	1.348	−4.645
	$t_{\delta1}$	−7.709	−3.608	−1.221	0.5817	1.866
	$t_{\delta2}$	−8.632	−4.622	−1.623	0.7520	2.557
	$t_{\delta3}$	0	0	0	0	0
	output	$a_{\delta0}$	$a_{\delta1}$	$a_{\delta2}$	$a_{\delta3}$	$a_{\delta c}$
		−13.69	19.62	−26.90	0	14.11
A_H	t_{h0}	−6.978	−5.297	1.414	0	2.808
	t_{h1}	0.1277	1.194	1.065	0	−1.829
	t_{h2}	−0.04698	2.424	−0.2856	0	1.295
	t_{h3}	23.41	11.57	0.752	0	−0.1234
	output	a_{h0}	a_{h1}	a_{h2}	a_{h3}	a_{hc}
		0.334	0.1068	0.2932	−0.5145	0.231
A_{DP}	t_{p0}	0	0.6838	0.2675	0.6366	−1.342
	t_{p1}	0	6.975	−6.934	1.736	−3.552
	t_{p2}	0	2.953	−5.823	2.808	−3.043
	t_{p3}	0	1.083	−0.3486	−0.03824	1.766
	output	a_{p0}	a_{p1}	a_{p2}	a_{p3}	a_{pc}
		0.05568	−0.01246	−0.04504	0.05967	−0.003888

Table A4. Same as Table A2, except for snow.

		a_{-1}	a_0	a_1	a_2	a_γ
Z_H	t_{z0}	0.2477	−5.420	6.352	−4.109	3.467
	t_{z1}	0.01378	−0.3920	0.1421	0.5022	−0.5715
	t_{z2}	−8.763	−2.383	−1.598	2.054	2.501
	t_{z3}	0	0	0	0	0
	output	a_{z0}	a_{z1}	a_{z2}	a_{z3}	a_{zc}
		−0.3077	−1.147	0.2820	0	0.1777
Z_{DR}	t_{d0}	7.733	−0.7882	−0.9181	−0.6930	−3.868
	t_{d1}	−0.1266	−1.283	0.8525	−2.086	1.889
	t_{d2}	−1.023	1.175	5.226	−5.609	1.139
	t_{d3}	−0.005021	−2.316	−1.243	1.150	0.5824

	output	a_{d0}	a_{d1}	a_{d2}	a_{d3}	a_{dc}
		−0.06725	0.1078	0.05854	0.7285	0.03203
K_{DP}	t_{k0}	0.09325	0.6652	3.066	−1.674	1.616
	t_{k1}	−0.01247	−1.341	−0.3037	−0.6067	0.1653
	t_{k2}	−1.992	−2.861	0.6924	−0.2363	−1.001
	t_{k3}	0	0	0	0	0
	output	a_{k0}	a_{k1}	a_{k2}	a_{k3}	a_{kc}
		1.647	5.914	2.633	0	−2.343
ρ_{hv}	$t_{\rho0}$	−0.4120	−4.986	2.187	−0.4946	−0.8524
	$t_{\rho1}$	8.273	−0.3446	−1.952	−0.01868	−3.576
	$t_{\rho2}$	−7.367	−3.318	−2.748	3.732	3.715
	$t_{\rho3}$	−4.815	−7.526	−1.167	0.7068	5.195
	output	$a_{\rho0}$	$a_{\rho1}$	$a_{\rho2}$	$a_{\rho3}$	$a_{\rho c}$
		−0.8614	0.1571	0.08104	0.09215	0.8293
δ	$t_{\delta0}$	26.50	5.173	2.768	−1.148	−6.644
	$t_{\delta1}$	−17.19	−6.126	5.476	−4.016	13.09
	$t_{\delta2}$	59.81	13.35	13.61	−7.992	−4.059
	$t_{\delta3}$	0	0	0	0	0
	output	$a_{\delta0}$	$a_{\delta1}$	$a_{\delta2}$	$a_{\delta3}$	$a_{\delta c}$
		−9.604	6.666	−4.051	0	13.88
A_H	t_{h0}	1.893	2.374	−2.534	0	−3.613
	t_{h1}	119.4	25.85	9.835	0	9.805
	t_{h2}	0.7472	3.217	−0.9619	0	0.2556
	t_{h3}	5.369	1.563	−1.925	0	−1.722
	output	a_{h0}	a_{h1}	a_{h2}	a_{h3}	a_{hc}
		−0.1984	−0.04032	0.7294	−0.344	−0.1391
A_{DP}	t_{p0}	0	2.725	−8.52	8.095	−3.116
	t_{p1}	0	2.347	−8.012	4.925	−3.404
	t_{p2}	0	−0.424	0.1438	−2.724	0.08503
	t_{p3}	0	−4.881	7.862	−4.221	2.512
	output	a_{p0}	a_{p1}	a_{p2}	a_{p3}	a_{pc}
		−0.05299	−0.09689	0.06275	0.08645	0.09212

Table A5. Same as Table A2, except for hail using Maxwell Garnett mixing formula with ice as the background (MGI).

		a_{-1}	a_0	a_1	a_2	a_γ
Z_H	t_{z0}	1.969	12.85	−6.792	3.314	−9.082
	t_{z1}	−0.02386	0.4358	0.2469	−0.09572	0.8608
	t_{z2}	0.3084	0.8933	−0.6076	−0.1360	−0.01861
	t_{z3}	0	0	0	0	0
	output	a_{z0}	a_{z1}	a_{z2}	a_{z3}	a_{zc}
		−0.2490	1.033	0.5041	0	−1.019
Z_{DR}	t_{d0}	−0.2451	5.097	−5.798	6.328	−4.983
	t_{d1}	−0.03651	−3.948	−0.5162	−1.152	0.9533
	t_{d2}	0.07146	−0.03650	1.244	−0.5895	1.951
	t_{d3}	−0.3217	6.689	−7.478	3.845	−6.896
	output	a_{d0}	a_{d1}	a_{d2}	a_{d3}	a_{dc}
		−0.03317	0.2582	0.1924	−0.08882	0.1282
K_{DP}	t_{k0}	−0.01165	1.705	−0.1046	0.06120	−1.840
	t_{k1}	−0.1423	6.877	−1.636	0.7571	−4.697
	t_{k2}	−0.1830	8.530	−1.439	0.1043	−5.105

	t_{k3}	0	0	0	0	0
	output	a_{k0}	a_{k1}	a_{k2}	a_{k3}	a_{kc}
		−1.718	−1.897	2.209	0	1.406
ρ_{hv}	$t_{\rho 0}$	5.448	11.46	−0.5069	0.6232	−7.835
	$t_{\rho 1}$	−1.039	−3.144	0.2676	0.5708	0.7921
	$t_{\rho 2}$	3.870	8.240	0.6461	−0.7132	−4.943
	$t_{\rho 3}$	−3.543	−12.14	9.444	−5.344	9.525
	output	$a_{\rho 0}$	$a_{\rho 1}$	$a_{\rho 2}$	$a_{\rho 3}$	$a_{\rho c}$
		0.2298	−0.2058	−0.4935	−0.1107	1.259
δ	$t_{\delta 0}$	7.542	7.893	−3.279	1.273	−4.209
	$t_{\delta 1}$	12.58	27.42	0.2794	0.07239	−14.99
	$t_{\delta 2}$	−7.049	−15.86	5.767	−2.684	11.06
	$t_{\delta 3}$	0	0	0	0	0
	output	$a_{\delta 0}$	$a_{\delta 1}$	$a_{\delta 2}$	$a_{\delta 3}$	$a_{\delta c}$
		−14.86	24.83	18.38	0	−9.861
A_H	t_{h0}	7.106	10.45	−1.068	0	−5.63
	t_{h1}	−5.208	−19.29	1.086	0	11.35
	t_{h2}	7.158	9.51	0.1395	0	−4.331
	t_{h3}	1.083	3.416	−1.33	0	−1.862
	output	a_{h0}	a_{h1}	a_{h2}	a_{h3}	a_{hc}
		−0.4062	0.3326	0.6711	−0.1967	−0.06544
A_{DP}	t_{p0}	−14.98	5.713	−3.192	8.213	−14.98
	t_{p1}	1.103	−0.1607	0.4336	−0.1742	1.103
	t_{p2}	−17.22	4.981	−2.877	10.76	−17.22
	t_{p3}	−6.135	3.967	−1.826	2.901	−6.135
	output	a_{p0}	a_{p1}	a_{p2}	a_{p3}	a_{pc}
		−0.2067	−0.02533	0.1224	0.2736	0.01857

Table A6. Same as Table A2, except for graupel using MGI.

		a_{-1}	a_0	a_1	a_2	a_γ
Z_H	t_{z0}	−0.7621	25.88	−8.422	4.102	−17.73
	t_{z1}	0.04349	0.8735	−0.4231	−0.4724	0.1538
	t_{z2}	−0.004853	0.3972	0.01577	0.01781	1.215
	t_{z3}	0	0	0	0	0
	output	a_{z0}	a_{z1}	a_{z2}	a_{z3}	a_{zc}
		−0.2170	0.3275	1.738	0	−1.663
Z_{DR}	t_{d0}	−0.3420	−2.457	0.1770	−2.255	1.324
	t_{d1}	0.1583	−1.338	0.6936	0.3917	3.628
	t_{d2}	−0.5387	11.22	−5.620	2.129	−10.32
	t_{d3}	−0.03549	−1.431	−0.05560	−1.417	−1.263
	output	a_{d0}	a_{d1}	a_{d2}	a_{d3}	a_{dc}
		0.02771	0.08166	−0.04951	−0.07893	0.1309
K_{DP}	t_{k0}	0.2231	−2.601	3.091	−3.865	2.285
	t_{k1}	−0.1121	−5.723	−1.014	−1.509	2.042
	t_{k2}	−0.2015	4.838	−3.134	1.486	−3.989
	t_{k3}	0	0	0	0	0
	output	a_{k0}	a_{k1}	a_{k2}	a_{k3}	a_{kc}
		0.3974	0.9118	−0.7191	0	0.7204
ρ_{hv}	$t_{\rho 0}$	−1.753	−5.242	−0.4363	1.051	1.849
	$t_{\rho 1}$	5.461	12.91	2.117	−1.913	−7.128

	$t_{\rho 2}$	0.8147	−46.47	−1.362	0.5362	33.98
	$t_{\rho 3}$	3.364	17.19	−4.640	2.755	−11.82
	output	$a_{\rho 0}$	$a_{\rho 1}$	$a_{\rho 2}$	$a_{\rho 3}$	$a_{\rho c}$
		−0.3535	−0.4214	−0.01893	0.1943	1.225
δ	$t_{\delta 0}$	−1.280	−9.823	3.537	−1.099	6.861
	$t_{\delta 1}$	−3.384	−27.98	6.299	−2.661	19.17
	$t_{\delta 2}$	5.661	18.08	0.9891	−0.4176	−9.478
	$t_{\delta 3}$	0	0	0	0	0
	output	$a_{\delta 0}$	$a_{\delta 1}$	$a_{\delta 2}$	$a_{\delta 3}$	$a_{\delta c}$
		10.07	15.48	54.48	0	−54.46
A_H	t_{h0}	−2.147	−12.32	−1.017	0	5.805
	t_{h1}	5.249	7.448	−0.9825	0	−3.17
	t_{h2}	−8.045	−19.1	0.7549	0	10.43
	t_{h3}	2.219	12.14	0.1614	0	−7.201
	output	a_{h0}	a_{h1}	a_{h2}	a_{h3}	a_{hc}
		1.865	−0.3045	0.4855	0.5757	−0.2697
A_{DP}	t_{p0}	0	−21.8	3.554	−0.6734	15.84
	t_{p1}	0	−6.738	−1.702	3.062	3.458
	t_{p2}	0	−17.41	3.163	−0.7356	12.25
	t_{p3}	0	−7.227	10.52	−6.534	3.256
	output	a_{p0}	a_{p1}	a_{p2}	a_{p3}	a_{pc}
		−0.06848	0.02779	0.112	0.0194	0.0001834

Table A7. Same as Table A2, except for snow using MGI.

C-band coefficients

		a_{-1}	a_0	a_1	a_2	a_γ
Z_H	t_{z0}	3.235	2.562	−4.434	1.475	0
	t_{z1}	0.1012	1.026	1.639	−2.569	0
	t_{z2}	−9.098	−2.463	2.545	−0.9853	0
	t_{z3}	0	0	0	0	0
	output	a_{z0}	a_{z1}	a_{z2}	a_{z3}	a_{zc}
		−0.1001	−0.07844	0.08443	0	0.1668
Z_{DR}	t_{d0}	1.512	−0.1586	−0.5136	−0.2452	0
	t_{d1}	−2.804	0.466	2.508	0.3974	0
	t_{d2}	0.2559	−0.3883	−1.181	−1.048	0
	t_{d3}	0	0	0	0	0
	output	a_{d0}	a_{d1}	a_{d2}	a_{d3}	a_{dc}
		−0.1836	0.2263	−0.1496	0	0.332
K_{DP}	t_{k0}	1.574	−0.1103	−1.41	−0.1625	0
	t_{k1}	0.03049	−1.246	0.3725	0.4116	0
	t_{k2}	−0.04068	−0.535	1.147	0.2914	0
	t_{k3}	0	0	0	0	0
	output	a_{k0}	a_{k1}	a_{k2}	a_{k3}	a_{kc}
		−1.5	1.266	0.7894	0	1.355
ρ_{hv}	$t_{\rho 0}$	0.9991	0.7667	−1.544	−1.302	0
	$t_{\rho 1}$	5.328	3.334	−3.117	3.386	0
	$t_{\rho 2}$	−2.76	−1.262	0.5456	−2.597	0
	$t_{\rho 3}$	−4.121	1.178	2.503	1.191	0
	output	$a_{\rho 0}$	$a_{\rho 1}$	$a_{\rho 2}$	$a_{\rho 3}$	$a_{\rho c}$
		−0.02548	0.0396	−0.002323	−0.0393	0.9859

A_H	$t_{\delta 0}$	−0.392	3.998	−2.5	0	0
	$t_{\delta 1}$	−0.0833	−1.201	2.174	0	0
	$t_{\delta 2}$	2.831	0.7369	−2.46	0	0
	$t_{\delta 3}$	0.07375	−2.189	1.641	0	0
	output	a_{h0}	a_{h1}	a_{h2}	a_{h3}	a_{hc}
		−0.226	0.2787	−0.06518	0.3021	0.309
A_{DP}	t_{h0}	0.116	0.268	0.8614	−0.8763	0
	t_{h1}	−0.5751	−1.271	1.008	1.294	0
	t_{h2}	−1.396	−0.6583	3.572	−0.9009	0
	t_{h3}	−0.2842	2.625	−0.02172	−1.77	0
	output	a_{p0}	a_{p1}	a_{p2}	a_{p3}	a_{pc}
		−0.02195	0.08626	0.06042	−0.0788	0.08954

Table A8. The coefficients of ML-fitted polarimetric radar variables (Z_H, Z_{DR}, K_{DP}, ρ_{hv}, A_H, and A_{DP}) for rain at C-band.

		a_{-1}	a_0	a_1	a_2	a_γ
Z_H	t_{z0}	−0.1383	0.2691	−1.204	0.098	1.043
	t_{z1}	10.53	4.210	0.8049	−0.518	−0.3794
	t_{z2}	0.3589	10.04	0.1357	−1.182	7.775
	t_{z3}	0	0	0	0	0
	output	a_{z0}	a_{z1}	a_{z2}	a_{z3}	a_{zc}
		0.6685	1.175	0.2066	0	−1.913
Z_{DR}	t_{d0}	−1.345	5.689	4.156	−1.840	1.571
	t_{d1}	0.1214	−2.18	0.8598	−1.756	1.299
	t_{d2}	0.02296	−0.318	−0.5148	0.9107	−1.318
	t_{d3}	−1.318	8.081	2.904	3.508	0.06051
	output	a_{d0}	a_{d1}	a_{d2}	a_{d3}	a_{dc}
		0.08962	0.2394	−0.1452	−0.0711	0.1433
K_{DP}	t_{k0}	−0.4013	−3.378	2.725	−7.087	1.668
	t_{k1}	4.876	2.375	0.09296	−0.01665	−1.301
	t_{k2}	−0.09144	7.811	−1.238	7.79	−1.326
	t_{k3}	0	0	0	0	0
	output	a_{k0}	a_{k1}	a_{k2}	a_{k3}	a_{kc}
		0.9198	1.56	−3.232	0	1.677
ρ_{hv}	$t_{\rho 0}$	0	2.249	−2.222	1.457	0.8306
	$t_{\rho 1}$	0	−16.63	8.862	−5.619	−8.879
	$t_{\rho 2}$	0	5.854	−6.793	2.967	−0.8105
	$t_{\rho 3}$	0	−7.8	4.654	−1.432	−1.278
	output	$a_{\rho 0}$	$a_{\rho 1}$	$a_{\rho 2}$	$a_{\rho 3}$	$a_{\rho c}$
		0.4507	−0.5716	0.3668	−0.9824	0.1706
δ	$t_{\delta 0}$	−1.154	2.121	−9.28	6.465	−1.501
	$t_{\delta 1}$	11.44	−6.961	0.1397	0.9847	−8.24
	$t_{\delta 2}$	−2.793	−1.496	0.1155	−1.332	1.195
	$t_{\delta 3}$	0	0	0	0	0
	output	$a_{\delta 0}$	$a_{\delta 1}$	$a_{\delta 2}$	$a_{\delta 3}$	$a_{\delta c}$
		−4.537	−3.581	9.168	0	8.088
A_H	t_{h0}	0	13.70	0.062	0	7.59
	t_{h1}	0	0.8674	1.404	0	−0.2197
	t_{h2}	0	3.251	2.819	0	1.103
	t_{h3}	0	−2.706	−1.303	0	0.5152
	output	a_{h0}	a_{h1}	a_{h2}	a_{h3}	a_{hc}

		0.847	−2.223	1.395	−2.735	0.3422
A_{DP}	t_{p0}	−0.08899	−3.304	1.838	−2.552	−1.492
	t_{p1}	−3.850	−1.168	1.115	−0.3871	−0.4544
	t_{p2}	−0.9767	0.8821	3.146	−1.651	0.7667
	t_{p3}	−0.1472	−8.175	1.441	−2.082	−3.236
	output	a_{p0}	a_{p1}	a_{p2}	a_{p3}	a_{pc}
		−0.9159	−0.6387	0.5433	4.522	0.02811

Table A9. The coefficients of ML-fitted polarimetric radar variables (Z_H, Z_{DR}, K_{DP}, ρ_{hv}, δ, A_H, and A_{DP}) for hail using MGW at C-band.

		a_{-1}	a_0	a_1	a_2	a_γ
Z_H	t_{z0}	−0.2213	−0.3155	−4.812	3.36	−1.702
	t_{z1}	0.03246	7.169	0.4518	−0.2383	3.471
	t_{z2}	3.95	1.95	−1.033	−0.003584	0.2257
	t_{z3}	0	0	0	0	0
	output	a_{z0}	a_{z1}	a_{z2}	a_{z3}	a_{zc}
		−0.3051	2.133	0.8198	0	−2.702
Z_{DR}	t_{d0}	3.132	−1.191	−3.679	2.365	−2.243
	t_{d1}	−0.04074	−1.092	0.07431	−0.2678	1.356
	t_{d2}	0.8756	−1.015	−3.321	1.516	−0.9345
	t_{d3}	−0.05054	−1.837	−0.9523	0.4011	−1.128
	output	a_{d0}	a_{d1}	a_{d2}	a_{d3}	a_{dc}
		−0.1041	0.2777	0.1134	−0.1688	0.113
K_{DP}	t_{k0}	−0.01015	−0.6399	−1.368	0.1128	−1.014
	t_{k1}	−4.358	−2.357	1.447	−0.472	0.6407
	t_{k2}	−0.03049	1.533	−0.05061	1.227	−1.21
	t_{k3}	0	0	0	0	0
	output	a_{k0}	a_{k1}	a_{k2}	a_{k3}	a_{kc}
		−2.75	−3.343	−2.673	0	5.014
ρ_{hv}	$t_{\rho0}$	0	−0.9247	0.8037	−1.427	−1.814
	$t_{\rho1}$	0	12.5	−3.082	−1.582	3.472
	$t_{\rho2}$	0	2.215	−0.2819	1.426	1.893
	$t_{\rho3}$	0	5.857	−6.774	3.056	0.512
	output	$a_{\rho0}$	$a_{\rho1}$	$a_{\rho2}$	$a_{\rho3}$	$a_{\rho c}$
		−0.2489	0.131	−0.2546	0.2401	0.8834
δ	$t_{\delta0}$	14.98	1.344	3.354	−2.077	−3.97
	$t_{\delta1}$	19.37	5.136	1.947	−0.5634	−3.227
	$t_{\delta2}$	21.17	9.39	1.597	−0.6634	−1.319
	$t_{\delta3}$	0	0	0	0	0
	output	$a_{\delta0}$	$a_{\delta1}$	$a_{\delta2}$	$a_{\delta3}$	$a_{\delta c}$
		−4.758	−4.857	−6.66	0	16.7
A_H	t_{h0}	0	5.449	−0.7732	0	2.051
	t_{h1}	0	1.661	−2.717	0	0.252
	t_{h2}	0	2.649	0.9352	0	−1.264
	t_{h3}	0	−0.4286	−2.06	0	−1.167
	output	a_{h0}	a_{h1}	a_{h2}	a_{h3}	a_{hc}
		2.137	0.3971	0.5588	−1.118	−1.827
A_{DP}	t_{p0}	0.1326	−3.445	1.902	−1.425	−1.519
	t_{p1}	−1.638	−9.6	3.222	−10.09	2.342
	t_{p2}	−1.673	−1.651	2.401	−1.985	1.562
	t_{p3}	0.1484	−5.749	2.197	−1.679	−3.105

	output	a_{p0}	a_{p1}	a_{p2}	a_{p3}	a_{pc}
		−2.023	−0.1266	0.3708	1.508	0.02905

Table A10. Same as Table A9, except for graupel using MGW.

		a_{-1}	a_0	a_1	a_2	a_γ
Z_H	t_{z0}	0.007744	−1.585	1.023	−0.7262	−2.204
	t_{z1}	0.01256	−2.111	0.4169	−0.8281	0.1196
	t_{z2}	0.005464	−8.765	0.1042	−0.08951	−3.898
	t_{z3}	0	0	0	0	0
	output	a_{z0}	a_{z1}	a_{z2}	a_{z3}	a_{zc}
		−0.6042	4.087	−8.348	0	−0.6156
Z_{DR}	t_{d0}	2.247	2.739	5.329	−2.142	7.751
	t_{d1}	2.719	−1.42	−0.1385	−2.1	−0.9967
	t_{d2}	−0.3524	3.523	−0.4017	0.2236	3.878
	t_{d3}	−6.084	−2.717	0.3569	0.128	1.594
	output	a_{d0}	a_{d1}	a_{d2}	a_{d3}	a_{dc}
		0.04765	−0.1181	0.1265	−0.1259	0.1343
K_{DP}	t_{k0}	−0.115	−1.788	−0.8112	−0.3111	−2.214
	t_{k1}	−0.4338	1.071	−3.161	1.302	0.035
	t_{k2}	−0.7303	4.608	−5.189	3.222	2
	t_{k3}	0	0	0	0	0
	output	a_{k0}	a_{k1}	a_{k2}	a_{k3}	a_{kc}
		−2.411	3.433	−2.538	0	1.483
ρ_{hv}	$t_{\rho0}$	0	2.272	0.4383	−0.352	−0.4351
	$t_{\rho1}$	0	6.567	−5.408	1.879	1.08
	$t_{\rho2}$	0	2.064	1.15	−0.01633	3.567
	$t_{\rho3}$	0	1.775	1.755	−1.12	3.79
	output	$a_{\rho0}$	$a_{\rho1}$	$a_{\rho2}$	$a_{\rho3}$	$a_{\rho c}$
		−0.2435	0.3097	−0.4115	0.3583	0.9185
δ	$t_{\delta0}$	0.01408	−0.7865	1.072	−0.8535	−1.438
	$t_{\delta1}$	12.66	3.921	−0.9244	0.6361	−5.396
	$t_{\delta2}$	0.04705	0.2457	1.639	−1.069	−1.445
	$t_{\delta3}$	0	0	0	0	0
	output	$a_{\delta0}$	$a_{\delta1}$	$a_{\delta2}$	$a_{\delta3}$	$a_{\delta c}$
		−28.96	−5.771	25.93	0	5.565
A_H	t_{h0}	0	−1.222	0.1411	0	1.267
	t_{h1}	0	−1.558	−2.69	0	−0.5041
	t_{h2}	0	0.9	−2.07	0	−2.366
	t_{h3}	0	1.667	−0.9254	0	1.249
	output	a_{h0}	a_{h1}	a_{h2}	a_{h3}	a_{hc}
		−1.012	−0.5144	−0.7463	1.11	0.5061
A_{DP}	t_{p0}	−0.004153	1.604	−0.6605	0.1596	2.76
	t_{p1}	18.32	7.349	−0.7055	2.266	−1.426
	t_{p2}	0.09889	1.586	2.465	−1.501	−1.67
	t_{p3}	5.607	1.785	−3.469	1.797	−3.662
	output	a_{p0}	a_{p1}	a_{p2}	a_{p3}	a_{pc}
		0.1107	−0.07899	0.09227	−0.06409	0.04226

Table A11. Same as Table A9, except for snow using MGW.

		a_{-1}	a_0	a_1	a_2	a_γ
Z_H	t_{z0}	0.02921	1.134	1.482	0.2217	−0.4902

	t_{z1}	−0.7831	−0.4285	−2.957	2.88	−1.262
	t_{z2}	−1.296	0.2211	−2.9	2.265	−1.327
	t_{z3}	0	0	0	0	0
	output	a_{z0}	a_{z1}	a_{z2}	a_{z3}	a_{zc}
		−1.091	−0.9758	0.7895	0	0.1865
Z_{DR}	t_{d0}	−0.4655	0.5771	0.3473	−1.098	1.492
	t_{d1}	−4.348	5.047	1.765	−0.9516	4.058
	t_{d2}	0.4385	8.37	5.93	−0.04232	−0.9195
	t_{d3}	−0.2257	2.022	−0.6006	1.462	−1.388
	output	a_{d0}	a_{d1}	a_{d2}	a_{d3}	a_{dc}
		0.1024	0.04827	−0.046	−0.2474	0.2808
K_{DP}	t_{k0}	0.08206	−8.48	1.304	−8.447	1.599
	t_{k1}	−5.533	−2.541	−0.2706	0.1571	1.585
	t_{k2}	−0.2773	−4.112	4.414	−9.556	1.944
	t_{k3}	0	0	0	0	0
	output	a_{k0}	a_{k1}	a_{k2}	a_{k3}	a_{kc}
		3	−1.46	0.8944	0	0.0301
ρ_{hv}	$t_{\rho0}$	0	−6.602	6.339	−3.302	−1.714
	$t_{\rho1}$	0	−3.331	5.805	−4.546	−1.054
	$t_{\rho2}$	0	−0.8516	0.1207	−0.5599	−0.3139
	$t_{\rho3}$	0	1.523	−0.8913	2.928	1.201
	output	$a_{\rho0}$	$a_{\rho1}$	$a_{\rho2}$	$a_{\rho3}$	$a_{\rho c}$
		−1.629	−0.7623	1.716	0.5546	0.05717
δ	$t_{\delta0}$	−17.56	4.312	−5.147	2.904	10.26
	$t_{\delta1}$	0.8658	1.889	−2.004	2.028	−0.6159
	$t_{\delta2}$	−3.496	−6.768	−5.934	5.704	−3.162
	$t_{\delta3}$	0	0	0	0	0
	output	$a_{\delta0}$	$a_{\delta1}$	$a_{\delta2}$	$a_{\delta3}$	$a_{\delta c}$
		5.689	−18.81	−5.681	0	19.03
A_H	t_{h0}	0	−0.1449	−1.073	0	0.2146
	t_{h1}	0	−1.629	−4.659	0	−0.8841
	t_{h2}	0	−2.191	−2.273	0	−1.189
	t_{h3}	0	−3.075	−0.7571	0	0.6652
	output	a_{h0}	a_{h1}	a_{h2}	a_{h3}	a_{hc}
		1.991	0.372	−1.944	−4.383	0.2081
A_{DP}	t_{p0}	−2.464	9.266	−11.16	20.59	−5.115
	t_{p1}	7.308	2.27	−1.229	0.6965	−2.364
	t_{p2}	−1.119	−1.291	−9.199	6.092	0.7994
	t_{p3}	−4.095	−2.761	1.846	−4.337	3.015
	output	a_{p0}	a_{p1}	a_{p2}	a_{p3}	a_{pc}
		−0.05911	−0.2023	0.113	0.1399	0.1334

Table A12. Same as Table A9, except for hail using Polder-van Santen (PS) mixing formula.

		a_{-1}	a_0	a_1	a_2	a_γ
Z_H	t_{z0}	−0.1056	−0.3707	0.4594	−0.5722	−1.262
	t_{z1}	−0.4249	1.252	−0.8763	2.521	0.09729
	t_{z2}	−0.3019	0.729	1.463	−1.88	−0.7065
	t_{z3}	0	0	0	0	0
	output	a_{z0}	a_{z1}	a_{z2}	a_{z3}	a_{zc}
		−1.454	−0.5338	0.81	0	0.1095
Z_{DR}	t_{d0}	0.01744	−2.56	−1.081	0.7366	1.186

	t_{d1}	0.6013	0.7827	1.558	0.02945	−2.059
	t_{d2}	−0.6319	−1.05	−3.375	1.351	−5.776
	t_{d3}	2.747	−0.3407	−2.658	2.155	−2.083
	output	a_{d0}	a_{d1}	a_{d2}	a_{d3}	a_{dc}
		0.2833	−0.06262	−0.0874	−0.09083	0.2455
K_{DP}	t_{k0}	0	2.55	−12.8	13.67	−2.384
	t_{k1}	0	−5.708	5.814	−11.66	3.215
	t_{k2}	0	7.137	0.5896	4.812	−1.719
	t_{k3}	0	0	0	0	0
	output	a_{k0}	a_{k1}	a_{k2}	a_{k3}	a_{kc}
		−0.8521	1.351	−2.336	0	3.167
ρ_{hv}	$t_{\rho0}$	0	9.646	−3.472	−0.6902	1.796
	$t_{\rho1}$	0	−5.171	5.442	−2.293	−1.084
	$t_{\rho2}$	0	−0.7355	3.518	−1.767	3.379
	$t_{\rho3}$	0	−0.1794	3.34	−1.204	3.223
	output	$a_{\rho0}$	$a_{\rho1}$	$a_{\rho2}$	$a_{\rho3}$	$a_{\rho c}$
		0.1286	−0.2582	0.6794	−0.6785	0.8622
δ	$t_{\delta0}$	2.539	0.07826	−3.543	1.092	−1.15
	$t_{\delta1}$	6.295	1.841	−2.372	1.018	−1.073
	$t_{\delta2}$	17.25	5.01	2.016	−0.9594	−6.602
	$t_{\delta3}$	0	0	0	0	0
	output	$a_{\delta0}$	$a_{\delta1}$	$a_{\delta2}$	$a_{\delta3}$	$a_{\delta c}$
		16.08	−21	−9.116	0	14.47
A_H	t_{h0}	0	−0.3236	−0.0122	0	−4.219
	t_{h1}	0	1.862	−3.318	0	−4.755
	t_{h2}	0	−2.495	−11.14	0	−5.384
	t_{h3}	0	4.833	2.548	0	−1.842
	output	a_{h0}	a_{h1}	a_{h2}	a_{h3}	a_{hc}
		−0.4242	−0.4198	−0.09428	0.6311	0.3095
A_{DP}	t_{p0}	−6.084	−4.376	2.243	−1.654	4.162
	t_{p1}	−0.1985	1.147	−0.1451	−0.9511	−11.13
	t_{p2}	−11.33	−1.303	−4.02	2.803	−2.018
	t_{p3}	−11	3.506	−4.883	8.186	−1.976
	output	a_{p0}	a_{p1}	a_{p2}	a_{p3}	a_{pc}
		0.1648	−0.04017	−0.2161	0.2008	0.0362

Table A13. Same as Table A9, except for graupel using PS.

		a_{-1}	a_0	a_1	a_2	a_γ
Z_H	t_{z0}	0.09276	−0.7412	0.559	−0.5506	−1.863
	t_{z1}	0.0135	−1.285	0.3644	−0.7903	0.05927
	t_{z2}	2.551	−3.034	1.761	−1.038	7.442
	t_{z3}	0	0	0	0	0
	output	a_{z0}	a_{z1}	a_{z2}	a_{z3}	a_{zc}
		−1.37	2.43	0.1494	0	−0.7653
Z_{DR}	t_{d0}	−13.05	−13.26	4.643	−2.693	8.259
	t_{d1}	−0.4044	0.04475	−1.283	1.702	−7.345
	t_{d2}	−0.1246	2.579	0.9486	2.02	1.067
	t_{d3}	−0.4894	5.415	−2.265	0.3545	−14.32
	output	a_{d0}	a_{d1}	a_{d2}	a_{d3}	a_{dc}
		−0.0642	−0.0597	0.1119	−0.07739	0.1491
K_{DP}	t_{k0}	0	3.584	−2.164	3.013	−1.917

	t_{k1}	0	3.456	−2.311	0.2302	−3.282
	t_{k2}	0	−1.721	−1.053	1.92	4.705
	t_{k3}	0	0	0	0	0
	output	a_{k0}	a_{k1}	a_{k2}	a_{k3}	a_{kc}
		−2.442	2.036	1.717	0	0.3942
ρ_{hv}	$t_{\rho 0}$	0	−8.003	15.27	−7.782	−2.479
	$t_{\rho 1}$	0	2.443	−3.049	0.9794	−4.249
	$t_{\rho 2}$	0	8.5	−3.665	−1.072	1.462
	$t_{\rho 3}$	0	3.195	−3.602	1.955	−4.532
	output	$a_{\rho 0}$	$a_{\rho 1}$	$a_{\rho 2}$	$a_{\rho 3}$	$a_{\rho c}$
		−0.07144	0.6249	0.1698	−0.6013	0.8038
δ	$t_{\delta 0}$	0	3.885	−1.473	0.7813	−5.176
	$t_{\delta 1}$	0	5.775	−9.592	4.492	−8.759
	$t_{\delta 2}$	0	5.202	−0.2134	−0.2494	−5.52
	$t_{\delta 3}$	0	−5.837	1.619	0.9384	4.063
	output	$a_{\delta 0}$	$a_{\delta 1}$	$a_{\delta 2}$	$a_{\delta 3}$	$a_{\delta c}$
		−24.18	−4.592	23.86	4.545	4.59
A_H	t_{h0}	0	3.285	−1.864	0	−3.77
	t_{h1}	0	4.728	1.163	0	−2.592
	t_{h2}	0	−4.828	3.008	0	2.15
	t_{h3}	0	3.743	−0.108	0	−8.515
	output	a_{h0}	a_{h1}	a_{h2}	a_{h3}	a_{hc}
		−0.9163	0.912	−0.427	−0.3491	0.3644
A_{DP}	t_{p0}	0.2285	−3.441	0.5537	−0.422	6.419
	t_{p1}	19.21	9.342	0.8556	0.6121	−2.61
	t_{p2}	−0.03362	4.652	2.7	−2.208	−4.342
	t_{p3}	9.486	7.87	−2.511	1.104	−8.008
	output	a_{p0}	a_{p1}	a_{p2}	a_{p3}	a_{pc}
		0.102	−0.1049	0.08967	−0.06301	0.0782

Table A14. Same as Table A9, except for snow using PS.

		a_{-1}	a_0	a_1	a_2	a_γ
Z_H	t_{z0}	−0.8221	0.6702	−1.089	−0.06782	0.03686
	t_{z1}	−6.198	1.04	−1.391	1.887	2.572
	t_{z2}	0.2503	−3.389	−0.2115	−1.498	0.1718
	t_{z3}	0	0	0	0	0
	output	a_{z0}	a_{z1}	a_{z2}	a_{z3}	a_{zc}
		1.05	0.3469	2.65	0	−1.674
Z_{DR}	t_{d0}	3.29	−0.8047	0.3762	0.828	−1.969
	t_{d1}	−0.05194	−1.716	−0.1455	−0.8896	1.389
	t_{d2}	0.07704	7.848	4.545	−1.14	−0.8523
	t_{d3}	−6.348	5.537	6.641	−4.009	5.558
	output	a_{d0}	a_{d1}	a_{d2}	a_{d3}	a_{dc}
		−0.07372	0.2561	−0.2649	0.02979	0.3389
K_{DP}	t_{k0}	0.08262	−4.865	8.679	−14.3	1.891
	t_{k1}	0.04771	−8.315	1.859	−8.741	1.404
	t_{k2}	−6.782	−3.211	−1.071	0.6195	1.855
	t_{k3}	0	0	0	0	0
	output	a_{k0}	a_{k1}	a_{k2}	a_{k3}	a_{kc}
		0.7921	3.718	−1.407	0	−0.01315
ρ_{hv}	$t_{\rho 0}$	0	0.713	1.677	−0.2046	1.849

	$t_{\rho 1}$	0	−4.42	−4.018	0.4154	−2.238
	$t_{\rho 2}$	0	−6.678	4.753	−2.486	−3.14
	$t_{\rho 3}$	0	−1.704	1.941	−0.5058	−0.07867
	output	$a_{\rho 0}$	$a_{\rho 1}$	$a_{\rho 2}$	$a_{\rho 3}$	$a_{\rho c}$
		0.3378	0.2882	−0.512	−0.5244	0.7076
δ	$t_{\delta 0}$	2.932	0.7153	5.619	−4.568	−1.686
	$t_{\delta 1}$	4.555	0.5413	1.673	−1.395	−3.643
	$t_{\delta 2}$	2.151	0.9454	2.845	−2.371	−1.35
	$t_{\delta 3}$	7.056	0.235	0.4152	0.7146	−2.186
	output	$a_{\delta 0}$	$a_{\delta 1}$	$a_{\delta 2}$	$a_{\delta 3}$	$a_{\delta c}$
		−27.22	−24.76	62.06	−14.43	4.778
A_H	t_{h0}	0	0.4477	−2.08	0	0.1268
	t_{h1}	0	−2.475	−4.501	0	−2.467
	t_{h2}	0	−8.124	−7.847	0	−1.294
	t_{h3}	0	4.454	−0.9084	0	3.046
	output	a_{h0}	a_{h1}	a_{h2}	a_{h3}	a_{hc}
		0.7031	−0.6707	−0.4468	0.2082	0.2416
A_{DP}	t_{p0}	−3.025	−4.01	0.6959	−3.283	2.824
	t_{p1}	12.8	3.731	0.3975	2.052	−3.854
	t_{p2}	−0.1296	−2.37	−3.38	−0.3726	0.6251
	t_{p3}	13.36	3.71	0.5156	−0.6667	−2.554
	output	a_{p0}	a_{p1}	a_{p2}	a_{p3}	a_{pc}
		0.1617	−0.09505	0.1333	−0.1441	0.1155

Table A15. Same as Table A9, except for hail using MGI.

		a_{-1}	a_0	a_1	a_2	a_γ
Z_H	t_{z0}	0.01426	−0.2353	0.1361	0.1206	−0.3417
	t_{z1}	−9.08	−7.893	−1.341	1.248	5.255
	t_{z2}	−1.037	−7.57	2.723	−0.9834	4.3
	t_{z3}	0	0	0	0	0
	output	a_{z0}	a_{z1}	a_{z2}	a_{z3}	a_{zc}
		−2.497	0.2727	−0.3075	0	0.6665
Z_{DR}	t_{d0}	0.3559	−7.018	1.465	−6.4	1.761
	t_{d1}	0.1872	1.149	0.2137	0.623	−1.554
	t_{d2}	−0.1173	−0.7881	−3.508	2.386	−2.243
	t_{d3}	0.1212	−2.782	6.967	−3.599	6.02
	output	a_{d0}	a_{d1}	a_{d2}	a_{d3}	a_{dc}
		0.07821	−0.1226	−0.1097	0.09675	0.2406
K_{DP}	t_{k0}	0	4.67	−3.734	2.316	−2.955
	t_{k1}	0	−3.17	0.4688	−1.732	1.682
	t_{k2}	0	−3.051	2.664	−2.023	2.263
	t_{k3}	0	11.5	2.744	2.818	−1.144
	output	a_{k0}	a_{k1}	a_{k2}	a_{k3}	a_{kc}
		4.864	3.082	4.931	−4.115	−0.741
ρ_{hv}	$t_{\rho 0}$	−2.166	−3.758	2.611	−0.9574	2.824
	$t_{\rho 1}$	11.2	5.996	4.472	−4.357	−4.949
	$t_{\rho 2}$	−8.759	−4.153	0.3936	0.8036	1.984
	$t_{\rho 3}$	−0.8972	−5.6	4.064	−1.783	−0.4491
	output	$a_{\rho 0}$	$a_{\rho 1}$	$a_{\rho 2}$	$a_{\rho 3}$	$a_{\rho c}$
		0.6034	0.162	−0.4186	−1.073	0.8303
δ	$t_{\delta 0}$	7.948	7.769	−2.042	1.525	−6.344

	$t_{\delta 1}$	−11.26	−5.078	0.814	−0.09126	2.701
	$t_{\delta 2}$	9.227	20.08	1.101	−0.4339	−12.18
	$t_{\delta 3}$	0	0	0	0	0
	output	$a_{\delta 0}$	$a_{\delta 1}$	$a_{\delta 2}$	$a_{\delta 3}$	$a_{\delta c}$
		−20.57	11.02	18.8	0	1.843
A_H	t_{h0}	1.873	3.601	−2.43	0	−0.09173
	t_{h1}	−10.77	−6.596	1.176	0	3.958
	t_{h2}	2.115	13.48	−3.533	0	−11.43
	t_{h3}	−0.06266	1.072	−1.986	0	−1.098
	output	a_{h0}	a_{h1}	a_{h2}	a_{h3}	a_{hc}
		0.2769	0.4576	−0.2375	−0.455	0.4192
A_{DP}	t_{p0}	19.46	15.69	3.39	−2.363	−9.415
	t_{p1}	−0.1112	0.7917	−1.112	2.728	−0.3995
	t_{p2}	−0.8055	−3.683	3.521	−1.638	3.8
	t_{p3}	−17.81	−9.184	1.596	−2.374	2.271
	output	a_{p0}	a_{p1}	a_{p2}	a_{p3}	a_{pc}
		−0.06826	−0.03652	0.162	0.1794	0.08272

Table A.16. Same as Table A.9, except for graupel using MGI.

		a_{-1}	a_0	a_1	a_2	a_γ
Z_H	t_{z0}	5.523	14.53	−1.309	−0.2948	−10.94
	t_{z1}	0.004242	−0.532	−0.04549	−0.06649	−1.39
	t_{z2}	0.003094	−0.7463	−0.01492	−0.5358	0.09897
	t_{z3}	0	0	0	0	0
	output	a_{z0}	a_{z1}	a_{z2}	a_{z3}	a_{zc}
		−0.1948	−1.468	1.698	0	−0.575
Z_{DR}	t_{d0}	0.01863	−2.352	0.05402	−2.291	−0.6322
	t_{d1}	0.1797	−1.29	2.064	−1.221	3.119
	t_{d2}	0.2699	−5.839	4.085	−1.669	6.409
	t_{d3}	−0.1667	2.289	−1.838	0.7262	−2.623
	output	a_{d0}	a_{d1}	a_{d2}	a_{d3}	a_{dc}
		−0.155	0.2614	0.2143	0.4359	−0.3066
K_{DP}	t_{k0}	0	12.35	2.796	3.809	−1.36
	t_{k1}	0	7.432	−3.595	2.011	−4.687
	t_{k2}	0	−4.477	2.496	−1.777	3.188
	t_{k3}	0	3.629	−0.5131	1.71	−2.011
	output	a_{k0}	a_{k1}	a_{k2}	a_{k3}	a_{kc}
		−1.371	2.824	2.824	−2.022	0.551
ρ_{hv}	$t_{\rho 0}$	1.718	5.563	−4.335	1.592	0.4788
	$t_{\rho 1}$	0.02967	−5.089	1.202	0.6895	5.157
	$t_{\rho 2}$	−4.514	−3.371	−0.2878	1.408	2.268
	$t_{\rho 3}$	0.08216	−4.288	1.798	−0.5119	3.498
	output	$a_{\rho 0}$	$a_{\rho 1}$	$a_{\rho 2}$	$a_{\rho 3}$	$a_{\rho c}$
		0.425	−0.4023	−0.2846	0.7098	0.573
δ	$t_{\delta 0}$	−0.02395	3.037	−0.5488	1.481	−0.03024
	$t_{\delta 1}$	−8.352	−6.733	0.6364	0.5852	4.24
	$t_{\delta 2}$	8.299	27.34	0.792	−0.1987	−16.48
	$t_{\delta 3}$	−7.363	−16.78	3.478	−2.428	12.36
	output	$a_{\delta 0}$	$a_{\delta 1}$	$a_{\delta 2}$	$a_{\delta 3}$	$a_{\delta c}$
		−12.55	12.88	16.92	12.27	−5.546
A_H	t_{h0}	0.4651	3.965	1.578	0	−4.199

	t_{h1}	12.28	8.496	0.07382	0	−2.716
	t_{h2}	−4.995	−15.1	0.3353	0	9.131
	t_{h3}	6.43	14.03	−0.5625	0	−7.346
	output	a_{h0}	a_{h1}	a_{h2}	a_{h3}	a_{hc}
		−0.02911	−1.973	1.381	2.451	−0.4464
A_{DP}	t_{p0}	−24.27	−18.55	−3.62	2.595	10.65
	t_{p1}	−0.7304	−34.29	9.748	−5.4	25.37
	t_{p2}	−0.2916	4.364	−6.47	6.545	−3.498
	t_{p3}	−16.49	−10.71	3.502	−2.203	4.091
	output	a_{p0}	a_{p1}	a_{p2}	a_{p3}	a_{pc}
		0.04148	0.03082	−0.03634	0.07744	0.03653

Table A17. Same as Table A9, except for snow using MGI.

X-band coefficients

		a_{-1}	a_0	a_1	a_2	a_γ
Z_H	t_{z0}	5.349	2.471	−2.577	1.137	0
	t_{z1}	−10.1	0.1185	−0.2824	−0.02934	0
	t_{z2}	7.977	0.6119	−1.602	−0.04086	0
	t_{z3}	0	0	0	0	0
	output	a_{z0}	a_{z1}	a_{z2}	a_{z3}	a_{zc}
		−0.07377	0.05493	−0.08402	0	0.154
Z_{DR}	t_{d0}	4.012	−1.019	−0.9984	−0.5203	0
	t_{d1}	−1.223	0.7873	0.5408	0.8622	0
	t_{d2}	−0.02782	−1.128	0.4081	0.5012	0
	t_{d3}	0	0	0	0	0
	output	a_{d0}	a_{d1}	a_{d2}	a_{d3}	a_{dc}
		−0.1696	0.2017	0.1416	0	0.1609
K_{DP}	t_{k0}	−0.02856	1.629	−0.6454	−0.2942	0
	t_{k1}	−2.62	−0.7569	0.4052	0.4018	0
	t_{k2}	−1.028	−0.8171	0.5377	0.3406	0
	t_{k3}	0	0	0	0	0
	output	a_{k0}	a_{k1}	a_{k2}	a_{k3}	a_{kc}
		−1.998	2.511	1.401	0	1.907
ρ_{hv}	$t_{\rho0}$	6.713	−4.5	−3.938	−1.139	0
	$t_{\rho1}$	−8.38	3.138	2.141	−0.9762	0
	$t_{\rho2}$	−4.403	−0.1302	−1.313	−0.3573	0
	$t_{\rho3}$	0	0	0	0	0
	output	$a_{\rho0}$	$a_{\rho1}$	$a_{\rho2}$	$a_{\rho3}$	$a_{\rho c}$
		0.005113	−0.004689	−0.003011	0	0.9948
A_H	$t_{\delta0}$	−0.02903	1.57	−0.9416	0	0
	$t_{\delta1}$	0.03268	−1.436	0.9193	0	0
	$t_{\delta2}$	−3.586	−1.243	0.901	0	0
	$t_{\delta3}$	−0.01682	1.296	−0.961	0	0
	output	a_{h0}	a_{h1}	a_{h2}	a_{h3}	a_{hc}
		−0.3936	0.5468	0.718	−0.5664	0.951
A_{DP}	t_{h0}	0.6328	0.9248	−0.3789	−1.113	0
	t_{h1}	−0.05277	−1.316	−0.7863	1.151	0
	t_{h2}	0.09256	−2.363	−0.1971	1.252	0
	t_{h3}	4.03	1.703	−0.49	−0.243	0
	output	a_{p0}	a_{p1}	a_{p2}	a_{p3}	a_{pc}

		−0.1841	0.2248	0.3521	−0.1819	0.3138

Table A18. The coefficients of ML-fitted polarimetric radar variables (Z_H, Z_{DR}, K_{DP}, ρ_{hv}, A_H, and A_{DP}) for rain at X-band.

		a_{-1}	a_0	a_1	a_2	a_γ
Z_H	t_{z0}	−0.1213	−0.6012	−2.096	0.7622	0.934
	t_{z1}	−4.58	−1.474	−0.03515	0.3785	0.3604
	t_{z2}	−0.166	−4.622	1.28	0.1269	−4.59
	t_{z3}	0	0	0	0	0
	output	a_{z0}	a_{z1}	a_{z2}	a_{z3}	a_{zc}
		0.7356	−1.279	−0.2138	0	−0.5863
Z_{DR}	t_{d0}	0.1266	2.82	0.01815	1.393	−2.038
	t_{d1}	1.752	3.891	0.1806	−1.207	−2.344
	t_{d2}	1.193	9.56	−4.575	1.915	−22.7
	t_{d3}	0.1463	−0.3019	−0.6296	3.04	−2.239
	output	a_{d0}	a_{d1}	a_{d2}	a_{d3}	a_{dc}
		−0.4019	0.2362	0.07236	−0.07866	0.1884
K_{DP}	t_{k0}	−0.0686	−1.722	−2.293	1.867	0.922
	t_{k1}	−0.8067	8.181	3.419	3.236	0.08037
	t_{k2}	−4.958	−2.903	−2.065	1.209	0.6359
	t_{k3}	0	0	0	0	0
	output	a_{k0}	a_{k1}	a_{k2}	a_{k3}	a_{kc}
		9.128	1.998	−17.01	0	−1.24
ρ_{hv}	$t_{\rho0}$	0	−1.728	3.157	−2.161	−0.8531
	$t_{\rho1}$	0	−2.39	3.215	0.04635	1.668
	$t_{\rho2}$	0	−11.34	5.029	−2.823	−7.348
	$t_{\rho3}$	0	6.233	−3.991	0.9533	−1.754
	output	$a_{\rho0}$	$a_{\rho1}$	$a_{\rho2}$	$a_{\rho3}$	$a_{\rho c}$
		−0.6211	−0.2452	−0.5031	0.6212	0.367
δ	$t_{\delta0}$	2.94	5.758	−3.629	6.855	−2.054
	$t_{\delta1}$	0.9636	0.4409	2.143	−2.761	−0.4892
	$t_{\delta2}$	−1.723	0.3734	−1.05	0.4784	1.23
	$t_{\delta3}$	0	0	0	0	0
	output	$a_{\delta0}$	$a_{\delta1}$	$a_{\delta2}$	$a_{\delta3}$	$a_{\delta c}$
		−6.432	15.84	17.13	0	−8.459
A_H	t_{h0}	0	−4.029	−2.39	0	0.8005
	t_{h1}	0	1.046	−1.931	0	0.05905
	t_{h2}	0	−7.294	−5.075	0	−0.6545
	t_{h3}	0	−3.133	−2.72	0	0.4458
	output	a_{h0}	a_{h1}	a_{h2}	a_{h3}	a_{hc}
		−2.535	0.6866	−2.516	3.125	0.2455
A_{DP}	t_{p0}	2.09	−5.542	−1.018	−4.376	1.133
	t_{p1}	1.909	−1.975	−2.398	1.078	−1.163
	t_{p2}	1.763	−0.6732	−0.6388	2.568	−3.807
	t_{p3}	0.02786	−2.523	−0.07464	−3.388	2.141
	output	a_{p0}	a_{p1}	a_{p2}	a_{p3}	a_{pc}
		0.4444	−0.5909	−0.0716	0.2	0.07987

Table A19. The coefficients of ML-fitted polarimetric radar variables (Z_H, Z_{DR}, K_{DP}, ρ_{hv}, δ, A_H, and A_{DP}) for hail using MGW at X-band.

		a_{-1}	a_0	a_1	a_2	a_γ
Z_H	t_{z0}	1.316	−0.06816	−1.316	1.305	−0.5837
	t_{z1}	0.6512	0.1254	−1.421	0.3604	0.04874
	t_{z2}	−0.06903	5.312	−0.1491	0.4316	2.222
	t_{z3}	0	0	0	0	0
	output	a_{z0}	a_{z1}	a_{z2}	a_{z3}	a_{zc}
		−0.596	1.561	2.292	0	−3.232
Z_{DR}	t_{d0}	0.0506	0.4296	0.8764	−1.042	1.098
	t_{d1}	0.2574	7.92	1.761	4.617	−0.7947
	t_{d2}	−0.03832	1.99	−0.8498	1.82	−1.53
	t_{d3}	5.171	−2.186	0.4012	−0.3149	−2.753
	output	a_{d0}	a_{d1}	a_{d2}	a_{d3}	a_{dc}
		0.1959	−0.08269	−0.1734	−0.04297	0.2606
K_{DP}	t_{k0}	9.163	3.947	1.087	−0.6601	−1.541
	t_{k1}	−0.2738	−2.673	3.088	−6.405	1.928
	t_{k2}	0.08854	−6.163	1.138	−6.326	1.489
	t_{k3}	0	0	0	0	0
	output	a_{k0}	a_{k1}	a_{k2}	a_{k3}	a_{kc}
		2.4	1.565	5.247	0	−2.44
ρ_{hv}	$t_{\rho0}$	0	−7.911	−3.134	1.156	−6.021
	$t_{\rho1}$	0	−0.01866	0.3335	−1.242	0.5407
	$t_{\rho2}$	0	7.86	3.7	−2.278	6.538
	$t_{\rho3}$	0	−6.628	4.748	−2.254	−2.453
	output	$a_{\rho0}$	$a_{\rho1}$	$a_{\rho2}$	$a_{\rho3}$	$a_{\rho c}$
		0.6235	0.269	0.5355	−0.8316	0.2352
δ	$t_{\delta0}$	−13.36	−4.112	−3.898	1.077	2.041
	$t_{\delta1}$	7.179	−0.5691	1.362	−0.4711	−2.985
	$t_{\delta2}$	0.1542	2.095	−8.036	5.475	−1.431
	$t_{\delta3}$	0	0	0	0	0
	output	$a_{\delta0}$	$a_{\delta1}$	$a_{\delta2}$	$a_{\delta3}$	$a_{\delta c}$
		4.511	−6.326	−4.238	0	11.5
A_H	t_{h0}	0	−1.481	−2.267	0	−0.6001
	t_{h1}	0	−0.9937	−0.4636	0	0.8246
	t_{h2}	0	−0.9788	−3.101	0	−0.3659
	t_{h3}	0	0.4739	−0.9646	0	0.5257
	output	a_{h0}	a_{h1}	a_{h2}	a_{h3}	a_{hc}
		−4.218	−2.368	1.971	2.949	0.5116
A_{DP}	t_{p0}	0.02792	1.667	0.1364	2.853	−2.421
	t_{p1}	−9.497	−2.407	−0.2629	0.4929	1.527
	t_{p2}	6.036	1.489	−0.5458	1.927	−2.64
	t_{p3}	6.203	−1.984	−0.08127	−4.482	1.756
	output	a_{p0}	a_{p1}	a_{p2}	a_{p3}	a_{pc}
		−0.2464	0.3317	−0.2315	0.1231	0.2036

Table A20. Same as Table A19, except for graupel using MGW.

		a_{-1}	a_0	a_1	a_2	a_γ
Z_H	t_{z0}	−0.02143	−5.243	−0.3347	0.2365	−1.729
	t_{z1}	−3.402	−0.4817	0.6083	0.6689	−0.1916
	t_{z2}	0.04592	−0.1809	4.232	−4.031	1.15
	t_{z3}	0	0	0	0	0

	output	a_{z0}	a_{z1}	a_{z2}	a_{z3}	a_{zc}
		−12.47	−1.044	0.3287	0	−0.05254
Z_{DR}	t_{d0}	11.61	1.824	5.686	−5.668	−0.8636
	t_{d1}	0.144	3.412	4.055	−0.6864	0.5986
	t_{d2}	−0.2628	1.976	1.571	−2.811	−0.09603
	t_{d3}	−0.1683	−2.531	−1.02	0.6798	−3.581
	output	a_{d0}	a_{d1}	a_{d2}	a_{d3}	a_{dc}
		0.1555	0.1554	0.08685	−0.1591	−0.06318
K_{DP}	t_{k0}	−0.07541	−7.522	1.111	−8.359	1.944
	t_{k1}	7.345	3.266	−1.896	0.8848	−2.395
	t_{k2}	−0.4251	3.785	−5.515	10.85	−3.602
	t_{k3}	0	0	0	0	0
	output	a_{k0}	a_{k1}	a_{k2}	a_{k3}	a_{kc}
		2.81	1.353	−1.095	0	−0.3281
ρ_{hv}	$t_{\rho0}$	0	1.764	0.6337	−0.77	3.097
	$t_{\rho1}$	0	6.077	−5.826	2.99	1.709
	$t_{\rho2}$	0	−0.5405	−0.1497	1.126	−0.4398
	$t_{\rho3}$	0	2.768	0.04094	1.054	2.891
	output	$a_{\rho0}$	$a_{\rho1}$	$a_{\rho2}$	$a_{\rho3}$	$a_{\rho c}$
		0.6089	0.9114	−0.2064	−0.6884	0.1618
δ	$t_{\delta0}$	0.3537	1.862	2.895	−2.357	−1.616
	$t_{\delta1}$	−8.494	1.205	−5.943	7.536	1.782
	$t_{\delta2}$	−0.4615	1.484	4.141	−3.71	2.632
	$t_{\delta3}$	0	0	0	0	0
	output	$a_{\delta0}$	$a_{\delta1}$	$a_{\delta2}$	$a_{\delta3}$	$a_{\delta c}$
		8.045	4.54	5.949	0	−4.928
A_H	t_{h0}	0	0.01699	1.696	0	−0.1383
	t_{h1}	0	1.818	1.021	0	−0.6789
	t_{h2}	0	−1.743	−2.335	0	−0.9868
	t_{h3}	0	−4.244	0.3416	0	−2.722
	output	a_{h0}	a_{h1}	a_{h2}	a_{h3}	a_{hc}
		−2.521	2.611	−2.043	−0.6046	0.8155
A_{DP}	t_{p0}	0.04439	1.831	0.8502	0.7173	−1.442
	t_{p1}	−9.17	−1.201	0.9798	−0.9489	1.542
	t_{p2}	5.029	−0.1206	−2.509	4.46	−2.026
	t_{p3}	−0.04239	−1.272	−0.2854	−1.784	1.097
	output	a_{p0}	a_{p1}	a_{p2}	a_{p3}	a_{pc}
		0.4588	0.1815	−0.07899	0.5628	−0.4539

Table A21. Same as Table A19, except for snow MGW.

		a_{-1}	a_0	a_1	a_2	a_γ
Z_H	t_{z0}	4.265	1.56	−0.09295	−0.3128	−0.3845
	t_{z1}	−0.1413	−1.285	2.566	−1.235	−2.332
	t_{z2}	−0.1523	−1.824	−2.179	0.588	1.429
	t_{z3}	0	0	0	0	0
	output	a_{z0}	a_{z1}	a_{z2}	a_{z3}	a_{zc}
		1.43	−0.3521	0.4681	0	−1.751
Z_{DR}	t_{d0}	0.02495	3.898	1.348	1.011	−2.1
	t_{d1}	1.245	−0.3094	−2.274	5.543	−3.076
	t_{d2}	0.7793	−4.756	4.391	−6.57	4.651
	t_{d3}	−0.1922	2.686	1.915	−2.125	−4.36

	output	a_{d0}	a_{d1}	a_{d2}	a_{d3}	a_{dc}
		−0.3530	−0.07590	0.1780	0.2607	0.1960
K_{DP}	t_{k0}	−6.733	−1.201	−1.164	0.1028	2.564
	t_{k1}	9.247	4.924	3.124	−1.132	−1.623
	t_{k2}	−0.1027	−2.264	−1.898	1.051	1.378
	t_{k3}	0	0	0	0	0
	output	a_{k0}	a_{k1}	a_{k2}	a_{k3}	a_{kc}
		−1.248	6.810	7.263	0	−6.883
ρ_{hv}	$t_{\rho0}$	0	−4.541	7.045	−8.224	−1.242
	$t_{\rho1}$	0	5.188	−5.512	2.53	−0.9756
	$t_{\rho2}$	0	−0.0613	2.85	2.535	1.002
	$t_{\rho3}$	0	−4.519	5.24	−2.792	−1.979
	output	$a_{\rho0}$	$a_{\rho1}$	$a_{\rho2}$	$a_{\rho3}$	$a_{\rho c}$
		−1.096	1.045	−0.1916	−0.8356	−0.06406
δ	$t_{\delta0}$	0.07509	−0.3936	0.684	−1.41	−0.143
	$t_{\delta1}$	−8.927	−7.331	0.1712	−0.3724	7.07
	$t_{\delta2}$	4.284	−3.923	0.02139	0.08013	−5.133
	$t_{\delta3}$	0	0	0	0	0
	output	$a_{\delta0}$	$a_{\delta1}$	$a_{\delta2}$	$a_{\delta3}$	$a_{\delta c}$
		34.79	6.421	−11.73	0	−9.109
A_H	t_{h0}	0	−4.875	−5.658	0	−0.4055
	t_{h1}	0	1.734	1.185	0	−0.03467
	t_{h2}	0	5.187	2.255	0	−0.8584
	t_{h3}	0	−4.44	−3.276	0	−0.9762
	output	a_{h0}	a_{h1}	a_{h2}	a_{h3}	a_{hc}
		0.8269	−4.79	4.237	−3.636	0.7667
A_{DP}	t_{p0}	−1.218	7.008	3.836	2.85	−1.067
	t_{p1}	−4.561	0.6928	1.434	−0.5559	1.934
	t_{p2}	−0.6929	−7.152	1.712	−8.479	2.54
	t_{p3}	4.979	2.354	2.005	1.183	−2.744
	output	a_{p0}	a_{p1}	a_{p2}	a_{p3}	a_{pc}
		−0.2576	0.2893	0.2298	−0.1483	0.1419

Table A22. Same as Table A19, except for hail using PS.

		a_{-1}	a_0	a_1	a_2	a_γ
Z_H	t_{z0}	−0.1018	−1.525	−1.76	−0.496	0.4442
	t_{z1}	0.2187	0.9067	0.3287	−0.1274	1.914
	t_{z2}	0.01797	0.08168	2.634	−3.285	0.5684
	t_{z3}	0	0	0	0	0
	output	a_{z0}	a_{z1}	a_{z2}	a_{z3}	a_{zc}
		0.8742	0.3702	0.4788	0	−1.345
Z_{DR}	t_{d0}	0.4296	−2.604	−2.021	0.5229	−3.936
	t_{d1}	0.08965	0.3081	−2.044	2.882	−1.162
	t_{d2}	0.1093	−2.702	−1.331	0.4408	1.701
	t_{d3}	−7.192	0.5178	3.38	−2.513	8.335
	output	a_{d0}	a_{d1}	a_{d2}	a_{d3}	a_{dc}
		−0.06204	−0.129	0.1837	0.04812	0.1864
K_{DP}	t_{k0}	0.05924	−7.434	1.065	−7.022	2.151
	t_{k1}	−9.68	−4.764	−0.8631	0.6135	2.466
	t_{k2}	−0.05548	−3.509	4.585	−8.145	2.3
	t_{k3}	0	0	0	0	0

	output	a_{k0}	a_{k1}	a_{k2}	a_{k3}	a_{kc}
		4.707	−2.224	1.677	0	0.02255
ρ_{hv}	$t_{\rho 0}$	0	1.949	−2.097	1.452	3.771
	$t_{\rho 1}$	0	−3.937	3.449	−1.793	−0.7408
	$t_{\rho 2}$	0	1.27	−1.699	2.115	2.382
	$t_{\rho 3}$	0	−0.7501	2.497	−3.487	−2.948
	output	$a_{\rho 0}$	$a_{\rho 1}$	$a_{\rho 2}$	$a_{\rho 3}$	$a_{\rho c}$
		0.9829	−2.598	−2.252	−1.125	2.248
δ	$t_{\delta 0}$	−4.067	−0.4172	8.12	−7.589	1.834
	$t_{\delta 1}$	−39.2	−19.02	27.35	−17.74	8.793
	$t_{\delta 2}$	14.01	−0.8039	5.405	−3.224	−6.189
	$t_{\delta 3}$	0	0	0	0	0
	output	$a_{\delta 0}$	$a_{\delta 1}$	$a_{\delta 2}$	$a_{\delta 3}$	$a_{\delta c}$
		5.837	1.948	−6.524	0	6.928
A_H	t_{h0}	0	−1.752	−2.255	0	−1.48
	t_{h1}	0	1.81	0.6059	0	−0.9528
	t_{h2}	0	−0.2764	−0.9148	0	0.466
	t_{h3}	0	4.728	4.615	0	0.4533
	output	a_{h0}	a_{h1}	a_{h2}	a_{h3}	a_{hc}
		−1.583	3.28	3.808	0.9652	−3.697
A_{DP}	t_{p0}	0.1295	1.734	0.707	1.899	−1.856
	t_{p1}	0.00512	−1.346	−0.03252	−0.3801	−0.3328
	t_{p2}	−9.465	−2.037	−1.076	0.9782	1.424
	t_{p3}	−6.534	−1.161	−1.421	−0.4787	2.74
	output	a_{p0}	a_{p1}	a_{p2}	a_{p3}	a_{pc}
		−0.3045	0.8575	0.4275	0.1973	−0.1045

Table A23. Same as Table A19, except for graupel using PS.

		a_{-1}	a_0	a_1	a_2	a_γ
Z_H	t_{z0}	0.02278	0.5921	−0.1191	0.311	1.754
	t_{z1}	−0.162	1.634	1.339	0.5666	−0.2344
	t_{z2}	0.307	0.7365	−1.463	1.787	0.002221
	t_{z3}	0	0	0	0	0
	output	a_{z0}	a_{z1}	a_{z2}	a_{z3}	a_{zc}
		1.455	−1.143	−1.083	0	−0.239
Z_{DR}	t_{d0}	0.9937	−1.236	1.762	−1.4	−3.71
	t_{d1}	0.7453	−2.238	3.168	−1.109	10.6
	t_{d2}	−1.52	−0.8825	4.075	−2.804	−0.4291
	t_{d3}	−11.75	−3.705	−1.624	2.106	0.314
	output	a_{d0}	a_{d1}	a_{d2}	a_{d3}	a_{dc}
		−0.09254	0.1136	0.2753	−0.2838	0.1034
K_{DP}	t_{k0}	0.07604	9.424	−0.9077	8.196	−2.9
	t_{k1}	−0.376	5.463	−5.978	3.175	−5.58
	t_{k2}	−0.3973	5.461	−6.526	11.01	−3.731
	t_{k3}	0	0	0	0	0
	output	a_{k0}	a_{k1}	a_{k2}	a_{k3}	a_{kc}
		−3.067	1.346	−1.197	0	2.882
ρ_{hv}	$t_{\rho 0}$	0	1.448	−1.138	0.9628	−6.154
	$t_{\rho 1}$	0	1.034	−0.2659	2.325	3.391
	$t_{\rho 2}$	0	4.529	−5.89	3.253	0.7944
	$t_{\rho 3}$	0	−1.398	1.375	−0.6226	7.992

	output	$a_{\rho 0}$	$a_{\rho 1}$	$a_{\rho 2}$	$a_{\rho 3}$	$a_{\rho c}$
		−1.702	−0.5433	1.656	−1.202	1.052
δ	$t_{\delta 0}$	3.197	−2.315	−3.708	2.858	−2.921
	$t_{\delta 1}$	2.824	−0.08216	−3.778	1.808	−2.771
	$t_{\delta 2}$	2.054	−0.8488	−1.792	0.7727	−1.978
	$t_{\delta 3}$	0	0	0	0	0
	output	$a_{\delta 0}$	$a_{\delta 1}$	$a_{\delta 2}$	$a_{\delta 3}$	$a_{\delta c}$
		−42.99	−35.21	71.46	0	8.819
A_H	t_{h0}	0	−4.281	−0.7514	0	−2.786
	t_{h1}	0	−2.236	−0.9494	0	−0.2543
	t_{h2}	0	−2.283	−2.294	0	−1.099
	t_{h3}	0	−3.516	−2.696	0	0.06734
	output	a_{h0}	a_{h1}	a_{h2}	a_{h3}	a_{hc}
		−1.182	12.13	−2.536	−3.395	0.6722
A_{DP}	t_{p0}	0.05593	−2.122	1.873	−2.271	−1.214
	t_{p1}	−3.1	6.98	2.463	3.643	3.111
	t_{p2}	−0.02778	0.9812	−2.037	2.995	1.227
	t_{p3}	−5.1	−3.116	−0.9711	−0.228	0.118
	output	a_{p0}	a_{p1}	a_{p2}	a_{p3}	a_{pc}
		−0.6883	0.06517	−0.3518	0.8427	0.3675

Table A24. Same as Table A19, except for snow using PS.

		a_{-1}	a_0	a_1	a_2	a_γ
Z_H	t_{z0}	−0.0168	−0.4326	−1.074	1.069	−0.506
	t_{z1}	5.488	2.019	−0.8517	0.4638	−1.207
	t_{z2}	−2.236	0.4859	0.5079	0.8881	−0.3842
	t_{z3}	0	0	0	0	0
	output	a_{z0}	a_{z1}	a_{z2}	a_{z3}	a_{zc}
		−1.148	0.6215	−1.075	0	−0.1407
Z_{DR}	t_{d0}	0	−27.99	−3.094	1.234	22.05
	t_{d1}	0	3.208	−0.04517	1.239	−0.9246
	t_{d2}	0	−0.006287	−0.4204	0.3625	−0.05335
	t_{d3}	0	24.55	3.217	−2.046	−19.69
	output	a_{d0}	a_{d1}	a_{d2}	a_{d3}	a_{dc}
		2.007	−1.142	−0.4093	2.136	−0.7628
K_{DP}	t_{k0}	0.05254	3.377	0.07147	1.868	−1.233
	t_{k1}	−4.706	−1.401	0.3902	−1.119	2.466
	t_{k2}	−7.827	−5.197	−2.165	−0.496	1.518
	t_{k3}	0	0	0	0	0
	output	a_{k0}	a_{k1}	a_{k2}	a_{k3}	a_{kc}
		−8.923	−1.117	−7.827	0	8.81
ρ_{hv}	$t_{\rho 0}$	0	3.062	−0.6991	−0.2154	−0.6639
	$t_{\rho 1}$	0	−1.989	−1.397	−1.547	−0.9214
	$t_{\rho 2}$	0	2.328	0.398	1.815	0.2365
	$t_{\rho 3}$	0	3.64	−3.238	1.949	1.765
	output	$a_{\rho 0}$	$a_{\rho 1}$	$a_{\rho 2}$	$a_{\rho 3}$	$a_{\rho c}$
		1.37	−0.9453	−1.699	1.026	0.09236
δ	$t_{\delta 0}$	1.871	1.191	0.7371	−0.7684	−1.39
	$t_{\delta 1}$	0.02493	0.05903	0.1814	−0.7451	0.009001
	$t_{\delta 2}$	−2.882	−2.653	−1.419	1.524	2.895
	$t_{\delta 3}$	0	0	0	0	0

	output	$a_{\delta 0}$	$a_{\delta 1}$	$a_{\delta 2}$	$a_{\delta 3}$	$a_{\delta c}$
		−92.07	56.42	−59.35	0	54.13
A_H	t_{h0}	0	1.618	1.363	0	−0.138
	t_{h1}	0	3.749	1.263	0	−0.7906
	t_{h2}	0	−4.929	−4.465	0	−1.891
	t_{h3}	0	−10.85	−8.022	0	−0.7773
	output	a_{h0}	a_{h1}	a_{h2}	a_{h3}	a_{hc}
		−4.426	3.53	−1.35	−1.415	1.179
A_{DP}	t_{p0}	6.302	2.365	1.019	2.06	−3.154
	t_{p1}	1.795	5.471	0.1715	4.437	−2.179
	t_{p2}	5.056	−0.5201	−1.146	0.383	−1.842
	t_{p3}	−0.0839	−6.555	−3.835	−2.43	0.6367
	output	a_{p0}	a_{p1}	a_{p2}	a_{p3}	a_{pc}
		−0.1084	−0.3009	−0.2872	0.3063	0.4312

Table A25. Same as Table A19, except for hail using MGI.

		a_{-1}	a_0	a_1	a_2	a_γ
Z_H	t_{z0}	−1.601	−0.9678	1.936	−0.3471	2.013
	t_{z1}	−0.002309	−2.003	−0.4264	−1.175	0.2901
	t_{z2}	0.003496	−0.4838	−1.301	1.758	−0.5467
	t_{z3}	0	0	0	0	0
	output	a_{z0}	a_{z1}	a_{z2}	a_{z3}	a_{zc}
		0.2759	1.679	−0.6127	0	−0.8448
Z_{DR}	t_{d0}	−5.261	−2.41	−4.302	5.221	−1.355
	t_{d1}	0.06925	0.246	−4.747	2.724	−3.64
	t_{d2}	−0.0536	−2.776	−0.9396	−0.4618	0.1617
	t_{d3}	−0.1674	0.3276	−3.986	4.622	−1.329
	output	a_{d0}	a_{d1}	a_{d2}	a_{d3}	a_{dc}
		0.1388	−0.1309	0.5393	−0.2578	0.2575
K_{DP}	t_{k0}	2.736	2.644	−1.275	1.495	−2.363
	t_{k1}	−0.01456	−4.697	0.03744	−2.148	1.616
	t_{k2}	1.58	3.036	−2.247	1.745	−2.3
	t_{k3}	0	0	0	0	0
	output	a_{k0}	a_{k1}	a_{k2}	a_{k3}	a_{kc}
		−5.654	10.07	8.275	0	−2.622
ρ_{hv}	$t_{\rho 0}$	2.615	−2.366	6.564	−3.726	2.975
	$t_{\rho 1}$	−9.382	−5.763	1.877	−0.9329	−0.5678
	$t_{\rho 2}$	2.391	−7.906	6.005	−8.526	2.665
	$t_{\rho 3}$	−1.162	−0.9191	3.162	−0.7923	1.102
	output	$a_{\rho 0}$	$a_{\rho 1}$	$a_{\rho 2}$	$a_{\rho 3}$	$a_{\rho c}$
		0.6522	−0.7034	−0.6585	−0.6741	0.9967
δ	$t_{\delta 0}$	2.42	2.704	−4.181	0.9799	−3.08
	$t_{\delta 1}$	8.744	3.439	2.336	−4.005	−3.099
	$t_{\delta 2}$	−25.78	−10.21	2.499	−2.435	2.867
	$t_{\delta 3}$	0	0	0	0	0
	output	$a_{\delta 0}$	$a_{\delta 1}$	$a_{\delta 2}$	$a_{\delta 3}$	$a_{\delta c}$
		253.1	−184.3	89.98	0	−68.04
A_H	t_{h0}	−0.7737	−1.767	−6.898	0	−3.904
	t_{h1}	15.76	5.824	3.125	0	−0.9995
	t_{h2}	−7.044	−9.129	3.892	0	10.7
	t_{h3}	−1.542	−1.083	2.94	0	4.532

	output	a_{h0}	a_{h1}	a_{h2}	a_{h3}	a_{hc}
		−0.2186	−0.9223	0.3016	0.4601	1.158
A_{DP}	t_{p0}	−0.01137	6.94	−5.533	8.392	−3.86
	t_{p1}	−10.27	−4.483	0.4053	−0.5473	2.221
	t_{p2}	7.241	4.171	−0.1154	0.2826	−0.6105
	t_{p3}	−5.048	−4.286	1.053	−2.252	2.933
	output	a_{p0}	a_{p1}	a_{p2}	a_{p3}	a_{pc}
		−0.1806	0.3971	0.6137	0.2711	−0.4313

Table A26. Same as Table A19, except for graupel using MGI.

		a_{-1}	a_0	a_1	a_2	a_γ
Z_H	t_{z0}	0.05035	0.1612	−0.9495	1.42	0.06475
	t_{z1}	−0.413	1.138	1.737	0.28	−0.1294
	t_{z2}	0.03136	0.3383	−0.2049	0.418	1.075
	t_{z3}	0	0	0	0	0
	output	a_{z0}	a_{z1}	a_{z2}	a_{z3}	a_{zc}
		−1.299	−0.6979	2.013	0	−0.9661
Z_{DR}	t_{d0}	0.01065	−0.3578	1.396	1.099	1.09
	t_{d1}	0.3089	4.831	−4.632	2.024	−8.112
	t_{d2}	−1.664	−0.6087	3.503	−2.733	−0.4736
	t_{d3}	−0.1273	0.4487	0.01367	0.2395	2.693
	output	a_{d0}	a_{d1}	a_{d2}	a_{d3}	a_{dc}
		−0.1931	−0.1168	0.1676	0.1364	0.1246
K_{DP}	t_{k0}	−0.01683	4.589	−0.4093	2.47	−1.895
	t_{k1}	5.392	6.377	−2.802	2.065	−3.562
	t_{k2}	−0.04357	3.648	−3.773	3.228	−3.944
	t_{k3}	0	0	0	0	0
	output	a_{k0}	a_{k1}	a_{k2}	a_{k3}	a_{kc}
		−4.033	3.138	−1.614	0	2.454
ρ_{hv}	$t_{\rho0}$	6.079	6.931	−2.759	0.5902	−2.558
	$t_{\rho1}$	3.26	5.217	−1.969	0.3566	−3.157
	$t_{\rho2}$	0.6283	7.186	−6.945	4.174	−5.393
	$t_{\rho3}$	15.14	6.05	1.224	−1.849	−0.3446
	output	$a_{\rho0}$	$a_{\rho1}$	$a_{\rho2}$	$a_{\rho3}$	$a_{\rho c}$
		−1.784	1.979	−1.135	1.118	0.8201
δ	$t_{\delta0}$	1.493	5.521	2.892	−7.179	−1.963
	$t_{\delta1}$	1.023	−9.487	14.14	−6.837	4.547
	$t_{\delta2}$	−11.03	−7.013	−4.67	6.262	2.509
	$t_{\delta3}$	−0.7814	11.4	−0.02834	−4.49	1.343
	output	$a_{\delta0}$	$a_{\delta1}$	$a_{\delta2}$	$a_{\delta3}$	$a_{\delta c}$
		126.3	−126	259.2	−370.2	244.3
A_H	t_{h0}	−13.2	−8.131	−1.023	0	3.382
	t_{h1}	2.473	10.14	−0.223	0	−6.866
	t_{h2}	5.693	4.098	−0.2904	0	−2.94
	t_{h3}	3.035	9.293	−0.5704	0	−5.574
	output	a_{h0}	a_{h1}	a_{h2}	a_{h3}	a_{hc}
		1.263	−1.847	−0.9443	3.192	−0.3877
A_{DP}	t_{p0}	−0.2315	8.2	−7.933	13.05	−2.995
	t_{p1}	0.231	−14.39	16.06	−19.47	8.873
	t_{p2}	−0.5697	−4.467	5.161	−3.041	4.445
	t_{p3}	−5.489	−6.355	7.946	−8.318	3.76

	output	a_{p0}	a_{p1}	a_{p2}	a_{p3}	a_{pc}
		−0.0998	0.05472	0.1126	0.07723	0.1005

Table A27. Same as Table A19, except for snow using MGI.

References

Aldana, M., S. Pulkkinen, A. von Lerber, M. R. Kumjian, and D. Moisseev, 2025: Benchmarking K_{DP} in rainfall: A quantitative assessment of estimation algorithms using C-band weather radar observations. *Atmospheric Measurement Techniques*, **18**, 793–816, doi:10.5194/amt-18-793-2025.

Anagnostou, E. N., M. Grecu, and M. N. Anagnostou, 2006: X-band polarimetric radar rainfall measurements in keys area microphysics project. *Journal of the Atmospheric Sciences*, **63**, 187–203, doi:10.1175/jas3592.1.

Andrić, J., M. R. Kumjian, D. S. Zrnić, J. M. Straka, and V. M. Melnikov, 2013: Polarimetric signatures above the melting layer in winter storms: An observational and modeling study. *Journal of Applied Meteorology and Climatology*, **52**, 682–700, doi:10.1175/jamc-d-12-028.1.

Aksoy, A., D. C. Dowell, and C. Snyder, 2010: A multicase comparative assessment of the ensemble Kalman filter for assimilation of radar observations. Part II: Short-range ensemble forecasts. Mon. Wea. Rev., 138, 1273–1292, https://doi.org/ 10.1175/2009MWR3086.1.

Augros, C., O. Caumont, V. Ducrocq, N. Gaussiat, and P. Tabary, 2015: Comparisons between S-, C- and X-band polarimetric radar observations and convective-scale simulations of the HYMEX First Special Observing Period. *Quarterly Journal of the Royal Meteorological Society*, **142**, 347–362, doi:10.1002/qj.2572.

——, C., O. Caumont, V. Ducrocq, and N. Gaussiat, 2018: Assimilation of radar dual-polarization observations in the Arome model. *Quarterly Journal of the Royal Meteorological Society*, **144**, 1352–1368, doi:10.1002/qj.3269.

Aydin, K., and Yang Zhao, 1990: A computational study of polarimetric radar observables in hail. *IEEE Transactions on Geoscience and Remote Sensing*, **28**, 412–422, doi:10.1109/tgrs.1990.572906.

——, V. N. Bringi, and L. Liu, 1995: Rain-rate estimation in the presence of hail using S-band specific differential phase and other radar parameters. *Journal of Applied Meteorology*, **34**, 404–410, doi:10.1175/1520-0450-34.2.404.

Baron, P., K. Kawashima, D.-K. Kim, H. Hanado, S. Kawamura, T. Maesaka, K. Nakagawa, S. Satoh, and T. Ushio, 2023: Nowcasting multiparameter phased-array weather radar (MP-PAWR) echoes of localized heavy precipitation using a 3D recurrent neural network trained with an adversarial technique. *Journal of Atmospheric and Oceanic Technology*, **40**, 803–821, doi:10.1175/jtech-d-22-0109.1.

Becerra-Zuniga, N., L. Lacasa, E. Valero, and G. Rubio, 2026: On the role of consistency between physics and data in physics-informed neural networks. arXiv preprint, arXiv:2602.10611, https://arxiv.org/abs/2602.10611.

Besic, N., J. Figueras i Ventura, J. Grazioli, M. Gabella, U. Germann, and A. Berne, 2016: Hydrometeor classification through statistical clustering of polarimetric radar measurements: A semi-supervised approach. *Atmospheric Measurement Techniques*, **9**, 4425–4445, doi:10.5194/amt-9-4425-2016.

Blair, S. F., D. R. Deroche, J. M. Boustead, J. W. Leighton, B. L. Barjenbruch, and W. P. Gargan, 2021: Radar-based assessment of the detectability of Giant Hail. *E-Journal of Severe Storms Meteorology*, **6**, 1–30, doi:10.55599/ejssm.v6i7.34.

Blanke, A., A. J. Heymsfield, M. Moser, and S. Trömel, 2023: Evaluation of polarimetric ice microphysical retrievals with Olympex Campaign Data. *Atmospheric Measurement Techniques*, **16**, 2089–2106, doi:10.5194/amt-16-2089-2023.

Bluestein, H. B., M. M. French, I. PopStefanija, R. T. Bluth, and J. B. Knorr, 2010: A mobile, phased-array Doppler radar for the study of severe convective storms. *Bulletin of the American Meteorological Society*, **91**, 579–600, doi:10.1175/2009bams2914.1.

Brookner, E., 2008: Phased-array and radar astounding breakthroughs—an update. *2008 IEEE Radar Conference*, doi:10.1109/radar.2008.4720771.

Bodine, D. J., R. D. Palmer, and G. Zhang, 2014: Dual-wavelength polarimetric radar analyses of tornadic debris signatures. *Journal of Applied Meteorology and Climatology*, **53**, 242–261, doi:10.1175/jamc-d-13-0189.1.

Bohren, C. F., 1986: Applicability of effective-medium theories to problems of scattering and absorption by nonhomogeneous atmospheric particles. *Journal of the Atmospheric Sciences*, **43**, 468–475, doi:10.1175/1520-0469(1986)043<0468:aoemtt>2.0.co;2.

——, and L. J. Battan, 1980: Radar backscattering by inhomogeneous precipitation particles. *Journal of the Atmospheric Sciences*, **37**, 1821–1827, doi:10.1175/1520-0469(1980)037<1821:rbbipp>2.0.co;2.

Borque, P., S. W. Nesbitt, R. J. Trapp, S. Lasher-Trapp, and M. Oue, 2020: Observational study of the thermodynamics and morphological characteristics of a Midlatitude Continental Cold Pool Event. *Monthly Weather Review*, **148**, 719–737, doi:10.1175/mwr-d-19-0068.1.

——, and ——, 1982: Radar backscattering of microwaves by spongy ice spheres. *Journal of the Atmospheric Sciences*, **39**, 2623–2628, doi:10.1175/1520-0469(1982)039<2623:rbombs>2.0.co;2.

Brecht, R., E. Cardoso-Bihlo, and A. Bihlo, 2025: Physics-informed Neural Networks for tsunami inundation modeling. *Journal of Computational Physics*, **536**, 114066, doi:10.1016/j.jcp.2025.114066.

Bringi, V. N., R. M. Rasmussen, and J. Vivekanandan, 1986a: Multiparameter radar measurements in Colorado convective storms. part I: Graupel melting studies. *Journal of the Atmospheric Sciences*, **43**, 2545–2563, doi:10.1175/1520-0469(1986)043<2545:mrmicc>2.0.co;2.

——, J. Vivekanandan, and J. Tuttle, 1986b: Multiparameter radar measurements in Colorado convective storms. part II: Hail detection studies. *Journal of the Atmospheric Sciences*, **43**, 2564–2577, doi:10.1175/1520-0469(1986)043<2564:mrmicc>2.0.co;2.

Bruggeman, D. A., 1935: Berechnung Verschiedener Physikalischer Konstanten von Heterogenen substanzen. i. Dielektrizitätskonstanten und leitfähigkeiten der mischkörper aus isotropen Substanzen. *Annalen der Physik*, **416**, 665–679, doi:10.1002/andp.19354160802.

Brook, J. P., A. Protat, J. Soderholm, J. T. Carlin, H. McGowan, and R. A. Warren, 2021: HailTrack—improving radar-based hailfall estimates by modeling hail trajectories. *Journal of Applied Meteorology and Climatology*, **60**, 237–254, doi:10.1175/jamc-d-20-0087.1.

Bukovčić, P., A. Ryzhkov, D. Zrnić, and G. Zhang, 2018: Polarimetric radar relations for quantification of snow based on disdrometer data. *Journal of Applied Meteorology and Climatology*, **57**, 103–120, doi:10.1175/jamc-d-17-0090.1.

Bytheway, J. L., M. R. Abel, R. Cifelli, K. Mahoney, and J. M. English, 2022: Demonstrating a probabilistic quantitative precipitation estimate for evaluating precipitation forecasts in complex terrain. *Weather and Forecasting*, **37**, 45–64, doi:10.1175/waf-d-21-0074.1.

Carlin, J. T., and A. V. Ryzhkov, 2019: Estimation of melting-layer cooling rate from dual-polarization radar: Spectral bin model simulations. *Journal of Applied Meteorology and Climatology*, **58**, 1485–1508, doi:10.1175/jamc-d-18-0343.1.

Cao, Q., G. Zhang, E. A. Brandes, and T. J. Schuur, 2010: Polarimetric radar rain estimation through retrieval of drop size distribution using a Bayesian approach. *Journal of Applied Meteorology and Climatology*, **49**, 973–990, doi:10.1175/2009jamc2227.1.

Chen, H., J. Gao, T. Sun, Y. Chen, Y. Wang, and J. T. Carlin, 2024: Assimilation of water vapor retrievals from ZDR columns using the 3DVAR method for improving the short-term prediction of convective storms. *Monthly Weather Review*, **152**, 1077–1095, doi:10.1175/mwr-d-23-0196.1.

——, J. Gao, Y. Wang, Y. Chen, T. Sun, J. Carlin, and Y. Zheng, 2021: Radar reflectivity data assimilation method based on background-dependent hydrometeor retrieval: Comparison with direct assimilation for real cases. *Quarterly Journal of the Royal Meteorological Society*, **147**, 2409–2428, doi:10.1002/qj.4031.

——, T. Sun, K. Zhao, Y. Chen, A. Zhou, and C. Tong, 2025: Dual-polarization radar data assimilation based on Hydrometeor classification and its impact on severe weather prediction. *Journal of Geophysical Research: Atmospheres*, **130**, doi:10.1029/2024jd042797.

Cheng, W.-Y., D. Kim, S. Henderson, Y.-G. Ham, J.-H. Kim, and R. H. Holzworth, 2024: Machine learning–based lightning parameterizations for the CONUS. *Artificial Intelligence for the Earth Systems*, **3**, doi:10.1175/aies-d-23-0024.1.

Cho, J. Y., 2017: A new radio frequency interference filter for weather radars. *Journal of Atmospheric and Oceanic Technology*, **34**, 1393–1406, doi:10.1175/jtech-d-17-0028.1.

de Burgh-Day, C. O., and T. Leeuwenburg, 2023: Machine learning for numerical weather and climate modelling: A review. *Geoscientific Model Development*, **16**, 6433–6477, doi:10.5194/gmd-16-6433-2023.

Deng, M., and Coauthors, 2014: Stratiform and convective precipitation observed by multiple radars during the Dynamo/AMIE experiment. *Journal of Applied Meteorology and Climatology*, **53**, 2503–2523, doi:10.1175/jamc-d-13-0311.1.

Dinh, T.-L., D.-K. Phung, S.-H. Kim, and D.-H. Bae, 2023: A new approach for quantitative precipitation estimation from radar reflectivity using a gated recurrent unit network. *Journal of Hydrology*, **624**, 129887, doi:10.1016/j.jhydrol.2023.129887.

Dixon, M., and U. Romatschke, 2022: Three-dimensional convective–stratiform echo-type classification and convectivity retrieval from radar reflectivity. *Journal of Atmospheric and Oceanic Technology*, **39**, 1685–1704, doi:10.1175/jtech-d-22-0018.1.

Depue, T. K., P. C. Kennedy, and S. A. Rutledge, 2007: Performance of the hail differential reflectivity (HDR) polarimetric radar hail indicator. *Journal of Applied Meteorology and Climatology*, **46**, 1290–1301, doi:10.1175/jam2529.1.

Dorsey, W. M., D. P. Scholnik, and A. Stumme, 2022: Performance comparison of planar, cylindrical, and polygonalized phased arrays for surveillance and ubiquitous radar. *IEEE Transactions on Aerospace and Electronic Systems*, **58**, 596–602, doi:10.1109/taes.2021.3111789.

Doviak, R. J., and D. S. Zrnić, 2006: *Doppler radar and weather observations*. Dover Publications, New York, NY.

Elmore, K. L., Z. L. Flamig, V. Lakshmanan, B. T. Kaney, V. Farmer, H. D. Reeves, and L. P. Rothfusz, 2014: MPING: Crowd-sourcing weather reports for Research. *Bulletin of the American Meteorological Society*, **95**, 1335–1342, doi:10.1175/bams-d-13-00014.1.

Fabry, F., and V. Meunier, 2020: Why are radar data so difficult to assimilate skillfully? *Monthly Weather Review*, **148**, 2819–2836, doi:10.1175/mwr-d-19-0374.1.

Fabry, F., and W. Szyrmer, 1999: Modeling of the melting layer. Part II: Electromagnetic. *Journal of the Atmospheric Sciences*, **56**, 3593–3600, doi:10.1175/1520-0469(1999)056<3593:motmlp>2.0.co;2.

Ferrier, B. S., 1994: A double-moment multiple-phase four-class bulk ice scheme. Part I: Description. *Journal of the Atmospheric Sciences*, **51**, 249–280, doi:10.1175/1520-0469(1994)051<0249:admmpf>2.0.co;2.

Ferrone, A., J. Kopp, M. Lainer, M. Gabella, U. Germann, and A. Berne, 2024: Double-moment normalization of hail size number distributions over Switzerland. *Atmospheric Measurement Techniques*, **17**, 7143–7168, doi:10.5194/amt-17-7143-2024.

Flora, M. L., P. Skinner, C. K. Potvin, B. Matilla, and A. Reinhart, 2025: Assessing the impact of biased target variables on machine learning models of severe hail. *Weather and Forecasting*, **40**, 1015–1028, doi:10.1175/waf-d-24-0051.1.

Fulton, C., P. Kenworthy, J. Lujan, M. Herndon, S. Garner, D. Thompson, and M. Yeary, 2022: Mutual coupling-based calibration for the Horus digital phased array radar. *2022 IEEE International Symposium on Phased Array Systems & Technology (PAST)*, doi:10.1109/past49659.2022.9974962.

Fulton, C., J. L. Salazar, Y. Zhang, G. Zhang, R. Kelly, J. Meier, M. McCord, D. Schmidt, A. D. Byrd, L. M. Bhowmik, S. Karimkashi, D. S. Zrnić, R. J. Doviak, A. Zahrai, M. Yeary, and R. D. Palmer, 2017: Cylindrical polarimetric phased array radar: Beamforming and calibration for weather applications. *IEEE Transactions on Geoscience and Remote Sensing*, **55**, 2827–2841, doi:10.1109/tgrs.2017.2655023.

Gao, J., and D. J. Stensrud, 2012: Assimilation of reflectivity data in a convective-scale, cycled 3DVAR framework with hydrometeor classification. *Journal of the Atmospheric Sciences*, **69**, 1054–1065, doi:10.1175/jas-d-11-0162.1.

Gastaldo, T., V. Poli, C. Marsigli, D. Cesari, P. P. Alberoni, and T. Paccagnella, 2021: Assimilation of radar reflectivity volumes in a pre-operational framework. *Quarterly Journal of the Royal Meteorological Society*, **147**, 1031–1054, doi:10.1002/qj.3957.

Grazioli, J., D. Tuia, and A. Berne, 2015: Hydrometeor classification from polarimetric radar measurements: A clustering approach. *Atmospheric Measurement Techniques*, **8**, 149–170, doi:10.5194/amt-8-149-2015.

Goda, K., Y. Li, S. Boodoo, J. Brimelow, K. Porter, and G. A. Kopp, 2025: Stochastic modeling of radar-derived maximum estimated size of hail for scenario-based hail loss estimation. *International Journal of Disaster Risk Reduction*, **130**, 105819, doi:10.1016/j.ijdrr.2025.105819.

Golbon-Haghighi, M.-H., M. Mirmozafari, H. Saeidi-Manesh, and G. Zhang, 2021: Design of a cylindrical crossed dipole phased array antenna for weather surveillance radars. *IEEE Open Journal of Antennas and Propagation*, **2**, 402–411, doi:10.1109/ojap.2021.3059471.

Heberling, W., and S. J. Frasier, 2021: On the projection of polarimetric variables observed by a planar phased-array radar at X band. *IEEE Transactions on Geoscience and Remote Sensing*, **59**, 3891–3903, doi:10.1109/tgrs.2020.3023640.

Heinselman, P. L., D. L. Priegnitz, K. L. Manross, T. M. Smith, and R. W. Adams, 2008: Rapid sampling of severe storms by the national weather radar testbed phased array radar. *Weather and Forecasting*, **23**, 808–824, doi:10.1175/2008waf2007071.1.

Ho, J., G. Zhang, P. Bukovcic, D. B. Parsons, F. Xu, J. Gao, J. T. Carlin, and J. C. Snyder, 2023: Improving polarimetric radar-based drop size distribution retrieval and rain estimation using a deep neural network. *Journal of Hydrometeorology*, **24**, 2057–2073, doi:10.1175/jhm-d-22-0166.1.

Honda, T., and Coauthors, 2022: Advantage of 30-s-updating numerical weather prediction with a phased-array weather radar over operational nowcast for a convective precipitation system. *Geophysical Research Letters*, **49**, doi:10.1029/2021gl096927.

Hu, J., and Coauthors, 2019: Polarimetric radar convective cell tracking reveals large sensitivity of cloud precipitation and electrification properties to CCN. *Journal of Geophysical Research: Atmospheres*, **124**, 12194–12205, doi:10.1029/2019jd030857.

Huang, H., K. Zhao, H. Chen, D. Hu, P. Fu, Q. Lin, and Z. Yang, 2020: Improved attenuation-based radar precipitation estimation considering the azimuthal variabilities of microphysical properties. *Journal of Hydrometeorology*, **21**, 1605–1620, doi:10.1175/jhm-d-19-0265.1.

Huangfu, J., Z. Hu, J. Zheng, L. Wang, and Y. Zhu, 2024: Study on quantitative precipitation estimation by polarimetric radar using deep learning. *Advances in Atmospheric Sciences*, **41**, 1147–1160, doi:10.1007/s00376-023-3039-0.

Ilotoviz, E., A. Khain, A. V. Ryzhkov, and J. C. Snyder, 2018: Relationship between aerosols, hail microphysics, and Zdr columns. *Journal of the Atmospheric Sciences*, **75**, 1755–1781, doi:10.1175/jas-d-17-0127.1.

Ivic, I., C. Curtis, E. Forren, R. Mendoza, D. Schvartzman, S. Torres, D. J. Wasielewski, and F. A. Zahrai, 2019: An overview of weather calibration for the advanced technology demonstrator. *2019 IEEE International Symposium on Phased Array Systems & Technology (PAST)*, doi:10.1109/past43306.2019.9021053.

Ivić, I. R., C. Curtis, and S. M. Torres, 2013: Radial-based noise power estimation for weather radars. *Journal of Atmospheric and Oceanic Technology*, **30**, 2737–2753, doi:10.1175/jtech-d-13-00008.1.

——, 2022: Quantification of polarimetric PAR effects on weather observables in the phase-coded STSR mode. *IEEE Transactions on Geoscience and Remote Sensing*, **60**, 1–22, doi:10.1109/tgrs.2022.3146358.

——, 2023: Cross-coupling mitigation in polarimetric PAR via antenna tilt. *Journal of Atmospheric and Oceanic Technology*, **40**, 587–604, doi:10.1175/jtech-d-22-0059.1.

Jekic, A., A. Natsaridou, S. Riemer-Sørensen, H. Langseth, and O. E. Gundersen, 2025: Examining the robustness of physics-informed neural networks to noise for inverse problems. arXiv preprint, arXiv:2509.20191, https://arxiv.org/abs/2509.20191.

Jung, Y., G. Zhang, and M. Xue, 2008: Assimilation of simulated polarimetric radar data for a convective storm using the ensemble Kalman filter. Part I: Observation operators for reflectivity and polarimetric variables. *Mon. Wea. Rev.*, **136**, 2228–2245, https://doi.org/10.1175/2007MWR2083.1.

——, M. Xue, and G. Zhang, 2010: Simulations of polarimetric radar signatures of a supercell storm using a two-moment bulk microphysics scheme. *Journal of Applied Meteorology and Climatology*, **49**, 146–163, doi:10.1175/2009jamc2178.1.

Kalnay, E., 2003: Atmospheric Modeling, Data Assimilation, and Predictability. Cambridge University Press, 341 pp.

Kaltenboeck, R., and A. Ryzhkov, 2013: Comparison of polarimetric signatures of hail at S and C bands for different hail sizes. *Atmospheric Research*, **123**, 323–336, doi:10.1016/j.atmosres.2012.05.013.

Karimkashi, S., and G. Zhang, 2013: A dual-polarized series-fed microstrip antenna array with very high polarization purity for weather measurements. *IEEE Transactions on Antennas and Propagation*, **61**, 5315–5319, doi:10.1109/tap.2013.2273813.

——, and G. Zhang, 2015: Optimizing radiation patterns of a cylindrical polarimetric phased-array radar for multimissions. *IEEE Transactions on Geoscience and Remote Sensing*, **53**, 2810–2818, doi:10.1109/tgrs.2014.2365362.

Kashinath, K., and Coauthors, 2021: Physics-informed machine learning: Case studies for weather and climate modelling. *Philosophical Transactions of the Royal Society A:*

Mathematical, Physical and Engineering Sciences, **379**, 20200093, doi:10.1098/rsta.2020.0093.

Kikuchi, H., T. Suezawa, T. Ushio, N. Takahashi, H. Hanado, K. Nakagawa, M. Osada, T. Maesaka, K. Iwanami, K. Yoshimi, F. Mizutani, M. Wada, and Y. Hobara, 2020: Initial observations for precipitation cores with X-band dual-polarized phased array weather radar. *IEEE Transactions on Geoscience and Remote Sensing*, **58**, 3657–3666, doi:10.1109/tgrs.2019.2959628.

Kim, D.-K., T. Suezawa, T. Mega, H. Kikuchi, E. Yoshikawa, P. Baron, and T. Ushio, 2021: Improving precipitation nowcasting using a three-dimensional convolutional neural network model from multiparameter phased array weather radar observations. *Atmospheric Research*, **262**, 105774, doi:10.1016/j.atmosres.2021.105774.

Kleist, D., J. R. Carley, A. Collard, E. Liu, S. Liu, C. R. Martin, C. Thomas, R. Treadon, and G. Vernieres, 2024: *Data assimilation strategy and development plan for NCEP's Environmental Modeling Center*. NOAA/NWS/NCEP Environmental Modeling Center Office Note 517, College Park, MD, https://doi.org/10.25923/kqra-6z66

Knight, C. A., 1979: Observations of the morphology of melting snow. *Journal of the Atmospheric Sciences*, 36, 1123–1130, doi:10.1175/1520-0469(1979)036<1123:ootmom>2.0.co;2.

Kollias, P., R. Palmer, D. Bodine, T. Adachi, H. Bluestein, J. Y. Cho, C. Griffin, J. Houser, P. E. Kirstetter, M. R. Kumjian, J. M. Kurdzo, W.-C. Lee, E. P. Luke, S. Nesbitt, M. Oue, A. Shapiro, A. Rowe, J. Salazar, R. Tanamachi, K. S. Tuftedal, X. Wang, D. Zrnić, and B. P. Treserras, 2022: Science applications of phased array radars. *Bulletin of the American Meteorological Society*, **103**, doi:10.1175/bams-d-21-0173.1.

Kopp, J., A. Manzato, A. Hering, U. Germann, and O. Martius, 2023: How observations from automatic hail sensors in Switzerland shed light on local hailfall duration and compare with hailpad measurements. *Atmospheric Measurement Techniques*, **16**, 3487–3503, doi:10.5194/amt-16-3487-2023.

Kouketsu, T., and Coauthors, 2015: A hydrometeor classification method for X-band polarimetric radar: Construction and validation focusing on solid hydrometeors under moist environments. *Journal of Atmospheric and Oceanic Technology*, **32**, 2052–2074, doi:10.1175/jtech-d-14-00124.1.

Kruger, A., and W. F. Krajewski, 2002: Two-dimensional video disdrometer: A description. *Journal of Atmospheric and Oceanic Technology*, **19**, 602–617, doi:10.1175/1520-0426(2002)019<0602:tdvdad>2.0.co;2.

Kuster, C. M., P. L. Heinselman, and T. J. Schuur, 2016: Rapid-update radar observations of downbursts occurring within an intense multicell thunderstorm on 14 June 2011. *Weather and Forecasting*, **31**, 827–851, doi:10.1175/waf-d-15-0081.1.

Kumjian, M. R., and A. V. Ryzhkov, 2008: Polarimetric signatures in supercell thunderstorms. *Journal of Applied Meteorology and Climatology*, **47**, 1940–1961, doi:10.1175/2007jamc1874.1.

——, A. P. Khain, N. Benmoshe, E. Ilotoviz, A. V. Ryzhkov, and V. T. Phillips, 2014: The anatomy and physics of ZDR columns: Investigating a polarimetric radar signature with a spectral bin Microphysical model. *Journal of Applied Meteorology and Climatology*, **53**, 1820–1843, doi:10.1175/jamc-d-13-0354.1.

Lei, L., G. Zhang, and R. J. Doviak, 2013: Bias correction for polarimetric phased-array radar with idealized aperture and patch antenna elements. *IEEE Transactions on Geoscience and Remote Sensing*, **51**, 473–486, doi:10.1109/tgrs.2012.2198070.

——, G. Zhang, R. J. Doviak, and S. Karimkashi, 2015: Comparison of theoretical biases in estimating polarimetric properties of precipitation with weather radar using parabolic reflector, or planar and cylindrical arrays. *IEEE Transactions on Geoscience and Remote Sensing*, **53**, 4313–4327, doi:10.1109/tgrs.2015.2395714.

Li, W., H. Chen, and L. Han, 2024: Improving explainability of deep learning for polarimetric radar rainfall estimation. *Geophysical Research Letters*, **51**, doi:10.1029/2023gl107898.

Li, X., J. R. Mecikalski, and D. Posselt, 2017: An ice-phase microphysics forward model and preliminary results of Polarimetric Radar Data assimilation. *Monthly Weather Review*, **145**, 683–708, doi:10.1175/mwr-d-16-0035.1.

Li, Z., G. Zhang, M.-H. Golbon-Haghighi, H. Saeidi-Manesh, M. Herndon, and H. Pan, 2021: Initial observations with electronic and mechanical scans using a cylindrical polarimetric phased array radar. *IEEE Geoscience and Remote Sensing Letters*, **18**, 271–275, doi:10.1109/lgrs.2020.2971471.

——, Y. Zhang, L. Borowska, I. Ivic, D. Mirkovic, S. Perera, G. Zhang, D. Zrnić, 2021: Polarimetric phased array weather radar data quality evaluation through combined analysis,

simulation, and measurements. *IEEE Geoscience and Remote Sensing Letters*, **18**, 1029–1033, doi:10.1109/LGRS.2020.2990334.

Liu, C., M. Xue, and R. Kong, 2020: Direct variational assimilation of radar reflectivity and radial velocity data: Issues with nonlinear reflectivity operator and solutions. *Monthly Weather Review*, **148**, 1483–1502, doi:10.1175/mwr-d-19-0149.1.

Liu, P., J. Gao, G. Zhang, and J. T. Carlin, 2024a: Assimilation of radar reflectivity data using parameterized forward operators for improving short-term forecasts of high-impact convection events. *Journal of Geophysical Research: Atmospheres*, **129**, doi:10.1029/2024jd041458.

——, J. Gao, G. Zhang, and J. T. Carlin, 2026: Direct assimilation of polarimetric radar data with a variational approach using both mixing ratio and total number concentration as analysis variables: Observing system simulation experiments. *Monthly Weather Review*, **154**, 79–98, doi:10.1175/mwr-d-24-0264.1.

——, G. Zhang, J. T. Carlin, and J. Gao, 2024b: A new melting model and its implementation in parameterized forward operators for polarimetric radar data simulation with Double moment microphysics schemes. *Journal of Geophysical Research: Atmospheres*, **129**, doi:10.1029/2023jd040026.

Lee, J.-W., K.-H. Min, and G. Lee, 2025: Improvement of a dual-polarization radar operator for ice-phase microphysical terms. *Advances in Atmospheric Sciences*, **43**, 550–564, doi:10.1007/s00376-025-4451-4.

Liou, Y.-C., T.-J. Chou, Y.-T. Cheng, and Y.-L. Teng, 2024: The improvement of short-term quantitative precipitation forecast in mountainous areas by the assimilation of meteorological state variables retrieved by multiple Doppler radar data. *Monthly Weather Review*, **152**, 1339–1355, doi:10.1175/mwr-d-23-0230.1.

Logan, J. T., W. M. Dorsey, and J. A. Valenzi, 2022: Modular all-metal ultrawideband cylindrical array for multifunction operation. *IEEE Transactions on Antennas and Propagation*, **70**, 9175–9183, doi:10.1109/tap.2022.3177504.

Mahale, V. N., G. Zhang, and M. Xue, 2016: Characterization of the 14 June 2011 Norman, Oklahoma, downburst through dual-polarization radar observations and Hydrometeor Classification. *Journal of Applied Meteorology and Climatology*, **55**, 2635–2655, doi:10.1175/jamc-d-16-0062.1.

——, G. Zhang, M. Xue, J. Gao, and H. D. Reeves, 2019: Variational retrieval of rain microphysics and related parameters from polarimetric radar data with a parameterized operator. *Journal of Atmospheric and Oceanic Technology*, **36**, 2483–2500, doi:10.1175/jtech-d-18-0212.1.

Matrosov, S. Y., 2008: Assessment of radar signal attenuation caused by the melting hydrometeor layer. *IEEE Transactions on Geoscience and Remote Sensing*, **46**, 1039–1047, doi:10.1109/tgrs.2008.915757.

——, R. Cifelli, and D. Gochis, 2013: Measurements of heavy convective rainfall in the presence of hail in flood-prone areas using an X-Band Polarimetric Radar. *Journal of Applied Meteorology and Climatology*, **52**, 395–407, doi:10.1175/jamc-d-12-052.1.

Matsui, T., B. Dolan, S. A. Rutledge, W. Tao, T. Iguchi, J. Barnum, and S. E. Lang, 2019: Polarris: A polarimetric radar retrieval and instrument simulator. *Journal of Geophysical Research: Atmospheres*, **124**, 4634–4657, doi:10.1029/2018jd028317.

Maxwell Garnett, J. C., 1904: Color in metal glasses and in metallic films. *Philos. Trans. Roy. Soc. London*, **203A**, 385–420, https://doi.org/10.1098/rsta.1904.0024.

Meneghini, R., and L. Liao, 1996: Comparisons of cross sections for melting hydrometeors as derived from dielectric mixing formulas and a numerical method. *Journal of Applied Meteorology*, **35**, 1658–1670, doi:10.1175/1520-0450(1996)035<1658:cocsfm>2.0.co;2.

Milbrandt, J. A., and M. K. Yau, 2005a: A multimoment bulk microphysics parameterization. Part II: A proposed three-moment closure and scheme description. *Journal of the Atmospheric Sciences*, **62**, 3065–3081, doi:10.1175/jas3535.1.

——, and ——, 2005b: A multimoment bulk microphysics parameterization. Part I: Analysis of the role of the spectral shape parameter. *Journal of the Atmospheric Sciences*, **62**, 3051–3064, doi:10.1175/jas3534.1.

Mirmozafari, M., G. Zhang, C. Fulton, and R. J. Doviak, 2019: Dual-polarization antennas with high isolation and polarization purity: A review and comparison of cross-coupling mechanisms. *IEEE Antennas and Propagation Magazine*, **61**, 50–63, doi:10.1109/map.2018.2883032.

——, G. Zhang, S. Saeedi, and R. J. Doviak, 2017: A dual linear polarization highly isolated crossed dipole antenna for MPAR application. *IEEE Antennas and Wireless Propagation Letters*, **16**, 1879–1882, doi:10.1109/lawp.2017.2684538.

Mitra, S. K., O. Vohl, M. Ahr, and H. R. Pruppacher, 1990: A wind tunnel and theoretical study of the melting behavior of atmospheric ice particles. IV: Experiment and theory for snowflakes. *Journal of the Atmospheric Sciences*, **47**, 584–591, doi:10.1175/1520-0469(1990)047<0584:awtats>2.0.co;2.

Mishler, R., G. Zhang, and V. N. Mahale, 2024: Improving estimation of specific differential phase and assessing differential backscattering phase. *J. Atmos. Oceanic Technol.*, **63**, 803–819, https://doi.org/10.1175/JAMC-D-23-0204.1.

Murillo, E. M., and C. R. Homeyer, 2019: Severe hail fall and hailstorm detection using remote sensing observations. *Journal of Applied Meteorology and Climatology*, **58**, 947–970, doi:10.1175/jamc-d-18-0247.1.

Neuper, M., and U. Ehret, 2019: Quantitative precipitation estimation with weather radar using a data- and information-based approach. *Hydrology and Earth System Sciences*, **23**, 3711–3733, doi:10.5194/hess-23-3711-2019.

NOAA National Severe Storms Laboratory, 2014: Multi-function phased array radar and cylindrical polarized phased array radar report to Congress. [Available online at https://www.nssl.noaa.gov/publications/par_reports/FY14_MPAR_CPPAR_Congressional_Report.pdf.]

——, 2020a: Spectrum efficient national surveillance radar (SENSR): OAR feasibility study final report. [Available online at https://www.nssl.noaa.gov/publications/par_reports/SENSR Final Report.pdf.]

——, 2020b: Preliminary report on polarimetric calibration for the advanced technology demonstrator. [Available online at https://www.nssl.noaa.gov/publications/par_reports/Preliminary Report on Polarimetric Calibration for the Advanced Technology Demonstrator.pdf.]

——, 2021: Advanced technology demonstrator system testing summary. [Available online at https://www.nssl.noaa.gov/publications/par_reports/ATD-System-Testing-Summary-Report.pdf.]

——, 2023: Feasibility and capability of a rotating phased array radar. [Available online at https://www.nssl.noaa.gov/publications/par_reports/Feasibility and Capability of a rotating Phased Array Report to Congress.]

O'Gorman, P. A., and J. G. Dwyer, 2018: Using machine learning to parameterize moist convection: Potential for modeling of climate, climate change, and extreme events. *Journal of Advances in Modeling Earth Systems*, **10**, 2548–2563, doi:10.1029/2018ms001351.

Ortega, K. L., J. M. Krause, and A. V. Ryzhkov, 2016: Polarimetric radar characteristics of melting hail. Part III: Validation of the algorithm for hail size discrimination. *Journal of Applied Meteorology and Climatology*, **55**, 829–848, doi:10.1175/jamc-d-15-0203.1.

Orzel, K. A., and S. J. Frasier, 2018: Weather observation by an electronically scanned dual-polarization phase-tilt radar. *IEEE Transactions on Geoscience and Remote Sensing*, **56**, 2722–2734, doi:10.1109/tgrs.2017.2782480.

Palmer, R., D. Bodine, P. Kollias, D. Schvartzman, D. Zrnić, P. Kirstetter, G. Zhang, T.-Y. Yu, M. Kumjian, B. Cheong, S. Collis, S. Frasier, C. Fulton, K. Hondl, J. Kurdzo, T. Ushio, A. Rowe, J. Salazar-Cerreño, S. Torres, M. Weber, and M. Yeary, 2022: A primer on phased array radar technology for the atmospheric sciences. *Bulletin of the American Meteorological Society*, **103**, doi:10.1175/bams-d-21-0172.1.

——, M. B. Yeary, D. Schvartzman, J. L. Salazar-Cerreño, C. Fulton, M. McCord, B. Cheong, D. Bodine, P. Kirstetter, H. H. Sigmarsson, T.-Y. Yu, D. Zrnić, R. Kelley, J. Meier, and M. Herndon, 2023: Horus—A fully digital polarimetric phased array radar for next-generation weather observations. *IEEE Transactions on Radar Systems*, **1**, 96–117, doi:10.1109/trs.2023.3280033.

Pan, Y., M. Xue, and G. Ge, 2016: Incorporating diagnosed intercept parameters and the graupel category within the ARPS cloud analysis system for the initialization of double-moment microphysics: Testing with a squall line over South China. *Monthly Weather Review*, **144**, 371–392, doi:10.1175/mwr-d-15-0008.1.

Park, J., M. Xue, and C. Liu, 2023: Implementation and testing of radar data assimilation capabilities within the joint effort for data assimilation integration framework with ensemble transformation Kalman filter coupled with fv3-lam model. *Geophysical Research Letters*, **50**, doi:10.1029/2022gl102709.

Pazmany, A. L., J. B. Mead, H. B. Bluestein, J. C. Snyder, and J. B. Houser, 2013: A mobile rapid-scanning X-band Polarimetric (raxpol) doppler radar system. *Journal of Atmospheric and Oceanic Technology*, **30**, 1398–1413, doi:10.1175/jtech-d-12-00166.1.

Polder, D., and J. H. van Santen, 1946: The effective permeability of mixtures of solids. *Physica*, **12**, 257–271, https://doi.org/10.1016/S0031-8914(46)80066-1.

Posselt, D. J., X. Li, S. A. Tushaus, and J. R. Mecikalski, 2015: Assimilation of dual-polarization radar observations in mixed- and ice-phase regions of convective storms: Information content and forward model errors. *Monthly Weather Review*, **143**, 2611–2636, doi:10.1175/mwr-d-14-00347.1.

Putnam, B. J., M. Xue, Y. Jung, N. A. Snook, and G. Zhang, 2017b: Ensemble probabilistic prediction of a mesoscale convective system and associated polarimetric radar variables using single-moment and double-moment microphysics schemes and EnKF radar data assimilation. *Mon. Wea. Rev.*, 145, 2257–2279, https://doi.org/10.1175/MWR-D-16-0162.1.

Raissi, M., P. Perdikaris, and G. E. Karniadakis, 2019: Physics-informed Neural Networks: A deep learning framework for solving forward and inverse problems involving nonlinear partial differential equations. *Journal of Computational Physics*, **378**, 686–707, doi:10.1016/j.jcp.2018.10.045.

Rasmussen, R. M., and A. J. Heymsfield, 1987: Melting and shedding of graupel and hail. Part I: Model physics. *J. Atmos. Sci.*, **44**, 2754–2763, https://doi.org/10.1175/1520-0469(1987)044<2754:MASOGA>2.0.CO;2.

——, V. Levizzani, and H. R. Pruppacher, 1984: A wind tunnel and theoretical study on the melting behavior of atmospheric ice particles: III. Experiment and theory for spherical ice particles of radius > 500 μm. *J. Atmos. Sci.*, **41**, 381–388, https://doi.org/10.1175/1520-0469(1984)041<0381:AWTATS>2.0.CO;2.

Reimann, L., C. Simmer, and S. Trömel, 2023: Assimilation of 3D polarimetric microphysical retrievals in a convective-scale NWP system. *Atmos. Chem. Phys.*, 23, 14 219–14 237, https://doi.org/10.5194/acp-23-14219-2023.

Reimel, K. J., and M. Kumjian, 2021: Evaluation of KDP estimation algorithm performance in rain using a known-truth framework. *Journal of Atmospheric and Oceanic Technology*, **38**, 587–605, doi:10.1175/jtech-d-20-0060.1.

Rodgers, C., 2000: Inverse Methods for Atmospheric Sounding: Theory and Practice. Series on Atmospheric, Oceanic, and Planetary Physics, Vol. 2, World Scientific, 256 pp.

Ronneberger, O., P. Fischer, and T. Brox, 2015: *U-Net: Convolutional networks for biomedical image segmentation*. arXiv:1505.04597

Rosenfeld, D., and C. W. Ulbrich, 2003: Cloud microphysical properties, processes, and rainfall estimation opportunities. *Meteorological Monographs*, **30**, 237–237, doi:10.1175/0065-9401(2003)030<0237:cmppar>2.0.co;2.

Ryzhkov, A. V., 2007: The impact of beam broadening on the quality of radar polarimetric data. *Journal of Atmospheric and Oceanic Technology*, **24**, 729–744, doi:10.1175/jtech2003.1.

——, S. E. Giangrande, V. M. Melnikov, and T. J. Schuur, 2005: Calibration issues of dual-polarization radar measurements. *Journal of Atmospheric and Oceanic Technology*, **22**, 1138–1155, doi:10.1175/jtech1772.1.

——, M. R. Kumjian, S. M. Ganson, and P. Zhang, 2013a: Polarimetric radar characteristics of melting hail. Part II: Practical implications. *Journal of Applied Meteorology and Climatology*, **52**, 2871–2886, doi:10.1175/jamc-d-13-074.1.

——, M. R. Kumjian, S. M. Ganson, and A. P. Khain, 2013b: Polarimetric radar characteristics of melting hail. Part I: Theoretical simulations using spectral microphysical modeling. *Journal of Applied Meteorology and Climatology*, **52**, 2849–2870, doi:10.1175/jamc-d-13-073.1.

——, M. Pinsky, A. Pokrovsky, and A. Khain, 2011: Polarimetric radar observation operator for a cloud model with spectral microphysics. *J. Appl. Meteor. Climatol.*, **50**, 873–894, https://doi.org/10.1175/2010JAMC2363.1.

——, T. J. Schuur, D. W. Burgess, and D. S. Zrnic, 2005: Polarimetric tornado detection. *Journal of Applied Meteorology*, **44**, 557–570, doi:10.1175/jam2235.1.

——, P. Zhang, P. Bukovčić, J. Zhang, and S. Cocks, 2022: Polarimetric radar quantitative precipitation estimation. *Remote Sensing*, **14**, 1695, doi:10.3390/rs14071695.

——, and D. S. Zrnic, 1995: Precipitation and attenuation measurements at a 10-cm wavelength. *Journal of Applied Meteorology*, **34**, 2121–2134, doi:10.1175/1520-0450(1995)034<2120:paamaa>2.0.co;2.

Saeidi-Manesh, H., S. Karimkashi, G. Zhang, and R. J. Doviak, 2017a: High-isolation low cross-polarization phased-array antenna for MPAR application. *Radio Science*, **52**, 1544–1557, doi:10.1002/2017rs006304.

——, M. Mirmozafari, and G. Zhang, 2017b: Low cross-polarization high-isolation frequency-scanning aperture-coupled microstrip patch antenna array with matched dual-polarization radiation patterns. *Electronics Letters*, **53**, 901–902, doi:10.1049/el.2017.1282.

Salazar Aquino, C. M., B. Cheong, and R. D. Palmer, 2021: Progressive pulse compression: A novel technique for blind range recovery for solid-state radars. *Journal of Atmospheric and Oceanic Technology*, doi:10.1175/jtech-d-20-0164.1.

Seo, B.-C., W. F. Krajewski, J. A. Smith, and A. V. Ryzhkov, 2026: Evaluation of radar-derived polarimetric precipitation estimates for extreme rain events using a dense network of rain gauges. *Journal of Hydrometeorology*, doi:10.1175/jhm-d-25-0127.1.

Shedd, L., M. R. Kumjian, I. Giammanco, T. Brown-Giammanco, and B. R. Maiden, 2021: Hailstone shapes. *Journal of the Atmospheric Sciences*, **78**, 639–652, doi:10.1175/jas-d-20-0250.1.

Siggia, A. D., and R. E. Passarelli, 2004: Gaussian model adaptive processing (GMAP) for improved ground clutter cancellation and moment calculation. *Proceedings of ERAD*.

Smith, P. L., C. G. Myers, and H. D. Orville, 1975: Radar reflectivity factor calculations in numerical cloud models using bulk parameterization of precipitation. *Journal of Applied Meteorology*, **14**, 1156–1165, doi:10.1175/1520-0450(1975)014<1156:rrfcin>2.0.co;2.

Snyder, J. C., H. B. Bluestein, D. T. Dawson II, and Y. Jung, 2017: Simulations of polarimetric, X-band radar signatures in supercells. Part I: Description of experiment and simulated ρhv rings. *Journal of Applied Meteorology and Climatology*, **56**, 1977–1999, doi:10.1175/jamc-d-16-0138.1.

——, and A. V. Ryzhkov, 2015: Automated detection of polarimetric tornadic debris signatures using a hydrometeor classification algorithm. *Journal of Applied Meteorology and Climatology*, **54**, 1861–1870, doi:10.1175/jamc-d-15-0138.1.

Stailey, J. E., and K. D. Hondl, 2016: Multifunction phased array radar for aircraft and weather surveillance. *Proceedings of the IEEE*, **104**, 649–659, doi:10.1109/jproc.2015.2491179.

Supinie, T. A., N. Yussouf, Y. Jung, M. Xue, J. Cheng, and S. Wang, 2017: Comparison of the analyses and forecasts of a tornadic supercell storm from assimilating phased-array radar and WSR-88D observations. Wea. Forecasting, 32, 1379–1401, https://doi.org/10.1175/WAF-D-16-0159.1.

Takeishi, A., and C. Wang, 2024: Parameterizing raindrop formation using machine learning. *Monthly Weather Review*, **152**, 649–665, doi:10.1175/mwr-d-22-0175.1.

Trömel, S., M. R. Kumjian, A. V. Ryzhkov, C. Simmer, and M. Diederich, 2013: Backscatter differential phase—estimation and variability. *Journal of Applied Meteorology and Climatology*, **52**, 2529–2548, doi:10.1175/jamc-d-13-0124.1.

Ueki, A., and Coauthors, 2024: Winter precipitation detection using C- and X-band radar measurements. *Remote Sensing*, **16**, 2630, doi:10.3390/rs16142630.

Ushio, T., D.-K. Kim, P. Baron, Y. Wada, T. Mega, F. Mizutani, M. Wada, E. Yoshikawa, S. Satoh, and H. Hanado, 2022: Recent progress on the phased array weather radar at X band. *2022 IEEE Radar Conference (RadarConf22)*, doi:10.1109/radarconf2248738.2022.9764164.

Vivekanandan, J., W. M. Adams, and V. N. Bringi, 1991: Rigorous approach to polarimetric radar modeling of hydrometeor orientation distributions. *J. Appl. Meteor.,* **30**, 1053–1063.

——, S. M. Ellis, R. Oye, D. S. Zrnic, A. V. Ryzhkov, and J. Straka, 1999: Cloud microphysics retrieval using S-band dual-polarization radar measurements. *Bulletin of the American Meteorological Society*, **80**, 381–388, doi:10.1175/1520-0477(1999)080<0381:cmrusb>2.0.co;2.

Wang, Y., T.-Y. Yu, and X. Xiao, 2011: Retrieval of microphysical properties for the mixture of rain and hail using Doppler spectral analysis and genetic algorithm; *35th Conference on Radar Meteorology*; Pittsburgh, PA, USA; American Meteorological Society; P9.86.

——, J. Zhang, A. V. Ryzhkov, and L. Tang, 2013: C-band polarimetric radar QPE based on specific differential propagation phase for extreme typhoon rainfall. *Journal of Atmospheric and Oceanic Technology*, **30**, 1354–1370, doi:10.1175/jtech-d-12-00083.1.

Waterman, P. C., 1965: Matrix formulation of electromagnetic scattering. *Proceedings of the IEEE*, **53**, 805–812, doi:10.1109/proc.1965.4058.

Weber, M. E., J. Y. N. Cho, J. S. Herd, J. M. Flavin, W. E. Benner, and G. S. Torok, 2007: The next-generation multimission U.S. surveillance radar network. *Bulletin of the American Meteorological Society*, **88**, 1739–1751.

Weber, M., K. Hondl, N. Yussouf, Y. Jung, D. Stratman, B. Putnam, X. Wang, T. Schuur, C. Kuster, Y. Wen, J. Sun, J. Keeler, Z. Ying, J. Cho, J. Kurdzo, S. Torres, C. Curtis, D. Schvartzman, J. Boettcher, F. Nai, H. Thomas, D. Zrnić, I. Ivić, D. Mirković, C. Fulton, J. Salazar, G. Zhang, R. Palmer, M. Yeary, K. Cooley, M. Istok, and M. Vincent, 2021: Towards the next generation operational meteorological radar. *Bulletin of the American Meteorological Society*, **102**, doi:10.1175/bams-d-20-0067.1.

Wilson, K. A., P. L. Heinselman, and C. M. Kuster, 2017: Considerations for phased-array radar data use within the National Weather Service. *Weather and Forecasting*, **32**, 1959–1965, doi:10.1175/waf-d-17-0084.1.

Wolfensberger, D., and A. Berne, 2018: From model to radar variables: A new forward polarimetric radar operator for Cosmo. *Atmospheric Measurement Techniques*, **11**, 3883–3916, doi:10.5194/amt-11-3883-2018.

Witt, A., M. D. Eilts, G. J. Stumpf, J. T. Johnson, E. D. Mitchell, and K. W. Thomas, 1998: An enhanced hail detection algorithm for the WSR-88D. *Weather and Forecasting*, **13**, 286–303, doi:10.1175/1520-0434(1998)013<0286:aehdaf>2.0.co;2.

Wu, B., J. Verlinde, and J. Sun, 2000: Dynamical and microphysical retrievals from Doppler radar observations of a deep convective cloud. *J. Atmos. Sci.*, 57, 262–283, https://doi.org/10.1175/1520-0469(2000)057<0262:DAMRFD>2.0.CO;2.

Wu, D., X. Dong, B. Xi, Z. Feng, A. Kennedy, G. Mullendore, M. Gilmore, and W. Tao, 2013: Impacts of microphysical scheme on convective and stratiform characteristics in two high precipitation squall line events. *Journal of Geophysical Research: Atmospheres*, **118**, doi:10.1002/jgrd.50798.

Wu, C., L. Liu, X. Liu, G. Li, and C. Chen, 2018: Advances in Chinese dual-polarization and phased-array weather radars: Observational analysis of a supercell in southern China. *Journal of Atmospheric and Oceanic Technology*, **35**, 1785–1806, doi:10.1175/jtech-d-17-0078.1.

Wurman, J., and M. Randall, 2001: An inexpensive, mobile, rapid-scan radar.

Xu, N., 2023: Scale-dependent inflation for multiscale ensemble-based data assimilation. M.S. thesis, University of Oklahoma, 123 pp., https://hdl.handle.net/11244/340073.

Yang, Y., X. Chen, and Y. Qi, 2013: Classification of convective/stratiform echoes in radar reflectivity observations using a fuzzy logic algorithm. *Journal of Geophysical Research: Atmospheres*, **118**, 1896–1905, doi:10.1002/jgrd.50214.

Yang, Z., P. Liu, and Y. Yang, 2019: Convective/stratiform precipitation classification using ground-based Doppler radar data based on the K-nearest neighbor algorithm. *Remote Sensing*, **11**, 2277, doi:10.3390/rs11192277.

Yokota, S., H. Seko, M. Kunii, H. Yamauchi, and H. Niino, 2016: The tornadic supercell on the Kanto Plain on 6 May 2012: Polarimetric radar and surface data assimilation with EnKF and ensemble-based sensitivity analysis. *Monthly Weather Review*, **144**, 3133–3157, doi:10.1175/mwr-d-15-0365.1.

Yu, T.-Y., M. S. McCord, J. L. Salazar, C. Fulton, R. D. Palmer, and H. B. Bluestein, 2019: Development of a shared mobile C-band polarimetric atmospheric imaging radar (PAIR). *39th Conference on Radar Meteorology*, 1–16.

Yu, Z., L.-Q. Bian, Z.-Y. Ma, B.-H. Chen, C.-C. Tan, and P.-L. Fu, 2020: Rapid-scan and polarimetric phased-array radar observations of a tornado in the Pearl River Estuary. *Journal of Tropical Meteorology*, **26**, 81–86, doi:10.46267/j.1006-8775.2021.008.

Zhang, G., 2016: *Weather radar polarimetry*, Crc Press, 1st Edition, https://doi.org/10.1201/9781315374666.

——, 2022: Cylindrical polarimetric phased array radar for weather observations: A review. *2022 IEEE Radar Conference (RadarConf22)*, doi:10.1109/radarconf2248738.2022.9764328.

——, and R. J. Doviak, 2007: Spaced-antenna interferometry to measure crossbeam wind, shear, and turbulence: Theory and formulation. *Journal of Atmospheric and Oceanic Technology*, **24**, 791–805, doi:10.1175/jtech2004.1.

——, R. J. Doviak, D. S. Zrnić, J. Crain, D. Staiman, and Y. Al-Rashid, 2009: Phased array radar polarimetry for weather sensing: A theoretical formulation for bias corrections. *IEEE Transactions on Geoscience and Remote Sensing*, **47**, 3679–3689, doi:10.1109/tgrs.2009.2029332.

——, R. J. Doviak, D. S. Zrnić, R. Palmer, L. Lei, and Y. Al-Rashid, 2011: Polarimetric phased-array radar for weather measurement: A planar or cylindrical configuration? *Journal of Atmospheric and Oceanic Technology*, **28**, 63–73, doi:10.1175/2010jtecha1470.1.

——, and Coauthors, 2019: Current status and future challenges of weather radar polarimetry: Bridging the gap between radar meteorology/hydrology/engineering and numerical weather prediction. *Advances in Atmospheric Sciences*, **36**, 571–588, doi:10.1007/s00376-019-8172-4.

——, J. Gao, and M. Du, 2021: Parameterized forward operators for simulation and assimilation of polarimetric radar data with numerical weather predictions. *Advances in Atmospheric Sciences*, **38**, 737–754, doi:10.1007/s00376-021-0289-6.

——, J. Vivekanandan, and E. Brandes, 2001: A method for estimating rain rate and drop size distribution from polarimetric radar measurements. *IEEE Transactions on Geoscience and Remote Sensing*, **39**, 830–841, doi:10.1109/36.917906.

Zrnić, D. S., J. F. Kimpel, D. E. Forsyth, A. Shapiro, G. Crain, R. Ferek, J. Heimmer, W. Benner, F. T. McNellis, and R. J. Vogt, 2007: Agile-beam phased array radar for weather observations. *Bulletin of the American Meteorological Society*, **88**, 1753–1766, doi:10.1175/bams-88-11-1753.

——, V. M. Melnikov, and J. K. Carter, 2006: Calibrating differential reflectivity on the WSR-88D. *Journal of Atmospheric and Oceanic Technology*, **23**, 944–951, doi:10.1175/jtech1893.1.

——, G. Zhang, and R. J. Doviak, 2011: Bias correction and Doppler measurement for polarimetric phased-array radar. *IEEE Transactions on Geoscience and Remote Sensing*, **49**, 843–853, doi:10.1109/tgrs.2010.2057436.

——, P. Zhang, V. Melnikov, and D. Mirkovic, 2020: Of fire and smoke plumes, polarimetric radar characteristics. *Atmosphere*, **11**, 363, doi:10.3390/atmos11040363.